ELEKTRONIKA

ELECTRONICS

PREFACE

The International journal "Electronics", published by University of Banja Luka, is devoting its special issue to the 14th International Symposium on Power Electronics - Ee2007. The editor of the journal Prof. Dr. Branko Dokić has invited me, as a guest-editor, to present the most interesting papers of the symposium.

The 14th International Symposium on **Power Electronics - Ee 2007 (Energetska elektronika - Ee 2007)** was held in Novi Sad from November 7-9, 2007. It was co-organized by Power Electronic Society (Serbia) sited in Novi Sad, Faculty of Technical Sciences - Institute for Power, Electronics and Communication Engineering from Novi Sad, Institute "Nikola Tesla" from Belgrade and Novi Sad Fair.

Ministry of Science of Republic of Serbia, Provincial Secretariat for Science and Technological Development of AP Vojvodina, Serbian Academy of Science and Art (SANU), IEEE Serbia & Montenegro Section and Engineering Chamber of Serbia sponsored it.

This significant event shows constant interest of researchers, university professors, engineers, manufacturers, students and other experts in the field of Power Electronics, which more widely comprise power electronics switches, power electronics converters, electrical machines, electric drives, control & measurement in power engineering, power electronics in communications, electric power quality and renewable energy sources.

The first gathering of the Ee, was held in Belgrade in 1973 with 47 presented papers from all over ex- Yugoslavia. Next conferences were in Belgrade in 1975, with 50 papers, in Zagreb in 1978, with 94 papers, in Sarajevo in 1981 with 95 papers, Ljubljana in 1984 with 104 papers, in Subotica in 1986, with 126 papers and in Belgrade in 1988, with 109 papers.

After a long brake, due to unfortunate events in ex-YU, Power Electronics has been revived in Novi Sad. It has re-started as a symposium in collaboration with Novi Sad Fair, as a parallel event during the traditional International Fair on Electronics and Informatics, in 1995, with 79 papers. Next symposiums were held in Novi Sad in 1997, with 98 papers and in 1999, with 82 papers. Significant participation of foreign authors resulted in upgrade of the symposium into International one, which in 2001 gathered 107 papers, in 2003 101 papers, in 2005 93 papers and in 2007 101 papers.

The Ee 2007 International Symposium presented the papers from various institutions of 20 countries (*Bosnia & Herzegovina, Bulgaria, Canada, Croatia, Czech Republic, France, Germany, Greece, Iran, Italy, Republic of Macedonia, Montenegro, Poland, Romania, Russia, Serbia, Spain, Switzerland, United Kingdom and USA*) and gathered more then 200 participants. All papers were published in electronic form (CD-ROM), which also contains multimedia presentations of the organizers and commercial sponsors, facts about Power Electronics Society, as well as complete bibliography from all symposiums on Power Electronics (1973-2007).

Besides, annual meeting of the Power Electronic Society and meeting of the IEEE Industrial Electronics, Industry Application & Power Electronics Joint Chapter were held. Parallel to the symposium, the 14th International Fair "Electronics & Informatics" enabled the participants to meet the latest design and realizations of devices, systems, hardware and software in the field of electronics, telecommunications and computer industry.

The symposium highlighted the problems and practical or virtual solution in many fields. Six topics were put forward: Power Converters, Electrical Drives, Electrical Machines, Control & Measurement in Power Engineering, Power Electronics in Telecommunications and Power Quality. The most interesting contribution were in the areas of power electronics application, industrial motor drives, vector control, distributed power generation, new or improved power electronic converters, power quality, etc.

The selection of the papers presented in this issue is the editor's choice and only one of several possible selections to represent the 14th Symposium on Power Electronics - Ee 2007. We would like to emphasize our thanks to the authors who have accepted our request for prompt respond and fast adaptation of the papers to journal requirements. More details about the symposium can be found at Internet address: www.ftn.ns.ac.yu/dee.

We would also like to invite all readers of the »Electronics« journal to take active participation by submitting the papers or attending the next, the **15th International Symposium on Power Electronics - Ee 2009,** which will be organized in **NOVI SAD, SERBIA in November, 2009** (www.ftn.ns.ac.yu/dee).

Guest Editors:

Prof. Dr. Vladimir Katić

BIOGRAPHY OF Prof.Dr. VLADIMIR KATIĆ

Prof. Dr. Vladimir A. Katić was born in Novi Sad, Serbia in 1954. He received B.Sc. degree from University of Novi Sad in 1978, and M.Sc. and Ph.D. degrees from University of Belgrade in 1981 and 1991, respectively, all in electrical engineering. Since 1978 he has been with Institute for Power, Electronics & Communication Engineering of the Faculty of Technical Sciences, University of Novi Sad, where he is currently Professor and Head of Power Electronics and Converters Group.

From 1993 to 1998 he was the Director of the Institute of Power, Electronics and Telecommunication Engineering and from 1998 - now the Vice-Dean of the Faculty of Technical Sciences of University of Novi Sad.

He is the author of *Electric Power Quality—Harmonics* (Novi Sad, Serbia: Univ. of Novi Sad, 2002, Eng. Monograph Series 6), *Microprocessor Application in Power Engineering – Laboratory Practice* (Novi Sad, Serbia: Univ. of Novi Sad-Faculty of Technical Sciences, 2006, Engineering Textbook Series 124), *Power Electronics —Laboratory Practice* (Novi Sad, Serbia: Univ. of Novi Sad, 2000, Univ. Textbook Series 149), *Power Electronics—Worked Problems* (Novi Sad, Serbia: Univ. of Novi Sad, 1998, Univ. Textbook Series 66), and the Editor of *Modern Aspects of Power Engineering* (Novi Sad, Serbia: FTN—Inst. of Power and Electron. Eng., 1995).

He is the author or co-author of more than 300 scientific papers published in international and national monographs, journals or conferences proceedings. He is also reviewer, member of international programme committees and session chairman of many international or national journals and conferences.

His current interests are in the areas of power electronics, electric power quality and renewable electric energy sources.

Prof. Katić is the Chair of the IEEE Serbia and Montenegro Section and Chairman of the IEEE Joint Chapter of the Industrial Electronics/Power Electronics/Industry Applications Societies and Senior Member of IEEE. He is also president of the Power Electronic Society of Serbia, observer Member at CIGRE SC36 (Paris), Member of International and National Committees of CIGRE and National Committees of CIRED and ETRAN.

IN MEMORIAM

Prof. Dr. Vladan Vučković
1928 - 2006

On October 6, 2006, our professor, friend, mentor, a founder of the Power Electronics conferences, founder and co-president of the Power Electronics Society, distinguished professor and scientist, Prof. Vladan Vučković has passed away.

He was born in Kragujevac (Serbia) on January 24, 1928. He finished his education in Belgrade at Electrical Engineering Faculty in 1953 (B.Sc.) and 1965 (Ph.D.). Since 1954 up to retirement in 1995 he has been employed at Institute Nikola Tesla, Belgrade, with only one break in period from 1989-1993 when he was professor at Electrical Engineering Faculty. He wa also guest professor at the Faculty of Technical Sciences in Novi Sad from 1983-1993.

He started his work on Power Electronics in 1961 when Academician Prof. Petar Miljanić brought the first SRC (Thyristor) at the Institute. In the following 1962 it was designed and developed the first variable-speed induction motor drive with thyristor inverter. That was the beginning of the application of the Power Electronics in Yugoslavia.

In 1981 in „Viskoza" factory in Loznica (Serbia) the first industrial variable-speed induction motor drive with transistor inverter and microprocessor control has been put into operation. In cooperation with "Sever" electrical machine factory from Subotica, prof. Vučković and his assistances developed and manufactured several microprocessor controlled induction motor drives with IGBT transistors and algorithms of vector control. Beside this achievements, numerous high power (up to several hundreds kVA) AC/DC converters, DC/AC converters, static switches, UPS devices have been developed, which found application in computer centers, hospitals, power stations, ships, submarines etc. all over ex-Yugoslavia.

At Faculty of Technical Sciences in Novi Sad Prof. Vučković has taught courses on Industrial and Power Electronics since 1983. His lectures, ideas and high skills inspired and gathered around him a number of young people. He made decisive influence on them to devote their career to the field of Power Electronics and to their future scientific and professional work, so Novi Sad now became one of the most important centers in this field. With Prof. Vladimir Katić in 1997 he has founded the Power Electronics Society in Novi Sad, which took the leading role in organization of further Power Electronics symposiums

He has published three books: »General theory of electrical machines«, »Fundamentals of Power Engineering: Power Converters« and »Electric Drive« and also around 100 scientific and professional papers, projects, studies etc.

With the highest respect, the Power Electronics Society will keep memory on our founder, colleague and a great man Prof. Vladan Vučković.

INTEGRATED POWER STAGES FOR SWITCHED MODE POWER SUPPLIES

Wai Tung Ng, Olivier Trescases, Guowen Wei

University of Toronto, Edward S. Rogers Dept. of Electrical and Computer Engineering,
10 King's College Road, Toronto ON Canada M5S 3G4

Abstract: *With the increasing need to incorporate more complex mixed-signal controller for switched mode power supplies, CMOS compatibility becomes a very important consideration for monolithic DC-DC converters. This paper examines the different power output stage designs and identifies the key device characteristics such as on-resistance, gate capacitance, switching speed that ensure optimized power conversion efficiencies. An integrated 1W DC-DC converter switching at 4MHz with multi-mode operation and a peak power conversion efficiency of 89% is used to illustrate various design trade-offs.*
Keywords: *Power Devices, Output Stage, DC-DC Converter, CMOS Compatibility.*

1. POWER OUTPUT STAGES

The key components in any smart power integrated circuit (PIC) are the output stage and the power devices. The first set of design considerations is the device breakdown voltage, current handling capability, switching speed and process compatibility. Once these initial requirements are satisfied, the attention should be turned to the optimization of the performance of the output stage(s) and the overall system.

In order to minimize power dissipation, most smart PICs are targeted for switched mode operation. The half and full or H-bridges (Fig. 1. and 2) are the most common output configurations in smart PICs. In both cases, the output transistors are called the high side (HS) driver or the low side (LS) driver, depending on its placement with respect to the power supply rail. The LS driver is normally an *n*-channel power MOSFET (*n*-MOS) with both its source and body connected to ground potential. The HS driver can be either another *n*-MOS (*totem pole output stage*) or a *p*-MOS (*push-pull output stage*).

2. N-MOS HIGH-SIDE DRIVER

The choice on which configuration to use is normally determined by the output power level. For high voltage and high current applications (e.g. 10's of volts and several amperes) it is more advantages to use an *n*-MOS transistor as the HS driver. The higher electron surface and bulk mobilities would lead to a smaller device area when compared to a *p*-MOS device for a given on-resistance. However, the drawback in using an *n*-MOS as the HS driver is the fact that a floating source *n*-MOS is required. In addition, in order to turn the HS driver on and off properly, a gate drive voltage that is higher than the supply rail (V_{DD}) is required. This voltage is normally generated using an on-chip bootstrap circuit (with integrated diode as seen in Fig. 2.).
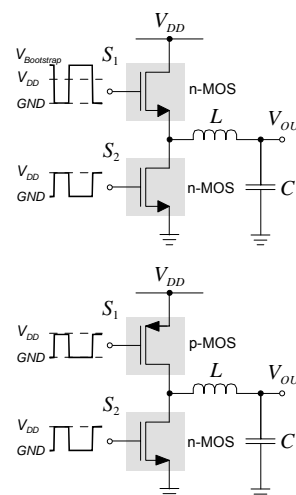

Fig. 1. *Two common output stage circuit configurations: (a) Totem pole output stage with two n-MOS transistors, (b) push-pull output stage with CMOS transistors.*
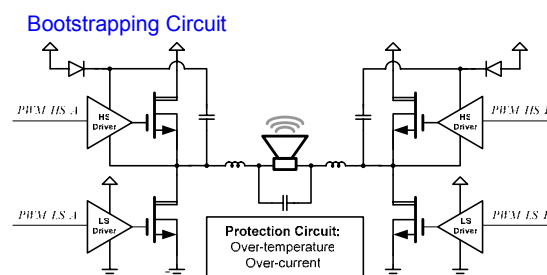

Fig. 2. *A pair of n-MOS/n-MOS totem pole output stages used to form an H-bridge for a class D audio amplifier. Bootstrap circuits are needed to provide gate drive voltages that are higher than V_{DD}.*

Since the power devices are required to support high supply voltage, the extended drain MOSFET (EDMOS) structure [1] is normally employed. A cross sectional diagram of a 40V CMOS compatible process [2] with *n*-MOS, *p*-MOS and floating source *n*-MOS extended drain MOSFETs is as shown in Fig. 3. Although the device cross sections appear to be rather complex, only 3 optional processing steps are introduced to a standard 0.35µm CMOS process to implement all the HV EDMOS devices. These include the addition of the n and p-drift region implant layers and the HV n-well implant layer for the floating source n-EDMOS.

An integrated H-bridge using the same fabrication process with *n*-EDMOS for both HS and LS drivers is as shown in Fig. 4. This output stage was designed for a 40W Class D audio power amplifier. The used of *n*-EDMOS as the power transistors allowed an area efficient
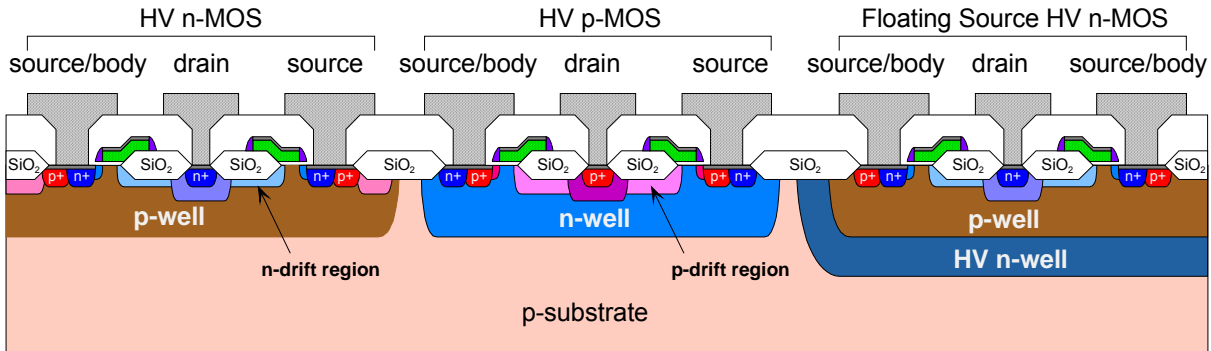
Fig. 3. *A typical range of high voltage power transistors (40V extended drain n-MOS, p-MOS and floating source n-MOS) that can be fabricated using a CMOS compatible technology [1].*

design with on-chip protection circuits, gate drivers, and bootstrap circuits. Both the HS and LS drivers have on-resistances of 220mΩ. With a supply voltage of 25V, the maximum efficiency achieved was 88%.
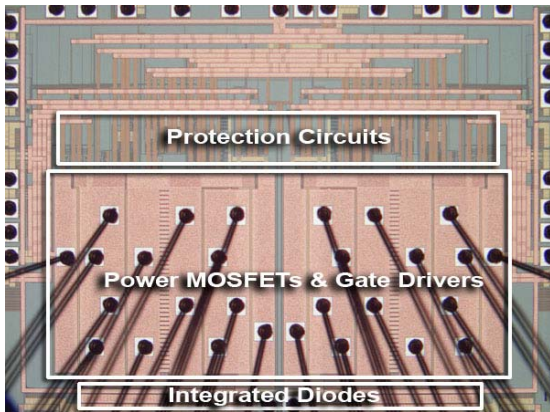

Fig. 4. *A micrograph of an H-bridge output stage for a 50W monolithic class D audio amplifier. This chip is fabricated using a 40V, 0.35µm CMOS technology. The die size is 2.8 ×3.5 mm².*

3. CMOS PUSH-PULL OUTPUT STAGE

In low power, low voltage DC-DC converter applications (e.g. battery powered, 1W operation), the amount of current that needs to be handled by the HS driver is normally less than 1A. In this case, conventional CMOS device structures such as those shown in Fig. 5 would be idea candidates for the HS and LS drivers. No additional process change to the standard CMOS technology is needed, making this approach highly economical and attractive. In addition, the fact that a p-MOS transistor is used as the HS driver, the gate drive signal can be the same PWM (Pulse Width Modulation) waveform with appropriate dead-times.
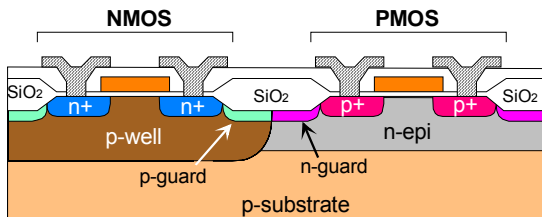

Fig. 5. *Cross section of a standard CMOS technology that can be used to form a push-pull output stage.*

Although the hole surface mobility is approximately three times lower than that for electron, it is often not necessary to design the HS p-MOS driver to have three times the area as the LS n-MOS driver. Since the duty cycle of PWM signal is approximately equal to the ratio of the output to input voltage,

$$\text{Duty Cycle} \simeq V_{out}/V_{in} \qquad (1)$$

the average duration that the HS driver turns on is not 50%. For example, with a Li-ion battery input voltage of 4.2V and an output voltage of 1.0V, the duty cycle for the HS and LS drivers are 24% and 76%, respectively. In order to achieve the best conduction loss versus efficient use of area, the on-resistance of the *p*-MOS transistor can be approximately three times higher (76/24 ≈ 3). Therefore, the same device area can be used for both the *n*-MOS and *p*-MOS.

4. SEGMENTED OUTPUT STAGE

Once the sizes of the HS and LS drivers are determine for a particular peak conversion efficiency and operating frequency, the overall performance of the output stage can be further improved by optimizing the switching loss. The typical source of power losses in a DC-DC converter is as shown in Fig. 6. The output stage is responsible for the gate drive and conduction loss. The gate drive loss, P_{gate} is dominant at low output current (see Fig. 7) and is given by
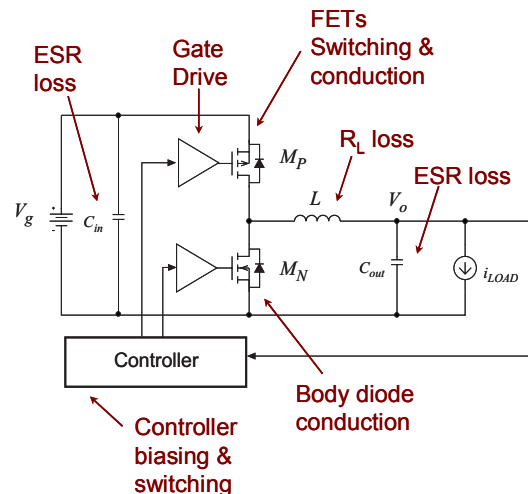

Fig. 6. *Various power losses in a DC-DC converters.*
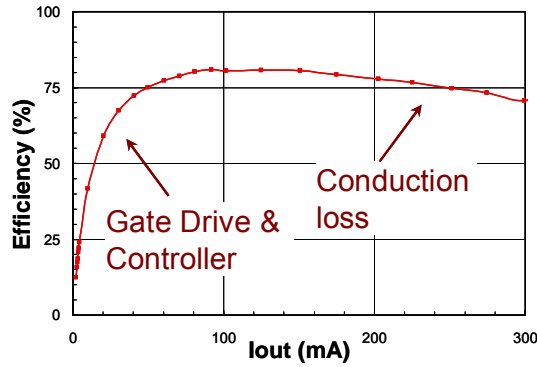
Fig. 7. *Typical power conversion efficiency versus output current. Gate drive and controller losses dominate in the low output current range. Conduction loss is more prominent at high output current.*

$$P_{gate} = f_S \left(C_{gate,P} + C_{gate,N} \right) V_{in}^2 \qquad (2)$$

P_{gate} is proportional to the size of the *n*-MOS and *p*-MOS drivers. If smaller size power transistors can be selected at low output current, P_{gate} can be reduced. This will maintain high power conversion efficiency over a wide range of output current.

The circuit configuration of the *n*-MOS and *p*-MOS drivers in a traditional output stage, as shown in Fig. 8, can be partitioned into parallel combinations of identical transistors. These transistors can be further grouped in to three independently controlled segments to achieve binary weighted sizes of 1, 2, and 4. The gate drive signals are connected to individual gate drivers such that only the gate capacitances of the selected segments are switched. With a digitally controlled DC-DC converter [3], different segment size can be selected according to output current. This allows dynamic optimization of P_{gate}.
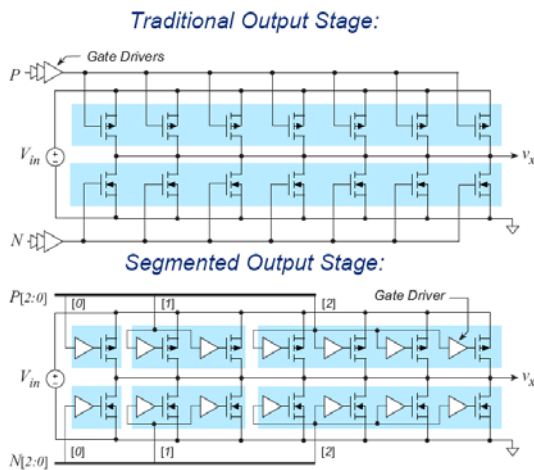

Fig. 8. *Schematic of a traditional CMOS push-pull output stage with two large gate drive circuits for the high-side and low side switches. The segmented output stage is basically a re-organization of the same layout with transistor segments grouped into sizes of 1, 2 and 4.*

This segmented output stage was implemented using a 0.6µm standard CMOS technology with a maximum breakdown voltage of 7V (see Fig. 9). The active device areas for the HS and LS drivers were chosen to minimize the conduction loss for an input voltage range of 2.7 to 4.2V and an output voltage of 1.8V with a

maximum output current of 500mA. The *n*-MOS and *p*-MOS transistors have active areas of 0.15 and 0.37mm^2, respectively. The measured range of on-resistance and P_{gate} are as plotted in Fig. 10. As the transistor size changes from a normalized size of 1 to 7, the gate drive power also increases proportionally for both *n*-MOS and *p*-MOS.
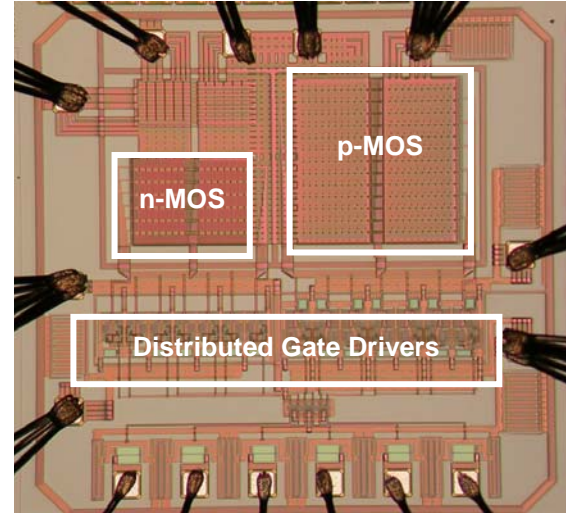
Fig. 9. *A segmented output stage fabricated using a 0.6µm CMOS technology. The n-MOS and p-MOS have active areas of 0.15 and 0.37mm^2, respectively.*
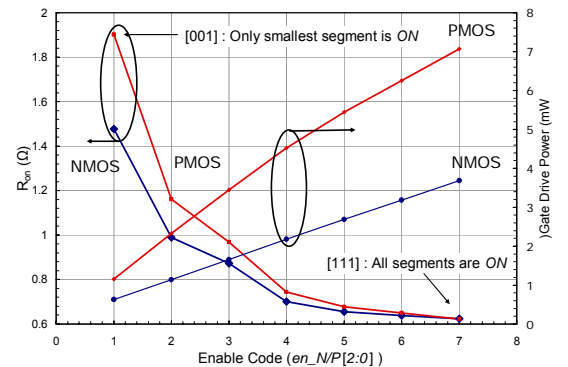
Fig. 10. *Measured on-resistance and gate drive loss for the segmented output stage, ranging from the smallest to the largest segment size.*

However, the on-resistance does not reduce by a factor of 7. The spreads of 0.62Ω to 1.5Ω for the *n*-MOS transistor and from 0.62Ω to 1.9Ω for the *p*-MOS transistor only constitute factors of 2.4 and 3.1. This is due to the fact that the metal interconnect resistance is comparable to the on-resistance of the power MOSFETs.

The efficiency measurements for V_{in} = 2.7V with different enable codes are shown in Fig. 11. Enable code of <111> is equivalent to select all transistor segments, hence the largest transistor size. The power conversion efficiency is highest for large current, but suffers significantly at low output current range. By contract, with enable code of <001>, only the smallest segment is selected. The power conversion efficiency is now highest at low current and reduces as the output current increases. Also included in Fig. 12 are the power conversion efficiencies for the PFM (Pulse Frequency Modulation) and DCM (Discontinuous Conduction Mode) for the largest and smaller power transistor sizes. For very low

output current, it is much more advantageous to switch from PWM to PFM mode. With the use of a digital controller [3], the optimal enable codes and operating mode (PWM or PFM) can be selected such that the peak power conversion efficiency can be maintained over the widest possible output current range. Using this approach, the converter achieved a peak efficiency of 89%. This is a significant improvement by a maximum of 6.9% when compared to the non-segmented case as shown in Fig. 12. The peak efficiency is limited by the relatively high series resistance from the inductor and high-switching losses in the power stage at 4 MHz.
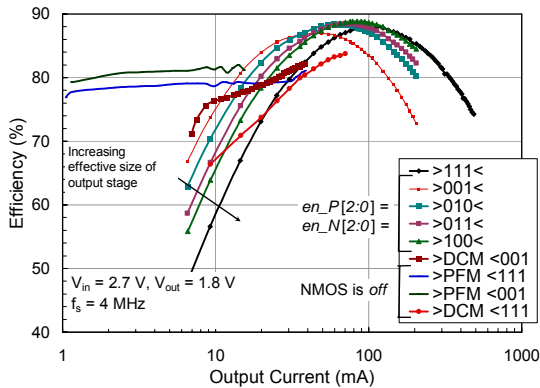
Fig. 11. *Measured efficiency versus output current for V_{in} = 2.7 V. The curves correspond to 5 different segment combinations out of 49 since the NMOS and PMOS use the same enable code.*
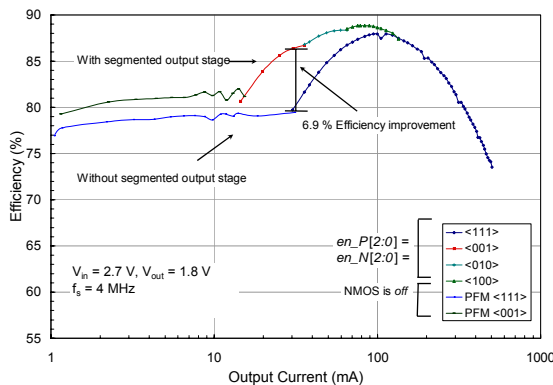
Fig. 12. *Measured efficiency versus output current for V_{in} = 2.7V. In the top curve, the optimal segments are enabled by selecting the appropriate segment size according to the output current. The bottom curve is achieved if segmentation is not used.*

5. CONCLUSIONS

This paper examined different CMOS compatible output stage configurations that are suitable for smart PIC implementation. *n*-channel EDMOS structures are more attractive for the HS driver in totem pole output stages in high voltage, high current applications. Standard CMOS technologies can be used to implement push pull output stages in battery operated low power applications. Further optimization of the power conversion efficiency over a wide range of output current can be realized by using segmented output stages and multi-mode operations.

7. REFERENCES

[1] Peter C. Mei, Katsumi Fujikura, Takaaki Kawano, Satwinder Malhi, "A High Performance 30V Extended Drain RESURF CMOS Device for VLSI Intelligent Power Applications," Symposium on VLSI Technology Digest of Technical Papers, pp. 81-82, 1994.

[2] V.W.Y. Ma, E.H.P. Xu, W.T. Ng, Y. Hara, Y. Furukawa, K. Sakai, H. Imai, T. Naito, S. Nobuyuki, S. Tamura, K. Takasuka, T. Kohno, "Integration of Complementary EDMOS in a Standard 0.35µm CMOS Technology for 40V Applications," EDSSC'03, Tech. Digest, Hong Kong, Dec. 16-18, 2003, pp. 301-304.

[3] O. Trescases, W.T. Ng, H. Nishio, M. Edo and T. Kawashima, "A Digitally Controlled DC-DC Converter Module with a Segmented Output Stage for Optimized Efficiency," 18th Inter-national Symposium on Power Semiconductor Devices and Integrated Circuits (ISPSD '06), Naples, Italy, June 4-9, 2006.

SMART DIGITAL CONTROLLERS FOR LOW-POWER HIGH-FREQUENCY SMPS

Aleksandar Prodić

Laboratory for Low-Power Management and Integrated SMPS Department of Electrical and Computer Engineering University of Toronto, ON, CANADA

Abstract: *A review of advanced digital controller architectures for low-power high-frequency dc-dc and ac-dc switch-mode power supplies (SMPS) is given. Practical implementations of "smart" features improving overall energy utilization, dynamic response, and allowing "plug-and-play" controller operation are described. In parcitular, the paper shwows arhitectures utilizing inherent nonlinearites and imperfections of digital controllers as well as those of controlled power stages. The architectures perform on-line auto-tuning, load estimation and multi-mode operation. Effectivness of the methods is demonstrated through experimental results.*

Keywords: *Low-power SMPS, digital control, auto-tuning, multi-mode*

1. INTRODUCTION

Digital controllers for SMPS supplying miniature portable devices, computers, and other loads ranging from a fraction of watt to several hundreds of watts have emerged as an atractive alternative to predominantly used analog solutions [1]-[4]. The reasons include superior flexibiliity of digital systems, simpler implementation of advanced power management and control techniques [5]-[9], often used in higher power systems. However, becuse of practical implementation problems, the advanced features have not been implemented in low-power systems. Mostly, beacuase of the complexity of the hardware required for their implemenatiation. The advanced control alghoritms usually rely on computation demending alghrotims and require a fairly powerful micrcoporcessor for their implementation. The complexity and cost of such a processor significantly exceed those of the complete low-power SMPS.

In the targeted applications it is required that the controllers are implemented with a simple hardware and have a low power consumption, not effecting the overall system efficency. Often, the total power budget allocated to the controller is measured in microwatts and the siclicon area they can occupy is limitted to a fraction of a mm^2. Because of such stringent requirments, the functionality of the digital controllers for low-power SMPS is often limitted to performing output voltage regulation only.

To introduce advanced control techniques in low-power SMPS, several advanced control techniques and architecrures have been proposed in recent publications [5]-[12]. The techniques improve SMPS efficienchy, dynamic response, system reliability, and can be implemented with a fairly simple hardware. As such, they are well-suited for the digitally controlled low-power SMPS.

The following sections of the paper give a review of a several such techniques and architectures. In Section II an auto-tunning and self-calibration technique and system relying on limit-cycle oscillations is described. Section III shows multimode controllers that utilize inofrmation from duty ratio control value to optimize SMPS efficiency over the full range of operation. A simple digital techniques for improving dynamic response of voltage loops in rectifiers with power-factor correction (PFC) is described in Section IV.

2. LIMIT-CYCLE OSCILLATION (LCO) BASED AUTO-TUNING SYSTEM

The dynamic and static characerics of an SMPS depend on the operating point and output load. They also change with external influences, such as temperature and aging. To account for these and provide stable system operation for all operating conditons, the voltage loop compensator is usually designed in a conservative manner. The bandwidth of the loop is reduced, resulting in a slower dynamic response than possible. As a consequence, the energy storage elements are oversized. In additon, the design is usually performed on the case-by-case basis, further increasing the cost of the SMPS.

To compensate for these, in high power systems, direct measurement of the SMPS parameters such as output load, temperature of components is often employed. The measured values are then used for on-line self-calibration of the controller, i.e. auto-tuning. Often, the measurements are also used to estimate the values of power stage filter components and further improvement of the controller performance. The esimation is usually based on fairly complex data processing [13]-[15], and, as such, not suitable for low-power applications.

The low-power auto-tuning system of Fig.1 does not require a complicated hardware and is used both for improving dynamic response and the SMPS efficency. In steady state it operates as an ordinary voltage mode pulse-width modulation digital controller [2]. A digital equivalent of the output voltage error signal $e[n]$ is passed to a programmable PID compensator that creates digital pulse-width modulator's (DPWM) control signal $d_c[n]$. In steady state, the resolution of the DPWM is high to eliminate nonlinear effects.

Auto-tuning is perfomed regularly or upon potential instability is detected. During that phase, the corner frequency of the power stage and output load are detected and the controller parameters adjusted accordingly. The detection is performed through the analysis of the frequency and amplitude of intentionally introduced small limit-cycle oscillations [16],[17]. The limit cycling is caused in very simple manner, by reducing the resolution of the DPWM and using a PI compensator with a pole at zero. As shown in [12],[18] for such conditions, the LCO at frequency

$$f_{LC} = \frac{1}{2\pi\sqrt{LC}} \tag{1}$$

occurs. Where the parameters L and C are the values of the power stage inductor and the total capacitance connected at the output port of the buck converter of Fig.1, respectively. The peak-to-peak amplitude of the oscillations is

$$A_{pp} = \frac{4}{\pi} D_q \frac{V_{out}}{D} \frac{R}{\omega_0 L} \qquad (2)$$

where, V_{out} is the dc-value of the output voltage, D steady state duty ratio value, D_q quantization step of the DPWM and R the resistance of the output load.

Equation (1) show that f_{LC} coincides with the corner frequency of the power stage, which is the key parameter in conventional PID compensator design [2], [19].
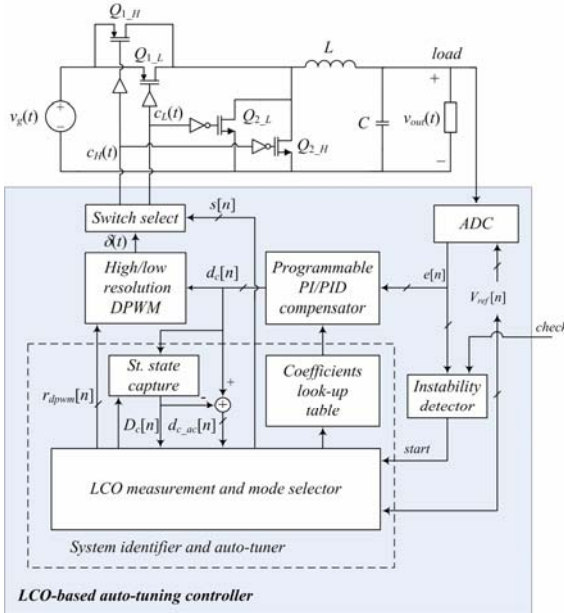

Fig. 1. *LCO-based auto-tuning controller regulating operation of a buck converter.*

By simply measuring this frequency the compensator can be set that for any given operating conditon provides optimal dynamic response.

From (2) it can be seen that the output load can also be estimated. The results can be used for overall efficency optimization, through the power stage segmentation. As shown in Fig.1, instead of having only one pair of switches, like in conventional topologies, two differently sized transistors are used. At low output currents, where switching losses are dominant, smaller and faster transistors Q_{1_L} and Q_{2_L} are active. As the current increases the larger transistors, having smaller on-state resistance R_{on}, start operating, to minimize conduction losses, having the larger impact at heavy loads [19]. The selection of the switches is performed by the auto-tuner, through a control signal $s[n]$. Equation (2) also shows that by changing D_q the amplitude of the oscillations can be set to an arbitrary small value.

It interesting to note that the shown architecture can also be used for design automatization and development of "plug-and-play" controllers. After connected to a power stage, the plug-and-play system "learns" the values of basic power stage parameters and adjust its own operation accoringly.

2.1. Experimental results and practical limitations

Experimental results comparing operation of a conventional single-mode PID compensator and the auto-tuning system are shown in Fig.2. The conventional regulator

is designed following widely adopted design guidelines [2], [19], to result in stable operation for all operating condtions. The auto-tuning compensator is set to have the bandwidth of 1/15 of the power stage switching frequency for any given condition [18].

It can be seen that the auto-tuning controller results in a faster dynamic response allowing for the reduction in the size of power stage filter components.
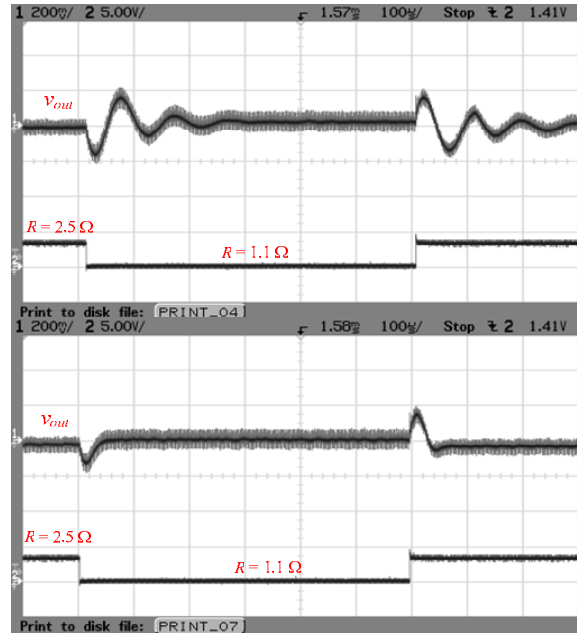
Fig. 2. *Load transient response of a conventional controller (top) and the auto-tuning system (bottom) for the output load changes between 1.3 A and 3A.*

Fig.3. shows auto-tuning for improving efficiency.
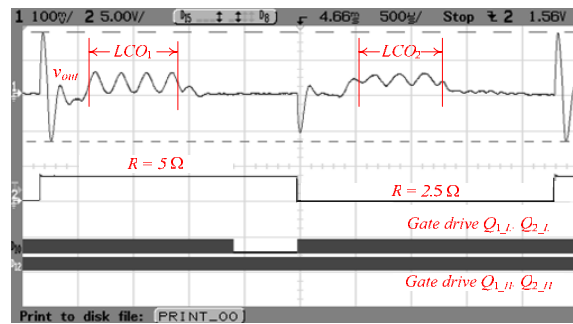
Fig. 3. *Efficiency optimization through the auto-tuning process adjusting the size of the power stage transistors.*

The auto-tuning is activated after load transients, causing LCO of small amplitude at the output. Based on the amplitude of the oscillations the output load is estimated and the transistor gating sequence selected. At the lighter load ($R = 5\ \Omega$) only small transistors are active, while when the load resistance drops to $2.5\ \Omega$ all transistors operate.

Experiments and analysis presented in [12] also revel system constrains. They show that the LCO based load estimation has very limitted accuracy and can only be used for a coarse current estimation. The inductor and capcitor series resistance as well as the dead time circuit significantly

affect the amplitude of the LCO reducing the estimation accuracy.

3. DUTY-RATIO BASED ESTIMATION AND AUTO- TUNING TECHNIQUES

In the ideal converter operating in continous conduction mode (CCM) the duty ratio depends on the ratio of the input and output voltages only. In closed loop operation, conduction and switching losses cause the duty ratio value D to be larger than the ideal.

To account for the losses, a dc-model of the buck converter can be represented with the diagram shown in Fig.4. The influence of all losses is lumped into a resistance r reducing the output voltage.

In duty ratio based estimation and auto-tuning methods [8], [9] this effect is utilized. The deviation from the ideal duty ratiio value is used to determine load
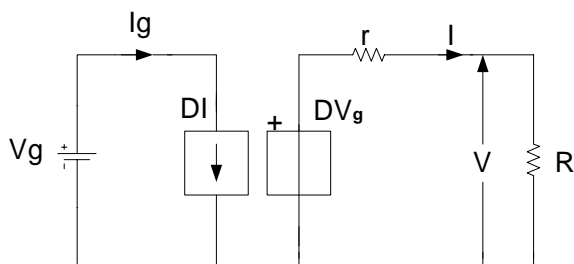
Fig. 4. *Equivalent dc-model of a buck converter including switching and conduction losses.*

current without a costly sensing circuit. Accordingly changes in the operating modes are performed.

The deviation is used to switch between the continous conduction mode (CCM) and pulse-frequency modulation (or discontinous conduction mode), which is more efficent at light loads. Also, as demonstrated in [8], the duty ratio deviation is used to set the optimal non-overlaping times, resulting in the lowest losses of a synchronus buck dc-dc converter.

The current estimation is performed by either calculating the following expression

$$I = \frac{DVg - V}{r} \qquad (3)$$

or, as mentioned earlier, by comparing the actual duty ratio value with the ideal $D_{ideal} = V_{out}/V_g$.

In the non-overlaping time, i.e. dead-time, optimization method [8], the delays between switching actions of the main switch and syncrhonous rectifier are gradually changed until the minimum duty ratio is achieved.

3.1. Experimental results

Fig. 5 demonstrates effective operation of a duty-ratio based current estimator and efficency plot of the system.
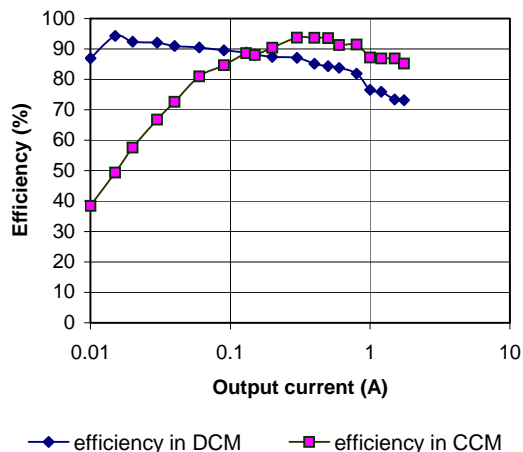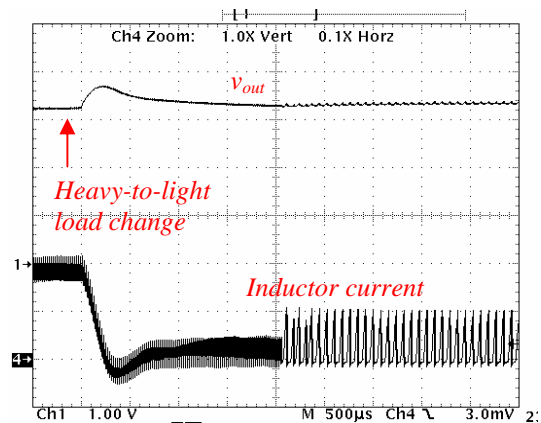
Fig. 5. *Dual-mode operation of a buck converter utilizing duty-ratio based current estimation (top). Efficiency plot (bottom).*

4. DEAD-ZONE METHOD FOR IMPROVING DYNAMIC RESPONSE OF PFC VOLTAGE LOOP

A block diagram of a typical rectifier with power factor correction (PFC) is shown in Fig.6.a. It contains a power stage controlled by two loops [19]. The task of the current loop is to make the input port of the PFC behaving as resistor. It is achieved by forcing the input (line) current $i_{line}(t)$ to follow the input voltage waveform. The outer voltage loop regulates the output voltage by changing the emulated resistance R_e, i.e. the ratio between the input voltage and the current.

An average model of the voltage loop describing its operation is shown in Fig.6.b [19].

Fig. 7. *A large-signal model of a PFC with a digital "dead-zone" voltage loop controller.*

Fig. 6. *A block diagram of a PFC (top); Average model of the voltage loop (bottom).*

In the model, the current loop is replaced with a "lossless" emulated resistor R_e and a controlled power source, whose average power over one converter switching cycle, $T_s = 1/f_s$, is

$$\langle p_{ac}(t) \rangle_{T_s} = \frac{V_g^2 \sin^2(\omega_L t)}{R_e} = \frac{V_g^2}{2R_e}(1 - \cos(2\omega_L t)) \qquad (4)$$

where V_g is the peak value of the input line voltage and $f_L = \omega_L/(2\pi)$ is its frequency. Since this power has dc and ac components, a ripple at twice the line frequency (and its harmonics) occurs across the output filter capacitor C. The voltage loop cannot attempt to remove the ripple. This would cause the emulated resistance to change at a frequency higher than the line frequency, and consequently introduce a significant distortion of the input current waveform [11], [19]- [21].

Commonly, the ripple influence is minimized by limiting the bandwidth of the voltage loop to a frequency significantly lower than the ripple frequency, typically 10 Hz to 20 Hz. As a result, the compensator behaves as a low pass filter strongly suppressing the ripple component.
The main shortcoming of this approach is a slow response to disturbances in the circuit. They cause large voltage drops and overshoots imposing additional stress on the PFC components, as well as on its downstream dc-to-dc converter.

To improve voltage loop dynamic response a very simple digital technique based on the utilization of an insensitive ("dead") zone in analog to digital conversion is employed [11] in the system shown in Fig.7. The output capacitor ripple is eliminated by setting the quantization step of the analog-to-digital converter (ADC) V_q to be larger than the ripple magnitude.

The main advantage of this method over other solutions is its very simple realization. The controller can be implemented with hardware simpler than that used in conventional systems, utilizing a lower-resolution less-expensive ADC.

4.1. Experimental results
Figs. 8 and 9 show a comparison of load transient responses of a conventional and the dead-zone compensator. It can be seen that, for this case, the dead-zone controller results in about five times smaller voltage overshoot and about eight times shorter settling time . Consequently it allows for the use of a much smaller output storage capacitor of the PFC and a downstream converter with a much lower product of the maximum voltage and current ratings.
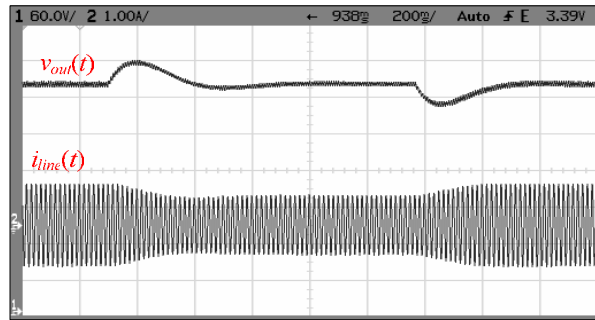
Fig.8. *Load transient response of the conventional controller for the output load change between 100 W and 175 W. The input line voltage is $V_{line} = 220\ V_{rms}$; Ch-1: $v_{out}(t)$ 60 V/div; Ch-2: $i_{line}(t)$ 1 A/div.*
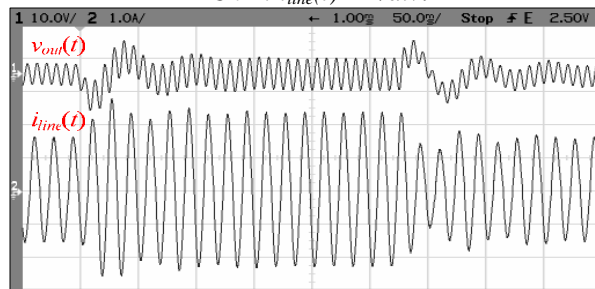
Fig. 9. *Load transient response of the fast dead-zone controller for load change between 100 W and 175 W. The input line voltage is: (a) $V_{line} = 110\ V_{rms}$, Ch-1: $v_{out}(t)$ 10 V/div – ac ; Ch-2: $i_{line}(t)$ 1 A/div.*

5. CONCLUSIONS

Several methods of implementing new features in digital controllers for low-power SMPS are shown. It is demonstrated that "smart" digital controllers improving overall system efficiency, dynamic response, and reducing the overall system size can be built without relying on costly and powerful processors. The methods utilize inherent nonlinear effects and converter imperfections, including limit-cycle oscillations, the influence of losses on the steady state duty ratio value, and a dead-zone in analog to digital conversion. Experimental results verifying effective operation of all of the methods are demonstrated.

6. REFERENCES

[1] A.V. Petrchev, J. Xiao, and S.R. Sanders, "*Architecture and IC Implementation of a digital VRM controller*," IEEE Trans. Power Electron., vol. 18, pp. 356-364, Jan. 2003.

[2] B. Patella, A. Prodić, A. Zirger, D. Maksimović, "*High-frequency digital PWM controller IC for DC-DC converters*," IEEE Trans. Power Electron., vol. 18, pp. 438-446, Jan. 2003.

[3] E. O'Malley, K. Rinne, "*A programmable digital pulse width modulator providing versatile pulse patterns and supporting switching frequencies beyond 15 MHz,*" in Proc. IEEE APEC Conf., 2004, pp. 53-59.

[4] A.P. Dancy, R. Amirtharajah, and A.P. Chandrakasan, "*High-efficiency multiple-output DC-DC conversion for low-voltage systems,*" IEEE Trans. VLSI Syst., vol. 8, pp. 252-263, June 2000.

[5] J. Xiao, A. Peterchev, J. Zhang, S.R. Sanders, "*An ultra low-power digitally-controlled buck converter IC for cellular phone applications,*" in Proc. IEEE APEC Conf., 2004, pp. 383-391.

[6] A.V. Petrchev, S.R. Sanders, "*Digital loss-minimizing multimode synchronous buck converter*" in Proc. IEEE PESC Conf., 2004, pp.20-25.

[7] A.P. Chandrakasan, R.W. Brodersen, "*Minimizing power consumption in digital CMOS circuits*," IEEE Proceedings, vol.83, pp. 498-523, Apr. 1995.

[8] V. Yousefzadeh D. Maksiomivić, "*Sensorless optimization of dead times in DC-DC converters with synchronous rectifiers,*" IEEE Trans. Power Electron., vol.21, pp. 994-1002, July 2006.

[9] A. Prodić and D. Maksimović, "*Digital PWM controller and current estimator for a low-power switching converter,*" in Proc. IEEE COMPEL Conf., 2000, pp.123-128.

[10] A. Prodić, D. Maksimović, "*Digital PWM controller and current estimator for a low-power switching converter,*" in Proc. IEEE COMPEL, 2000, pp. 123-128.

[11] A. Prodić, D. Maksimović, and R.W. Erickson, "*Dead-zone digital controllers for improved dynamic response of low harmonic rectifiers,*" IEEE Transactions on Power Electronics, vol. 21, Issue 1, pp.173-181, Jan. 2006.

[12] Z. Zhao, H. Li, A. Feizmohammadi, and A. Prodić , "*Limit-Cycle Based Auto-Tuning System for Digitally Controlled Low-Power SMPS*," in Proc. IEEE Applied Power Electronics Conference (IEEE APEC), March 2006, pp. 1143-1147.

[13] K. Hirayama, Y. Tone, K. Takagi, H. Murakami, M. Shibata, H. Nagamura, and Y. Takagi, "*Digital AVR application to power plants*," IEEE Trans. Energy Conversion, Vol. 8, pp.602-609, Dec. 1993.

[14] K. J. Åström, T.Hagglund, "*Automatic tuning of PID controllers*," Instrument Society of America, (ISBN 1-55617-081-5), 1988.

[15] S. Majhi and D. P. Atherton, "*Autotuning and controller design for processes with small time delays,*" in Proc. IEE Proc. Control Theory and Applications, vol. 146, pp. 415 – 425, Sept. 1999.

[16] A.V. Peterchev, S.R. Sanders, "*Quantization resolution and limit cycling in digitally controlled PWM converters,*" IEEE Trans. Power Electron., Special Issue on Digital Control, vol.18, pp. 301-308, January 2003.

[17] H. Peng, A. Prodic, E. Alarcon and D.Maksimovic, "*Modeling of quantization effects in digitally controlled DC-DC converters,*" IEEE Trans. Power Electron., vol.22, pp. 1-8, January 2007.

[18] Z. Zhao, A. Prodić, P. Mattavelli,"*Self-Programmable PID Compensator for Digitally Controlled SMPS,*" in Proc. IEEE COMPEL, 2006, pp.112-116.

[19] R. W. Erickson and D. Maksimovic, *Fundamentals of Power Electronics* - Second Edition, Kluwer, 2000

[20] J. B. Williams, "*Design of feedback loop in unity power factor AC to DC converter,*" in Proc. IEEE PESC Conf., 1989, pp. 959-967.

[21] G.Spiazzi, P.Mattavelli, L.Rossetto "*Methods to Improve Dynamic Response of Power Factor Preregulators: An Overview,*" in Proc. IEE European Power Electronics (EPE) Conf., 1995, Vol.3, pp.754-759.

HIGH FREQUENCY POWER SUPPLY FOR ELECTROSTATIC PRECIPITATORS

Slobodan N. Vukosavić, Igor Cvetković, Ilija Stevanović, Dušan Arnautović
University of Belgrade, Electrical Engineering Faculty, Belgrade, Serbia
Institut Nikola Tesla, Belgrade, Serbia
boban@etf.bg.ac.yu

Abstract: *The environmental pollution problems have become global over the past decade. Widely discussed, they are the outcome of the world wide increase in energy consumption and industrial growth. In turn, the overall amount of waste gasses has increased, including the emission of fine, 1 – 50 μm particles, particularly harmful and being a well known health risk. Therefore, both large industrial sites and the power plants require dust cleaning equipment and on-line pollution control. Automated control is required for the equipment to operate on its own, without the need for a continuous operator intervention. Control goals include the need to meet the environmental regulations, keeping at the same time the power losses and the overall energy consumption under control, in order to reach the energy efficiency goals. In this article, an overview of electric filter performance problems is discussed, and the summary of available technologies and solutions is outlined. Experimental data is obtained from TENT-A power plant, where the electric filters of the waste gasses have been reconstructed and improved in cooperation with ETF, University of Belgrade, INT, IMP and Energoprojekt.*

Key Words: *Electrostatic precipitation, waste gasses, polution control, electrofilters, power plants.*

1. INTRODUCTION

The state of the art dust cleaning methods include the electrostatic precipitators (ESP), forcing the waste gas to flow between large electrode plates, exposed to pulsating DC voltages of several tens of kV. Exposure to high strength electric field charges dust particles and they migrate towards the collecting plate, which is the positive one, and in most cases grounded. The other, negative electrode is attached to the negative supply rail of the controllable DC voltage source. The electrode surface is barbed and equipped with appropriate protruding spikes, responsible for an enhanced ionization. The migration of the charged dust particles takes place due to the electric forces exerted by the field. The drift velocity of the particles and their collection efficiency largely depend on the gas speed and the eventual turbulent flow. To enhance the filtering, the ESP comprise several (up to 8) series connected sections, wherein the output gas from the previous section becomes the input to the next. In such cases, the subsequent section may collect the dust particles that were properly ionized within the previous section, but were not collected due to an insufficient particle drift and/or too large speed of the gas stream.

In an attempt to enhance the ionization, drift speed and filtering, the voltage between electrodes can be increased. Though, along with the voltage increase, corona effects do pass into arcing. The electric arc within the filter effectively short circuits the power source and results in large currents and mass ionization. Following the arcing, the filter should be kept off the power source for several tens of milliseconds in order to allow for the ionized gasses to

evacuate. Otherwise, at the reconnection without the de-ionization interval, the filter won't be able to withstand the reconnected voltage and will fall into arcing and short circuit again.

2. ESP OPERATING PRINCIPLES

ESP filter comprises a system of emission and collection electrodes. The former are connected to a negative DC voltage ranging from -50kV to -100kV, and they are equipped with protruding spikes or barbed elements, giving a rise to increased corona and ionization effects. On the other hand, the collection electrodes are grounded and their surface is mostly flat. The waste gasses run at a speed of 1-3 m/s through the space between the electrode plates, separated by 30-40 cm. The presence of ionized gas and a relatively strong electric field results in ionization of waste particles and their motion towards the collection electrodes. Waste particles are ionized by both the diffusion and the effects of the electric field. The charge received by a particle through the effects of the later can be estimated [3] as:

$$n = \left(\frac{3\varepsilon}{\varepsilon_r + 2} \right) \left(\frac{Ed^2}{4e} \right) \left(\frac{\pi \cdot eZ_i N_i t}{1 + \pi \cdot eZ_i N_i t} \right) \tag{1}$$

where

n – stands for the waste particle charge expressed in terms of single electron charges (e),
ε - represents the equivalent permeability of the gas mixture,
E – stands for the strength of the electric field,
e – is the electron charge,
d – stands for the waste particle diameter,
Z_i – represents the ion mobility,
N_i – is the ion concentration,
t – stands for the time.

In Eq. (1), the product of the two leading factors represents the peak charge, while the third factor describes dynamics of the charging process. The Eq. (1) indicates that the particle charge acquired through the electric field effect increases with the square of the particle diameter. On the other hand, the charge induced by the diffusion is given in Eq (2):

$$n = \frac{dkT}{2e^2} \ln \left(1 + \frac{\pi \cdot dc_i e^2 N_i}{2kT} t \right) \tag{2}$$

where

k – stands for the Bolcman constant,
T – stands for the absolute temperature,
c_i – represents the average speed of the ion thermal drift.

From Eq (1) and (2), the charge increases with the particle size and appears to be unlimited. Smaller particles are charged mainly by diffusion, due to logarithmic dependence in Eq. (2). In Fig. 1, precipitation efficiency is given as a function of the particle size.
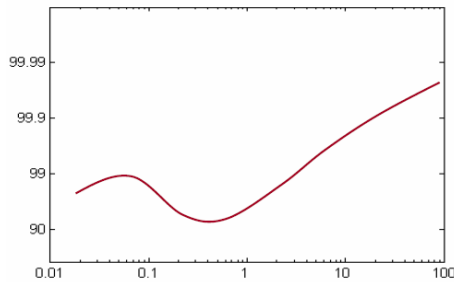
Fig. 1. *Precipitation efficiency, given in logarithmic scale on vertical axis, changes as a function of the particle size, given in μm on the abscise.*

Below 0.1 μm, diffusion charge is sufficient to yield an efficient precipitation. Particles above 1 μm are removed efficiently due to their charging through the electric field effects. In the intermediate zone, where the diffusion effect does not follow an increase in particle size, while the field effects is not yet pronounced, the particle extraction is less efficient. In order to bring the collection efficiency of the particles with 0.1 mμ < D < 1 mμ up to the required level, the ESP unit control can be modified. One of possibilities is the introduction of adaptive intermittent power supply of the ESP plates.

2.1. Positive and negative corona

In the vicinity of protruding elements of the electrode, such as the edges and spikes, the electric field has an increased value may reach the level where gasses get ionized. Up to reasonable voltages, the effect, known as corona, is strictly local and does not develop into mass ionization and arcing. Corona produces ionized particles, and is therefore crucial for the precipitation efficiency. Next to the spike mounted on a positive electrode, gas particles are deprived of electrons and turned into positive ions. The ESP unit can operate with either positive or negative corona.

Positive corona has a lower breakdown voltage. Therefore, the voltage across the plates and the electric field would both be lower, resulting in lower precipitation efficiency. Negative corona withstands higher voltages and offers better filtering. On the other hand, negative corona releases more ozone (O_3) into the output stream. Elevated levels of ozone are known to be health risk as well. Therefore, all the air cleaning and conditioning devices in commercial, office and residential area are based on positive corona. The negative corona gets used in industrial, large filters [3], where the output gasses get released into the atmosphere at high levels above the ground, using chimneys and other gas ducts.
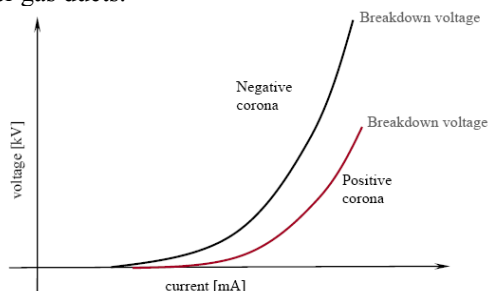

Fig. 2. *Voltage-current characteristics for positive and negative corona.*

It has to be noted that negative corona cannot take places with some gasses, such as the hydrogen, due to the intrinsic lack of the possibility to produce the ions of the appropriate polarity.

3. PERFORMANCE OF INDUSTRIAL ESP UNITS

ESP units with negative corona are widely used in nowadays industries and power plants, due to their capability to provide efficient filtering of gas flows of several hundred cubic meters per second, with a minimal drop in the air pressure. Key feature leading to desired cleaning efficiency is the proper power supply of the electrodes. Controlled high voltage power supply has to maximize the particle charge. In the area next to the collection electrodes, it has to provide the electric field as high as possible, in order to improve the precipitation process. According to White [2], the mechanism of the power supply affecting the ESP efficiency has to do with the migration speed:

$$\omega_k = \frac{K \cdot E \cdot Q}{3\pi \eta d} \tag{3}$$

where

E- stands for the electric field,
Q- stands for the particle charge,
η – stands for the gas viscous coefficient,
d – stands for the particle diameter,
K – is the function of dielectric permeability, $K=f(\varepsilon)$.

Precipitation is largely affected by the gas content. Chemical composition of the exhaust gasses depend upon the fuel (coal in cases of thermal power plants). Precipitation mainly depends on:
- chemical composition of the exhaust gasses,
- chemical composition of the fine particles carried by the gas flow,
- ionization characteristics of the gas,
- conductivity and dielectric permeability of the fine particles (i.e. ashes).
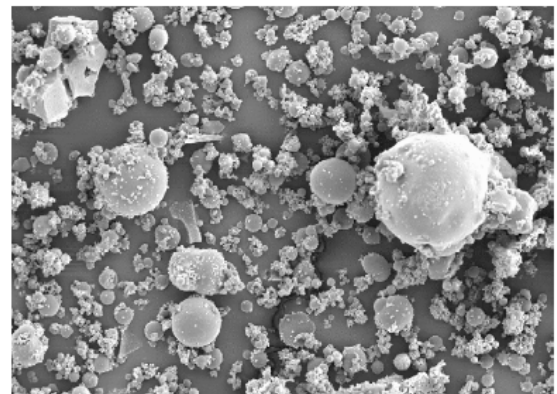
Fig. 3. *Microscopic view of fine particles (ashes) collected on positive, collecting electrode.*

The space between electrodes consists of the area next to the negative, emission electrode, where the ionization process takes place. In between, the interelectrode space is filled with gasses and flying fine particles. Next to the collecting (positive) electrode, which is grounded in most cases, a thin layer of collected fine particles and ashes is attached to the flat surface of the collector. Key factors determining the ionization and precipitation performance are the particle electrical resistance, their surface and ionization characteristics of the exhaust gas. At coal run power stations,

the gas characteristics are mainly beneficial, while the particle specific resistance and surface are often causing problems.

Specific electric resistance (i.e. conductivity) of fine particles is a variable, hardly predictable parameter. It depends on chemical composition of the fuel, the contents of water and sulphur, on the size and form of particles, electric field strength and other conditions. Whenever the specific resistance exceeds 1010 Ωcm, the ESP operation is prone to problems and the filtering efficiency is low. High resistance of the ashes often results in the back corona, the adverse phenomenon where the field strength increases within the accumulated dust layer clinging on the collector, explained in Section 2.1. The next figures illustrate the change in the specific electric resistance of particles with the sulphur contents and the temperature.
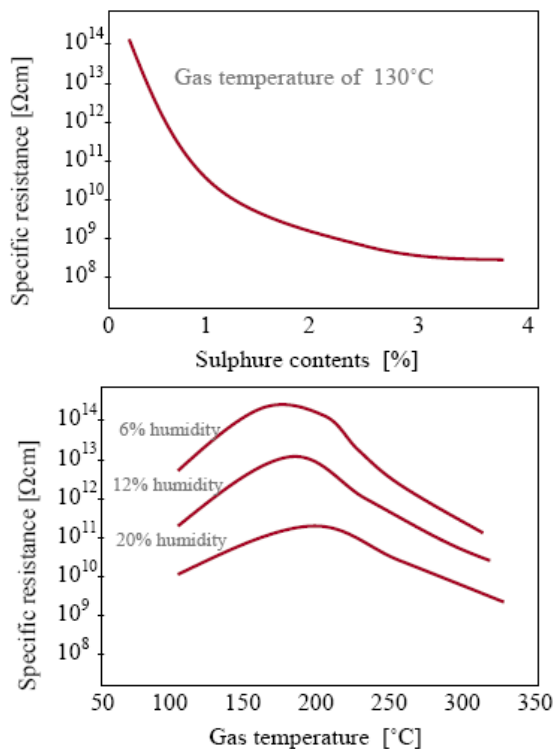
Fig. 4. *Specific resistance change with temperature and sulphure contents.*

Besides other effects, the specific surface of particles, expressed in square meters per gram (m2/g), represent another factor which affects greatly performance of the ESP. This factor has a key role in particle charging process, and it makes either the field effect charging or the diffusion the prevailing mechanism of the particle charging.

3.1. Back corona

The ESP units running at coal-driven thermal power plants frequently suffer the back corona effect. Heated coal dust is brought to the burner, and the exhaust gasses, being the product of combustion, are fed to the ESP units. The gas temperate exceeds 150 degrees Centigrade, while the gas speed ranges from 1 m/s to 2 m/s. Whenever the coal has a low sulphur contents, conductivity of the ashes is low (Fig. 4). As the dust accumulates at the flat collection electrode, the layer gets thicker. With a low conductivity, the field strength within the layer is rather high. With thickness increase, the voltage across the layer goes up, eventually

leading to the dielectric breakdown of non-conductive ashes. This phenomenon is called the back corona effect.

The back corona takes place at the positive electrode. It heats up the dust and produces ions of the opposite polarity. Interacting with the ions generated by the emission electrodes by negative corona, recombination process takes place, impairing the ionization and precipitation process, leading to an increase in the power consumption, and reducing the filtering efficiency.
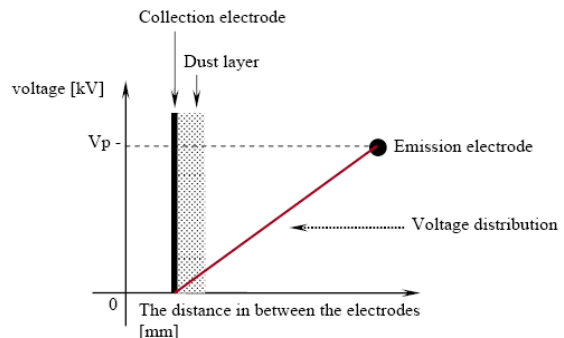
Fig. 5. *The voltage distribution between the electrodes in cases with a thin layer of conductive dust on the collection electrode.*
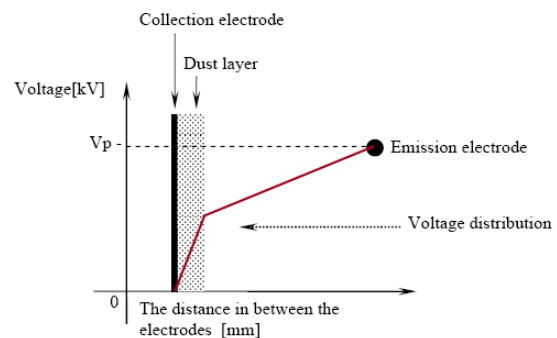
Fig. 6. *The voltage distribution between the electrodes in cases with a thick layer of highly resistive dust.*

The principal drawback of the back corona is generation of the opposite polarity ions, giving rise to recombination within the inter-electrode space and reducing the precipitation efficiency. The net charge of the particles is reduced, as well as their drift speed, while the power consumption is increased, worsening the overall performance. In extreme cases, the dust layers may heat up and begin to glow.

In most practical ESP units, the back corona appears mainly due to a high electrical resistance of the flying ashes [2]. When the back corona takes place, control actions such as the voltage reduction, a brief power down interval, and rapping may provide for a remedy. The back corona can be detected from the spectral properties of the electrode current, but also from the plain U-I characteristics of the plates.

3.2. U-I Characteristics of the plates

In Fig. 7, the U-I characteristic of the plates is given for the case when the ESP operates properly and the back corona is absent. At the onset voltage, the corona effect, generated by the emission electrode cuts in and the discharge current begins to rise as the voltage further increases. Stable corona discharge ends as the voltage reaches the breakdown level, where the field strength in certain areas of the ESP inner space reaches the breakdown levels for the given gas

mixture. At this point, mass ionization and the electric arc are generated, and the voltage between the plates drops down next to zero. In such conditions, the power supply unit is short circuited, and it must be powered off for a short while. The power down interval following the arc must be sufficient for all the arc-generated charges to get neutralized. Any attempt to power up the plates while the mass ionized gasses are still in between the plates would just result in another arc and short circuit.

Difficulties of the efficient ESP control arise from the fact that the precipitation efficiency reaches the maximum just next to the breakdown voltage. According to measurements performed on the block A1 ESP within the TENT-A thermal power plant, the voltage reduction from 100% to 90% of the maximum sustainable results in an increase in the amount of dust within the exhaust gas of merely 4 times. Hence, the voltage between the plates has to be controlled in such way that the system is brought to the edge of the breakdown, yet never passing the breakdown threshold. Luckily, as the voltage is increase and reaches the breakdown level, the nature of the corona phenomena changes and such changes do affect the spectral contents of the electrode current, thus providing the means of detecting the voltage margin and allowing for the proper ESP control to be formulated.
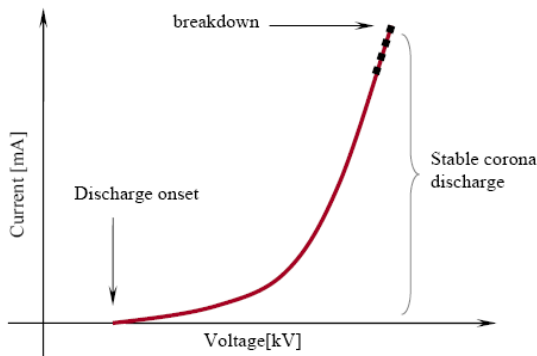

Fig. 7. *U-I characteristic of the plates in cases with no back corona.*

In Fig. 8, the U-I characteristics is given for cases where the back corona builds up within the layers of the dust compressed on the collecting electrode. Due to the back corona modulated conductivity of the inner space and the recombination of the opposite ions, progressive increase in the ESP current leads to a decline in the voltage. This phenomenon may be advantageously used for detecting the back corona and providing the control remedy.
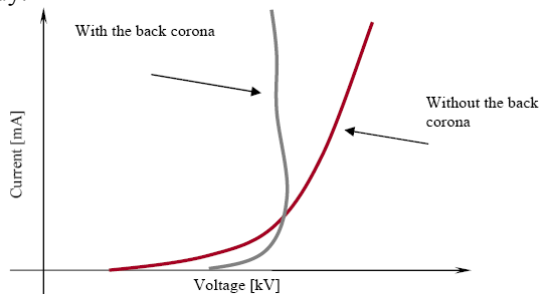
Fig. 8. *U-I characteristic of the plates in cases with back corona.*

4. HIGH FREQUENCY ESP UNITS

Conventional 50 Hz design had been predominant solution for controlling the particulate emission from large electrostatic precipitators. Although capable to reach removal efficiencies up to 99,8%, 50 Hz design suffers a number of drawbacks, leading to a poor energy efficiency, very large size of electrode plates, and it can not compete with the high frequency HFESP.

In Fig. 9, simplified power supply circuit for the 50Hz, SRC driven ESP is given. Resulting voltages and currents are presented in Fig. 10. Essentially, the plates are supplied with rectified 50Hz waveform. Therefore, the voltage pulsates at a pace of 100Hz, passing quickly the crest value and falling down into dale. Hence, the time interval when the instantaneous voltage is close to the breakdown value, leading to a rich ionization and efficient precipitation, is very short. In brief, the ESP filters only at the peaks of the voltage crest, while operating idle in between the two 10ms spaced crests.

With conventional 50 Hz design, the output DC current is discontinuous, depending on the thyristor firing angle. The input line current is therefore distorted and lagging. As a consequence, the input power factor is very poor, with a high harmonic distortion in the mains supply. Reactive and apparent power are very large, with $\cos(\varphi) < 0.65$, whilst power factor $\lambda=P/S < 0.5$. On the other hand, the HFESP high frequency supply has diode rectifier in input stage with $\cos(\varphi)$ above 0.95 and power factor above 0.75.

During the intermittent operation of conventional 50Hz system, the ESP pulsations reflect directly to the main 6kV/0.4kV transformer, supplying the whole ESP; as the system does not have any intermediate filters or intermediate DC-link. Low frequency (3-10 Hz) pulsations introduce a flicker, mechanical stress and audible noise. These problems are resolved with HFESP, by adopting a 3-phase rectifier, turning the 3x400V, 50 Hz main supply into a stable DC-link voltage, followed by a 10-20 kHz IGBT H-bridge.
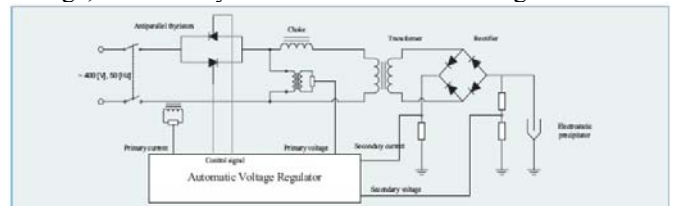
Fig. 9. *Simplified schematic diagram of the 50Hz, SCR power supply unit.*
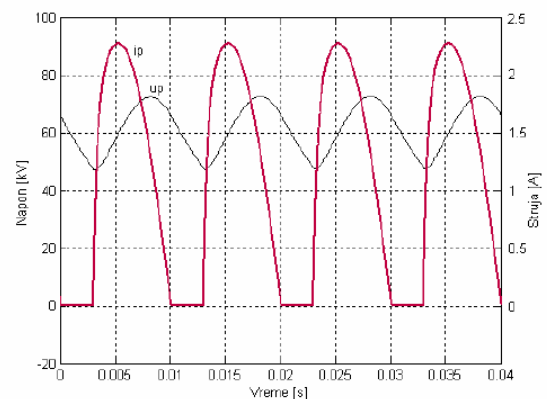
Fig. 10. *Typical voltage and current waveforms obtained with a 50Hz supplied, SCR driven ESP.*
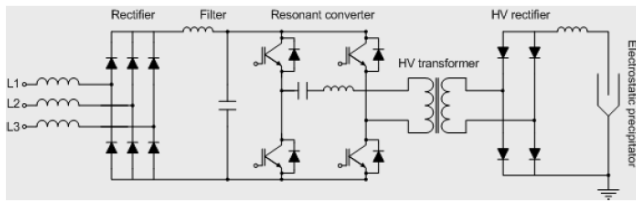
Fig. 11. *High frequency ESP supply.*
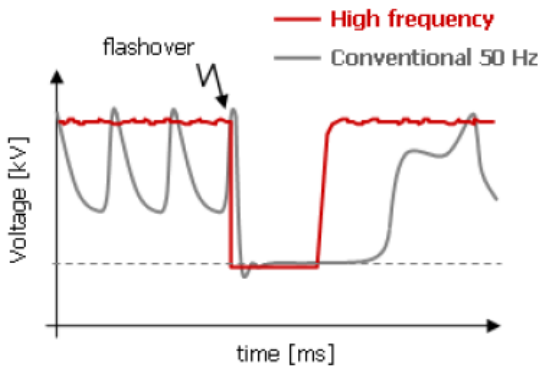
Fig. 12. *HFESP reaction to the flashover.*

The efficiency of the precipitation can be increased by providing the power supply which keeps the voltage closer to the breakdown threshold over longer time intervals. With $f = 10$ kHz supply of the transformer in Fig. 9, the rectified pulses at the output would be spaced 50 μs. In such case, due to a finite capacitance of the plates and the associated low pass filtering, the voltage across the plate would be almost ripple-free, without any significant crests and deeps. As a consequence, it would be possible to control the plate voltage more accurately, and keep it next to the breakdown level almost at all times.

In Fig. 11, simplified electrical schematic of the high frequency ESP supply is shown. It comprises:

- Three phase diode rectifier,
- IGBT H bridge,
- High frequency - high voltage transformer,
- High voltage, high frequency diode rectifier,
- Digital Voltage, rapping and heating Controller & Integrated PLC.

HFESP (high frequency ESP power supply and control) require a lower size and weight of electrodes, offers significant energy savings, prevents back corona, brings up a very fast reaction to flashover, results in a much higher high power factor, and has a transformer/rectifier set several times smaller and lighter compared to traditional 50Hz design. Compared to conventional 50Hz power supply, the HFESP package offers a significant weight and size reduction. For the ratings of 75kV and 1000mA, the weight of the complete system is some 300kg, which can be installed directly on ESP roof. Notice at this point that the 50Hz transformer only weighs over 1500 kg.

Development and deployment of HFESP units rated 1000mA and 2000mA is performed at the Department of Electrical Engineering, University of Belgrade. Key element of any ESP is the proper control, allowing for the proper corona control, sufficient ionization, and the suppression of the back corona effect. Digital Voltage Controller represents the most important component of the HFESP device. It is developed on the bases of the last generation Digital Signal Processors, and comprises the proprietary adaptive algorithm

of voltage control, tested at major Serbian thermal power plants and confirmed a superior particle filtering and energy efficiency performance.

Controller has a number of operating modes. One of them is the adaptive-intermittent mode of power supply. Result is energy saving and improved collection efficiency. This algorithm eliminates the back corona risks, and re-entry of collected particles. Due to adaptive algorithm of intermittent power supply, digital Voltage Controller maintains the emission under required 50 mg/Nm3, reducing at the same time the power losses and the power consumption.

With the power supply no longer dependent on the mains frequency, the response time of the system will be shortened by an order of magnitude. The HFESP reacts in hundreds of microseconds, and it quickly minimizes the adverse effects of flashover, such as the short circuit current spikes, massive ionization, and a significant deionization time. As a consequence, the HFESP-controller voltage, with a very low incidence of flashover, increasing thus the particle filtering. With the HFESP high frequency supply, reaction time is below 500 μs (Fig. 12). Conventional 50Hz supply has the reaction time of 10 ms or more. Result is a significant improvement of precipitator performances in terms of energy saving and improving the collection efficiency.

Very fast microprocessors can provide real time parameter estimation of the DC-current spectrum, which allows back corona detection, estimation of the dust layer thickness, early corona detection and prevention of arcing. Hence, de-ionization intervals are rarely used, and the precipitation efficiency increases. A DC-current spectrum content is detected through the parameter spectral estimation, leading to an ease in detecting the corona phases. At the same time, this eliminates the need for the operator to adjust the references manually in cases when the coal/fuel parameters change during the operation.

For the maximum efficiency of particle collection, the ESP needs to operate as close to the breakdown potential as possible. With the highest voltage feasible and the maximum electric field, the collection efficiency improves. The collection efficiency is proportional to the square of the applied voltage.

With conventional 50 Hz system, the breakdown occurs at the crest of rectified sinusoidal voltage halfwave. Thus, amplitude of half wave should not cross breakdown voltage. The mean voltage is lower (maximum mean value is $2/\pi \cdot Umax$). Therefore, the average of the squared voltage at the ESP is roughly twice lower than the breakdown voltage squared. On the other hand, the HFESP can control the voltage with a minimum voltage ripple, keeping it close to the breakdown level where needed. Hence, as a rough estimate, the HFESP offers the high voltage on the electrodes which has the average square value twice larger than the one encountered with a 50Hz system (Fig.13).

High frequency power supply has a negligible ripple, below 1%, and the mean value of voltage can achieve 98.5% of Umax.

5. CONCLUSION

From the above analysis, we conclude that the HFESP bring considerable advantage in terms of cost, precipitation efficiency, energy efficiency and weight over the conventional ESP systems, based on 50Hz SCR control. In brief, the HFESP approach results in:

- High collection efficiency,
- Significant energy savings,
- High power factor,
- Much lower size and weight of electrodes,
- Suppression of back corona,
- Early corona detection, analysis and flashover Suppression,
- Fast recovery from arcing and a scarce needs for power down intervals,
- Flexibility and modularity.

ESP controller implemented at TENT-A offers an improved collection of fine particles, improves the energy efficiency of the ESP, benefits on coordinated control of the ESP voltage, rapping and distributed heating, includes the spectrum based flashover supression and the back corona elimination, and comprises the adaptation mechanism with respect to the fuel parameters.

Although there has been an increasing awareness of the atmospheric pollution, the tendency to limit uncontrolled emissions from all sources has became larger. Enacted legislation is continously reviewed and is becoming more stringent.

The new control technology for electrostatic precipitators, developed at the University of Belgrade, minimizes the atmospheric pollution problem and offers a number of side benefits. The package includes the hardware and software bases for this new ESP control technology process.
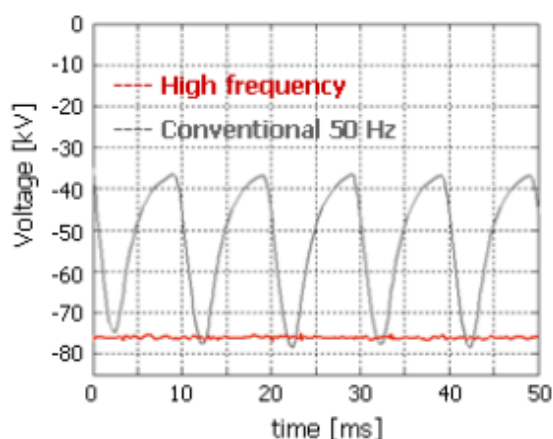
Fig. 13. *Voltage waveforms with conventional and high frequency power supply.*

	50Hz system	HFESP system
cos(φ)	< 0.65	> 0.95
λ=P/S	< 0.5	> 0.75
η (%)	< 60	> 97

Fig. 14. *Comparison of the power factor and the efficiency with conventional and high frequency power supply.*

Fig. 15. *Front panel view of the PLC functions related to the ESP rapping control.*

Fig. 16. *Front panel view of the PLC functions related to the ceramic insulator pre-heating.*

6. LITERATURE

[1] K. Parker, "*Electrical operation of electrostatic precipitators*", The Institution of Electrical Engineers, London, 2003.

[2] V. Dimić, B. Buha, M. Ilić, "*Impulsno napajanje i njegova primena na postojećim i novoinstaliranim elektrostatičkim izdvajačima*", Elektrotehnički institut "Nikola Tesla", Beograd, 1990.

[3] J. H. Davidson, "*Electrostatic precipitation*", Lectures, 2000.

DEVELOPMENT OF THE INDUCTION MOTOR FROM TESLA UNTIL TODAY

Slobodan Mircevski, Milan Cundev, Zdravko Andonov
Faculty of Electrical Engineering and Information Technologies,
Skopje, Republic of Macedonia

Abstract: *The induction motor is one of the 10 - th most significant inventions of mankind. It is commonly refered to as a "working horse" in the industry. If the genious inventor of the wheel remains unknown, the inventor of the wheel in the industry will always be Nikola Tesla. It is said that Tesla did everything for the induction motor; he developed it from an idea to a product and solved the problem of its supplying with the development of his alternate system for transfer of electric energy.*

Is it so? Did Tesla leave no room for improvement on his invention? What is changed today?

Induction motor development is best characterized with its mass [kg/kW]. The first induction motors had an enormous mass, cca 100 [kg/HP]. Today theirs mass is cca 7 [kg/kW]. How can we explain this reduction of mass? The answer is complex. Now the motors are designed with the help of sofisticated computer programs based on optimizing. The production of induction motor today is influenced of energy efficiency aspects. The progress of magnetic, electric and isolation materials is great and evident. The ways of cooling are continuously improving. Duration of induction motor serial production is reduced more of 100 times. Therefore induction motor is the cheapest motor in general. Now induction motor is adapted for supplying with variable frequency and its usage in adjustable speed drives is increasing. Also using 3/2 transformations, development of digital technique (Digital Signal Processors-DSP) and vector systems are rapidly improving induction motor control. So induction motor with its dominant dynamic characteristics today surely press back DC motor from adjustable speed drives.

The paper is dedicated to 150 anniversary of Nikola Tesla birth (1856 - 2006).

Key Words: *Induction motor (IM), Development, Design, Power Electronics, Control.*

1. INTRODUCTION

To evaluate the importance of some invention, as unavoidable criterions are its durability (temporality) and usage spread. IM is in usage from 1888, its application is still growing and the end of this process is not visible. The reason is quite simple. With IM in the easiest way, at the best conditions (efficiency, control, environment polution) the mechanical energy (work) is obtained from electric energy, necessary for humanity survival and progress. Today, development countries in IM drives consume more than 40 % of produced electric energy. The famous sentence is that "IM is working horse in industry". Without IM usage the industry would end to work, the factories would die out, the electric transport (train, crans, lifts, elevators etc.) would stop, the continuation of life would become uncertain.

The invention of IM is developed from an idea to final product, with support provide (electric supply) for its workig, and it is exclusive rare case in invention history. Nikola Tesla also was patented, worked out and used the AC system of producing and transmissioning electric energy, necessary for IM working. His merit is that AC transmission system in USA (and other countries) is with frequency of 60 Hz.

2. GENERAL CIRCUMSTANCES WHEN IM IS DISCOVERED

The time when Nikola Tesla was born and educated (1856-1880) was the time of electrical engineering. M. Faraday in 1821 demonstrated electromagnetic rotation. Later in 1831 he discovered the ingenious low of electromagnetic induction, which did him reputation of the best experiment worker in electric engineering and founder of electromechanical engineering.

In 1834-1838 Moritz Herman von Jacobi (that is Boris Simeonovich Jacobi) in Sanct Petersburg - Russia built a motor with a commutator, supplied from galvanic battery [3], [5], [6]. With that motor he drived a boat with 14 persons in river Neva, quite enough for begining of electric drives.

In Wien international fair 1873 Belgium Z. T. Gramme presented DC generator 25 V, 400 A, with more lamells collector, significant improvement instead of 2 (two) lamells collector, which produced very pulsated DC current. With that machine the student Nikola Tesla experimented 1875 in Gratz University. In 1878 F. Hefner-Alteneck discovered cylindric armature (instead ring armature), which improved the efficiency of machine. So DC machine obtained today look.

In 1873 J. C. Maxwell wrote "Treatise on Electricity and Magnetism", epochal work from which stemmed many of the most significant discoveries of the 20-th century.

In spite of many shortages, the industry accepted DC machine. The machines were very large and heavy. Commutation problem was without solution, circulation fire berween brushes and collector was often case. Constructive solution for iron losses problem was not treated regulary. The production of machines was manualy, very slow and expensive. In that time even Werner von Siemens was not profitable producer of electric machines.

What were the states in AC area? The first knowledge about rotating magnetic field is from D. Arago in 1824, [5], [8]. He noticed rotation of magnetic needle hanged above rotating copper plate. Ch. Babbage and J. F. W. Herschel in 1825 did the opposite experiment from D. Arago, rotating magnet which would create rotation of disc, [5]. That was the first step to induction motor, not repeated in later 50 years. Gaulard and Gibbs, which worked for George Westinghouse, produced AC transformer. In 1884 Blathy and Zipernowsky from company "Ganz" - Budapest also made AC transformer, [2]. G. Ferraris and M. von Doliwo-Dobrowolsky in the same time and independently from Nikola Tesla worked to make induction motor, [3], [5], [6], [8], [9]. But, they lated with the results, they had diferent opinions about practical use of induction motor, even more they did not believe in spread and long application of it. Now it is clear why. They could

not see the complete process of AC system - produce, distribution and consume. M. von Doliwo-Dobrowolsky, engineer from company AEG, had registrated German patent number 51083 for three phase squirrel cage induction motor from march 8, 1889. The battle about author's rights of rotating magnetic field and induction motor was with great effort and duration, with many changes in opinion and dominant influence from scientific circles from USA, Germany, Great Britain and Italy. Today the whole world accepted that the unique inventor of the great polyphase system with all its details is Nikola Tesla. Therefore the unit for magnetic induction B in SI is T (Tesla).

3. TESLA'S INVENTION OF IM

The first idea for electric motor without commutator and brushes Nikola Tesla has got experimenting with Gramme dynamo machine during studies in High technical school in Gratz (1875-1878).

The invention of induction motor has happened 1882 in Budapest, where Nikola Tesla was employed in Hungarian Post Office in january 1881. Some period before discovering he had a great nervous hypersensitive. Therefore he usualy walked on sunset through city park with his friend and assistant Antal Szigety. Once while was walking his thought flashed as lightning and he at once discovered the thruth. He immediately drew with his stick in the sand the figures about induction motor which would presented in American Institution of Electic Engineers (AIEE) 6 years later, [1].

In [3] the special, verbal tradition about IM invention is given. At world exibition 1893 in Chicago Nikola Tesla has explained to professor Sakulka that the final step about invention of IM was taken by transformer defect, over which by pure chance there was an iron ball. This case professor Osan from Technical faculty in Ljubljana has told to professor A. Dolenc from Faculty of electrical engineering in Zagreb. When transformer was on Tesla noticed rotation of the iron ball. He found out short circuit between transformer's secundar turns. Because of iron over saturation the reactive component of primary current was considerable big and therefore the angle between primary and short circuit secundar current was relatively big (see vector diagram in Figure 1). That means, between primary current and secondary current in short circuit turns existed phase displacement and in the same time state displacement. Therefore in the lekeage magnetic field (where was the iron ball), was created rotating field, enough strong to drive the iron ball. It is not clear why Tesla did not write anywhere about this case. Today in all museums dedicated to Nikola Tesla rotating magnetic field is demonstrated by rotating iron egg.
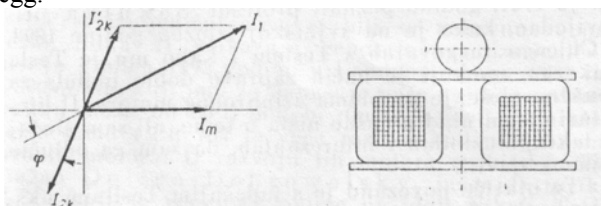

Fig. 1.- *Transformer in defect with iron ball over it and its vector diagram.*

Nikola Tesla arrived in Paris in autumn 1882, where worked in Edison telephone company. His main work was instalation of DC electric stations with specialization in dynamo current regulators. About this work he stayed in

Strassburg longer time (1883-1884), where by strange accident stayed also other persons which became famous later. Nikola Tesla produced in Strassburg his motor without commutator and brushes with materials from Paris and help of Antal Szigety. In summer 1883 he finished the experiment when saw with satisfaction rotation produced by AC in different phases, exactly as he imagined in Budapest one year before, [1]. In the spring 1884 he came back in Paris and demonstrated his motor to Edison's people. They recomended him to go in USA in Edison company.

Nikola Tesla arrived in New York in June 6, 1884. He was employed in Edison company immediately, he became the best assistant and hard worker, but not endured even one year with Edison. They were different kind of man and inventors with different directions in electrical engineering (DC - Edison, AC - Tesla).

In april 1887 by helpe (investment of 500000 USD) of A. K. Brown, manager of "Western Union" company, a great AC supporter, started to work "Tesla Electric Company". Only for one year Nikola Tesla created 40 patents about polyphase systems - motors, generators, transmission and distribution of electric energy. He has made 2 motors as prototypes which sent to test in USA Patent Office, on demand of the investor A. K. Brown. The motors were tested by professor   W. Anthony (1835-1908) from Cornell University, comparing them with DC motors. He was very impressed of their characteristics, specialy of the efficiency. He also suggested to Tesla to give a lecture in AIEE. The lecture "A New System of Alternate Current Motors and Transformers" was given in May 16, 1888 with theoretical part about AC system, and practical presentation and demonstation of induction motor and patents for producing, transmission and distribution of AC electric energy.
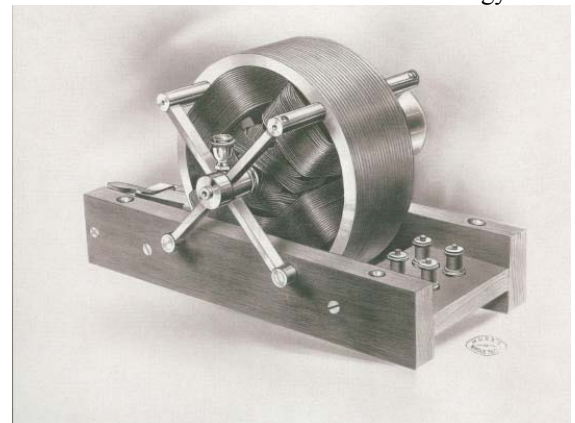
Fig. 2. -*The first Tesla's induction motor, presented and demonstrated in May 16, 1888 at AIEE.*

After that (May 1888) George Westinghouse (1846-1914) offered to Tesla to buy up all his patents about polyphase system. Tesla sold the patents to company "Westinghouse Electric and Manufacturing Company" for 25 000 USD/patent (total 1 million USD). Also he had a difficult task to begin production of induction motors in Pitsburg for 1 year. The process of acceptig serial production of IM lasted till end of the summer 1889. During this period Tesla solved many practical problems. The most difficult was adapting to 133 Hz, frequency which "Westinghouse" engineers has accepted before and did not like to change because of standard dimensions of machines. He also had to produce monophase motor for this frequency, [1]. Tesla recognized

the problems of isolation and cooling of machines. More his patents gave contribution in this area.

The greatest promotion of Tesla's polyphase system was the world exibition in Chicago 1893 (400 years of Columbus America discovery). From the first idea for motor without commutator and brushes in Gratz 1875 till wider application of IM after starting electric station in Niagara falls 1896, past nearly 20 years.

Tesla did not enjoyed financial benefits of IM invention. After 1896 he was occupied with his the greatest project - wireless transmission of informations and energy.

4. IM STATE OF ART

4.1 Designing of IM

From the electric machines theory, every induction motor has five mutual dependent systems: electrical system, magnetic system, insulation system, cooling system and mechanical system. In induction motor design has to be calculated characteristic values of each system, has to be selected modern material and in the proper way has to be dimensioned all elements of the each system.

When Nikola Tesla invented induction motor, the principles of machine design were unknown. The manufacturers had developed prototypes with the multiple attempts. Therefore, machines were heavy, in the beginning with 400 [kg/HP], and with the countinious development the machnine mass was reduced, as is shown in Table 1, [3], [10], [11], [12].

Table 1. *Induction motor development AEG 4 kW, 2p=4 , until 1954 according [3], until 2000 according [10].*

Year	1891	1896	1899	1924	1930	1954	1980	2000
kg	350	268	168	84	48	44	30	28

The electrical machines classical design theory was developed in the 30-ties of the XX century. According this theory, three the most important induction motor specific loads were defined: specific electric load defined by current load A (1-8) 10^4 [A/m], specific magnetic load defined by air gap magnetic induction B (0,9-1,2) [T] and specific mechanical load defined by rotor speed n (for the 50 Hz and magnetic poles 2p, the most often in range (250-3000) [1/min]). The progress of magnetic, electric and isolation material quality is evident.

The first iron sheets had specific losses of 10 [W/kg] with the 1 [T] induction, but the today used iron sheets has about 1 [W/kg] with the same induction. Insulation materials also have significant improvement, so today usually the F class (100 ^{0}C over temperature) is used. Because of inverter high switch frequencies, higher du/dt and di/dt values, the transition to H class is expected. The ways of cooling are continuously improving and they are used as power increasing method, [12].

A lot of electrical machine numerical design methods are developed as a result of increased computer capabilities: finite differences method (1970), 2D finite elements method (1980), 3D finite elements method (1990), which is used for better magnetic induction distribution calculation. All this methods are used for the correct machine magnetic core dimensioning [14].

With the computer development, the optimal induction motor design methods are introduced. One of the most frequently optimal induction motor design method is genetic algorithm stochastic method. In the induction motor optimization process, stochastic algorithms work with the huge number of parameter combinations, and with the evolutionary principles eliminate worse and force better solutions. Genetic algorithm is defined as computer based optimization routines, which connect evolutionary principles with the genetic principles: crossover, selection, mutation and repetition. This method requires proper objective function. The recommended objective function is motor efficiency. In this case of the induction motor optimal design, efficiency has to be maximized (objective function maximum) and the genetic algorithm has to be set in proper way. Because, for the objective function calculation all motor parameters has to be involved, the each parameter range (lower and upper limit) has to be defined. Also, the chromosomes in the population and number generations has to be determined. The number of the generations has to be larger, and as a result the induction motor optimal design will be more accurate. In this way the motor efficiency will be increased [14].

4.2 Power electronics application

Adjustable speed induction motor drive development is induced by the voltage frequency converters and researches in the field of discrete fully controlled power components, electric circuit integration and module manufacturing [13].
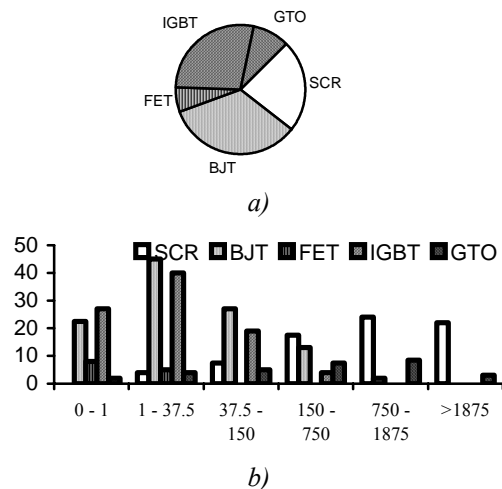
Fig. 3. - *Global breakdown of power semiconductor components a), breakdown by power range [kW] b).*

In Table 2 are given characteristics (peak voltage, maximal current and switching frequency) of the most used semiconductor components – thyristor (SCR), fast thyristor, bipolar junction transistor (BJT), MOSFET, IGBT and GTO thyristor [12], [13].

Table 2. *Power semiconductor components characteristics.*

	SCR	fast SCR	BJT	IGBT	MOSFET	GTO
Peak voltage [kV]	6	1,5	1,4	0,2	1,7	4,5
Max. current [kA]	5	1,5	0,5	0,15	0,6	3
Switching frequency [kHz]	1	3	5	30/40	10/20	1

The most promising component which is in beginning of development are MCT thyristors (MOS controlled thyristors). There are MCT with 600/1200 V, 60 A RMS on market. The new perspectives in new generation of semiconductor materials (GaAs, SiC, diamond) will not be discussed.
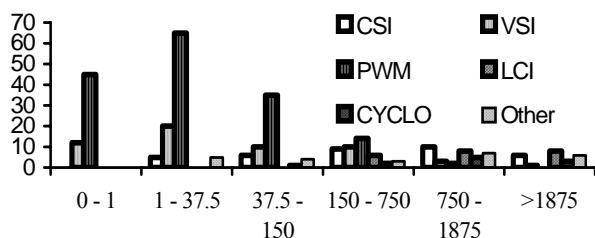
Fig. 4. - *Breakdown of power converter by power range [kW].*

There are two major type of the voltage – frequency power converter: indirect (with DC link) and direct. The standard indirect converter topology is expected to be dominant in the near future because of the best performance/price ratio. It is suitable for the single or multi motor different applications with the power range of 10^2 - 10^7 [W], with 6 or 12 pulse rectifier and the output frequency usually up to 200 Hz. There are no expectations for greater topology changes. In figure 4 is given breakdown of the different converters by power range [13].

The development of induction motor ASD is very expensive, so only the large companies have capabilities for it. For example, ABB reports that for development of direct torque control (DTC) were involved over 100 man/year engineers in a period of more than 5 years.

4.3 Control systems

Induction motor drive control depends on working machine type and application. Electric drives can be classified as: general purpose (about 90 %), special drives (high performance drives) and high power drives in industry, traction and energy production. General purpose drives can be single or multi motor drives, with the voltage source inverters (VSI) and scalar control, for example U/f=const for the constant load torque. Special drives are usual with single motor and with vector control. The high power drives mainly are also with vector control.


a)

b)
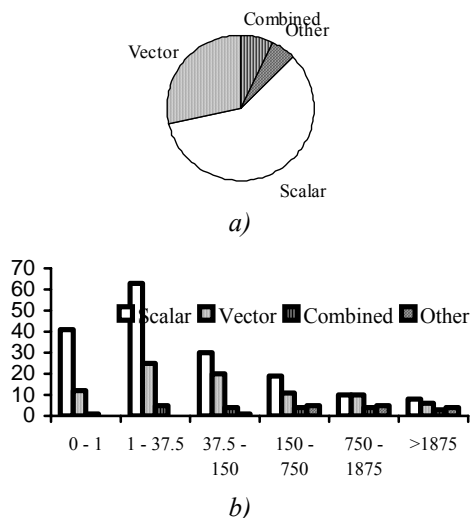
Fig. 5. - *Breakdown of scalar and vector control a) global, b) by power range [kW].*

In figure 5 is shown breakdown of scalar and vector control. A simple and economic scalar control has been accepted by industry for lower power and performance drives. From the other side, vector control which is made possible with microprocessor and digital signal processor DSP development, nowadays is used in expensive high performance drives. Vector controlled induction motor drives surpassed characteristics of ASD with separately excited DC motors [12], [13].

In electric drive control are involved different adaptive methods, as selftuning regulation (STR), variable structure system (VSS), model referencing adaptive control (MRAC) and robust control models. The artificial intelligence techniques as expert system, fuzzy logic and artificial neural network are promising and they are implemented in intelligent adaptive control and drive estimation. This progress is result of microprocessor technology, application specific integrated circuit (ASIC), and usage of digital signal processors (DSP).

Today, there are several induction motor DSP manufacturers, but the most popular are: Analog Devices with ADMC-3xx and ADMC-401 series and Texas Instruments with TMS320F243 and TMS320F241, based on TMS320Cxx controller. Other manufacturers (Hitachi H8/300, SH 1,2 series, Motorola 68H908MR24, Mitsubishi M30624FG, ABB ICMC-IA613A etc.) produce microcontrollers interesting for AC drives control application. The price of available fix point DSP is less then 5 US $.The different manufacturers offer DSPs with very similar characteristics. The limitations are in processor memory and peripheral capabilities.

5. CONCLUSION

The induction motor, simillar to the wheel is an invention forever. During application it is continuosly improving and spreading. Tesla invented IM, but also predicted directions of its development. He had more patents about isolation and cooling of IM.

The induction motor is an exclusive case where one inventor, Nikola Tesla, from an idea (Gratz 1875) arrived to realization of serial production (Pitsburg 1889). But, that process lasted nearly 15 years.

The development of IM is a result of general technological progress, such it is happened in automobil industry, aircraft industry etc. The consequencies are in decreasing volume (dimensions) nearly half after every 20 years, decreasing poduction time for more than 100 times, as a result of automatization of the process, at the same time increasing the quality of the product and working hours. Therefore the IM is the cheapest motor today without any competition. Because of spread application the drives with IM in development countries consume cca 40 % of the produced electric energy and so the question of energy efficiency is very important. The general direction is to use adjustable speed drives.

Application of IM today is unbreakable connected with power electronics and modern control systems. So, IM spread application areas and replace DC motor in adjustable speed drives. Therefore are necessary improvements in its design, usage of high quality electric and magnetic materials, rising isolation class (from "F" to "H"), better cooling for low speed, usage bearings for for wider speed diapason etc.

6. REFERENCES

[1] N. Tesla, *My Inventions (Moji pronalasci)*, Školska knjiga, Zagreb, 1984.

[2] T. Bosanac, *Pogovor (Moji pronalasci)*, Školska knjiga, Zagreb, 1984.

[3] A. Dolenc, *Nikola Tesla i razvoj elektrotehnike jake struje*, Elektrotehnički vesnik br. 9-10 (str.239-248), Ljubljana, 1956.

[4] Aleksandar Damjanović, *Proslava stogodinjice rođenja Nikole Tesle*, Elektrotehnički vesnik br. 9-10, str. 233-239, Ljubljana, 1956.

[5] B. Drury, *The Control Techniques Drives and Controls Handbook*, The Institution of Electrical Engineers, London, 2001.

[6] T. Kenjo, *Electric Motors and their Controls*, Oxford University Press, 1999.

[7] *The U. S. Patents of Nikola Tesla* (Freely available at the U. S. Patent and Trademark Office).

[8] V. Muljević, *Nikola Tesla slavni izumitelj*, Zagreb, 2000.

[9] John J. O Neill, *Prodigal Genius, The Life of Nikola Tesla (извадоци)*, New York, 1944 (превод), Elektrotehničar br.1 (godina III), str. 4-11, 1949.

[10] N. Srb, *Elektromotori (priručnik)*, Rade Končar, Zagreb, 1980.

[11] E. L. Owen, *Evolution of Induction Motors - The Ever - Shrinking Motor*, IEEE Industry Applications Magazine, January/February 1977.

[12] С. Мирчевски, З. Андонов, *Актуелни состојби во електромоторните погони*, 4 Советување Мако CIGRE, Охрид, 26-29 септември 2004.

[13] E. Lajoie- Mazenc, D. Pratmarty, *Europrean Market of AC - adjustable speed drives*, 93NR00071 EDF, 1993.

[14] M. Cundev, L. Petkovska, V. Stoilkov, *Actual CAD Trends Based upon Postprocessing in 3 D FEM*, 3as Jornadas Hispano - Lusas de Ingenieria Electrica, p.p. 391 - 397, Barcelona, Espania, 1993.

EFFICIENCY CLASSES INDUCTION MOTORS, SAVING ENERGY AND EVALUATION OF EFFICIENCY ECONOMICS

Miloje M. Kostic

Institute "Nikola Tesla", Belgrade, Republic of Serbia

Abstract: *In this paper are presented new-proposed efficiency classes of three-phase cage induction motor(IE-code), for motors from 0.75 kW up to 370 kW. It is estimated that electric motors with improved efficiency alone can save about 7% of electric energy. The results of the evaluation by present worth life cycle analysis, for purchasing of higher efficiency motors (eff1) instead of lower efficiency motor (eff2), are presented.*

Keywords: *Induction motors (IM)/Efficiency classes of IM / New-proposed IE-code/Saving Electric Energy/ Present worth life cycle analysis.*

1. INTRODUCTION

As induction motors are the single biggest "consumer" of electric energy in industry they still offer the significant opportunity for improvement in the area of efficiency. On January 1 2000 in the European Union – following the US EPA classification already in force since October 1 1997, a law introduced three efficiency classes for standard electric motors from 1.1 kW to 90 kW – based on an agreement between the European Commission and CEMEP the European Committee of Manufacturers for Electrical Machines and Power Electronics [1].

The classification scheme insists on three efficiency classes (eff1, eff2 and eff3) whose minimum efficiency limits are shown in fig.1 [1]. On average an eff2 motor reduces losses by up to 20%, and an eff1 motor reduces losses by up to 40% [1].
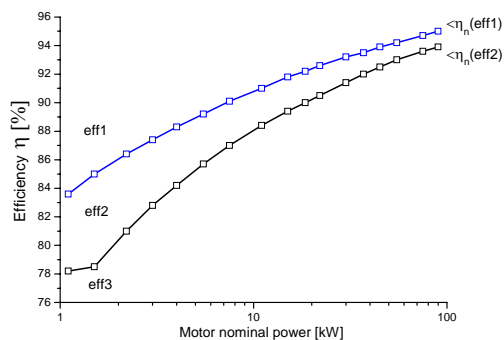

Fig.1. *Nominal Efficiency under limits class eff1 and eff2 motors available in the European market*

Many different energy efficiency classes for cage induction motors are currently in use (i.e. NEMA, EPACT, CEMEP, Australia, Japan , Brazil etc.) and new classes are being developed (Chine, India). Therefore it becomes increasingly difficult for manufacturers to design motors for a global market. The proposal standard [2] is intended to harmonize the different requirements so that one motor design per efficiency class can fit the global market for both 50 Hz and 60 Hz. This will also reduce the growing confusion of international customers about different efficiency requirements in different countries.

2. EFFICIENCY CLASSES OF THREE-PHASE CAGE INDUCTION MOTORS

Three energy efficiency class are proposed, IE1, IE2 and IE3 [2]. The 60 Hz efficiency values for class IE3 (premium) and IE2 (high) were taken from existing NEMA Premium and EPACT tables. The 50 Hz values of class IE1 (standard) and IE2 (high) are similar to the existing CEMEP-EU eff2 and eff1. However the values have been adjusted to take the different test procedure into account (CEMP: additional load losses P_{LL} flat 0.5% of input power; this standard determined from tested in accordance with IEC 60034-2-1 [3]. The 50 Hz efficiency values for class IE3 (premium) are newly designated. On average the IE3 motors have less energy losses 15%-20% than B motors (Fig.2).
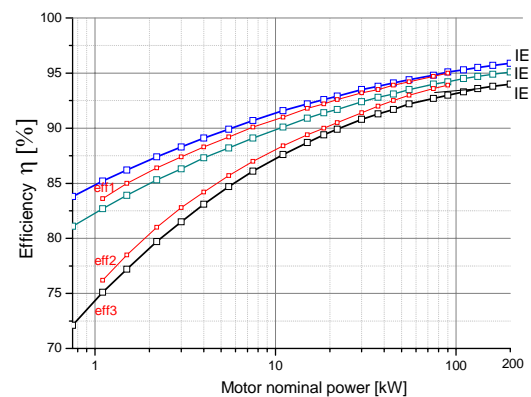
Fig. 2. *Comparative Survey of efficiency rated values for classes IE1, IE2, IE3 [2] and eff1, eff2, eff3[1]*

3. SUPER-PREMIUM EFFICIENCY (IE4)

An new Super-Premium (IE4) efficiency class is introduced in this standard-Annex A in [2]. IE4 is specifically designed for power electronic operated motors – but these electronic devices have a limited efficiency themselves. It should be ensured, that product (IE4 efficiency • inverter efficiency) is not lower than IE3 (line operated)**.** For these reasons of the high reduction in losses of IE4 over IE3, from 20-24 %. These advanced motors usually require power electronics frequency converters) to operate. Since gird frequency and number of poles of converter-fed machines are not directly related to speed these motors are typically rated for a speed and classified by torque rather than power.

Losses of inverter controlled motors over a whole speed range can only be determined by direct input/output tests since all other (improved) test methods require sinusoidal voltage, fixed frequency and fixed (rated) voltage. The absolute limit of efficiency of IE4 can not exceed some 95% since no reliable tests are available for higher values. Comparative survey of efficiency rated values for classes

IE1, IE2, IE3 and IE4 [2], for motors with 2- pole, 4-pole and 6-pole, for 50 Hz, is served on the fig.3.
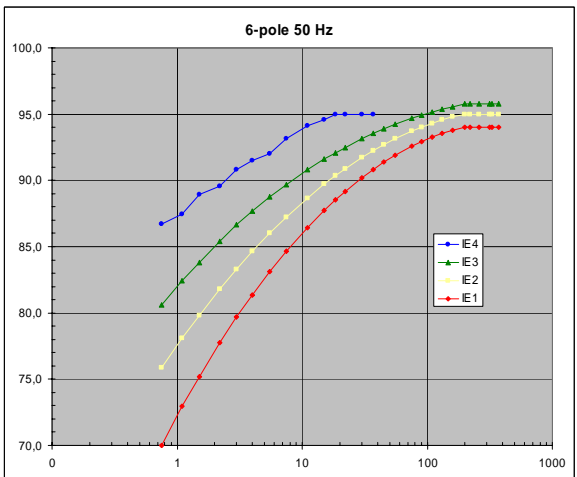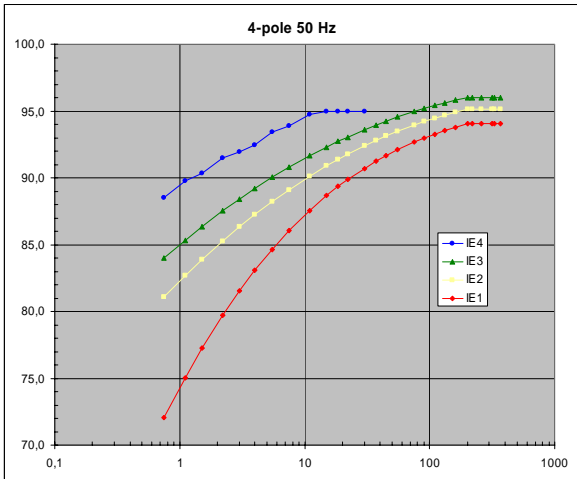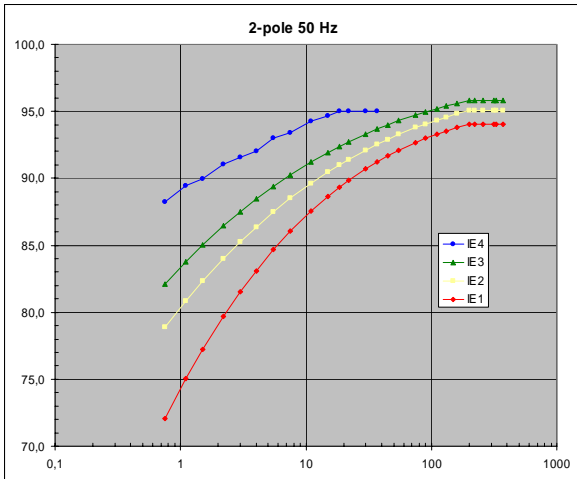
Fig.3. *Comparative Survey of efficiency rated values for class IE4 and classes IE1, IE2 and IE3*

A normative IE4 class is envisaged for the next edition of this standard. However, for information purposes the following proposed nominal limits of Super-Premium Efficiency are given [2]–tabl1 1. It is expected that advanced technologies will enable manufacturers to design motors for this efficiency class with mechanical dimension (flanges, shaft height,….) compatible to existing motors of lower efficiency classes (see EN 50347 and NEMA MG1).

Table 1: *Efficiency rated values for class IE4 [2]*

| IE4 - Super Premium Efficiency 50 Hz			
kW	2-pole	4-pole	6-pole
0,75	86,8	88,0	86,0
1,1	88,0	89,2	86,7
1,5	88,6	89,7	88,1
2,2	89,1	90,8	88,7
3	90,2	91,3	90,0
4	90,7	91,7	90,6
5,5	91,7	92,6	91,1
7,5	92,1	93,0	92,2
11	93,0	93,8	93,1
15	93,4	94,1	93,6
18,5	93,8	94,4	94,0
22	94,1	94,8	94,4
30	94,5	95,0	94,7
37	94,8	95,3	95,0
45	95,1	95,6	95,3
55	95,4	95,8	95,6
75	95,6	96,0	95,8
90	95,9	96,2	96,0
110	96,1	96,4	
132		96,5	
160	96,3		
200	96,5		

4. ENERGY SAVING

Motors from 0.75 kW up to 370 kW make up the vast majority of installed motor population, and covered by considered standard *IEC 60034-XY: ROTATING ELECTRICAL MACHINES – part XY: Efficiency classes of single-speed three-phase cage induction motors.* Efficiency analysis are shown [2], electric motors with improved efficiency alone can save about 7% of electric energy.

Industrial users frequently make decisions about the purchase of motors for new installations, and about repair, rewinding, or replacement of existing motors have failed in service. It is becoming increasing important to consider the economic impact of motor efficiency on the business when making such decisions. In many situations, decisions are based upon the quickest delivery or lowest initial cost. The tools of economic analysis can help users make more intelligent decisions regarding motor purchase and repair.

When economically comparing two motors of the same size but different efficiency rating, it is necessary to determine the annual savings generated by use of the higher efficiency motor. The annual energy savings are calculated by the following equation:

$$W_1 = p_L \cdot P_N (100 / E_B - E_A / 100) \cdot N \qquad (1)$$

where

W_1 - annual energy savings, *kWh/year*
P_N - is rated output power, *(kW)*
$p_L = P_L / P_N$ – is related load of motor
E_B - lower motor efficiency, *%*
E_A - higher motor efficiency, *%*
N – annual hours operation, *h/year*

Economic evaluation is a useful tool to determine the relative merit of motors proposals with different efficiencies. The results of the evaluation help the users to choose the

alternative that is most profitable for the business. Differential guide lines must be used, depending upon whether the motor expenditure will be capitalized or charged to cost [4]. Each user must make own decision based upon interpretation of the Internal Rate of Return (IRR).

5. EVALUATION OF EFFICIENCY ECONOMICS

In order to obtain accurate results during the economic evaluation process, it is extremely important that only efficiencies determined by the same method are compared. There are a number of ways to evaluate the economic impact of motor efficiency. Two of these methods are simple payback analysis and present worth life cycle analysis [5].

5.1. Simple Payback Analysis

The simple payback method gives the number of years required to recover the differential investment for higher efficiency motors. To determine the payback period, the premium for the higher efficiency motor is divided by the annual savings. First, the annual savings must be determined using the following formula:

$$S_1 = p_L \cdot P_N \cdot C_{E1} \cdot N \cdot (\frac{100}{E_B} - \frac{100}{E_A}) \quad (2)$$

where:
S_1 - Annual Euro savings, *Euro/year*
P_N - The rated power, *kW*
$p_L = P_L/P_N$ – is related load of motor
C_{E1} - Energy cost, *Euro/kWh*
E_B - Lower motor efficiency, *%*
E_A -   Higher motor efficiency, *%*

The efficiencies for the percent load at which the motor will be operated must be used, since motor efficiency varies with load.

Then, the motor cost premium is divided by the annual savings to compute the payback period for the higher efficiency motor. If motor A costs 300 Euro more than motor B and yields annual savings of 100 Euro, the simple payback period is 300Euro/100 Euro or 3 years. The simple payback method is easy to apply but ignores savings occurring after the end of the payback period and does not consider the time value of money or changes in energy costs.

5.2. Present Worth Life Cycle Analysis

For greater precision, the present worth method of life cycle savings may be employed. This method considers the time value of money. First, the user will determine the required internal rate of return and expected energy cost inflation. For, the effective interest rate (i) can be determined present worth (PW) using the following formula:

$$PW = \frac{(1+i)^n - 1}{i(1+i)^n} \quad (3)$$

where:
PW- Present worth
i   -   Effective interest rate, *pu*
n   -   Expected operating lifetime of the motor, *years*

Table 2: *Present worth values (PW) for different values of interest rate (i) and lifetime of motor (n)*

n (year)→	6	8	10	12	15
i (%)↓					
7	4.766	5.971	7.023	7.942	9.108
8	4.623	5.746	6.710	7.536	8.559
10	4.357	5.336	6.145	6.813	7.606
12	4.111	4.968	5.650	6.194	6.810
15	3.784	4.487	5.018	5.420	5.847
20	3.326	3.837	4.193	4.439	4.675

Once PW is solved, the present worth evaluation factor (PWEF) can be calculated:

$$PWEF = S_1 \cdot PW \quad (4)$$

and

$$PWEF \geq C_A - C_B \quad (5)$$

where:
S_1 -   Annual Euro savings, *Euro/years*
C_A- Purchase price of higher motor efficiency, *Euro*
C_B- Purchase price of lower efficiency motor, *Euro*

On the base equations (4) and (5), following equation can be obtained

$$S_1 \geq (C_A - C_B)/PW \quad (6)$$

or

$$PW \leq (C_A - C_B)/S_1 \quad (7)$$

By equation (6) and table 2, simple payback analysis becomes alike to present worth life cycle analysis. Namely, the motor cost premium is divided by the annual savings to compute the lowest the present worth values to purchase higher motor efficiency be capitalized. If motor A costs 300 Euro more than motor B and yields annual savings of 100 Euro, and the present worth values should to be PW≥ 300Euro/100Euro=3 (PW values calculated by equation (3) or corresponding values in table 2).

Sample Calculation

How many annual hours of operation N (h/year), that additional cost to purchase higher efficiency class motor (eff1≡ IE2), instance of lower efficiency class motor (eff2≡ IE3), be capitalized in following cases:
a) $p = P/P_N = 1$, and
b) $p = P/P_N = 0.75$

Given:
15 kW, 2p=4, Motor eff1 class with efficiency E_A=92.0%,
15 kW, 2p=4, Motor eff2 class with efficiency E_A=90.0%
$C_{eff1} - C_{eff2}$ = 410 Euro
Assumed:
C_{E1}=0.075 Euro/kWh, i=15 % and n=10 years
Calculation:
- PW values calculated by equation (3) or corresponding values in table 2): PW=5.018
- By equation (6), it can be obtained
   $S_1 \geq (C_A - C_B)/PW$ =410/5.018=81.706 Euro
- By equations (2) and (6), it is obtain following express for calculation values N (h/year):

$$N = \frac{S_1}{p \cdot P_N \cdot C_{E1} \cdot (100/E_B - 100/E_A)}$$

Case (a): $p = P/P_N = 1$

$$N \geq \frac{81.706}{1 \cdot 15 \cdot 0.075 \cdot (100/90 - 100/92)} = 3006 h / year$$

Case (b): $p = P/P_N = 0.75$

$$N \geq \frac{81.706}{0.75 \cdot 15 \cdot 0.075 \cdot (100/90 - 100/92)} = 4009 \, h/year$$

6. PURCHASE OF EFFICIENCY MOTORS FOR NEW INSTALATIONS

Efficiency guide lines have been prepared to assist users in making the decision whether to spend additional money to purchase higher efficiency class motor for a new installation. The assumption is made that the purchased motor will be capitalized. Two different efficiency ratings for the same motor may be economically compared.

a) Simple payback analysis

It is useful to determine an total operating period – $\Sigma N\,(h)$ for that additional costs to purchase higher efficiency class motor be capitalized:

$$\sum N = \frac{C_A - C_B}{C_{E1} \cdot (P_L/P_N) \cdot (100/E_B - 100/E_A)} \quad (8)$$

where

C_A-purchase price of higher motor efficiency, *Euro*
C_B-purchase price of lower efficiency motor, *Euro* C_{E1}-electricity cost, *Euro/kWh*.

b) Present worth life cycle analysis.

It is still more usual to determine an annual operating hours – N (*h/year*). From (3) and (6), it is given:

$$N = \frac{(C_A - C_B)/PW}{C_{E1} \cdot (P_L/P_N) \cdot (100/E_B - 100/E_A)} \quad (9)$$

If PW=5, i.e. corresponding to values *i=15%* and n=10 years-table 2 or (3), then additional annual costs are:

$$C_{A1} - C_{B1} = (C_A - C_B)/PW = 0.20(C_A - C_B)$$

and

$$N = \frac{0.2(C_A - C_B)}{C_{E1} \cdot (P_L/P_N) \cdot (100/E_B - 100/E_A)} \quad (9a)$$

The results of the evaluation by equation (9a), for purchasing of higher efficiency motors (eff1) instead of lower efficiency motor (eff2), are interesting. The calculated *N(h/years)* values, for full load ($P_L/P_N=1$) and ¾ load ($P_L/P_N=0.75$) and electricity price 0.10 Euro/kWh, for SIEMENS motor about prices from 2005 year, are given in tables 3 and 4.

Table 3: *Annual operating hours – N (h/year), for two pole motors (2p=2*

P	E_{eff1}	E_{eff2}	$0.2(C_A - C_B)$	N (h/year)	
kW	%	%	Euro	P_N	¾P_n
0.55	75	71	51	2476	2321
0.75	80	73	56	1433	1228
1.1	84	77	65	1456	1092
1.5	85	79	79	1179	1910
2.2	86.5	82	100	1433	1910
3.0	87	84	121	1965	2620
4.0	88.5	86	147	2238	2983
5.5	89.5	86.5	187	1755	2340
7.5	90.5	88	231	1962	2616
11	91	89.5	310	3060	4080
15	91.5	90	400	2928	3905
18.5	92.3	91	450	3143	4209
22	93	91.7	520	3101	3591
30	93.5	92.3	620	2973	3963
37	94	92.8	730	2868	3534

Table 4: *Annual operating hours – N(h/year), for four pole motors (2p=4)*

P	E_{eff1}	E_{eff2}	$0.2(C_A - C_B)$	N (h/year)	
kW	%	%	Euro	P_N	¾P_n
0.55	77	67	55	1032	1376
0.75	81	72	60	1037	1382
1.1	84	77	75	1260	1680
1.5	85	79	88	1313	1751
2.2	86.5	82	107	1513	2314
3.0	87.5	83	123	1320	1906
4.0	88.5	85	153	1644	2218
5.5	89.5	86	194	1551	2069
7.5	90.3	87	240	1524	2252
11	91.5	88.5	330	1620	2183
15	92	90	410	2263	2890
18.5	92.5	90.5	450	2036	2184
22	93	91.2	530	2270	2487
30	93.5	91.8	650	2188	2266

Calculated operating hours – *N (h/year)* will be different, from motor to motor (tables 2 and 3), i.e.:
- from 1200-3143 h/year, for motors with rated load, and
- from 1400-4209 h/year, for motors with 3/4 load.

For different values for
- electricity price (C_{EI}) in *Euro/kWh*, and
- average loads (P_L/P_N),

calculated operating hours – N (h/year) will be different. For electricity price 0.05 Euro/kWh, calculated operating hours – N (h/year) will be two times higher then corresponding values given in tables 2 and 3, i.e.:
- from 2400-6286 h/year, for motors with rated load, and
- from 2800-8418 h/year, for motors with ¾ load.

Approximatively, calculated values (N), will be higher for 4/3 times, for same motors when operated with ¾ rated load (eq.9), as $E_{3/4} \approx E_N$.

7. EFFICIENCY AT PARTIAL LOAD

The topic of part load efficiencies was considered in detail [2]. Some countries stated that they nominal efficiency for a given class motors be reached at 75% or 100%. Other countries requested the nominal efficiency to be reached at both 75% and 100% or even over the whole range from 60 to 100%.

Technically, the vast majority of motors (especially energy efficient motors) have at least the same if not a greater efficiency at 75% compared to 100%. With the exception of very small motors (typically 1.1 kW and lower) it would actually be more expensive for a manufacturer to designed a motor a lower efficiency at 75% compared to 100%.

This author presented a calculation procedure for the estimation of any part load efficiency when two load points are given [6]. This procedure is accepted, in principle, and proposes to include this into a newly created document "Guide for energy efficient usage of electrical motors and variable speed drives", by the working group IEC TC2 WG31.

8. CONCLUSIONS

Electric motor applications in industry consume between 30% and 40% of the generated electric energy worldwide. Improving efficiency of the complete drive system (i.e. motor and adjustable speed drives) is therefore a major concern in energy efficiency efforts. As, it is analysis are shown, electric motors with improved efficiency alone can save about 7% of electric energy.

Motors from 0.75 kW up to 370 kW make up the vast majority of installed motor population, and covered by considered standard IEC 60034-30: Efficiency classes of single-speed three-phase cage induction motors

The results of the evaluation, by present worth life cycle analysis, for purchasing of higher efficiency motors (eff1) instead of lower efficiency motor (eff2), are presented.

APPENDIX 1:

IEC 60034-1 Rating and Performance (published April 2004, under review by IEC WG 12)

Tolerances come from motor production (precision, material quality, quality control) and from testing accuracy details of standards understood by the testing person and in the testing procedure applied, instrumentation quality and environmental data precision). IEC 60034-1 defines tolerances as maximum -15% of losses for motors up to 150 kW and max -10% above.

The discussion has started in IEC WG 28 to discuss the tolerances (i.e. the necessary instrumentation, the required environmental conditions temperature, time, etc.) in order to make the tolerances smaller, i.e. the accuracy and repeatability larger.

The necessary definition of nominal efficiency (statistical average of a sample, in the US 5 equal motors) that is the base for setting MEPS versus the rated efficiency of one single motor, that can have a tolerance not larger than the standard prescribes.

The problems of regulators that have to certify (ex ante) and spot check (ex post) imported and domestically produced motors and motors in packaged systems has to be defined separately. IEC has decided in June 2007 to start the revision of IEC 60034-1. The results of the new Round-Robin test can be then incorporated.

APPENDIX 2:

IEC 60034-2-1: Standard methods for determining losses and efficiency from test

Chapter 5.3: Preferred methods [3]

It is difficult to establish specific rules for the determination of efficiency. The choice of test to be made depends on the information required, the accuracy required, the type and size of the machine involved and the available field test equipment (supply, load or driving machine). Preferred methods are given for Induction machines in Table 2 (*IEC 60034-2-1:* - The test method should be selected from the procedures with the lowest uncertainty).

Uncertainty - The concept of "Uncertainty" is explained in Note 4:

• Low a procedure determining all loss-components from tests;

• Medium a procedure which is based on a simplified physical model of the machine;

• High a procedure that does not determine all loss-components by tests.

The additional stray load losses in different testing methods (Summary :

• All methods (also IEEE 112B) have considerable inaccuracies, as the results of the additional stray load losses in different testing methods can vary up to ±50% (The results of 5 tests with 42 motors from 1.5 kW - 315kW [7]).

• The average error between IEEE 112B and Eh-Star of the total losses (i.e. the efficiencies) is less than 0.3% ;

• The max error between IEEE 112B and eh Star is 0.7% of efficiency (these numbers have to be reviewed);

• The conclusion (Anibal de Almeida) presented at the SEEEM side event on 14 June 2007-[7]:

1.Eh-Star is an inexpensive method with fairly good accuracy where stray load losses are calculated mathematically.

2.Comparison input-output methods and the Eh-Star method show a fair to good matching of the test results.

3. Additional tests may be used to confirm the repeatability and accuracy of test results

4 The ongoing campaign for an IEC Round Robin test should be used to refine testing methods, qualify testing laboratories and to reduce necessary tolerances.

Table 2 *[IEC 60034-2-1]:*

Method	Clause	Preferred method	Required facilities	Uncertainty
Direct				
Torque measurement	8.1.1	All single phase and polyphase ≤ 1 kW	Torquemeter/dynamometer for full-load	Low
Calibrated machine test	Annex D		Calibrated machine	See Note 5
Dual-supply, back-to-back test	8.1.2		Machine set for full-load Two identical units	Low
Total losses				
Calorimetric method	Annex D		Special thermal enclosure	See Note 5
Single supply back-to-back test	8.2.1		Two identical units (wound rotor)	Low
Summation of losses, with and without load test				
P_{LL} determined from residual loss	8.2.2.5.1	Three phase > 1 kW up to 150 kW	Torquemeter/dynamometer for ≥ 1,25 × full-load	Low
P_{LL} from assigned value	8.2.2.5.3			Medium to high
P_{LL} from removed rotor and reverse rotation test	8.2.2.5.2		Auxiliary motor with rated power ≤ 5 × total losses P_T	High
P_{LL} from Eh-star test	8.2.2.5.4	(see Note 3)	Resistor for 150 % rated phase current	Medium
Summation of losses, without load test				
Currents, powers and slip from the equivalent circuit method P_{LL} from assigned value	8.2.2.4.3		If test equipment for other tests is not available (no possibility of applying rated load, no duplicate machine)	Medium/high

NOTE 1   Due to measurement inaccuracies, the determination of P_{LL} from residual losses is limited to correlation coefficients (see 8.2.2.5.1.2) greater than 0,95 and may have uncertainties of the determined efficiency exceeding ±0,5 %.

NOTE 2   In the "Uncertainty" column, "Low" indicates a procedure determining all loss-components from tests; "Medium" indicates a procedure which is based on a simplified physical model of the machine.

NOTE 3   The method for P_{LL} from Eh-star test is suitable for motors between 1 kW and 150 kW; larger ratings are under consideration. The method requires that the winding can be connected in star.

NOTE 4   In the "Uncertainty" column, "Low" indicates a procedure determining all loss-components from tests; "Medium" indicates a procedure which is based on a simplified physical model of the machine; and "High" indicates a procedure that does not determine all loss-components by tests.

NOTE 5   Uncertainty to be determined.

9. REFERENCES

[1] EURODEEM, "Efficiency Classes for A.C. Electric Motors", CEMEP Working Group Low Voltage A.C. Motors.

[2] Future IEC 60034-30: ROTATING ELECTRICAL MACHINES – part XY: Efficiency classes of single-speed three-phase induction motors.

[3] Standard *IEC 60034-2-1*

[4] Dale M. Brethauer, Richard L. Doughty, and Robert J. Puckett, " The Impact of Efficiency on the Economics of New Motors, Motor Repair, and Motor Replacment", *IEEE Transc. on Ind. Applications, Vol.30, No 6/1994*, pp.1525-1537.

[5] *Standard NEMA MG10*, Energy Management Guide for Selection and Use of Fixed Frequency Medium AC Squirrel-Cage Polyphase Induction Motors, *NEMA, 2001*.

[6] M. Kostic, "Analysis of Efficiency Deviation with Load change compared to rated", 14th International Symposium on Power Electronics-Ee 2007, Novi Sad, Serbia, 2007.

[7] International Standards for Electric Motors, Status 30 August 2007, Zürich, 30. August 2007, (CUB:*c:\daten\seeem\overview 30 august 07.doc)*. Draft 6 Conrad U. Brunner

POWER REGULATOR DESIGN FOR FUEL CELL APPLICATIONS

Boris Šašić, Miloš Živanov*, László Nagy*, Miroslav Lazic**

Spellman High Voltage El. Corporation, New York, USA
*EE Dept., University of Novi Sad, Faculty of Technical Sciences, Novi Sad, Republic of Serbia
** IRITEL Beograd, Beograd, Serbia

Abstract: *Fuel cells are gaining popularity in a wide range of industries. This paper outlines critical steps in designing power regulators for hybrid fuel cell systems. Such systems are gaining acceptance in industrial vehicles, forklifts, etc. Harsh operating environments (temperature and peak load demand) along with price pressures require optimized design for peak performance and easier market penetration. 5kW converter described in the paper has met or exceeded all of the requirements with comfortable margin.*

Keywords: *DC-DC converter, fuel cell, multiphase boost, ripple cancellation, interleaved converter*

1. INTRODUCTION

Fuel cells technology is coming off age. Even though there are many new and exciting developments, the technology is now considered mature and ready for prime time. Fuel cells are implemented in several applications (chemical industry, power generation) and considered a serious contender in many others.

Power generation is one of the earliest implementations. Chlorine recovery in the chemical industry is another one. Fuel cells range in 200kW to 5MW in these applications. Tests in traction applications are making a great progress, from locomotives (multiple 100-150kW fuel cells), to busses and passenger cars (50-100kW), to industrial vehicles (forklifts and "people movers") in the 3-10kW range.

In some of these industries fuel cells will gain faster acceptance than in others. Material handling industry is among those where benefits of fuel cells can be easily documented and increased cost of initial implementation justified. A fuel cell based system that replaces standard forklift battery pack has many advantages, such as: fast refueling, longer run time between refueling, longer life of the energy source and low maintenance requirements.

In a typical electric vehicle fuel cells are augmented by an energy storage element, such as supercapacitor, flywheel or battery. Such hybrid system makes some of the fuel cell deficiencies (high output impedance, for example) transparent to the final user.

Hybrid systems with small lead acid battery (Fig. 1) have many advantages in material handling applications. Most significant two are: (1) battery provides peak current handling capabilities and (2) it ensures reserve power to drive the vehicle to refueling station should hydrogen tank be completely depleted.
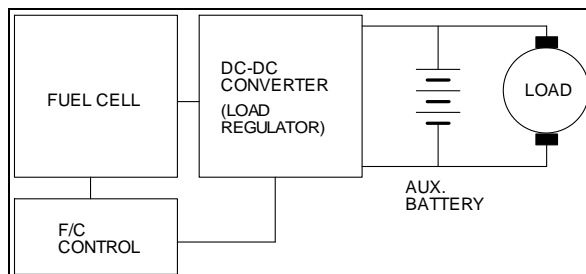

Fig. 1. *Block schematic of a hybrid fuel cell system*

A critical part of such fuel cell system is the load regulator. Its main role is to enable controlled current draw from the fuel cell. It also needs to maintain the auxiliary batteries in a fully charged state and to regulate load current.

2. LOAD REGULATOR REQUIREMENTS

A typical load regulator requirements for a forklift energy source can be summarized as follows:
- Input current regulation;
- Output current regulation;
- Output voltage regulation;
- Continuously variable control;
- Low input current ripple;
- Automatic crossover between the modes;
- High peak load handling capability;
- Full complement of protection circuits;
- High efficiency (>95%);
- High reliability;
- Low cost.

As an example, we will showcase one regulator solution with the following electrical parameters:
- Output power: 5,5kW
- Fuel cell voltage:24-36V
- Output voltage: 36-60V
- Output current: 150A

In addition, the protection against reverse current flow (into the fuel cell) and ability to sustain peak currents of up to 800A for up to 5 seconds are required features.

3. CONVERTER TOPOLOGY

There are several competing converter topologies for the fuel cell load regulation. Some recent developments are outlined in [1-4]. Common to those topologies is relative complexity and, consequently, high price. They are better suited for applications where there are lower pricing pressures and their expanded feature set is desired.

Among various topologies, boost converters (Fig. 2) stand out for their simplicity which is closely correlated to low costs and high efficiency.
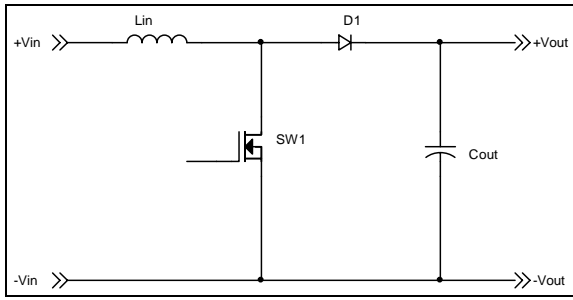
Fig. 2. *Boost converter*

As the load voltage is higher than the fuel cell voltage and input inductors effectively control current ripple, boost topology seems to be a good basis for meeting the most critical requirements.

Connecting two power stages in parallel (both, input and output) and shifting drive signals by 180° results in an interleaved configuration. Benefits of interleaving are numerous: each stage handles half of the power, input and output effective frequency is doubled and, when the circuit operates at duty cycle of 0,5, there is an input ripple cancellation effect. It has been shown [5,6] that an interleaved converter may actually have lower physical volume and lower price than comparable single-phase unit. Adding more phases increases benefits of interleaving. At a certain number of phases the point of diminishing results is reached and benefits are no longer commensurate with the increased complexity and costs.

However, the optimum number of phases is relatively easy to come by. Increasing number of phases also reduces current ripple (input and output) by partial or complete ripple cancellation (depending on the duty cycle) as shown in Figs. 3 and 4 [7]. The graphs show normalized values of input current ripple and output capacitor RMS current.
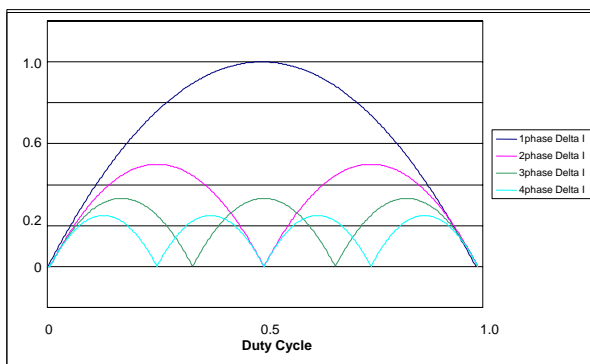

Fig. 3. *Input current ripple vs. duty cycle*
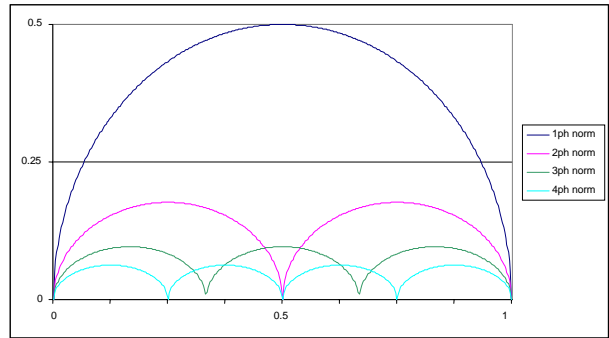
Fig. 4. *Output capacitor RMS current vs. duty cycle*

Based on Figs. 3 and 4 and converter's actual perating point it is easy to find number of phases offering minimum ripple [7]: by superimposing the operating duty cycle on the graphs, the number of phases with minimum stress can be easily found for that particular operating point. Increasing the number of phases beyond optimum will not only increase circuit complexity and price, but may also increase losses and electromagnetic emissions of the unit. For our showcase design, the converter's maximum duty cycle range is 0,03 to 0,60. However, considering load characteristic of the fuel cell (Fig. 5), the converter's typical operating point is operating in a narrow range centered around duty cycle of 0,32 [7,8]. It turns out that the optimum number of phases for this application is three.
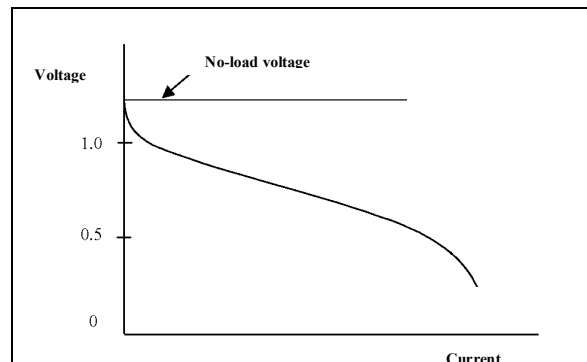

Fig. 5. *A typical fuel-cell load curve*

Simplified representation of the three-phase boost converter power stage is shown in Fig. 6. The switching frequency is set to 25kHz which results in 75kHz input and output ripple. Low switching frequency helps increase efficiency and lower radiated emissions.
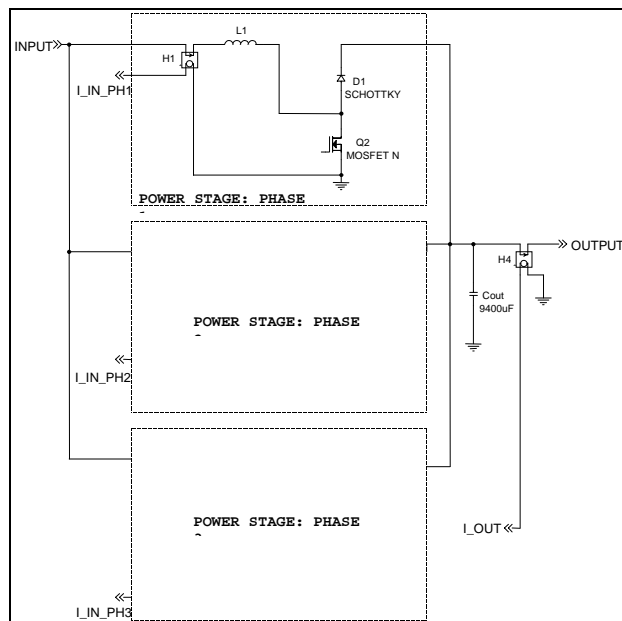
Fig. 6. *Block schematic of the three-phase boost converter*

One atypical thing to notice here is that this converter does not utilize synchronous rectification. Instead, we opted to use Schottky rectifiers. Tests with synchronous rectification showed peak efficiency improvement of about 0,5%. At this power this is not insignificant, however, there are three reasons that made Schottky diodes prevail in this design: (1) they are less expensive than mosfets with equivalent ratings - there is a total of 18 diodes in the circuit and price savings are significant, (2) during fault conditions, typical drivers keep synchronous rectifier switch closed, which will cause reverse current and create hazardous condition; solving this problem would increase complexity of the control scheme and further increase unit price and (3) standard rectifiers enable significantly better load sharing among the phases during fast load transients.

4. CONTROL CIRCUIT

Low voltage, high current boost converter has inherently slow response, limited by the Right Half Plane (RHP) zero in its transfer function [9]. Fortunately, fuel cells are electrochemical sources and their response time is in order of several milliseconds, or tens of milliseconds and designing adequate feedback compensation is, therefore, not a problem.

The circuit uses multiple error amplifiers in OR-ing configuration, as shown in Fig. 7.

The unit operates in master-slave operation to ensure accurate current sharing. Master error amplifiers respond to control signal for input current and output voltage, OR-ing their outputs ensures that, at any point in time, only an error amplifier with lower error voltage is in control of the circuit. Third error amplifier sets output current limit and has fixed reference signal. Slave amplifiers that control phase two and three have only one task - to closely replicate input current of the phase one. This ensures very accurate current sharing among the phases.
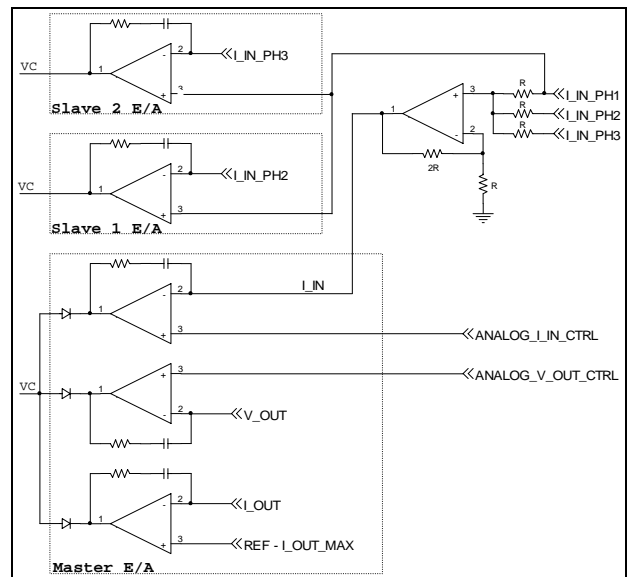
Fig. 7. *Block schematic of the error amplifiers section*

The three phase PWM source is shown in Fig. 8.
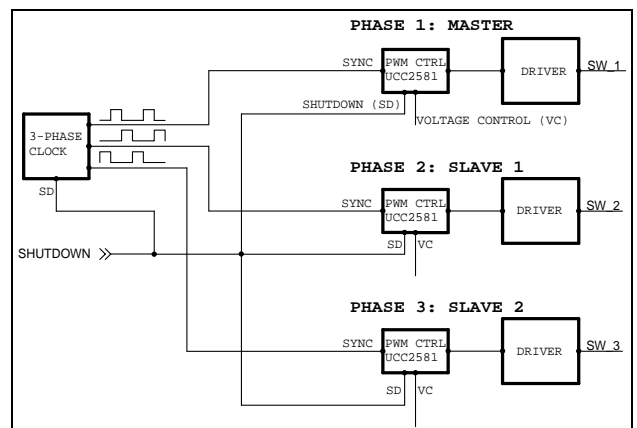
Fig. 8. *Block schematic of the PWM control circuit*

Three-phase clock circuit ensures synchronized and interleaved operation of the individual phases. Each phase has its own dedicated PWM controller with individual duty cycle control.

5. PRACTICAL RESULTS

First production unit is shown in Fig. 9. The three input inductors are easily identifiable on the photograph. Heavy bus bars are designed to handle up to 250A of input current and 150A output current with minimum loss.
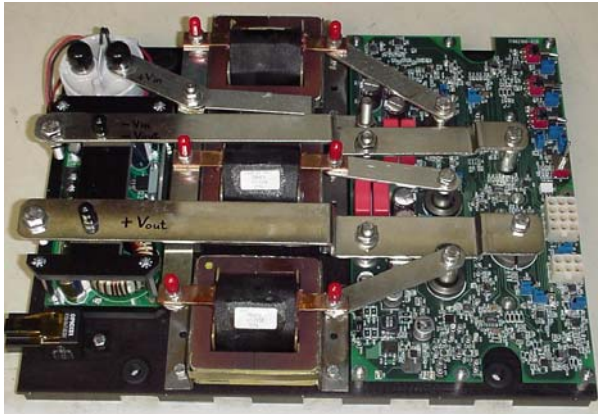
Fig. 9. *Photograph of the 5kW converter*
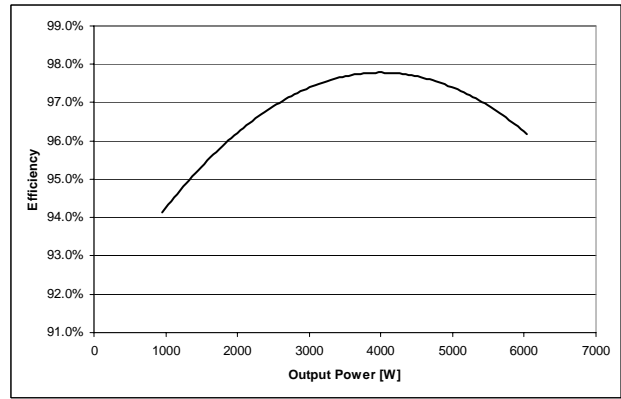
Fig. 10. *Efficiency plot*
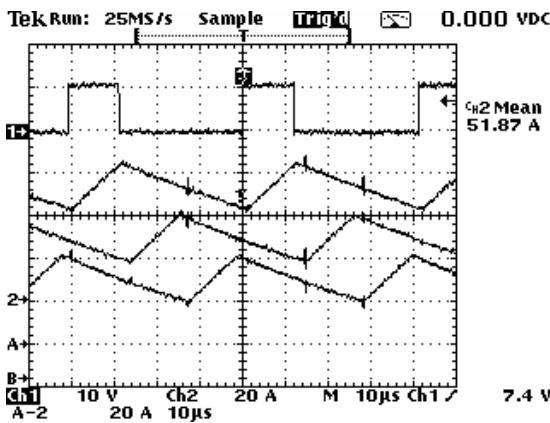
Fig. 10. *Phase 1 drive signal and three input inductor currents*

Current ripple of each phase is 20A$_{pk-pk}$. Fig. 11 shows total input current and illustrates benefits of interleaving.
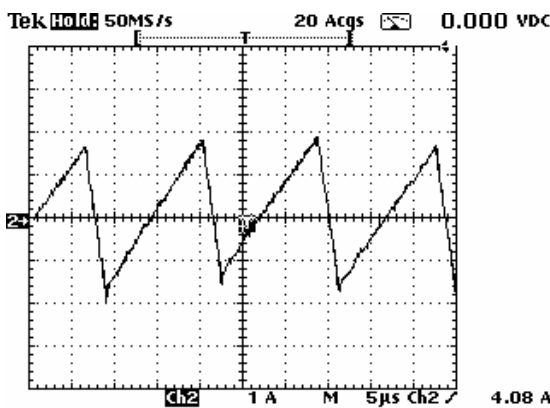
Fig. 11. *Input current ripple*

Frequency of the ripple current has tripled and absolute value has reduced to less than 4A$_{pk-pk}$. If the input is bypassed by capacitance of only 1800µF, input ripple current drops to less than 1A$_{pk-pk}$, which is less than 0,5% of maximum rated current of 220A.

Efficiency plot for the converter is shown in Fig. 12. With the peak efficiency of over 97%, and light load efficiency exceeding 94%, the requirements for a low-loss power converter are met with a comfortable margin.

6. CONCLUSION

Fuel cells are quickly becoming top contender for cost-effective and safe use in industrial vehicles. Battery pack replacement in electric forklifts is one application where they may find very appropriate home.

In order to satisfy very demanding load as presented by traction and lift systems in a forklift, the fuel cell system requires a load regulator to enable efficient energy transfer. This paper presents a solution based on non-isolated interleaved boost converter, rated at 5kW.

Understanding load requirements is the first critical step for successful design implementation. By analyzing the converter's steady-state operation it is possible to uncover areas for optimization – in case of a fuel cell operation, even though specified input range varies widely (24-40V in our case), the majority of operation is conducted at relatively narrow range of input voltages (41-42V). This helped optimize converter around the three phase operation, rather than needlessly increasing number of phases to lower stress over the full specified range which is inconsequential for the unit's performance. A prototype converter was built and the most interesting results are discussed in Section 5. The converter's input current ripple is below 0,5% and peak efficiency nears 98%, exceeding requirements by a wide margin.

Functional testing was performed in laboratory setting with peak loads of 12kW without any negative effects on the converter or fuel cell.

The fuel cell system was tested in the field, lifting pallets weighting 1500kg and drawing peak currents in excess of 800A.

Operation of three systems over the 9 months period, in a battery manufacturer's facility operating 24 hours, seven days a week, without a single failure, is a solid proof of validity of approach.

7. REFERENCES

[1]   B. Fahimi, *"Automotive Fuell Cell Power Electronic Converters"*, IEEE APEC Conference Seminar workbook, Vol. 3, February 2007.

[2]   X. Kong and A. M. Khambadkone, *"Analysis and Implementation of a High Efficiency, Interleaved Current-Fed Full Bridge Converter for Fuel Cell System"*, IEEE Transactions on Power Electronics, Vol. 22, No. 2, March 2007, pp. 543-550

[3] J. L. Duarte, M. Hendrix and M. G. Simoes, *"Three-Port Bidirectional Converter for Hybrid Fuel Cell Systems"*, IEEE Transactions on Power Electronics, Vol. 22, No. 2, March 2007, pp. 480-487

[4] Z. Jiang and R. A. Dougal, *"A Compact Digitally Controlled Fuel Cell/Battery Hybrid Power Source"*, IEEE Transactions on Industrial Electronics, Vol. 53, No. 4, August 2006, pp.1094-1104

[5] J. Betten and R. Kollman, *"Interleaving DC/DC converters boost efficiency and voltage"*, EDN magazine, October 13, 2005, pp. 77-86

[6] M. O'Loughlin, *"An Interleaving PFC Pre-Regulator for High-Power Converters"*, TI Power Supply Seminar Handbook SEM1700, pp. 5.1-5.14, 2006

[7] B. Sasic and L. Nagy, *"An Approach to Optimizing Number of Phases in an Interleaved Boost Converter"*, 14th International Symposium on Power Electronics - Ee2007, Novi Sad, Serbia, 2007

[8] B. Sasic, M Zivanov and M. Lazic, *"Design of a Multiphase Boost Converter for Hybrid Fuel Cell/Battery Power Sources"*, 14th International Symposium on Power Electronics - Ee2007, Novi Sad, Serbia, 2007

[9] R. W. Erickson and D. Maksimovic, *"Fundamentals of Power Electronics"*, second edition, Kluwer Academic Publishers, 2001

NEW DEVELOPMENTS IN LIGHTNING AND OVERVOLTAGE PROTECTION

Manfred Kienlein

DEHN + SOEHNE, Neumarkt, Germany, manfred.kienlein@dehn.de

Abstract: *The new lightning protection standard IEC 62305-3; Protection against lightning, part 3: »Physical damage to structures and life hazard defines« maintenance tests and test intervals for lightning protection systems. One part of this system are surge protection devices (SPD). The testing of SPDs in MCR – Systems costs a lot of time and maintenance cost. With the new technology „LifeCheck" the testing is very easy. The test can be done manual or automatically.*
The lecture describes the differences from the old to the new test technology of SPDs.
Keywords: *Power Electronics, Control and Measurement*

1. INTRODUCTION

Surge arresters repeatedly discharge surges and impulse currents caused by lightning strikes without destruction. However, overload of a surge arrester can never be completely excluded. Overload may occur if the nominal data specified by the surge arrester manufacturer such as nominal current and nominal voltage are exceeded, but may also be caused by discharge processes exceeding the specified limits.

Surge arresters for power engineering are installed between the active conductor and earth. In case of an overload, the surge arrester elements are isolated from power supply thus removing the protective effect of surge arresters. Due to the circuit design of surge arresters for information technology systems, the energetic overload of surge arresters generally interrupts the transfer signal. This interruption is caused by the fail-safe performance (short-circuit) after an overload of protection elements or melting of conductor paths in the duct.

Since unfortunately only few surge arresters for information technology systems have fault indication, the cause of a system failure may not be determined. Trouble shooting by the maintenance personnel may be time-consuming and costly as the "no signal transfer" fault pattern may be caused by a line short circuit or the like. If the protective circuit of the surge arrester cannot be isolated from the installation level for testing, the surge arrester has to be removed. In order to keep efforts and costs as low as possible, the trend is towards pluggable surge arresters. Pluggable surge arresters consist of a base part, which is connected to the wires, and a pluggable SPD module, in which the entire protective circuit is integrated. In the majority of cases only the module has to be replaced in case of a faulty protective circuit.

2. REGULAR TESTING OF INSTALLED SPDS

Multiple discharges with values beyond the specification of the device affected can overload surge arresters in telecommunications and signalling networks. To ensure a high system reliability, it is therefore recommendable to subject SPDs to systematic tests.

IEC 62305-3 Ed. 1.0 [1] (see Table) defines maintenance tests and test intervals for lightning protection systems. The maintenance programme should include the testing of SPDs designed for lightning equipotential bonding:

Protection level	Complete inspection	Visual inspectin
I and II	2 years	1 year
III, IV	4 years	2 years

This table shall be considered generally a recommendation for lightning protection systems. For individual cases, however, these values can differ from the requirements or critical systems and specific directives (e.g. Regulations of the Nuclear Power Committee (KIA) for Lightning Protection of Nuclear Power Installations).

3. EASY TESTING WITH LIFECHECK

Pluggable SPDs and corresponding test adapters can only be tested in a time-consuming way, as the SPD modules have to be removed, tested and then plugged in again. Moreover, the signal circuit is unprotected during the test. LifeCheck allows for quick and easy SOD testing. Removing the module is no longer required. Being integrated into the SPDs, the RFID system used requires no batteries or power supply. The proper condition of the SPD is constantly controlled. An extreme thermal or electrical load is detected reliably and can be registered with DEHNrecord DRC LC M1 reader in a second and without contacting.

4. SIGNAL BEFORE DAMAGE

The control device of the SPD is designed to generate a signal as soon as the SPD is threatened to be overloaded. This helps to take precautionary measures to avoid standstills within the installation

Fig. 1. *Testing an SPD module with RFID system (LifeCheck).*

The control Indicator system consists of two operating units:

1. **RFID Reader:**

This consists of a hand-held device with indicator and antenna. The reader transmits energy to the RFID transmission unit (transponder) within the SPD without contacting. This reads out the operating state and displays the same.

2. **Control unit within the SPD:**

This controls the protective circuit for impermissible overloads by thermal (overheating) or electrical (impulse currents) incidents. The control unit is connected directly with the transponder. If an overload is detected, the affected protection module has to be replaced.

How does LifeCheck work?
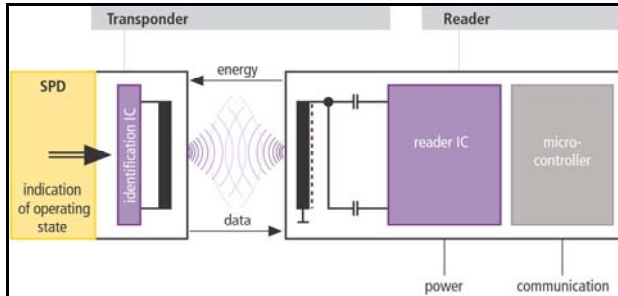
Fig. 2. *Testing an SPD module with RFID system (LifeCheck).*

5. CONCLUSION

RFID communication ok   = SPD ok
No RFID communication = replace the SPD

The LifeCheck circuit within the SPD detects two types of overloads:

1.   Thermal overloads

If the discharge elements are working in the critical temperature range, thermal fuse elements interrupt the RFID communication permanently.

2.   Electrical overloads

If construction elements are threatened to be destroyed by peak overloads, the transponder interrupts the communication permanently.

Overloaded SPD modules have to be replaced as soon as possible in order not to threaten the availability of the installation.

6. REFERENCES

[1]   IEC 62305-3; Protection against lightning, part 3: Physical damage to structures and life hazard

ANALYSIS AND DESIGN OF A LOSS-FREE RESISTOR BASED ON A BOOST CONVERTER IN SLIDING-OPERATION

A. Cid-Pastor, L. Martínez-Salamero, U. Ribes–Mallada and A. El Aroudi

Escola Tècnica Superior d'Enginyeria, Universitat Rovira i Virgili, Tarragona, 43007 Spain

Abstract: *The synthesis of a boost-converter-based loss-free resistor (LFR) operating in sliding mode is presented. The resulting LFR can be used as a pre-regulator for power factor correction in one-phase circuits. A dynamic model of the loss-free resistor is also reported, this allowing the design of the output voltage regulation loop, which results in good transient behavior and small output ripple. PSIM simulations illustrate the performances of the designed LFR and show a good agreement with the theoretical predictions.*

Keywords: *Loss-free resistor, power converter, sliding-mode control.*

1. INTRODUCTION

The loss-free resistor (LFR) is a two-port element, which, like the DC transformer and DC gyrator, belongs to a class of circuits named POPI (DC power output=DC power input) that, in turn, constitute the canonical elements in the synthesis of numerous high–frequency power processing functions. The notion of LFR was introduced by Singer [1] and, so far, it has been limited to the recognition that certain switching converters exhibit resistive input impedance in steady-state in discontinuous conduction mode. This is the case of the buck-boost, SEPIC and Ćuk converter, which have been employed, due to this property, as power factor correctors by including only one loop of voltage regulation with pulse width modulation [2]-[8].

On the other hand, the introduction of sliding–mode control in the power factor correction has its main antecedent in the work of Rossetto et al. [10], in which a switching surface defined as a linear combination of the input current error and output voltage error was proposed in the Ćuk converter with galvanic isolation. Depending on the relative values of the coefficients multiplying each error, the input current or the output voltage can be more precisely regulated. The result is a good example of the existing trade-off between the increase of the circuit response velocity and the reduction of the input current distortion.

In this work, we present the synthesis of an LFR and its subsequent application as both pre-regulator and power factor regulator. The main goal of this research is to demonstrate that the synthesis of LFR´s can be systematically performed by imposing certain sliding modes in some converters. Although the reported work is focused on the boost converter, the method employed can be directly applied to other converters with a series inductor at the input port such as the SEPIC and Ćuk converter provided that the resulting sliding regime is stable.

A complementary goal is to apply the resulting LFR to the power factor correction by developing a pre-regulator first, and then a complete regulator in a single stage. In the first case, we make use of the power source nature of the LFR at the output port, and verify its capacity to exhibit a unity power factor and, at the same time, transfer without losses to the output port all the power absorbed at the input port. In the second case, the dynamic behavior of the LFR is studied by linearizing the ideal sliding dynamics around the equilibrium point. The resulting dynamic model allows the design of an external control loop that regulates the output voltage in spite of the load perturbations.

The remains of this paper are organized as follows. In section 2, an LFR is designed by imposing a particular sliding regime in the boost converter. The use of this LFR as a pre-regulator in a power factor correction circuit is analyzed in section 3. In section 4, a dynamic model of the LFR is developed, and a voltage regulation loop is designed by inserting a PI controller. Simulation results of the LFR acting both as pre-regulator and as voltage regulator with power factor correction in a single stage are presented in section 5. The conclusions of the work and future research directions are discussed in section 6.

2. SYNTHESIS OF LOSS–FREE RESISTORS

The goal of the synthesis is the design of a two-port switching structure whose steady-state equations are the following

$$V_1 = rI_1 \tag{1}$$

$$V_1 I_1 = V_2 I_2 \tag{2}$$

where I_1, V_1 and I_2, V_2 are the steady -state averaged values of input and output variables respectively.

Equations (1) and (2) define a loss-free resistor (LFR), which can be represented by the block diagram of Fig. 1. It consists of a switching converter, which is controlled by means of a sliding-mode regulation loop whose switching surface is given by $S(x) = v_1 - ri_1$. In steady-state $S(x) = 0$, i.e, $V_1 = rI_1$. On the other hand, since the converter in Fig. 1 is ideal and therefore is a POPI structure (DC Power output=DC Power input), equation (2) will be automatically satisfied.

In the case of the boost converter, imposing the above mentioned sliding surface results in a stable equilibrium point with LFR characteristics.
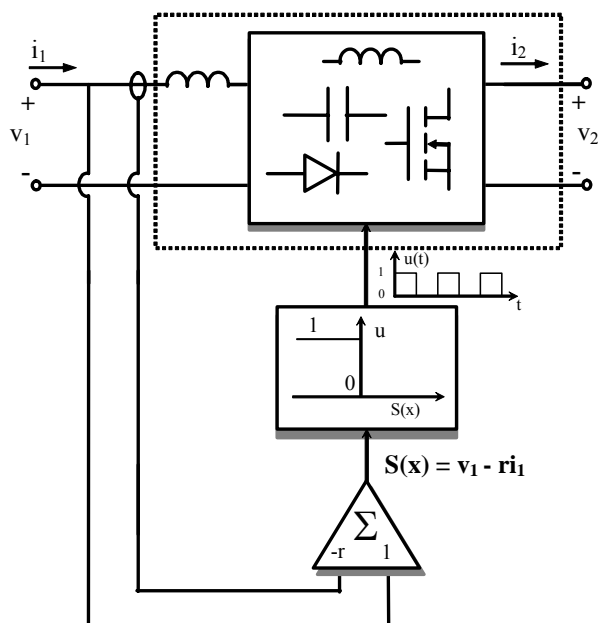
Fig. 1. *Block diagram of a DC-DC switching converter with LFR characteristics.*

It has to be pointed out that imposing a sliding-mode to the input current requires i_1 to be a continuous function of time [11], this implying the existence of a series inductor at the input port. The simplest converters with this constraint at the input port are the boost converter and other fourth order structures, namely, the buck converter with input filter (BIF), the boost converter with output filter (BOF), the Ćuk converter, the Ćuk converter with galvanic isolation and the SEPIC converter as illustrated in Fig. 2.

2.1. Analysis of the boost converter in LFR operation

2.1.1. Equivalent control

In the continuous conduction mode the converter has only one structural change in a switching period and it can be represented by means of two linear vector differential equations

$$\dot{x} = A_1 x + B_1 \qquad \text{during } T_{ON} \qquad (3)$$

$$\dot{x} = A_2 x + B_2 \qquad \text{during } T_{OFF} \qquad (4)$$

where x is the state vector defined as $x = [\ i_1,\ v_2\ ]^+$ and matrices A_1, B_1, A_2, B_2 are given by

$$A_1 = \begin{bmatrix} 0 & 0 \\ 0 & -1/RC \end{bmatrix} \quad B_1 = \begin{bmatrix} V_g/L \\ 0 \end{bmatrix}$$

$$A_2 = \begin{bmatrix} 0 & -1/L \\ 1/C & -1/RC \end{bmatrix} \quad B_2 = \begin{bmatrix} V_g/L \\ 0 \end{bmatrix} \qquad (5)$$

and it has been assumed $v_1 = V_g$.
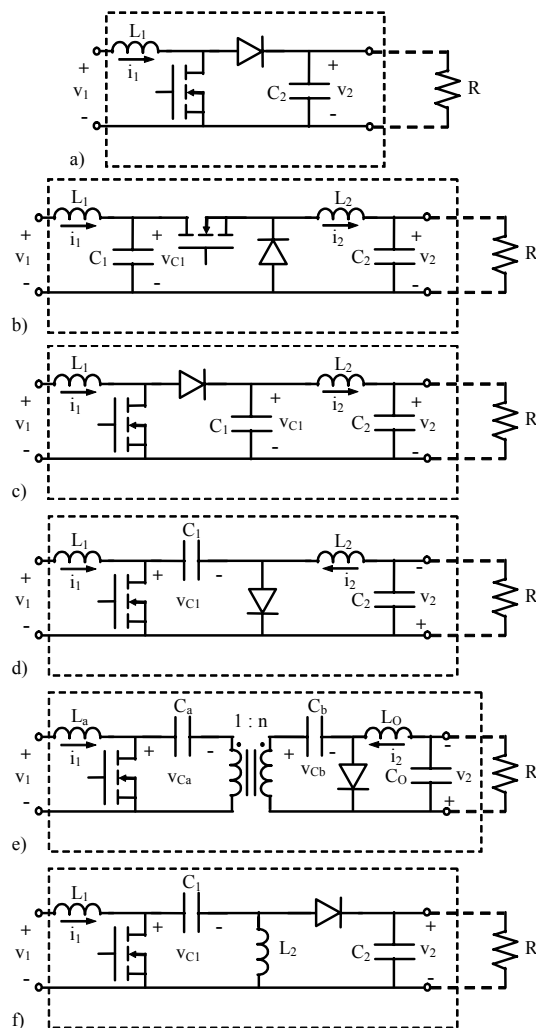
Fig. 2. *Converters with non pulsating input current a) boost converter, b) buck converter with input filter (BIF) c) boost converter with output filter (BOF) d) Ćuk converter) e) Ćuk converter with galvanic isolation f) SEPIC converter.*

Equations (3) y (4) can be combined in only one bilinear expression

$$\dot{x} = (A_1 x + B_1) u + (A_2 x + B_2)(1 - u) \qquad (6)$$

where $u=1$ during T_{ON} and $u=0$ during T_{OFF}

Equation (6) can be expressed as follows:

$$\dot{x} = A_2 x + B_2 + (A_1 - A_2) x\,u + (B_1 - B_2) u \qquad (7)$$

From (5) y (7), we obtain the following set of differential equations

$$\frac{di_1}{dt} = \frac{-v_2}{L_1}(1-u) + \frac{V_g}{L}$$

$$\frac{dv_2}{dt} = \frac{i_1}{C}(1-u) - \frac{v_2}{RC} \qquad (8)$$

Assuming $S(x)=v_1-ri_1$ as sliding surface and imposing the invariant conditions $S(x)=0$ and $\dfrac{dS}{dt} = 0$ in (7) lead to the following expression of the equivalent control

$$u_{eq}(x) = 1 - \frac{V_g}{v_2} \qquad (9)$$

Now, the discrete variable *u* is substituted in (8) by the continuous variable $u_{eq}(x)$ that can take any value between 0 and 1. This variable $u_{eq}(x)$ represents the control law that describes the system behavior on the switching surface where the system dynamics takes place on average. Therefore, $u_{eq}(x)$ is limited by both maximum and minimum values of *u*

$$0 < u_{eq}(x) < 1 \qquad (10)$$

2.1.2. Equilibrium point

Substituting *u* by $u_{eq}(x)$ in (8), and taking into account the constraint $V_g = rI_1$ imposed by the sliding surface, we obtain the following ideal sliding dynamics:

$$\frac{dv_2}{dt} = \frac{I_1}{C}\frac{V_g}{v_2} - \frac{v_2}{RC} \qquad (11)$$

The coordinates of the equilibrium point $x^* = [I_1, V_2]^+$ of the ideal sliding dynamics are given by:

$$x^* = \left[\frac{V_g}{r}, V_g\sqrt{\frac{R}{r}}\right]^+ \qquad (12)$$

Note that

$$P_2 = \frac{V_2^2}{R} = \frac{V_g^2\frac{R}{r}}{R} = V_g\frac{V_g}{r} = V_g I_1 = P_1 \qquad (13)$$

as it can be expected since the boost converter is a POPI circuit.

On the other hand, from (9) and (12), we derive

$$u_{eq}(x^*) = 1 - \frac{1}{\sqrt{\frac{R}{r}}} \qquad (14)$$

which is limited by the maximum and minimum values of *u*

$$0 < 1 - \frac{1}{\sqrt{\frac{R}{r}}} < 1 \qquad (15)$$

2.1.3. Stability analysis

The ideal sliding dynamics given by equation (11) is nonlinear. The linearization of this equation around the equilibrium point *x** results in the following characteristic equation

$$\left(s + \frac{2}{RC}\right) = 0 \qquad (16)$$

which corresponds to a stable system.

3. APPLICATION IN POWER FACTOR CORRECTION PRE-REGULATORS

A direct application of a boost converter-based LFR is a power factor correction (PFC) pre-regulator as shown in Fig. 3. The rectified bridge is supplied by an AC source of 22Vrms and 50 Hz. Figs. 4 and 5 show the PSIM simulated responses in steady and transient-states respectively
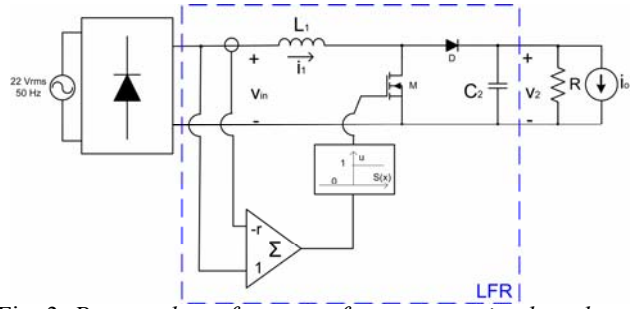

Fig. 3. *Pre-regulator for power factor correction based on a loss-free resistor in sliding operation.*

The simulation parameters are V_{AC}=22 V_{rms} 50Hz, R=60 Ω, L=100 µH, C=1000 µF and r=3.75 Ω. Note that the phase–shift between LFR input voltage and current is zero in Fig.4, this implying a unity power factor at the rectifier input.
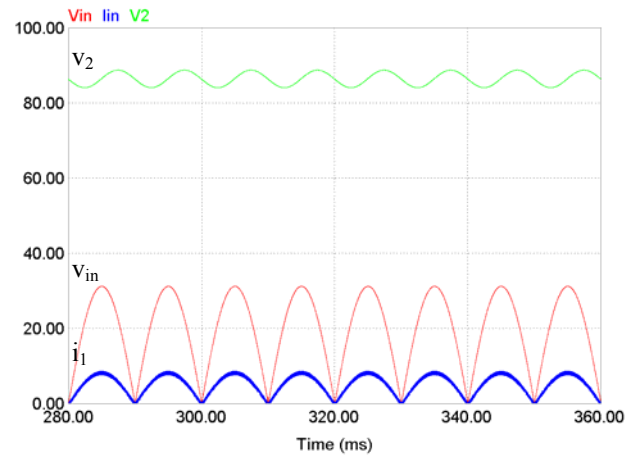
Fig. 4. *Steady-state response of the boost converter-based LFR acting as PFC pre-regulator.*
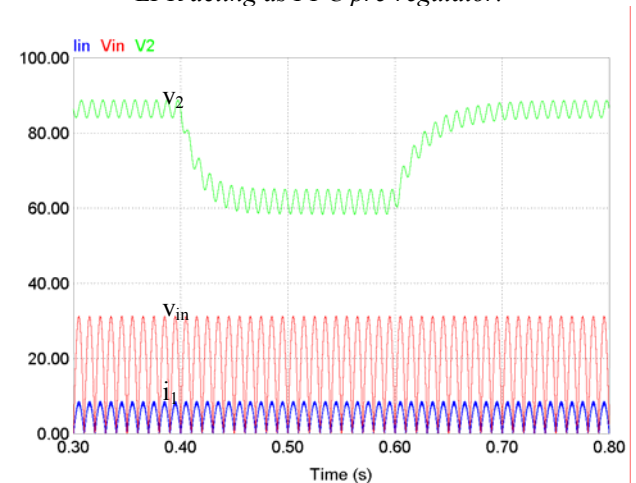
Fig. 5. *Transient response of the PFC pre-regulator depicted in Fig. 3 to load perturbations of step type (60 Ω-30 Ω-60 Ω).*

Figure 5 illustrates, in turn, the transient response of the LFR operating as PFC pre-regulator when step-type load perturbations of 50 % are introduced. Note that the average input power does not change and that the output voltage decreases proportionally to the output current following the load resistance variations.

4. LINEARIZED MODEL OF THE LOSS-FREE RESISTOR

In order to combine in only one stage a unity power factor behavior and output voltage regulation, we have to develop first a dynamic model of the LFR that can be eventually used in the design of a voltage regulation loop. Figure 6 shows the block diagram of the LFR linearized model corresponding to the boost converter–based circuit depicted in figure 3. The model takes into account the different external perturbations of the LFR, namely, load and input voltage perturbations as well as variations of parameter r.
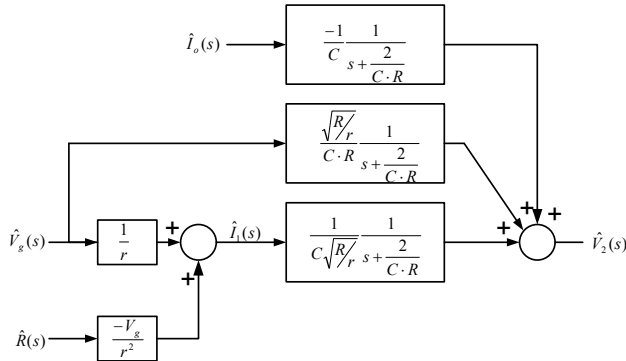
Fig. 6. *Linearized dynamic model of the boost converter -based LFR.*

Figure 7 shows the inclusion of a compensating network $G_C(s)$ in the block diagram of figure 6 in order to regulate the LFR output voltage. The controller $G_C(s)$ processes the output voltage error to provide the variations of the parameter r that is required to meet output voltage regulation and transient response specifications.
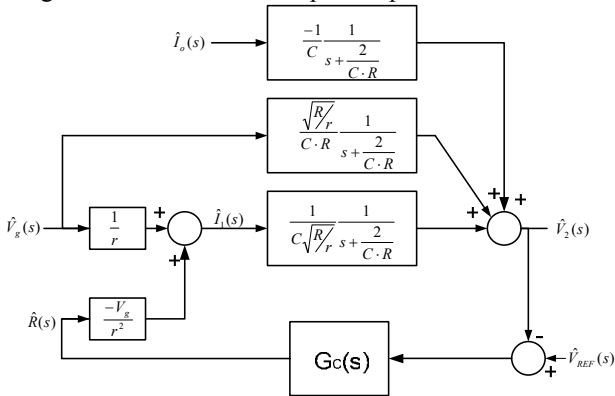
Fig. 7. *Dynamic model of a LFR-based voltage regulator.*

5. SIMULATION

5.1. LFR-based voltage regulation

Figure 8 shows the PSIM simulated start–up from zero initial conditions of a voltage regulator based on a LFR implemented by means of a boost converter in sliding operation. The power delivered to the load in steady–state is 60 W .The simulation parameters are V_{in}=15 V, R=60 Ω, L=100 µH, C=1000 µF and V_{REF}=60 V. The transfer function $G_C(s)$ corresponds to a PI control

$$G_C(s) = K_P + \frac{K_I}{s} \qquad (17)$$

where K_P=-52·10^{-3} and K_I= 7.428.

It can be observed that the output voltage reaches the desired regulated value of 60 V after a transient regime of approximately 100 ms. On the other hand, figure 9 illustrates the LFR response for load variations of 50%. It can be observed that the output voltage reaches the steady–state after a transient state of near 50 ms.
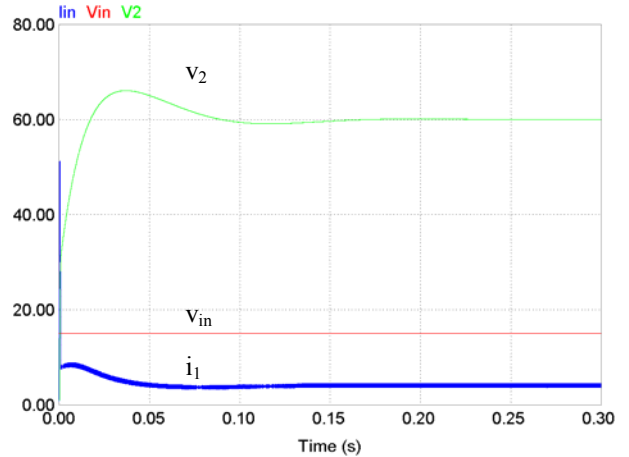
Fig. 8. *Start-up of the boost converter –based LFR acting as a voltage regulator.*
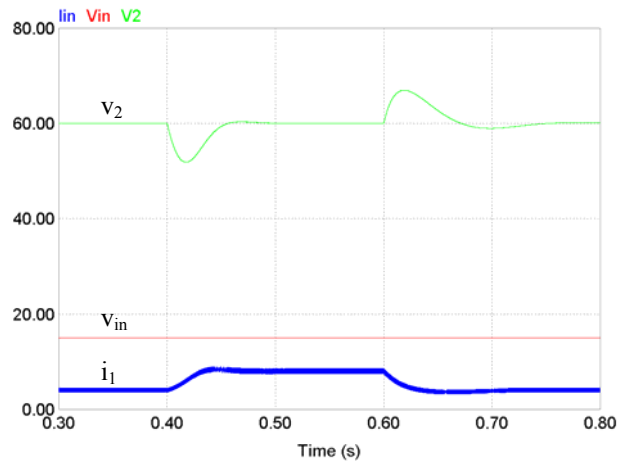
Fig. 9. *Response of a LFR-based voltage regulator to pulsating load perturbations LFR (60 Ω-30 Ω-60 Ω).*

5.2. Voltage regulation and power factor correction in a single stage based on LFR

By using the same regulation scheme depicted in figure 7, we have simulated the LFR behavior when it performs both power factor correction and voltage regulation functions in a single stage. In this case, the LFR is supplied by a non regulated rectifier bridge. The simulation parameters are the following V_{AC}=22 V_{rms} 50 Hz, R=60 Ω, L=100 µH, C=1000 µF, V_{REF}=60 V, K_P=-52·10^{-3} and K_I= 7.428. It can be observed in la figure 10 that the phase–shift between both input voltage and current is zero, this implying a unit power factor at the rectifier output. Note also that at the same time

the LFR provides a regulated voltage of 60 V at the output. Figure 11 shows the circuit response to load perturbations of 50% .The steady-sate is reached after a transient state of 100 ms.
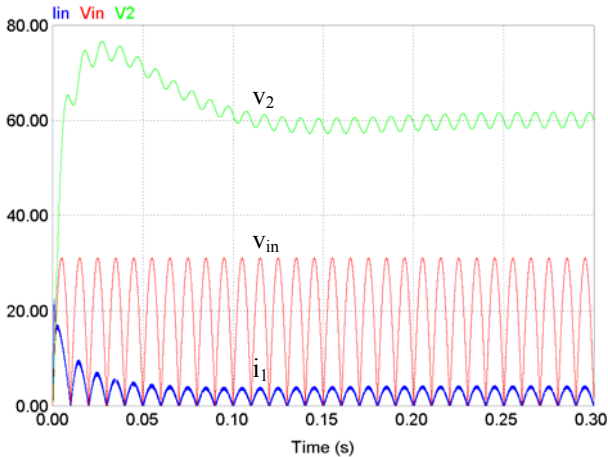
Fig. 10. *Start-up of a LFR-based voltage regulator acting as both power factor corrector and output voltage regulator.*
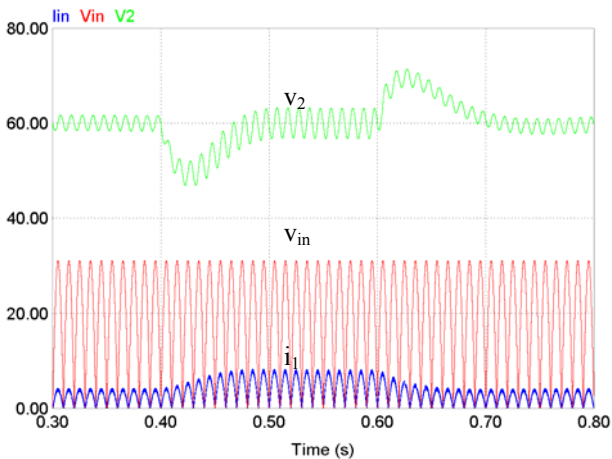
Fig. 11. Response to pulsating load perturbations (60 Ω-30 Ω-60 Ω) of a LFR-based voltage regulator acting as both power factor corrector and voltage regulator.

6. CONCLUSIONS AND FUTURE WORK

In this work, we have presented a systematic procedure to design loss-free resistors from their definition equations. Research is in progress in experimentation where a prototype is being developed to verify both theoretical and simulation predictions.

Also, the application of LFR to solve the problem of DC impedance matching in photovoltaic systems will be soon studied.

7. REFERENCES

[1] S. Singer, "*Realization of loss-free resistive elements*", IEEE Transactions on Circuits and Systems, Volume 37, No. 1, Jan. 1990 pp 54 – 60.

[2] M. J. Kocher, R. L. Steigerwald, "*An AC-to-DC Converter with High Quality Input Waveforms*," IEEE Trans. on Industry Applications, Vol. 1A-19, No. 4, July/August, 1983, pp. 586-599.

[3] J. Lo Cascio, M. Nalbant, "*Active Power Factor Correction Using a Flyback Topology*," PCIM Conf. Proc., 1990, pp. 10-17.

[4] R. Erickson, M. Madigan, S. Singer, "*Design of a Simple High-Power-Factor Rectifier Based on the Flyback Converter*," APEC Conf. Proc., 1990, pp. 792-801.

[5] K. H. Liu, Y. L. Lin, "*Current Waveform Distortion in Power Factor Correction Circuits Employing Discontinuous-Mode Boost Converters*", PESC Conf. Proc. 1989, pp. 825-829.

[6] D. S. L. Simonetti, J. Sebastian, F. S. dos Reis, J. Uceda, "*Design Criteria for Sepic and Ćuk Converters as Power Factor Preregulators in Discontinuous Conduction Mode*," IECON Conf. Proc., 1992, pp. 283-288.

[7] M. Brkovic, S. Ćuk, "*Input Current Shaper using Ćuk Converter*," INTELEC Conf. Proc., pp. 532-539, 1992.

[8] G. Spiazzi, L. Rossetto, "*High-quality Rectifier based on Coupled-Inductor Sepic Topology*," PESC Conf. Proc., 1994, pp. 336-341.

[9] Valderrama-Blavi, H.; Alonso, C.; Martinez-Salamero, L.; Singer, S.; Estibals, B.; Maixe-Altes, J.; "*AC-LFR concept applied to modular photovoltaic power conversion chains*", ,Electric Power Applications, IEE Proceedings,Volume 149, No. 6, Nov. 2002 pp 441-448

[10] L. Rossetto, G. Spiazzi, P. Tenti, B. Fabiano, C. Licitra, "*Fast-Response High-Quality Rectifier with Sliding-Mode Control*," APEC Conf. Proc., 1993, pp. 175-181.

[11] R.Venkataraman., "*Sliding Mode Control of Power Converters* ", Ph.D. Dissertation, California Institute of Technology 1986.

PARAMETER SPACE MAPS OF THE BOOST CONVERTER

Denis Pelin, Kruno Miličević

J.J.Strossmayer University of Osijek, Faculty of Electrical Engineering, Osijek, Croatia

Abstract: *The steady-state responses of the boost converter are identified by means of computer simulation and presented in a form of parameter space maps. The three parameters are used in the process of creating the parameter space maps: input voltage E, period of sawtooth ramp voltage T and output resistance R_d. By combining two parameters, three parameter space maps are created. The period doubling for all parameter space maps is recognised. The simulation results are compared with measurements carried out on physical model of the boost converter by using trajectories in phase plane and waveforms of state variables.*
Key words: *boost converter, steady-state responses, parameter space maps, period doubling.*

1. INTRODUCTION

DC converters are time-varying, nonlinear dynamical systems. It is well known that these systems have several steady-state responses depending on converter parameters [1-5]. Only one steady-state response, so called period- -one operation, is normal or desired operation mode. The other steady-state responses observed in practice as subharmonic solutions or quasiperiodic solution, as well as chaos are assumed to be unstable [6] and designers are always trying to avoid them.

Electronic equipment has typically the disadvantage that a diode bridge capacitor rectifier at the front of power circuit results in distorted input current with high crest factor and undesirable harmonic contest. Such disadvantage has been reduced by using power factor correction circuits. The boost converter is a basic building block of power factor correction circuits. Therefore, it is essential for the application of the power factor correction circuits to design the boost converter in such reliable modality.
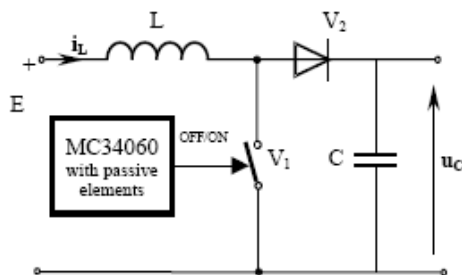

Fig.1. *The basic scheme of the boost converter controlled by pulse-width modulator MC34060.*

It means that for the given scheme of control circuit and power circuit of the boost converter, characteristic steady-state responses as well as interdependency of characteristic converter parameters should be known in advance. The visual correlation between steady-state responses and converter parameters can be point out by using parameter space maps. The parameter space map is colour-coded, two-dimensional plane, depending on the characteristic steady-state responses [7-8].

In our study of boost converter a special attention is paid to the calculation of parameter space maps. We are interested how to recognise the zones of possible steadystate responses of converter in the parameter space map and relate them with characteristic converter parameters. The knowledge of all possible steady-state responses is of great importance to the power system designers as it helps them in the design and allows the avoiding of unstable behaviour of converter in advance.

2. BOOST CONVERTER MODEL

The main devices consisting the boost converter are the switch V_1, the diode V_2, the input inductor L and the output capacitor C_d. In the chosen boost converter the switch V_1 is controlled by naturally-sampled constant frequency pulse-with modulator MC 34060, Fig.1. The internal scheme of the MC 34060 with all ingredients was shown on Fig.2. in purpose to identify mathematical model of the boost converter.
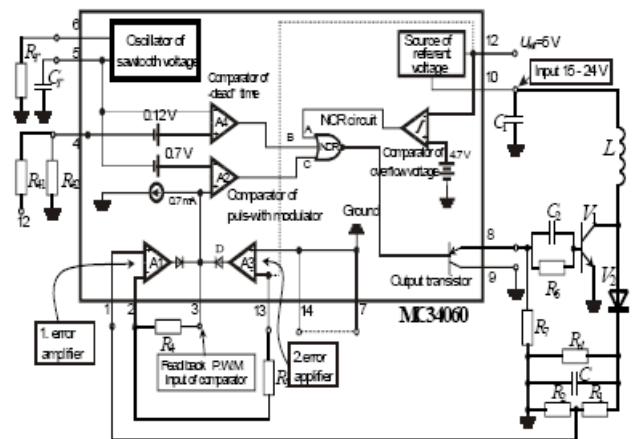
Fig.2. *Functional scheme of the boost converter with all ingredients of MC34060.*

In order to facilitate the mathematical modelling, a special attention was paid to design of converter power circuit. The input inductor was modelled as a series connection of the linear inductance and the linear resistance. The diode V_2 with negligible recovery charge was used. The switch V_1 is realised by bipolar transistor. A low switching frequency, *f*=2 kHz, guarantees that high-frequency effects are minimised.
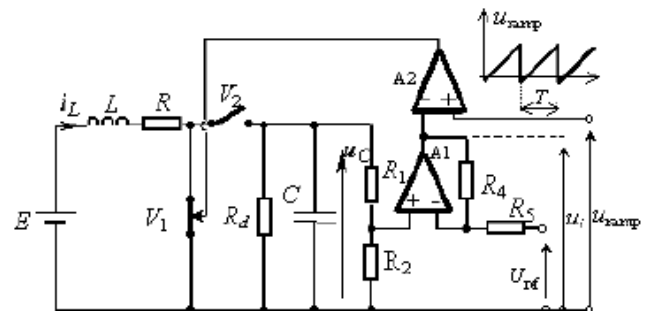
Fig. 3. *Functional diagram of the boost converter.*

The control of output transistor was determined with the state of the comparator of the pulse-width modulator. The state of output of the comparator of the pulse-width

modulator was determined by comparison of the sawtooth ramp voltage u_{ramp} and feedback voltage u_i. When $u_{ramp} \geq u_i$ the controlled switch V_1 is in ON-state and the diode V_2 is in OFF-state. In other case, when $u_{ramp} < u_i$ the controlled switch V_1 is in OFF-state. The sawtooth ramp voltage was determined by measurement and was given with:

$$u_{ramp} = \frac{3}{T}t + 0{,}7 \ [\text{V}]$$

(1)

Therefore, the boost converter can be modelled by piecewise linear time-varying network which is shown in Fig.3.

The three systems of the two first order linear differential equations in state variables, inductor current i_L and feedback voltage u_C were written according to the comparison between sawtooth ramp voltage u_{ramp} and feedback voltage u_i:

a) $u_{ramp} \geq u_i$,

$$\frac{du_C}{dt} = -\frac{1}{CR_d}u_C$$

$$\frac{di_L}{dt} = \frac{1}{L}\left(E - Ri_L\right)$$

(2)

b) $u_{ramp} < u_i$,

$$\frac{du_C}{dt} = \frac{1}{C}\left(i_L - \frac{u_C}{R_d}\right)$$

$$\frac{di_L}{dt} = \frac{1}{L}\left(E - Ri_L - u_c\right)$$

(3)

c) $u_{ramp} < u_i$, $iL=0$,

$$\frac{du_C}{dt} = \frac{1}{CR_d}u_C$$

$$i_L = 0$$

(4)

where the u_i is given by:

$$u_i = \frac{-R_4}{R_5}U_{ref} + \left(1 + \frac{R_4}{R_5}\right) \cdot \frac{R_2}{R_1 + R_2}u_C$$

(5)

In all simulations the fourth-order Runge-Kutta method with the same step size $h=50$ns was used for the numerical integration of state equations. The parameters of converter which were taken as constant are: $R1=22$kΩ, $R2=1.22$kΩ, $R4=2.7$MΩ, $R5=3.9$kΩ, $R=0.73\Omega$, $C=470\mu$F, Uref$=5$V and $L=698\mu$H.

3. VERIFICATION OF THE PROPOSED MATHEMATICAL MODEL

In order to verify proposed mathematical model of boost converter the simulation results were compared with measurements. Some of simulations results and measurements are selected and presented as trajectories in the phase plane u_C-i_L.
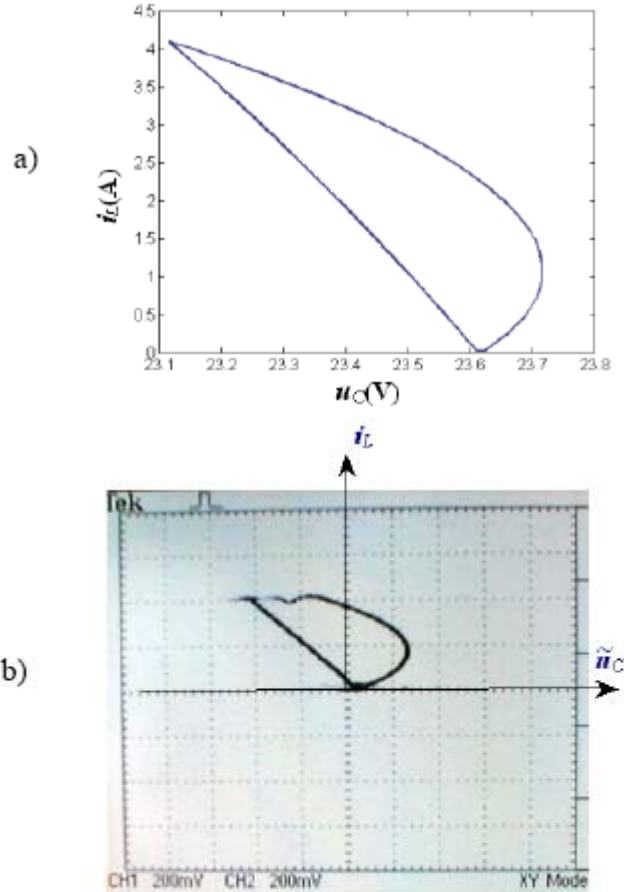
Fig. 4. a) *Calculated trajectory at E=15.25*V, b) *measured trajectory in phase plane* (200mV/div, 2A/div), *at E=15.25*V.

Trajectories typical for period doubling route to chaos are shown in Fig.4.-6. The input voltage was increased while the value of period of sawtooth ramp voltage was T=500μs and value of output resistance was R_d=22Ω. The boost converter is operated in discontinuous conduction mode of operation. The periodone operation was observed when the input voltage is 15.25 V, Fig.4. If we increase input voltage at 17.92 V the trajectory in phase plane is duplicated, which is characteristic for the period two-operation, Fig.5. For the value of input voltage of 21.41V another characteristic steady-state response was observed, Fig.6. At the first sight, it looks like the trajectories on Fig.5. as well as on Fig.6. represent the trajectories of the same steady-state response. It seems that analysis of the trajectories only is not sufficiently in process of recognition of the steadystate responses of the chosen boost converter.

a)

b)
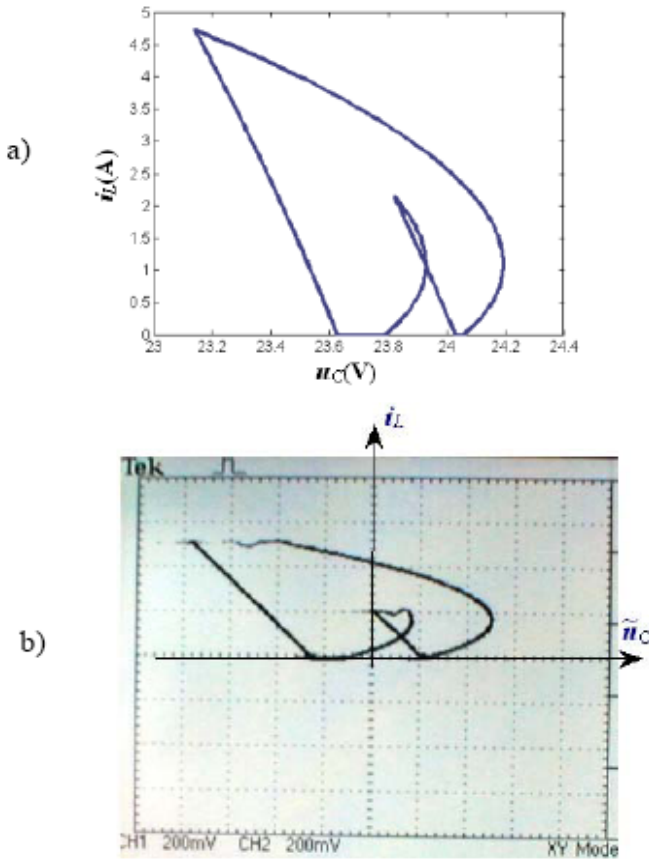
Fig. 5. a) *Calculated trajectory at E=17.92*V, b) *measured trajectory in phase plane (200mV/div, 2A/div), at E=17.92*V.

a)

b)
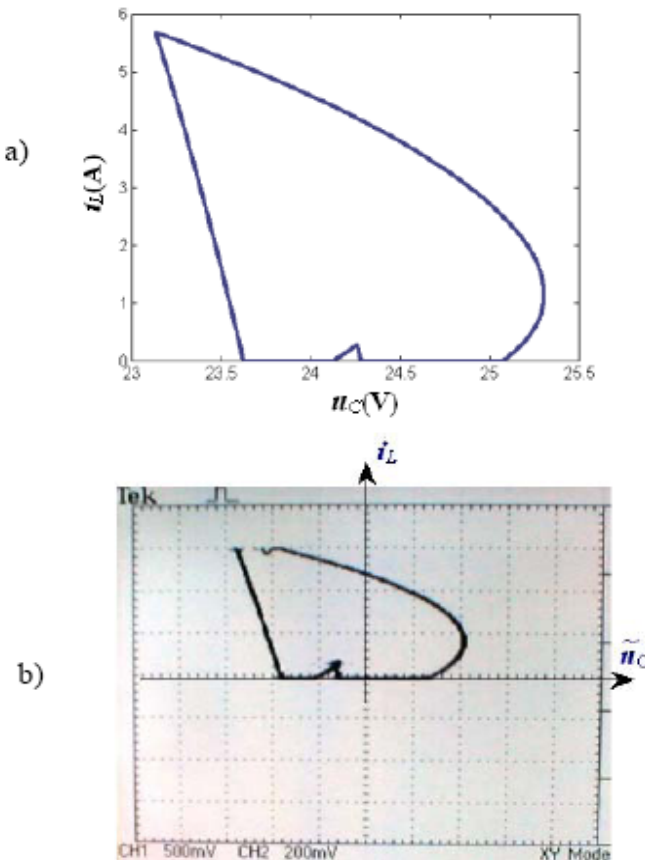
Fig. 6. a) *Calculated trajectory at E=21.41*V, b) *measured trajectory in phase plane (200mV/div, 2A/div), at E=21.41*V.

All information of the steady-state responses were given when the trajectories and waveforms of the state variables, for example, of the inductor current i_L were observed simultaneously with sawtooth ramp voltage, u_{ramp}, Fig.7-8.
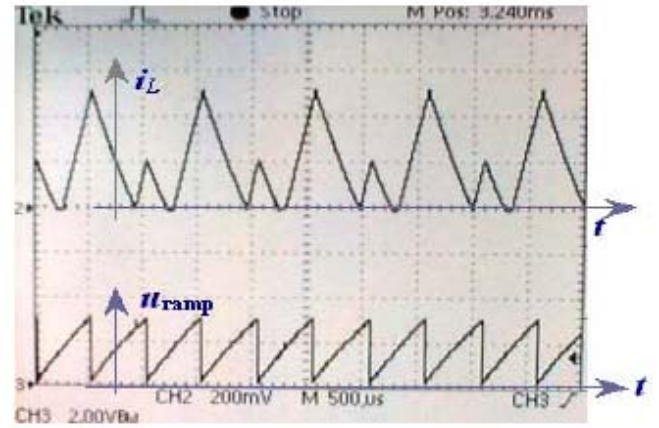
Fig.7. *Measured inductor current at E=17.92*V (2 A/div, 500μs/div).
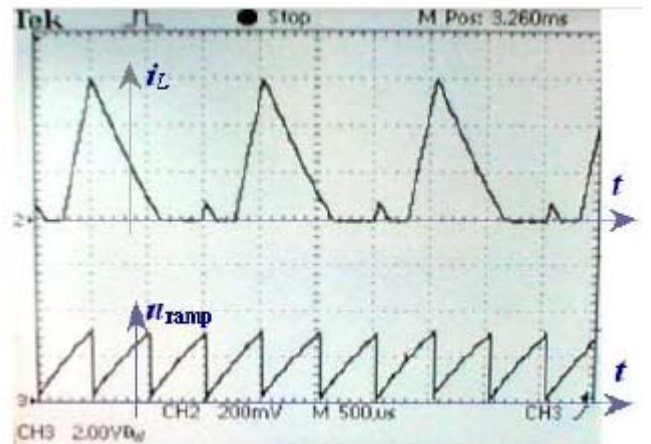
Fig.8. *Measured inductor current at E=21.41*V (2 A/div, 500μs/div).

The number of periods of the sawtooth ramp voltage in observed waveform determines type of steady-state response of the boost converter. Thus, the different steady-state responses were observed on Fig-7 and Fig.8, nevertheless the similarity of the trajectories. The period-two operation was shown on Fig.7., and period-three operation was shown on Fig.8.

By increasing the input voltage E from 15V to 24V the different steady-state responses of the boost converter are identified by observing the waveform of the inductor current as well as the trajectory in phase-plane u_C-i_L. The computed results as well as results obtained by measurements are shown in Table I.

Table 1. *Regions of steady-state responses of the boost converter.*

Steady-state responses	Input voltage E,V	
	Measured values	Computed values
Period-one operation	15-17.78	15-17.5
Period-two operation	17.78-18.86	17.5-19.02
Period-four operation	18.86-19.22	19.02-19.52
Period-eight operation	/	19.52-19.68
Chaos	19.22-20.70	19.68-20.72
	20.74-21.26	20.76-21.39
	21.56-24	21.59-24
Period-five operation	20.70-20.74	20.72-20.76
Period-three operation	21.26-21.49	21.39-21.46
Period-six operation	21.49-21.56	21.46-21.59

A good agreement between simulation results and measurement implies the validity of the chosen mathematical model. It can be used in converter design process especially in the first evaluation of the converter parameters. [9].

4. PARAMETER SPACE MAPS

The parameter space maps provide the insight into transition between different steady-state responses of the boost converter. In parameter space maps one of the state variables, i.e. inductor current i_L was sampled according to the principle of stroboscope mapping, so called Poincaré maps [10]. The 100 samples of inductor current i_L (t_k) are taken, after safety margin of 50 periods, in moments:

$$t_k = kT \; ; \; k = 50,51,...,151 \qquad (6)$$

The process of sampling is carried out simultaneously when two parameters of model are varied. It is important to recognise steady-state response of the boost converter by using the series of sampled points obtained for each pair of choosing parameters values.

The sampled points, which inhere in area of selected tolerance from the first sampled point, were counted in order to identify the steady-state responses. Then, the number of all sampled points was divided with this number. The integer of the result N corresponds to the one of the characteristic steady-state responses. The characteristic steady-state responses ($N=1,2,3,4,8$) are coded with different colour in parameter space map. All other values of calculated number N were assigned to the chaos.

The three parameters were selected: input voltage E, period of sawtooth ramp voltage T and output resistance R_d. Therefore, three parameter space maps were created: ET space map, ER_d space map and R_dT space map, Fig.9.-11. The parameter space maps provides clear image about regions of steady-state responses of the boost converter.
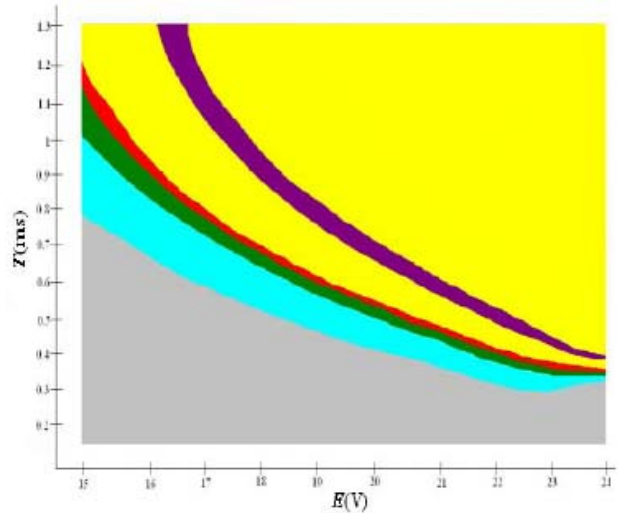
Fig.9. *ET space map ($R_d=56\Omega$) representing zones of period-N operation and chaos, $\Delta E=0.05V$, $\Delta T=5\mu s$. (N=1,2,3,4,8)* ▢1 ▢2 ▢3 ▢4 ▢8 ▢chaos
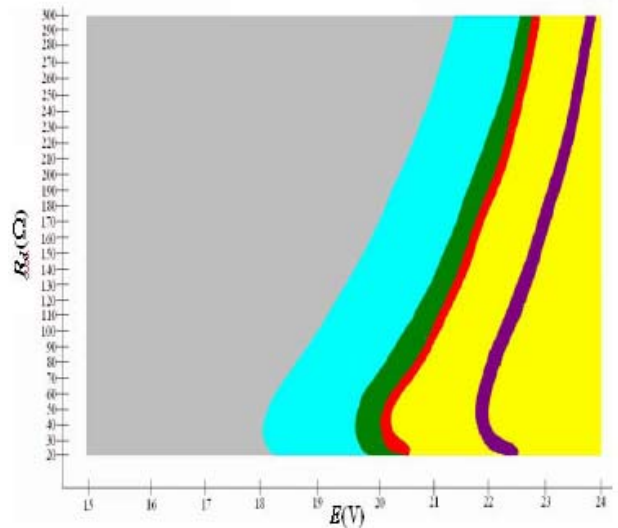
Fig.10. *ER_d space map ($T=500\mu s$) representing zones of period-N operation and chaos, $\Delta E=0.05V$, $\Delta R_d=1\Omega$. (N=1,2,3,4,8)* ▢1 ▢2 ▢3 ▢4 ▢8 ▢chaos

It is also important that from the parameter space map the tendency of varying the parameters for the desired operation mode can be observed. For example, from the ER_d space map, Fig.10., the period-one operation will be reached when the input voltage is decreased and at the same time, the output resistance is increased. The designers can choose the converter parameters in a such way that the desired operating point of the converter is placed at the safe distance from the zone boundaries irrespectively to the variations of converter parameters.
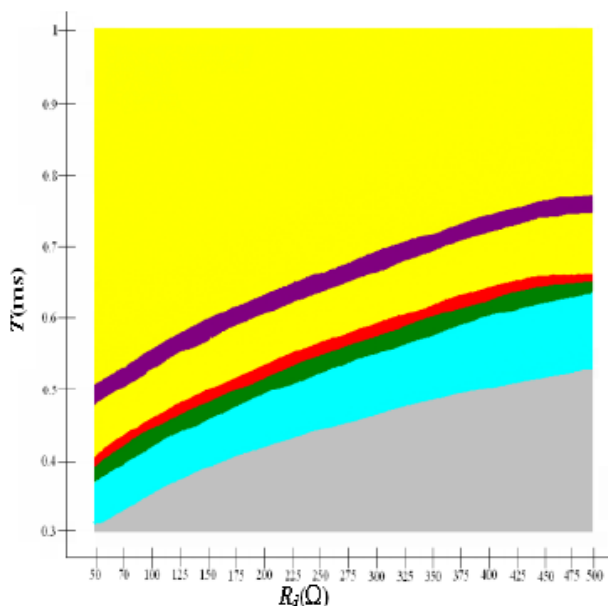
Fig.11. R_dT space map $(E=22V)$ representing zones of period-N operation and chaos, $\Delta R_d=2\Omega$, $\Delta T=5\mu s$. $(N=1,2,3,4,8)$ ☐1 ☐2 ☐3 ☐4 ☐8 ☐chaos

5. CONCLUSIONS

The proposed mathematical model of the boost converter was verified by measurements. It can be used for calculation of the parameter space maps.

The parameter space maps provide a clear picture about boundaries between zones of the steady-state responses and in this way help the designers in process of selecting the converter parameters for the desired operating mode.

6. REFERENCES

[1] J.H.B.Deane, "*Chaos in current-mode controlled boost DC-DC converter*", IEEE Transactions on Circuits and Systems-1, vol.39, 1996, pp. 680-683.

[2] C.K.Tse, "*Flip bifurcation and chaos in three-state boost switching regulators*", IEEE Transactions on Circuits and Systems-1, vol.41, no.1, 1994, pp. 16-23.

[3] A.El Aroudi, L.Benadero, E.Toribo, G.Olivar, "*Hopf bifurcation and chaos from torus breakdown in a PWM voltage-controlled DC-DC boost converter*", IEEE Transactions on Circuits and Systems, vol.46, no.11, 2000, pp. 1374-1382.

[4] J.H.B.Deane, D.C.Hamill, "*Instability, subharmonics and chaos in power electronic systems*", IEEE Transactions on Power Electronics, vol.5, no.3, 1990, pp. 260-268

[5] W.GY.Chan, C.K.Tse, "*Study of bifurcation and chaos in current-programmed DC-DC boost converters: From quasi-periodicity to perioddoubling*", IEEE Transactions on Circuits and Systems, vol.44, no.12, 1997, pp. 1129-1142.

[6] M.Orabi, T.Ninomiya, "*Numerical and experimental study of instability phenomena of a boost PFC converter*", Proceedings of IEEE International Conference of Industrial Technology, Maribor, Slovenia, December 2004, pp. 854-859.

[7] S.Banerjee, K.Chakrabarty, "*Nonlinear modeling and bifurcation in the boost converter*", IEEE Trans. on Power Electronic, vol.13, no.2, March 1998, pp.252-260.

[8] E.Toribo, A.El Aroudi, G.Olivar, L.Benadero, "*Numerical and experimental study of the region of period-one operation of a PWM boost converter*", IEEE Transaction on Power Electronic, vol.15, no.6, 2000, pp. 1163-1171.

[9] I.Flegar, D.Pelin, "*Steady-state responses of the boost converter*", Proceedings of IEEE International Conference of Circuits and System*s*, vol.2, Dubrovnik, Croatia, July 2005, pp. 830-835.

[10] I.Flegar, D.Pelin, T.Adamović, "*Identifying attractors in a boost converter*", 7th WSEAS International Multiconference on Circuits, Systems, Communications and Computers (CSCC 2003), Corfu, Greece, July 2003, pp. 264-268.

IMPLEMENTATION OF COMPACT SWITCHING POWER SUPPLY WITH HIGH POWER FACTOR

Marko Dimitrijević, Vančo Litovski
Faculty of Electronic Engineering Niš

Abstract: *In this paper we will present a power supply – three phase AC/DC converter – with special requirements for power factor and dimensions. Development of such compact devices – up to 8cm3 – provides possibility for mass production of electronic subsystems intended to be implemented within the low voltage grid, reducing emission of higher harmonics (up to 40th) in the power grid and achieving maximal efficiency. Indirectly, this concept enables control of electric energy consumption of small loads. Development of power supply following these characteristics is significant for all producers of electronic equipment compatible with IEC-1000-3 standard.*

Keywords: *power supply, power factor*

1. INTRODUCTION

Special requirements are related to power factor. The industry standards regulate the limits (minimum) of power factor. Switched-mode power supply (SMPS) with passive power factor correction (PFC) can achieve power factor of about 0.7 – 0.75, SMPS with active PFC – up to 0.99, while SMPS without any PFC has power factor of about 0.55 – 0.65 at the best. The current EU standard EN61000-3-2 appoints that all SMPS-es with output power more than 75W must include at least passive power factor correction.

The other requirements for power supply are nominal output voltage 5V, output current 400mA, three phase operation, input voltage range $90V_{RMS}$-$240V_{RMS}$, possibility of only one phase operation, overvoltage protection and galvanic isolation. We will also consider development of the integrated circuit for power factor correction that will be mounted in SMPS with active power correction.
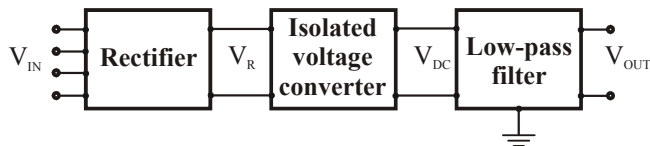
Figure 1. *Power supply scheme.*

2. IMPLEMENTATION AND ELECTRICAL PROPERTIES

Power supply consists of three stages: three-phase full-wave rectifier, isolated voltage converter and output low-pass filter (Figure 1.).

The three-phase full-wave rectifier (Figure 2.) is implemented using high-voltage 1N4007 diodes D1-D16. The number of diodes is doubled to increase maximum input voltage. The neutral is connected symmetrically to phases, providing possibility of one phase operation, as well as normal operation with wrong neutral/phase connection. Rectified voltage VR is limited to circa

400VDC by diodes D21, D22 (BZY97C200) and transistor Q1 (KSA1625).
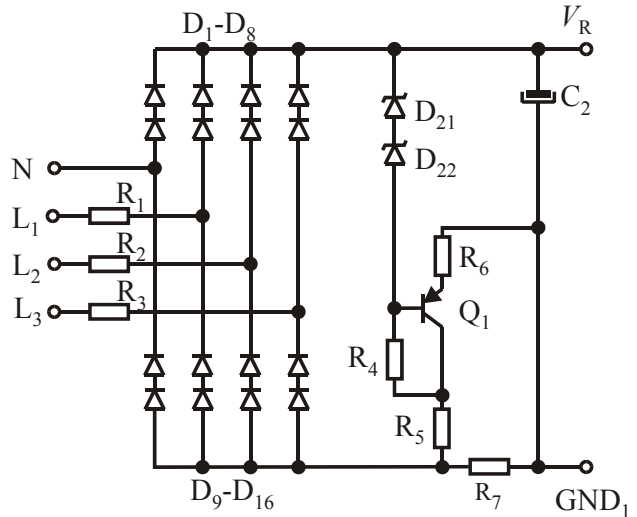
Figure 2. *Full wave three-phase rectifier with protection circuit.*

Basically, there are several types of switched-mode power supplies that can be classified according to the circuit topology. Following the given requirements, the isolated flyback convertor (Figure 3.) concept is used [1].
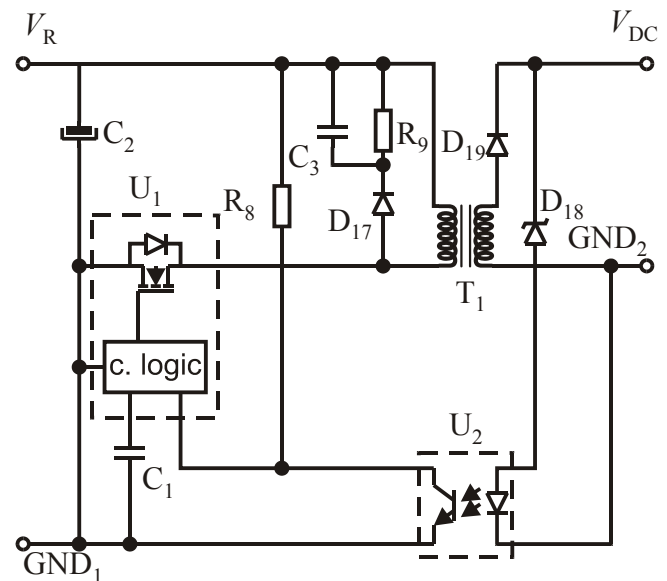
Figure 3. *Voltage convertor.*

Flyback converter is based on TNY267P integrated circuit (U1 on Fig. 3): a power MOSFET, oscillator, a high voltage switched current source, current limit and thermal shutdown circuitry are integrated onto a monolithic device. The start-up and operating power are

derived directly from the voltage on the MOSFET drain, eliminating the need for a bias winding and associated circuitry. This device also includes auto-restart, line undervoltage sense, and frequency jittering. The integrated auto-restart circuit safely limits output power during fault conditions such as output short circuit or open loop, reducing component count and secondary feedback circuitry cost. A line sense resistor R8 (1.5MΩ) externally programs a line under-voltage threshold, which eliminates power down glitches caused by the slow discharge of input capacitor C2 (4.7µF, 450V). The operating frequency of 132 kHz is jittered to significantly reduce both the quasi-peak and average electromagnetic interference, minimizing filtering cost. The integrated circuit breakdown voltage is 700V. C1 (0.1µF, 25V) is external bypass capacitor for the internally generated 5.8V supply. Additional circuit protection is performed by diode D17, connected to C3, R9.

During normal operation, switching of the power MOSFET is controlled by voltage driven from optocoupler U2 (L817B). MOSFET switching is terminated when the collector current is greater than 240µA. Full galvanic isolation is achieved using optocoupler U2 and transformer T1.
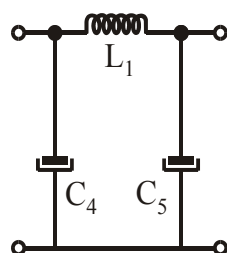
Figure 4. *The low-pass filter.*

The low-pass output filter (fig. 4) is implemented using capacitors C4, C4 (220µF) and inductivity L1 (150µH).

Device implementation is shown on Figure 5.

Figure 5. *Device implementation.*

3. MEASUREMENT INSTRUMENTATION

The measurement of power factor and distortion usually requires special equipment. For example, a classical ampermeter will return incorrect results when attempting to measure the AC current drawn by a non-linear load and then calculate the power factor. A true RMS multimeter must be used to measure the actual RMS

currents and voltages and apparent power. To measure the real power or reactive power, a wattmeter designed to properly work with non-sinusoidal currents must be also used.
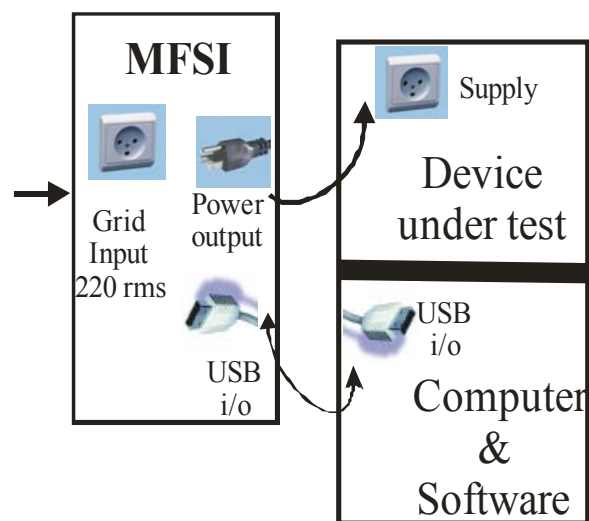
Figure 6. *System for power factor and distortion measurement (denoted as MFSI)*

Computer-based acquisition modules and software provide possibility of creation of simple and non-expensive methods and virtual instruments for power factor measurement and distortion characterization up to 40th harmonic of small loads and bring all advantages of virtual instrumentation [2,3] (Figure 6.). Figure 7. shows virtual instrument implemented in LabVIEW developing environment, which is used for distortion characterization and power factor measurements. Data acquisition is performed using an acquisition module. The system for power factor and distortion measurement is based on National Instruments NI USB-9215A acquisition module (DAQ). The data acquisition module has four channels of simultaneously sampled voltage inputs with 16-bit accuracy, 100kSmpl per channel sampling rate and $250V_{RMS}$ channel-to-earth isolation, adequate for voltage measurements up to 40th harmonic (2 kHz). It also provides portability and hot-plug connectivity via USB interface.

Interface to acquisition module is implemented as device driver. USB-9215A module is supported by NIDAQmx drivers. All the measurements are performed using virtual channels. A virtual channel is collection of property settings that can include name, a physical channel, input terminal connections, the type of measurement or generation, and scaling information. A physical channel is a terminal or pin at which an analogue signal can be measured or generated. Virtual channels can be configured globally at the operating system level, or using application interface in the program. Every physical channel on a device has a unique name.

The user interface of the virtual instrument consists of visual indicators (Figure 8). It provides basic functions for measurement. The indicators – gauges and graphs – show measured values. All measured values are placed in a table, and after the measurement process in appropriate file.
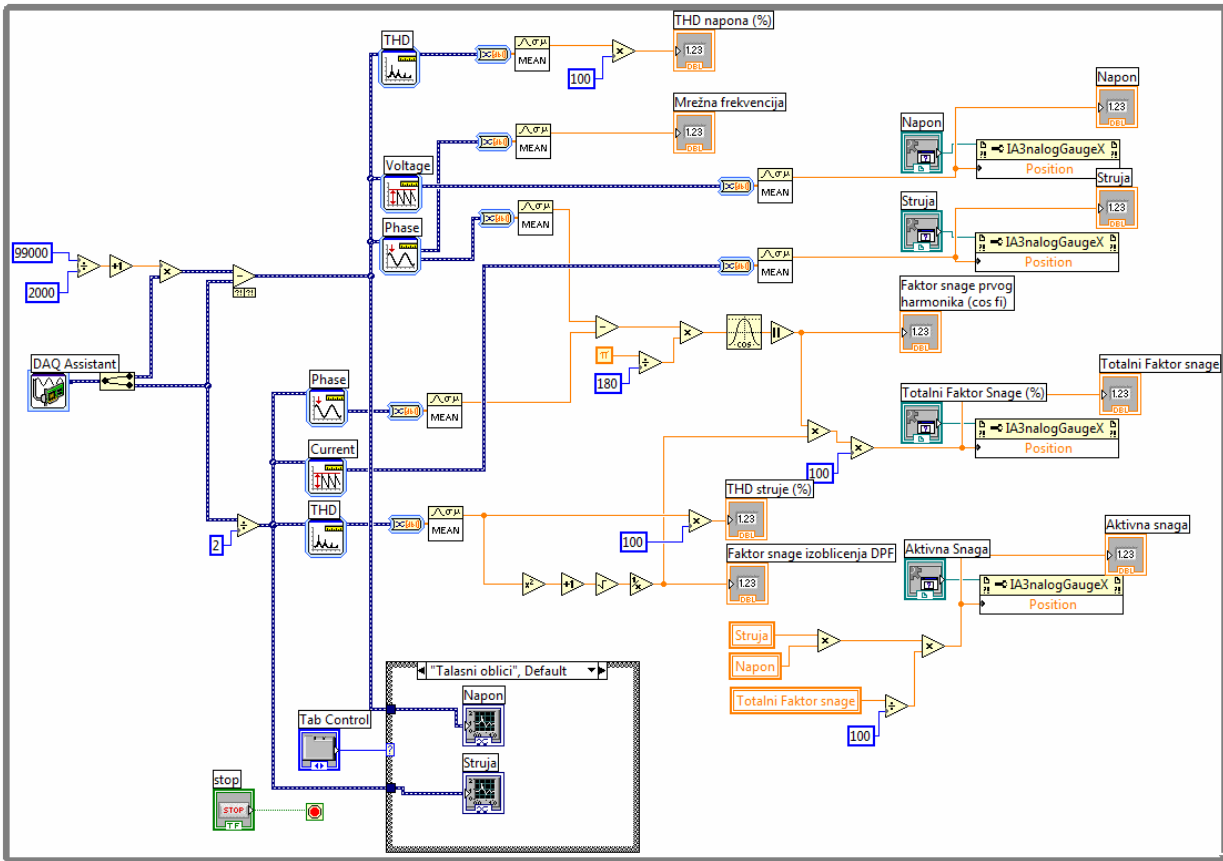
Figure 7. *Virtual instrument implemented in LabVIEW..*
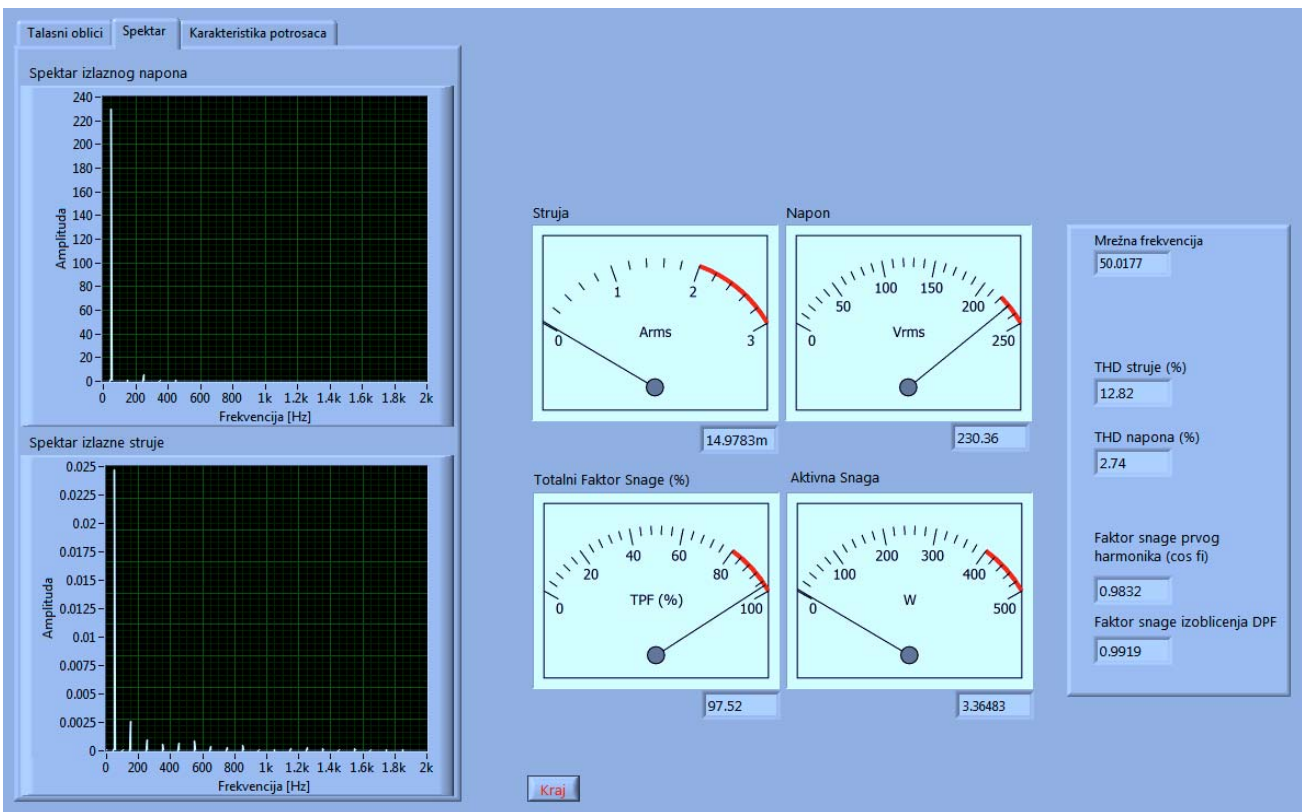
Figure 8. *Virtual instrument user interface..*

User interface also provides controls for data manipulation and saving measured values.

Figure 8. shows measured values for presented voltage converter. Voltage and current power spectrums are shown in panels at the left side of the virtual

instrument. The gauge indicators and numeric indicators in the middle of virtual instrument shows RMS value of input current and voltage (in this case 14.97mA and 230.96V), total power factor (97.52) and real power (3.36W). Measured power grid frequency (50.0177Hz), current THD (12.82%), voltage THD (2.74%), displacement power-factor (power factor of the first harmonic, $\cos(\varphi)$ is 0.9832), distortion power factor DPF (0.9919) are shown at the right pane. The measurement is performed using 66Ω output load. In this case, output DC voltage is 5.7V and output current is 86mA.

The virtual instrument also shows waveform (Figure 9.) and input voltage/current characteristic.
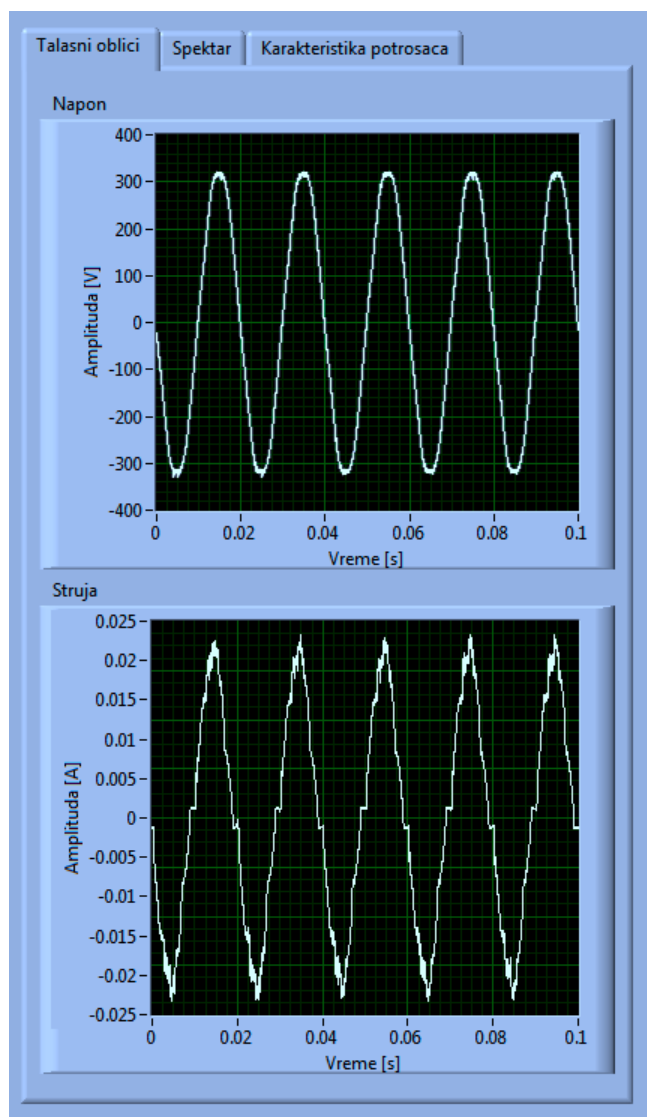
Figure 9. *Current and voltage waveforms.*

4. CONCLUSION

The preliminary results show that power factor and distortions of given power supply concept satisfy the requirements and IEC-1000-3 standard. The measurements are performed for one phase operation.

Table 1 shows measured output voltage and current dependences of input AC voltage.

Table 1: *Output voltage dependences of input voltage*

Startup AC voltage V_{in} [V_{RMS}]	Input AC current I_{in} [mA_{RMS}]	Output DC voltage V_{out} [V]	Output DC current I_{out} [mA]
80	9.5	5.8	50
85	28.5	5.7	170
85 - 200	28.5 - 10.3	5.7	170

With continual change of input AC voltage from 85V_{RMS} to 200V_{RMS} and output current 170mA, output DC voltage is constant and equal to 5.7V.

Table 2 shows output DC voltage dependences on the load, maintaining input AC voltage on 200V_{RMS}.

Table 2: *Output voltage dependences of load (output current)*

Output DC curent I_{out} [mA]	Input AC current I_{in} [mA_{RMS}]	Output DC voltage V_{out} [V]
50	3.7	5.8
170	10.3	5.7
340	19.5	5.65
460	26.1	5.55

4. REFERENCES

[1] Dokić, B.: *Power Electronics – transducers and regulators*, Akademska misao, Belgrade, 2007, (in serbian).

[2] Litovski V., Lazović M.: *Osnovi elektronike*, Niš, 1996.

[3] Dimitrijević, M., Savić, M., Litovski, V.*: Sistem za merenje faktora snage i izobličenja*, Proc. of the INDEL 2006 Conference, pp. 168-171, Banja Luka, Bosnia and Hercegovina.

[4] Dimitrijević, M., Litovski, V.: *Power Factor and Distortion Measuring for Small Loads Using USB Acquisition Module*, Proc. of REV2006 Conference, Maribor.

[5] Dimitrijević M., Litovski V.: *Computer Integrated Analogue Electronics Laboratory for Undergraduate Teaching*, Proceedings of Remote Engineering Virtual Instrumentation Symposium, Brasov, Romania

[6] Dimitrijević, M., Litovski V.: *Implementation of the Component Characteristic Curve Tracer Using PC-based Acquisition Card*, Proc. of Small System Simulation Symposium 2005, pp. 63-66

[7] Dimitrijević, M., Litovski V.: *Implementation of 1MHz Scalar Network Analyzer Using PC-based Acquisition Card*, Proc. of 49th Conference of ETRAN, pp. 90-93

[8] Dimitrijević M.: *Computer Integrated Laboratory for Electronics*, MSc thesis, 2005

THE DSP TMS320F2812 IN CONTROL SYSTEMS OF THE AC DRIVES

Lukáš Osmančík, Petr Moravčík, Petr Chlebiš

VSB – Technical University of Ostrava, Department of Electronics, Czech republic

Abstract: *This paper deals with the application of the signal processor TMS320F2812 in electric drives. An interface is described for a kit with this signal processor. This interface was created at the Department Electronic. Our interface with the DSP is a general-purpose control system for power converters and electric drives. Further, there are discussed two practical applications: the first is the drive of a Four-Quadrant Current Source Rectifier, its Vector Modulation algorithm and other control problems, the second is the drive of an induction motor with a Three-Level Inverter, modulation technique and the possibilities of application of Direct Torque Control are discussed there. Both converters were building like the laboratory models, so there are illustrated real waveforms of important values.*

Key Words: *DSP, Three-level Voltage Inverter, Four-quadrant Current Source Rectifier, DTC, Space Vector Pulse Width Modulation.*

1. INTRODUCTION

Nowadays, digital signal processors are used in electric drives. DSP TMS320F2812 is one of these, and is a member of the TMS320C28x DSP generation. It is a highly integrated, high-performance solution for demanding control applications. This DSP provides the computational power e.g. for powerful vector control algorithms of electric machines and has important peripherals for control the converters. The DSP is a very efficient C/C++ engine that enables users to develop their system control soft-ware in a high-level language. It also allows a mathematical algorithm to be developed using C/C++.

1.1 CHARACTERISTICS OF THE DSP

The starter kit contains the development kit Code Composer Studio, which is fully compatible and enables the engineers to simplify the source code. This software tool chain provides the user with a C compiler, assembler, linker, and a Windows-based debugger. The Processor TMS320F2812 is distinguished by the following characteristics:

- High-Performance static CMOS technology
- 150 MHz (6.67-ns Cycle Time)
- On-Chip memory
- Boot ROM (4K x 16)
- Three external interrupts
- Peripheral interrupt expansion (PIE) block
- Three 32-Bit CPU-timers
- Motor control peripherals
- Two event managers (EVA, EVB)
- Serial port peripherals
- Serial peripheral interface (SPI)
- Enhanced controller area network (eCAN)
- 12-Bit ADC, 16 channels
- Up to 56 General Purpose I/O (GPIO) Pins

2.1. Interface for a Kit with the DSP TMS320F2812

At the Department of Power Electronics and Electrical Drives we have lately been using the microprocessor system with a TMS320F2812 signal processor. This drive system with DSP in the near future will completely replace the original drive with previous microprocessor systems based on slide-in cards. The development kit with DSP cannot be immediately used, therefore we developed at this department an interface for this kit (Fig. 1.), which allows its use in the control of semiconductor converters and modern electric drives.

Inputs of the A/D converter were boosted in such a way that the input voltage level was increased from 0 - 3V to ± 10V. So it is ready for connecting with the current and voltage transducers utilized in power electronics. Then PWM outputs were boosted so that they could be directly connected to the desk for IGBT drivers, which was likewise developed in the department and is used in the majority of currently used converters. There were used opto-isolation elements for Capture units of the DSP. The interface was also equipped with a serial line (SCI). We also used a four-channel, twelve-bit D/A converter, which was connected to the SPI interface.

Fig. 1. *DSP TMS320F2812 with the Interface.*

3. CONTROL OF A FOUR-QUADRANT CURRENT SOURCE RECTIFIER

For control of a four-quadrant current source rectifier (Fig.2), a kit with a TMS 320F2812 signal processor was used. The converter uses switch off components, and this allows the use of modern methods of control, giving us certain advantages. This converter is capable of using current in a sine form with the possibility of selecting a power factor and allows work in all four quadrants. A reverse diode with each IGBT acts as a dividing, blocking diode for the adjacent transistor. For example, a reverse diode in V21 has the function of a separating diode for V11 and vice versa. The condenser battery at the converter input works together with the line inductance like a filter of harmonics. The output inductor serves to smooth the current. Thanks to the quality of the modulation, a smaller value of smoothing induction

may be chosen (which is another advantage of this type of rectifier).
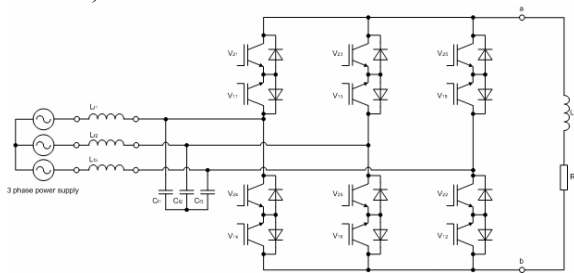
Fig. 2. *Power part of the converter*

There was used the Space Vector Pulse Width Modulation (SVPWM). The pulses of the SVPWM are send on switches according to vector diagram (Fig. 3.). Vector diagram is divided by active vectors into the six sectors. Every active vector is represented by the switching combination, which effect conducting of current from the power supply to the load (or conversely). In the centre, there are located three zero vectors. This zero vectors effect disconnecting the load from the supply and the current is closed (decay) trough switches and the load. The vector diagram is synchronized by space vector of three input phase voltages. This space vector is observed and all of his transitions are respected by the algorithm. The position of the vector in sector is constituted by the duty ratio of switching active vectors inherent to this sector. The magnitude of this vector is confered by duration of switching zero vector. The control algorithm was implemented for modern DSP TMS 320F2812. This rectifier could be used like direct power conversion stage from three phase constant frequency system to one phase variable amplitude and frequency system. Realised converter was used for fed RL load. Software sine generator was add instead of constant request value. In this way, the algorithm was modified for operation such as Matrix Converter 3/2. There were also realised an external control circuits for overlap of the PWM pulses, because of current character of the converter.

AV_{1-6} Active Vector
ZV_{1-3} Zero Vector
V_{fa}, V_{fb}, V_{fc} phase voltages
I. – VI.   sector
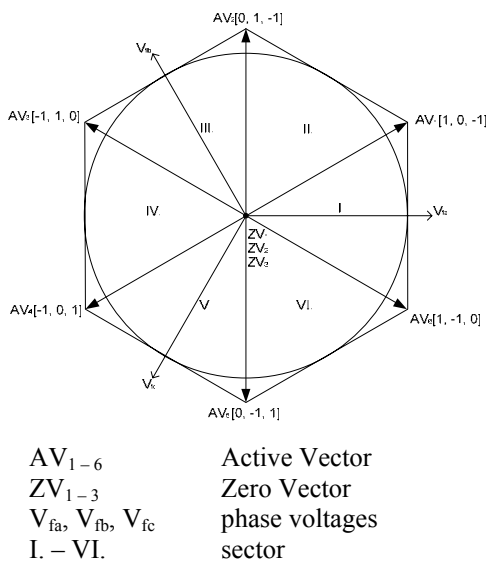
Fig. 3. *The diagram of the SVPWM.*

3.1. Experimental Results
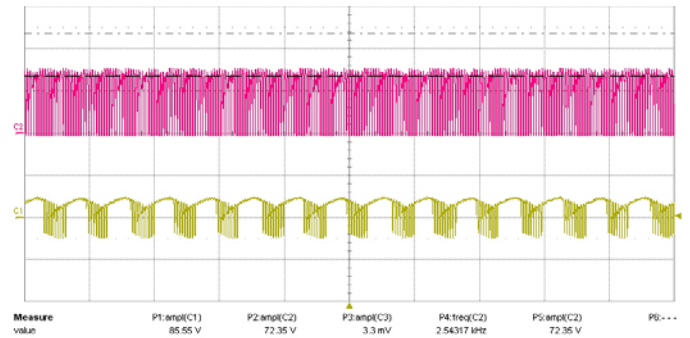
Fig. 4. *Maximum output voltage (up- at output 50V/div, down-output to ground 100V/div).*
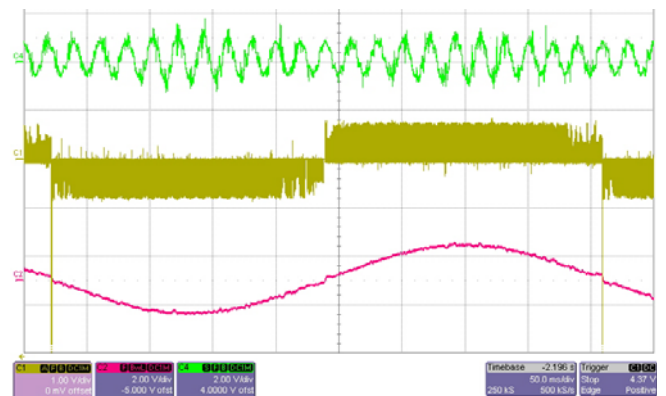
Fig. 5. *Matrix Converter 3/2 (up – input phase current 2V/div 1V≈1A , center – output voltage 1V/div 1V≈50V , down – output current 2V/div 1V≈1A).*

Two-stage or generally called Indirect Matrix Converter is a special type of direct frequency converter. In comparison with conventional Matrix Converter 3/3 makes possible to practice detach input and output stage connected through DC link, without big energy storage elements. The power part is composed from input Four Quadrant Current Source Rectifier, which was described previously and output part formed on VSI. This configuration bears some important benefits: simplest commutation of output and whole converter (compared to conventional Matrix Converter) and possibilities of multi-output stage converter.
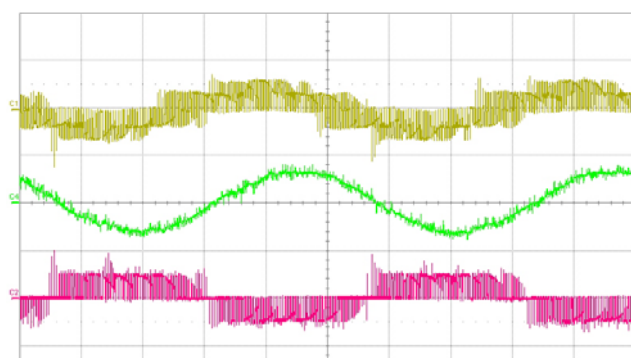
Fig. 6. *Indirect Matrix Converter 3/3 (up – output phase voltage 50V/div, center – output phase current 200mV/div 1V≈1A, down – output line to line voltage 100V/div), output frequency 18Hz .*

4. CONTROL OF THREE-LEVEL VOLTAGE INVERTER

Direct Torque Control (DTC) is a method that has emerged to become one possible alternative to the well-known Vector Control of Induction Motors. This method provides a good performance with a simpler structure and control diagram. In DTC it is possible to control directly the stator flux and the torque by selecting the appropriate Voltage Source Inverter state. The main advantages offered by DTC are:

- Decoupled control of torque and stator flux.
- Excellent torque dynamics with minimal response time.

Inherent motion-sensorless control method since the motor speed is not required to achieve the torque control.

- Absence of coordinate transformation (required in Field Oriented Control (FOC)).
- Absence of voltage modulator, as well as other controllers such as PID and current controllers (used in FOC).
- Robustness for rotor parameters variation. Only the stator resistance is needed for the torque and stator flux estimator.

These merits are counterbalanced by some drawbacks:

- Possible problems during starting and low speed operation and during changes in torque command.
- Requirement of torque and flux estimators, implying the consequent parameters identification (the same as for other vector controls).
- Variable switching frequency caused by the hysteresis controllers employed.
- Inherent torque and stator flux ripples.
- Flux and current distortion caused by sector changes of the flux position.
- Higher harmonic distortion of the stator voltage and current waveforms compared to other methods such as FOC.
- Acoustical noise produced due to the variable switching frequency. This noise can be particularly high at low speed operation.

The basic principle of methods of direct torque control is the same: The three-level voltage inverter is able to provide maximally twenty-seven correct switching combinations, which, on the basis of a theory of complex vectors, corresponds to twenty-seven voltage vectors from $\underline{u}_1$ to $\underline{u}_{27}$. Rotating magnetic field in the stator is created on the basis of an algorithm using switching of active vectors, in which the speed of rotation of the magnetic field, as well as the amount of motor torque, can be driven by switching of zero vectors, or switching active vectors working in the opposite direction of the magnetic field rotation.
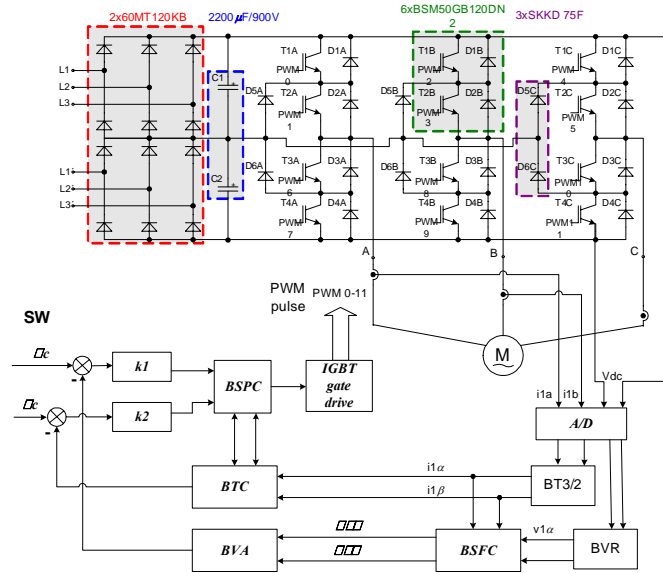
Fig. 7. *Block diagram with the New Method of Direct Torque Control.*

Note:

M   - induction motor
BTC   - block of calculation of torque
BSP   - block of pulse creation
BVR   - block of reconstruction of voltage
BT3/2 - block of transformation 3/2
BSFC   - block of calculation of stator flux
BVA   - block of vector analyzer
BSPC   - block of calculation of switching combination

The stator flux and inner motor torque are calculated on the basis of measured voltage of the DC-link and phase currents. In the Fig.7 is illustrated block diagram with the method of direct torque control.

4.1. The Calculation of Switching Combination

The advantage of the new method compared to earlier ones is the fact that the algorithm provides a direct vector of voltage, which is to be switched for every position of stator flux. In Fig. 8 it is possible to see vectors **g1** and **g2**, in which **g1** is always coaxial with the flux, whereas **g2** is always perpendicular to the flux.

$$\Delta\Psi_1 = \Psi_{\check{z}} - \left|\Psi_1^S\right|$$

$$\Delta m = m_{\check{z}} - m$$

$$\left|\mathbf{g1}\right| = k_1\,\Delta\Psi_1 \qquad (1)$$

$$\left|\mathbf{g2}\right| = k_2\,\Delta m$$
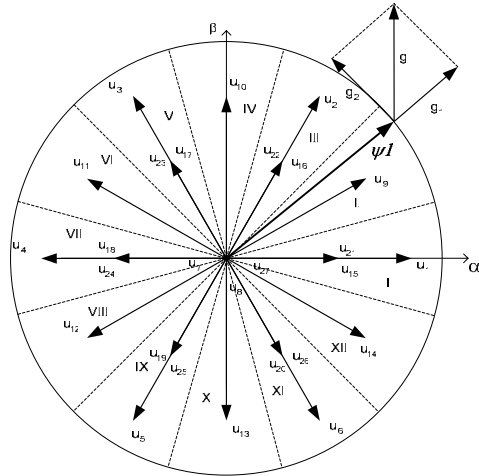
Fig. 8. *Trajectory of the vector of stator magnetic flux according to the Method.*

By adding vectors **g1** and **g2**, we arrive at the resultant vector **g**. If the vector of voltage is switched on, whose direction is the same as the direction of vector **g**, then it is apparent that the value of vector **g1** determines the amount of activation, and the amount of vector **g2** determines the speed of rotation of the vector of stator flux, as well as the amount of torque.

Considering that the three-level voltage inverter uses twenty-seven voltage vectors, of which three are zero vectors, it is necessary to select the vector whose direction most closely resembles that of vector **g** coaxial with the flux, whereas **g2** is always perpendicular to the flux.

4.2. Implementation of five-level hysteresis torque comparator

The SV diagram is divided into twelve sectors and one sector have 30° (See you in the Fig.8). Input values for five-level hysteresis torque comparator are: number of sector, torque errors, voltages on capacity divider vc1, vc2 and value of comparator hysteresis. Five-level hysteresis comparator is included in block of calculation of switching combination. Comparator has five level of torque namely: zero change of torque, positive small change of torque, negative small change of torque, positive large change of torque, negative large change of torque. On the based input values of variables is executed selection of switching combination.

4.3. Experimental results

Some experimental results have been obtained for the Classical DTC (Takahashi's methods) with a three-level VSI and New Method of Direct Torque Control with a three-level VSI to establish a comparison between both systems. In the first method of control – Classical DTC was switched only twelve active vectors and two zero vectors. In the Fig.9 are illustrated measure waveforms for first method: First waveform is output line to line voltage V_{L-L} on asynchronous motor, second waveform is stator flux component $\psi_{1\alpha}$ and last waveform is phase stator current $i_{1\alpha}$.

In the second method: New Method of Direct Torque Control, was switched all active vectors (24) and three zero vectors. Reconstruction voltage is realized with all vectors (27). In the Fig.10 are illustrated measure waveforms for second method: First waveform is stator flux component $\psi_{1\alpha}$, second waveform is $u_{1\beta}$ component, and next waveform is phase stator current $i_{1\alpha}$ and last waveform is torque of motor. The measurement was implement for following parameters: Vdc = 120[V], fs = 5 and 10 kHz.
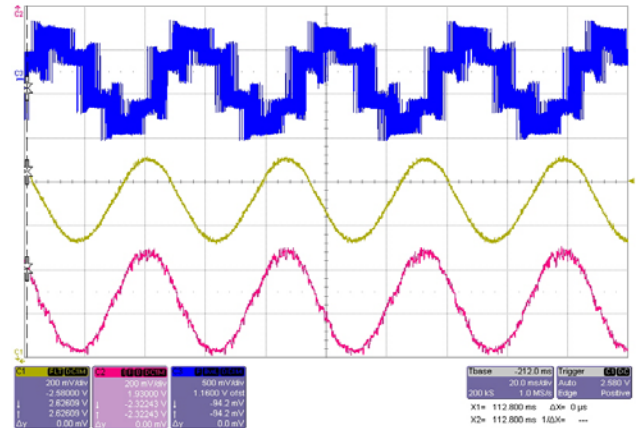
Fig. 9. *Measured values with asynchronous motor, (fs = 10kHz) C1: $\psi1\alpha = f(t)$ C3: $i_{1\alpha}=f(t)$, C4: $V_{L-L.}$ The first method: Modified Takahashi's methods for three-level VSI.*
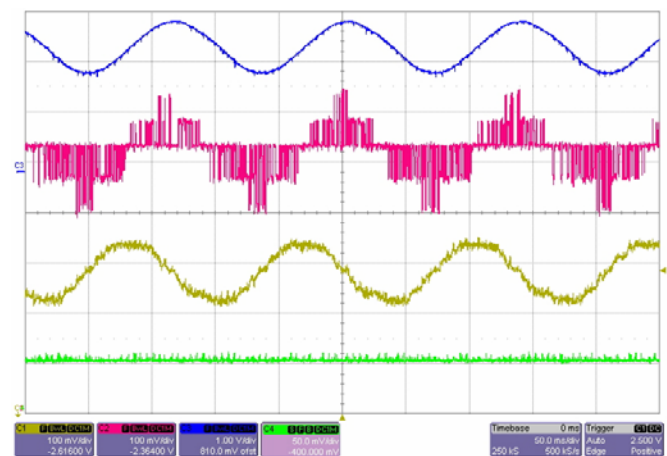
Fig. 10. *Measured values with asynchronous motor, (fs = 5kHz), stator flux, line-line voltage, phase current, torque. The second method: New Method of Direct Torque Control.*

5. CONCLUSION

There was proved some methods of control the modern power converters. Experimental results acknowledge the right way in development of those control strategies and was confirmed some advantages of conception of Indirect Matrix Converter. Matrix converters have better operation in cases where is needed four quadrant operation, lower harmonic emission and low compact dimensions then conventional voltage source inverter. Complicated commutation, rather complex method of control, behavior

during distortion of input voltage and lower voltage at output are disadvantages of those converters. Future work will be focused on tune of those methods for implementation of modern regulation algorithms (vector control or direct torque control). The Three-level voltage inverter have better reduction in torque ripple, flux ripple, harmonic distortion in stator currents and switching frequency when compared with classical DTC system utilizing two-level VSI.

6. ACKNOWLEDGEMENTS

7. REFERENCES

[1] Jussila, M., Salo, M., Kähkönen, L. Tuusa, H., "*A Vector Modulated Three Phase Four Quadrant Rectifier*", Institute of Power Electronics, Finland, 2004

[2] Osmancik, L., "*The Four Quadrant Current Source Pulse Rectifier by DSP Controlled*", Diploma thesis, VSB-TU Ostrava, 2005

[3] Kolar, J.W., Baumann, M., Schafmeister, F., Ertl, H., "*Novel Three Phase AC-DC-AC Sparse Converter*", Interactive Power Electronics Seminar

[4] Empringham, L., Wheeler, P., W., Clare, J., C., "*Intelligent Commutation of Matrix Converter Bi-directional Switch Cells using Novel Gate Drive Techniques*", PESC, 1998

[5] Brandštetter, P., "*A.C. Control Drives - Modern Control Method*", VSB-Technical University of the Ostrava, 1999. ISBN 80-7078-668.

APPLICATION OF SHAFT-SENSORLESS INDUCTION MOTOR DRIVE IN A WASHING-MACHINE

Darko P. Marčetić, Vladan R. Jevremović*

Faculty of Technical Sciences, University of Novi Sad, Novi Sad, Serbia
*SR Drives Ltd – Emerson Motor Technologies, Harrogate, United Kingdom

Abstract: *This paper presents the vector controlled induction motor (IM) drive suitable for high-end washing-machine applications. Firstly, the main features of a washing-machine drive application are discussed, such as the required motor torque-speed characteristic, specific torque ripple and dynamic performance during motor startup and low speed operation. Secondly, Indirect Field Oriented Control (IFOC) drive with Model Reference Adjustable System (MRAS) speed estimator is proposed. The drive is shaft-sensorless and operates with single shunt resistor in DC link. The overall system price is highly competitive, and it can be a suitable replacement for a traditional scalar controlled drive. To insure robust and optimal sensorless operation in low speed range, two simple yet practical solutions are proposed. Both solutions are experimentally verified.*

Key Words: *washing-machine, induction motor drive, sensorless control, MRAS.*

1. INTRODUCTION

Modern high performance washing-machine drives can be made possible only by implementation of the vector control technique. The vector controlled IM drive can achieve high drum speed dynamic performance, advanced flux control in wash; and optimal field-weakening operation in spin. Vector controlled drive also offers robust motor control using minimum number of sensors, which makes it more favorable than old-fashioned scalar controlled drive [1]. Scalar drive is still highly applicable in the today's washing-machines mainly due to its low price. Fierce competition on the appliance market does not permit almost any drive price growth; however more robust drive operation is always welcome. Consistent price reductions of motor control Digital Signal Processors (DSP), capable of running advanced shaft-sensorless vector control algorithms, finally encouraged the use of vector controlled drives for the latest washing-machine applications. The design of IM drive for a high-end washing-machine is not a straightforward task [2]. Firstly, one must account extremely low drive price, limited number of sensors, simple power supply, single layer printed circuit board and low-cost DSP with limited computational capabilities and memory. Secondly, several application requirements, all directly resulting from wide speed range operation, have to be addressed. In the front-load washing-machine the motor torque is usually transferred from the motor shaft to a drum using belted transmission, with typical belt transfer ratio from 11:1 to 14:1. Consequently, motor speed is higher than drum speed, while motor torque is lower than drum torque. Typical washing-machine torque-speed characteristic for the motor applied in front-load washing-machine with the belt system is shown on Fig 1.
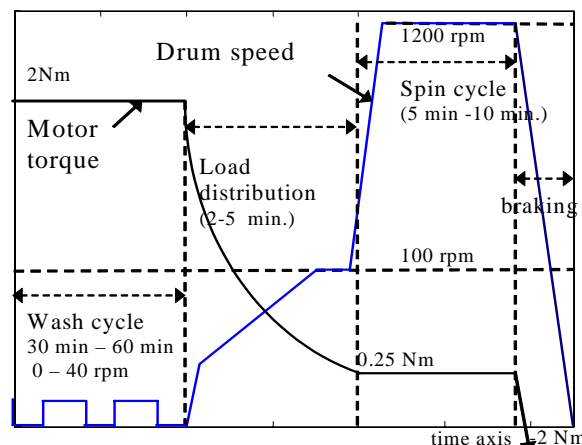
Fig. 1. *Typical wash cycle showing motor torque vs. drum speed.*

The required characteristic is specified for wide speed range. One can clearly distinguish two modes of operation - wash (low speed) and spin (high speed) cycle. Typically, washing-machine mostly operates in wash cycle, having high torque startup every 15 seconds, and high steady state torque. During that phase, significant motor temperature rise and large motor parameter variations can be expected. On the other hand, spin cycle is mainly used for water extraction and it has low torque but high power requirements.
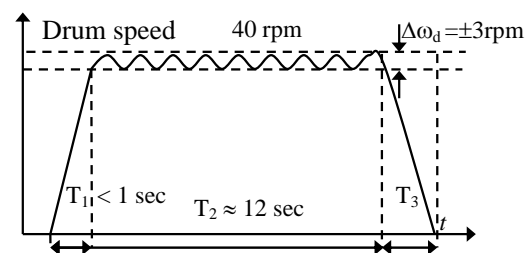
Fig. 2. *Typical speed profile during the wash cycle*

This paper addresses only problems associated with the shaft-sensorless drive operation in wash cycle (Fig. 2). Beside tight speed control requirement in the presence of high torque ripple, there are two other, diametrically opposite requirements - fast ramp-up of the drum speed during the startup phase (T_1) and optimal flux level setup during the motor run phase. Obviously, superior dynamic performance of the vector controlled drive can improve the speed ripple but it is also the best solution for the other two listed requirements. We are proposing a simple shaft-sensorless vector controlled IM drive with minimal number of sensors, capable of giving high starting torque. The drive is additionally equipped with simple flux controller, which adapts flux level to the actual mechanical load and insures minimal motor losses.

2. MRAS SPEED ESTIMATOR WITH MINIMUM NUMBER OF SENSORS

In order to be competitive in the appliance market, the washing-machine drive has to be shaft-sensorless and based on a low cost DSP or microcontroller. Having that in mind, advanced speed estimation associated with high-end processors, expensive peripherals and power supply circuitry should be avoided [3]. Shaft-sensorless algorithm of our choice is simple MRAS speed estimator based on two rotor flux models with different structures [4]. The reference (voltage) model and the adjustable (current) rotor flux model are given in (1) and (2), respectively. The error signal used for tuning of the estimated speed is phase angle between two flux vectors (3).

$$p\vec{\psi}_r^{vi} = \frac{L_r}{L_m}\left(\vec{v}_s - \left(R_s + \sigma L_s p\right)\vec{i}_s\right) \qquad (1)$$

$$p\vec{\psi}_r^{\omega i} = \frac{L_m}{T_r}\vec{i}_s - \left(\frac{1}{T_r} - j\hat{\omega}_r\right)\vec{\psi}_r^{\omega i} \qquad (2)$$

$$\varepsilon = \vec{\psi}_r^{\omega i} \times \vec{\psi}_r^{vi} = \psi_{\alpha r}^{\omega i}\psi_{\beta r}^{vi} - \psi_{\beta r}^{\omega i}\psi_{\alpha r}^{vi} \qquad (3)$$

where $\vec{\psi}_r^{vi} = [\psi_{\alpha r}^{vi} \ \psi_{\beta r}^{vi}]^T$, $\vec{\psi}_r^{\omega i} = [\psi_{\alpha r}^{\omega i} \ \psi_{\beta r}^{\omega i}]^T$, $\vec{v}_s = [v_{\alpha s} \ v_{\beta s}]^T$, $\vec{i}_s = [i_{\alpha s} \ i_{\beta s}]^T$ are outputs of the rotor flux voltage and current model, stator voltages and currents, respectively; $\hat{\omega}_r$ is estimated rotor angular frequency; L_m, L_s, L_r are magnetizing,

stator and rotor inductances; $\sigma = 1 - L_m^2/L_sL_r$ is total leakage factor. Equations (1)-(3) are defined in stationary reference (α-β) frame.

In order to match the phase angle between two estimated rotor flux vectors, the MRAS error signal is fed to the linear regulator (Fig. 3) which in turn tunes the estimated speed variable and hence performs the correction of the model (2) result.
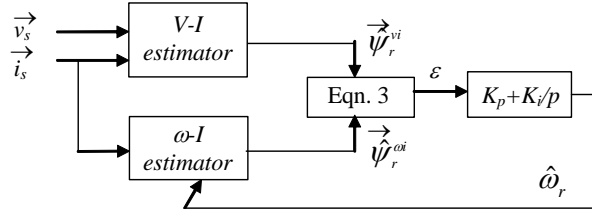
Fig. 3. *Block diagram of MRAS speed estimator*

MRAS speed estimator eliminates the need for expensive speed sensor. Usage of sensors in the drive is also minimized, whenever it is possible. Phase voltages are not measured; they are rather reconstructed using PWM pattern and measured DC link voltage. Only DC link current is measured with simple shunt resistor, and used for the phase currents reconstruction [5]. Block diagram of the system with minimal number of sensors, is given in Fig 4.
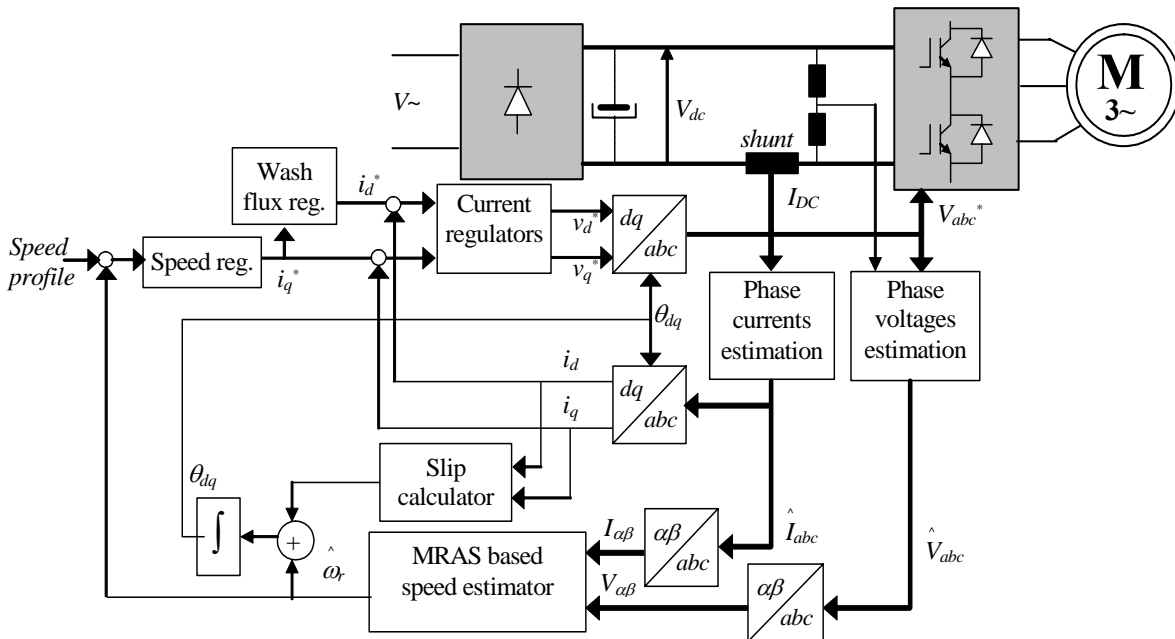
Fig. 4. *Block diagram of shaft-sensorless induction motor drive with minimal number of sensors and MRAS speed estimator*

3. SIMPLE SOLUTION FOR SENSORLESS MOTOR STARTUP

Washing-machine shaft-sensorless drive application is most demanding during the motor startup. Specified drum speed rise time is relatively short, and has to be accomplished with high starting torque. The problem gets more complex for shaft-sensorless drive which estimates rotor position using available motor terminal quantities. For low speeds, including standstill, the rotor-induced voltage diminishes on stator

terminals making MRAS speed estimate sensitive to the stator voltage and stator resistance voltage drop estimation errors. To avoid unstable speed and position estimation, the stator voltage estimation must include all the inverter nonlinearity effects, such as the switching devices dead-time and conducting voltage drop [6]. Also, stator resistance thermal drift has to be taken into account. For a washing-machine application, one can take advantage of motor wash duty cycle, having relatively long stoppage time between two runs. During stoppage, the stator resistance can be measured

with simple DC current injection [7]. However, low stator frequency during the motor startup causes additional problem, originating in MRAS usage of quasi integrators. The quasi integrators $1/(p+\omega_l)$, used to suppress oscillations in estimated reference flux, create an unwanted phase lag, especially for frequencies close to or below the cut-off frequency ω_1. This can be canceled for frequencies above the ω_1, by using the first order filter to process the current vector signal, as it is shown in Fig 5.
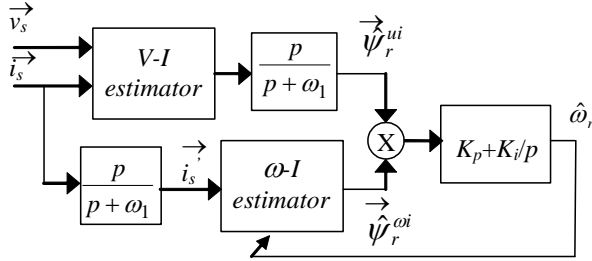
Fig. 5. *Modified MRAS speed estimation scheme.*

This compensation does not work well for frequencies below the cut-off frequency. The proposed motor startup solution is simple and suggests that these frequencies should be avoided. Before the run, both stator current d-q references must be set to their nominal values. The speed estimator should be stopped ($\hat{\omega}_r = 0$) until the actual current values get close to the reference values, when also output stator frequency should have exceeded the cut-off frequency, set in drive to 1Hz.

$$\omega_s = \hat{\omega}_r + \frac{1}{T_r^*}\frac{I_q}{I_d} = \frac{1}{T_r^*}\frac{I_q}{I_d} > \omega_1 = 2\pi \ rad \ / \ s \quad (4)$$

With the rotor time constant close to 100ms, and $I_q \approx I_d$, starting stator frequency is already above the cut-off frequency and rotor speed estimator can start.

4. OPTIMAL FLUX LEVEL CONTROL DURING WASH CYCLE

During the wash cycle motor can heat up to the highest temperature point in the entire cycle. To prevent extensive motor heat-up, especially above the rated 150 C°, the flux reference (I_d^*) optimization criteria in wash phase must be the minimization of overall motor losses. The washing machine drive is speed controlled, and in the steady state the achieved electrical torque must be equal to the load torque.

$$T_{el} = K_t \Psi_d I_q = K_{t1} I_d I_q = T_{load} \quad (5)$$

But, there is still one degree of freedom for d and q current reference selection, which can be used for rotor flux level optimization. Most of the motor losses during the low speed wash cycle are the resistive losses (6), (7).

$$P_{losses} \approx P_{cu} = R_s(I_d^2 + I_q^2) \quad (6)$$

$$P_{cu} = R_s\left(\left(\frac{T_{load}}{K_{t1}}\right)^2 \frac{1}{I_q^2} + I_q^2\right) \quad (7)$$

Minimizing only resistive losses would still be sufficient to bring the overall motor losses in wash cycle to the acceptable level. Minimum resistive losses

$$\frac{dP_{cu}}{dI_q} = R_s\left(-2\left(\frac{T_{load}}{K_{t1}}\right)^2 \frac{1}{I_q^3} + 2I_q\right) = 0 \quad (8)$$

can be obtained for

$$I_q = \sqrt{\frac{T_{load}}{K_{t1}}} \quad (9)$$

Using (5) and (9), I_d and I_q values that insure optimal flux level for any given load torque can be found as:

$$I_d = I_q = \sqrt{\frac{T_{load}}{K_{t1}}} \quad (10)$$

Direct assignment of I_q^* to the flux current reference I_d^* would deteriorate the speed control dynamics and cannot be applied in practice. Instead, a simple integral action can be used:

$$I_d^*(k) = I_d^*(k-1) + K_f(I_q^*(k-1) - I_d^*(k-1)) \quad (11)$$

The selection criteria for the flux loop gain K_f must address the short run time during the wash cycle. In practice flux reference must adapt to the steady state load value within the first two to three seconds after the start.

Sense the drive now has variable d-axis current command, MRAS parameters (L_m, T_r) should be altered with the change of the main flux saturation level [8].

5. EXPERIMENTAL RESULTS

The induction motor (rated power 700W, rated voltage 195V, Δ connection, two poles, $R_s = 9.1\Omega$, $R_r = 5.73\Omega$, $L_m = 0.585H$, $L_s = 0.615H$, $L_r = 0.615$ H, $\sigma L_s = 0.058H$, under rated conditions) was loaded with MAGTROL 5410 dynamometer. Three-phase voltage source inverter was controlled digitally, using the low-cost Freescale DSP 56F8013 at 32MHz with 16k flash memory. DC link current was measured using single shunt in DC link circuit and phase currents were reconstructed from that signal. The motor voltage was estimated using DC link voltage samples and the PWM duty cycles, with the compensation of dead-time and voltage drop on switching devices. The PWM frequency was set to 15.6 kHz, which is the same sampling frequency for all other calculations: phase currents reconstruction, phase voltages estimation, MRAS rotor speed and position estimator. Speed and flux controllers operate at sampling frequency of 200Hz. The cut-off frequency of quasi integrators used in MRAS was set to 1Hz. Bandwidths of speed and current control loops are set to 20Hz and 200Hz, respectively. The rotor speed was monitored for verification purposes using AC tachometer. The effectiveness of the proposed shaft-sensorless scheme can be well demonstrated with two experimental results, showing relevant signals during the motor startup with minimum and nominal load torque on the shaft.

Figures 6-7 show: motor rotor speed (commanded value is 540 rpm - 13.5:1 belt ratio and 40 rpm drum speed), estimated torque, and average stator d and q axis current. In both cases, fast drum speed ramp-up is achieved. Drum speed settle time in both cases is about 700 ms, which is below usually specified drum speed ramp-up time. Also, for the motor free shaft startup, one can note prompt flux reference excursion to the lowest allowed value (0.55A). At that point, motor has steady state speed around 540 rpm,

running with only 15 Vrms, which is set as the absolute lowest limit to achieve optimal single DC shunt reading. The motor losses can be neglected, since the flux level saturation is avoided. Quite the opposite,
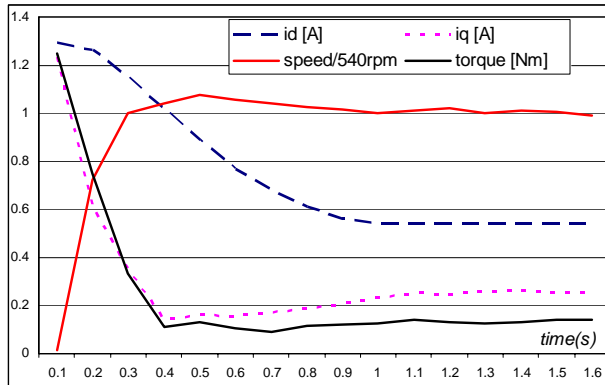

Fig. 6. *Motor speed, torque and current waveforms for low load start*
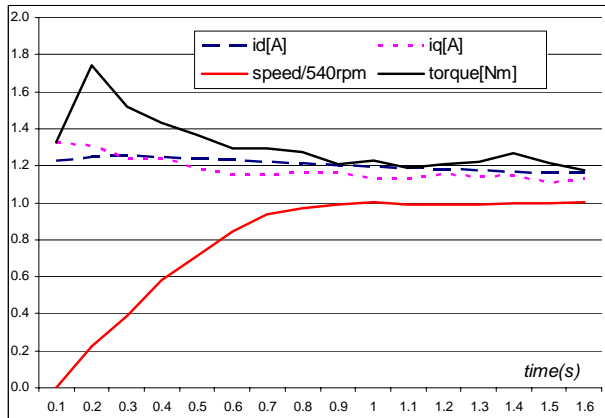
Fig. 7. *Motor speed, torque and current waveforms for nominal load start*

for high load start, one can note parallel traces of both stator current components. Flux reference has slower dynamics, as it is expected from (10). At the steady state, motor speed settles at 540 rpm, with the optimal flux level set to mechanical load on the shaft. Any other arbitrarily selected flux reference increases the motor input power, and consequently the motor losses.

6. CONCLUSION

In this paper, a simple shaft-sensorless drive solution for washing-machine application is proposed. All the drive features are specified under the assumption of price restriction. The selected shaft-sensorless MRAS algorithm is not computationally intensive and does not require significant processor power. Major MRAS drawback, which is the operation with stator frequency lower than quasi integrators cut-off frequency, is simply avoided. In addition, this solution increases the starting torque and decreases the ramp-up time. Finally, the control software is improved by adding simple flux reference regulator which insures minimum motor losses during wash cycle. The flux regulator operates in parallel with speed regulator, and adapts drive performance to the load right from the startup.

7. REFERENCES

[1] J. Holtz, "*Methods for speed sensorless control of AC drives*", Sensorless Control of AC motors, IEEE Press Book, 1996.

[2] Z. Zhang, H. Xu, L. Xu, L. E. Heilman, "*Sensorless Direct Field-Oriented Control of Three-Phase Induction Motors Based on "Sliding Mode" for Washing-Machine Drive Applications* ", IEEE Trans. Ind. Appl., vol. 42, no. 3, pp. 694-701, May/June, 2006.

[3] J. Holtz, "*Sensorless Control of Induction Machines — With or Without Signal Injection?*", IEEE Trans. Ind. Electron., vol. 53, no. 1, pp. 7–30, Feb. 2006.

[4] C. Schauder, "*Adaptive speed identification for vector control of induction motors without rotational transducers*", IEEE Trans. Ind. Appl., vol. 28, no. 5, pp. 1054-1061, Sept/Oct, 1992.

[5] H. Kim, T. M. Jahns, *"Phase Current Reconstruction for AC Motor Drives Using a DC Link Single Current Sensor and Measurement Voltage Vectors"*, IEEE Trans. Power Electron., vol. 21, no. 5, pp. 1413–1419, Sept. 2006.

[6] J. Holtz, J. Quan, "*Drift and Parameter Compensated Flux Estimator for Persistent Zero Stator Frequency Operation of Sensorless Controlled Induction Motors*", IEEE Trans. Ind. Appl., vol. 39, no. 4, pp. 1052-1060, July/Aug. 2003.

[7] S. Thorn, et. al., "*Estimation of Motor Temperature From Terminal Voltages and Automatic Calibration Thereof*", Emerson Electric Patent No. EMC-04-023, 2005.

[8] E. Levi and M. Wang, "*A Speed Estimator for High Performance Sensorless Control of Induction Motors in the Field Weakening Region*", IEEE Trans. Power Electron., vol. 17, No 3, pp 365-377, May, 2002.

INFLUENCE OF VELOCITY LEVEL ON DYNAMICS OF THE DRIVE

Mikolaj Babicz, Roman Muszynski

Poznan University of Technology, Faculty of Electrical Engineering, Poznan, Poland

Abstract: *The paper deals with the system: Pulse Width Modulated Voltage Source Inverter – Permanent Magnet Synchronous Motor – load with flexible mechanical coupling. A special model considering the velocity influence on limit of the current change rate was built. The influence of velocity level on dynamics of the drive is tested. Recommendations relating to tuning the controller for wide range of the velocity and others factors are also elaborated.*
Key Words: *Servodrives/Dynamics/Robust Controller.*

1. INTRODUCTION

The current control loop of electrical drives for analysis and designing the velocity controller is often reduced [2, 3] to the simple inertia block with equivalent time constant or even to proportional block. It is due to fast operation of this circuit which usually is much faster than the velocity control loop. But in modern drives (with high value of torque-to-inertia ratio) [1, 6] the dynamics of

Fig.1.*The PMSM drive.*

velocity change is so high that the time of torque (current) change can be considerable part of whole period of dynamical state duration. It is especially visible during operation of the drive with high velocity when the difference between the supply voltage and EMF of the motor is small. The phenomenon must be taken into consideration in the case of drive with flexibility of mechanical coupling between motor and load. In this case the controller should active damp the torsional oscillation of high frequency [1, 6]. Such operation of the controller depends considerably on the value of current change rate.

The aim of the paper is to show how is influence of the velocity level on the current change rate and on the dynamics of the system and how to tune the controller in order to obtain a good properties of the drive in wide range of the velocity.

2. STRUCTURE AND PARAMETERS OF THE SYSTEM

The plant containing PWM (Pulse Width Modulated) VSI (Voltage Source Inverter), PMSM (Permanent Magnet Synchronous Motor) and load with flexible mechanical coupling (Fig. 1) is analysed. The system together with the current control loop and velocity state controller is replaced with the block diagram shown in Fig. 2 [4]. The part of the diagram with three integration blocks is a model of two-mass system with flexible coupling. For investigation the following data of real plant were chosen: maximum velocity of the motor Ω_{max}=4500 rev/min, maximum current I_{max}=18 A, maximum torque – 23.9 N·m, motor inertia J_M=7 kg·cm^2. The load inertia and coupling stiffness have preliminary values J_L=15 kg·cm^2 and C_F=350 (N·m)/rad, respectively.

The velocity controller is linear. The following quantities were chosen as the state variables:
– motor current i (or torque m_M),
– motor shaft velocity ω_M,
– flexibility torque m_F,
– load shaft velocity ω_L.

They can come from sensors or can be obtained by
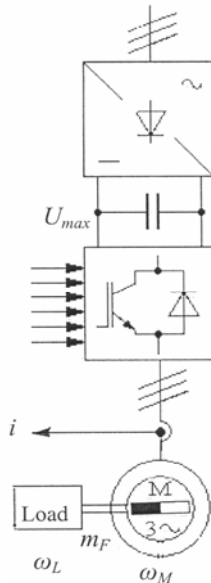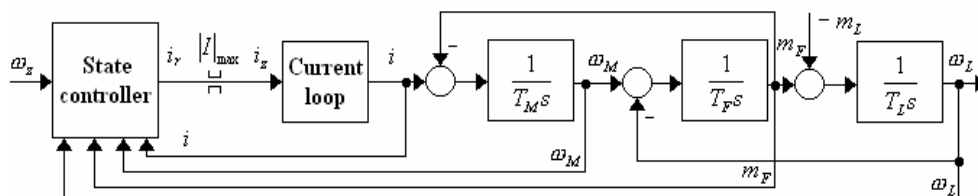

Fig. 2. *Block diagram of the drive and its control.*
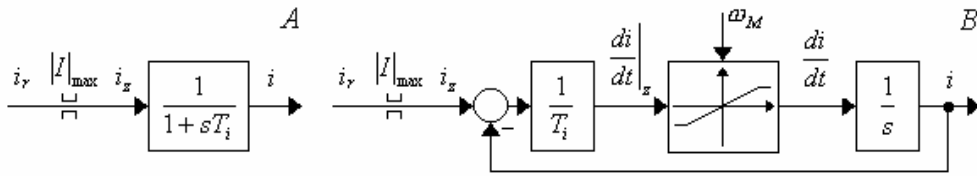
Fig. 3. *Current control loop: linear (A) and with consideration of velocity influence on limit of the current change rate (B).*

observer. On the base of these signals and velocity reference ω_z the state controller calculates the reference current i_z (torque m_z) according to the equation:

$$i_z = k_\omega \omega_z + k_i i - a k_\omega \omega_M - (1-a) k_\omega \omega_L - k_F m_F, \quad (1)$$

where a is the weight of the motor velocity feedback and $1-a$ is the weight of the load speed feedback. The coefficients k_ω, a, k_i and k_F are the parameters of the controller influencing the properties of the system. Their preliminary values are: k_ω=161 A·s/rad, a=0.47, k_i=40 and k_F=75 A/N·m.

According to above parameters the drive has high dynamics. Two-mass system, whose time constants depend on parameters J_M, J_L and C_F, generates torsional vibrations in transient state. Their natural frequency for given values of parameters equals to 136 Hz. In order to active damp the oscillation the high value of torque (current) change rate is necessary.

As a reference signal the linear course (ramp) of velocity from ω_{zo} to ω_{zo}+ 0.15 Ω_{max} during the time equal to 10 ms as well as velocity step equal to 0,04 Ω_{max} from ω_{zo} was used. The results are presented in p.u. values. The above given maximum values of the quantities are the bases for normalisation. For estimation of control quality the following index was introduced [5]:

$$I = \int_0^\infty |\varepsilon| dt \cdot \int_0^\infty \left|\frac{d\varepsilon}{dt}\right| dt \quad (1)$$

where $\varepsilon = \omega_z - \omega_L$ is the velocity error during dynamical state after change of the reference velocity ω_z.

3. CURRENT CONTROL LOOP MODEL

Instead of commonly used linear current control loop model (Fig. 3A) the another one was built (Fig 3B), in which the non-linear dependence of current derivative on velocity is considered with upper and lower limits according to formulas [4]:

$$\frac{di}{dt}\bigg|_{max} = \frac{2}{3} \frac{U_{max} - k\omega_M}{L_q}, \quad (2)$$

$$\frac{di}{dt}\bigg|_{min} = \frac{2}{3} \frac{-U_{max} - k\omega_M}{L_q} \quad (3)$$

where U_{max} is the DC voltage on the input of the VSI (output of the rectifier), k is the coefficient for calculation of the motor EMF (e), L_q is the q axis motor inductance and the 2/3 coefficient follows the transformation of the phase quantities to the d-q frame.

The equations (2) and (3) reflect the voltage equation of the real system. They are substitution for full circuit model of the motor with neglected resistance. According to them the value of the rate of current change is kept between two lines in the Fig. 4. For model from Fig. 3A the current as well as torque change rate can be infinite. It influences the dynamics of the drive. Realisation of non-linear part of the model from Fig. 3B is shown in Fig. 5.

4. INFLUENCE OF VELOCITY LEVEL ON DYNAMICS OF THE DRIVE

Figure 6 shows the chosen characteristics $I = f(\omega_{zo})$ of control quality given by index (1) versus initial velocity
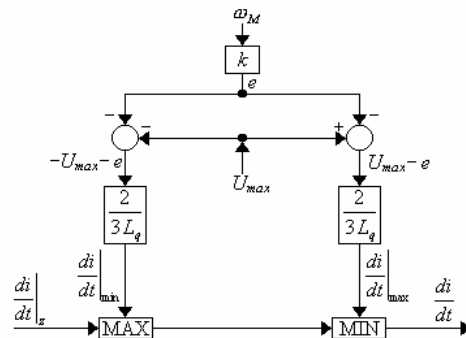

Fig. 5. *Realisation of the nonlinear part of the current control loop model using MIN and MAX blocks.*


Fig. 4. *Maximum and minimum current change rates versus velocity*
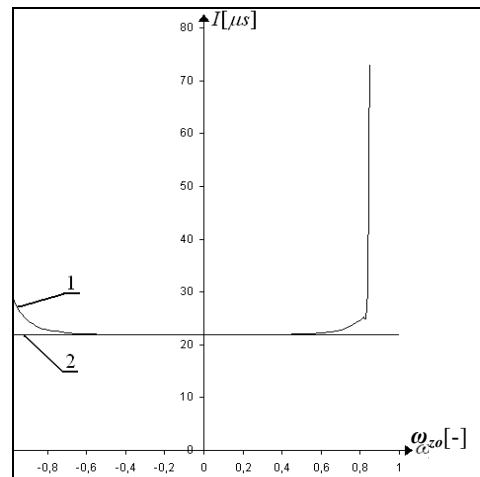
Fig. 6. *Quality index I versus initial velocity for ramp input: 1 – nonlinear model and 2 – linear model*

for both models of the current loop from Fig. 3 and for preliminary values of drive and controller parameters. Divergence of the characteristics begins at velocity equal to 0.5. The higher is the absolute value of the initial velocity the greater is divergence between characteristics for linear and nonlinear model. For opposite change of reference signal (ramp from ω_{zo} to $\omega_{zo} - 0.15\ \Omega_{max}$) the characteristics are the mirror reflections of the characteristics from Fig. 6 in a vertical axis.

Figure 7 shows the difference between courses of dynamical states for both models in the region of high velocity. Oscillograms present course of the following quantities of the system: flexibility torque m_F, the motor current i, the velocity of motor ω_M and load ω_L, the velocity error ε as well as the reference $(di/dt)_z$, maximum $(di/dt)_{max}$ and minimum $(di/dt)_{min}$ current change rate. In the Fig. 7 for the case of nonlinear model the demanded current derivative $(di/dt)_z$ during the long time exceeds its upper limit $(di/dt)_{max}$. Because of it setting time is here much longer and I greater than in the case of linear model.

5. TUNING THE CONTROLLER FOR WIDE RANGE OF VELOCITY

Demanding the very fast changes of the current by velocity controller is not profitable in the situation when their obtaining is not possible due to high velocity level. It can cause great values of the current control error and oscillation in the control loops (Fig.7). In order to avoid such situation the velocity controller should be tuned with consideration also of velocity ranges in those there are not possible the fast changes of the current (torque). It means robustness of the controller to velocity level.

In order to obtain it the procedure for tuning with consideration different conditions (different parameters and different forcing function) elaborated in [5] can be used. According to it for aggregation of results of separate tuning tests the following Robust oriented Aggregation of quality index is used

$$RA = \prod_{i=1}^{r}\prod_{k=1}^{u} Q_{ik} \qquad (4)$$
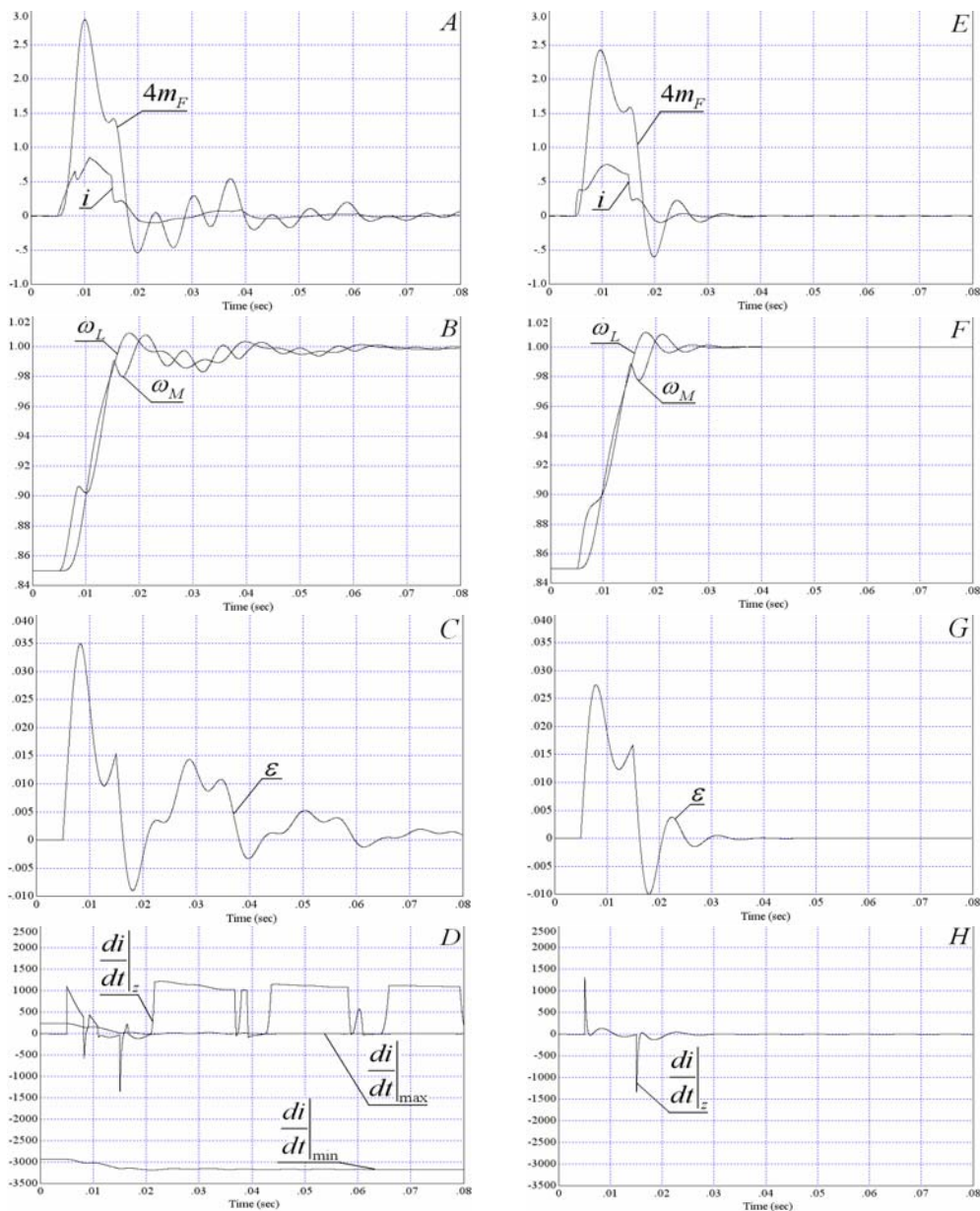
Fig. 7. *Dynamical state after the ramp input from 0.85 to 1 for preliminary parameters of the drive and controller: left – nonlinear model, I = 73.2 μs and right – linear model, I = 21.9 μs.*

where r is the number of type of forcing functions applied in the reference or/and disturbance path, u is the number of variable parameters of the system and Q_{ik} is the value of partial quality factor obtained for forcing function i and parameter k in the form

$$Q_{ik} = \frac{I_{ik}}{R_{ik}} \quad . \tag{5}$$

In formula (5) R_{ik} is the range of parameter k in which the system operates stable under forcing i and I_{ik} is the average value of quality index obtained in the range R_{ik}. In practice the average value can be calculated on the base of results of few tests uniformly distributed in the range. On the place of I_{ik} the quality index (1) is used.

Optimisation of the velocity controller according to (4) with $r=2$ (two forcing functions: ramp and step) and $u=1$ (level of the initial velocity) gave the controller with parameters: $k_\omega=131$ A·s/rad, $a=0,54$, $k_i=75$ and $k_F =121$

A/N·m, that is robust to type of forcing function and velocity level. Three values: –0.8, 0 and 0.8 of initial velocity ω_{zo} were taken into consideration for each input function during tuning the controller. New parameters of the controller give reduction ratio of index (4) equal to 43, in comparison with preliminary parameters. Figure 8 shows comparison of dynamical state course for controller with preliminary parameters (tuned for velocity equal to zero) and for controller tuned for wide range of velocity. The robust controller gives smaller value of the reference current derivative and more damped transient state than the preliminary tuned one. Although for ramp the kinetic error (Fig.8G) and quality index I are relatively great for robust controller, this controller gives better value of aggregated index (4), due to very suitable operation of the system at step reference signal.
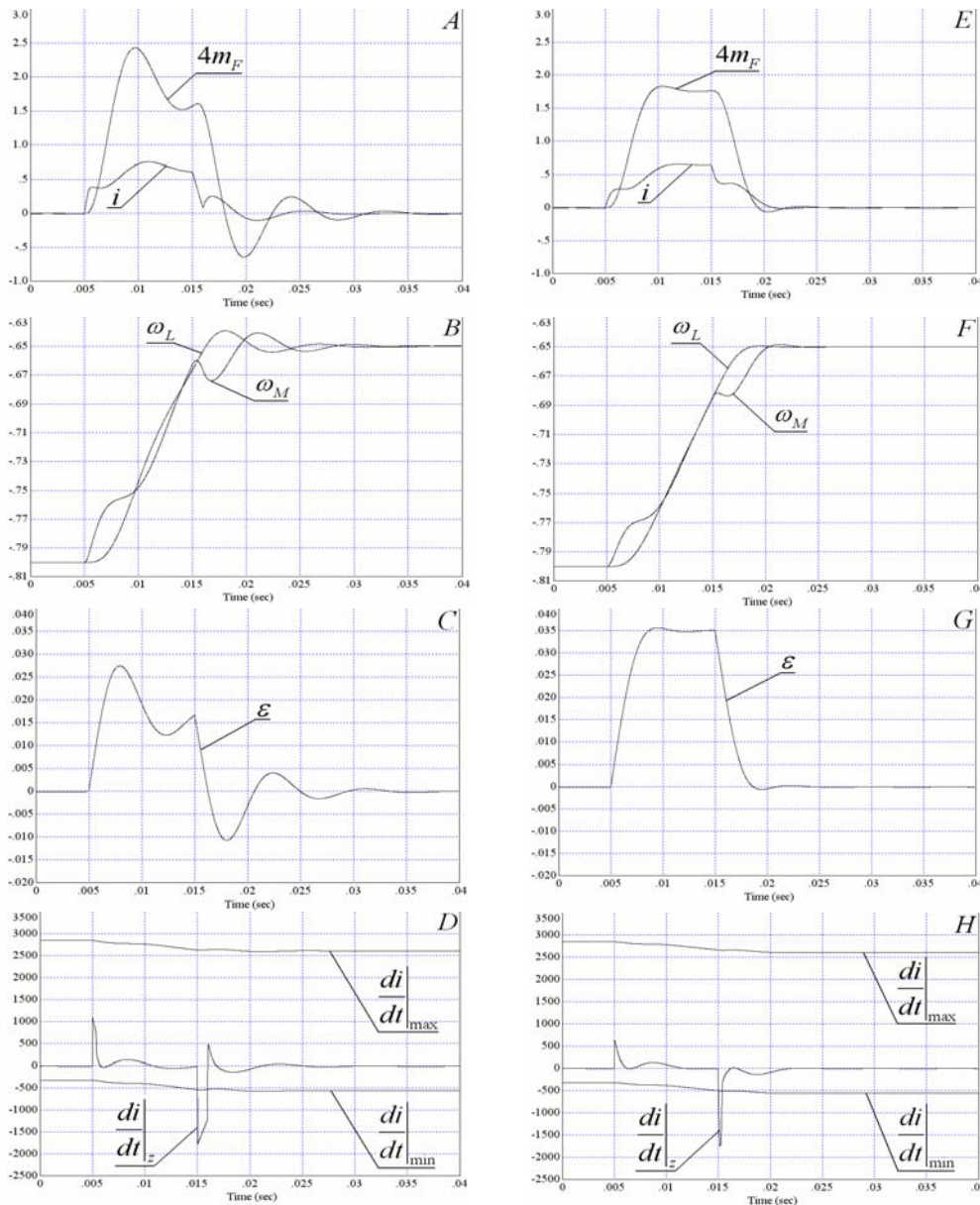

Fig. 8. *Dynamical state after the ramp input from –0.8 to –0.65 for nonlinear model and preliminary parameters of the drive: left pictures – controller preliminary tuned, I = 22.7 µs and right pictures – controller tuned for wide range of velocity, I = 26.1 µs.*
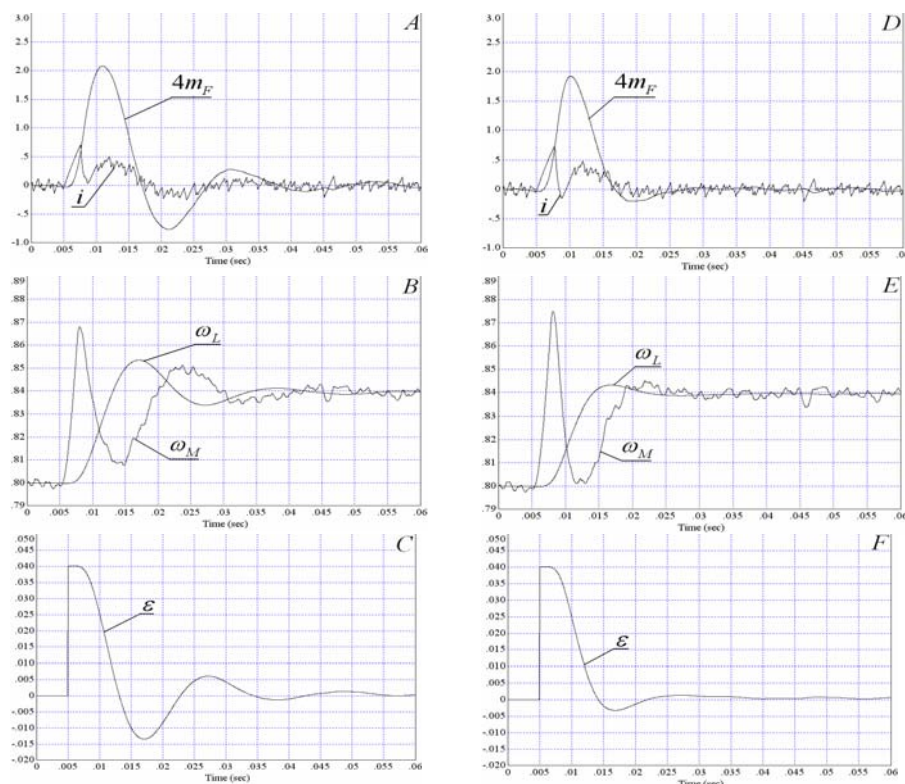
Fig. 9. *Dynamical state after the step input 0.8 to 0.84 for nonlinear model, J_L=31 kg·cm^2, C_F =150 (N m)/rad and noise σ=0.1: left – controller preliminary tuned, I =54 μs and right – controller tuned for robustness to many factors, I =35 μs.*

6. TUNING THE CONTROLLER FOR ROBUSTNESS TO MANY FACTORS

Optimisation described in section 5 was done for one set of mechanical parameters J_L=15 kg·cm^2 and C_F =350 (N·m)/rad and for the case without noise in the feedback path. Aggregated index (4) allows to consider many factors at the stage of controller tuning.

The robust controller was tuned considering the following four (u=4) variable parameters:

− initial velocity ω_{zo} – range −0.72 ÷0.85,
− load inertia J_L – range (5.8 ÷31) kg·cm^2,
− coupling stiffness C_F – range (60 ÷ 641) (N·m)/rad,
− standard deviation σ of stochastic noise of frequency 5 kHz [4] added to the current feedback signal i (Fig.2) – range 0 ÷ 0.8

together with two (r=2) input functions (ramp and step). The parameters of this controller are: k_ω=139 A·s/rad, a=0.35, k_i=36 and k_F =113 A/N·m. They give reduction ratio of index (4) equal to 77, in comparison with the case of preliminary parameters (section 2). Figure 9 shows comparison of quantities course for controller with preliminary parameters and for robust one. Robust controller suppresses well the torsional vibration and gives notable reduction of the quality index *I*.

7. CONCLUSIONS

The model of current control loop considering influence of velocity level has been elaborated.

The level of velocity can influence notable the dynamics of the high dynamics drives in the range of high velocity. Due to limited value of current change rate the oscillation can be excited in drive with flexibility of mechanical coupling.

Suitable tuning the velocity controller allows to decrease the unprofitable influence of velocity (and other factors) on dynamics of the drive. It consists in aggregating the results of the tests done for different values of velocity (and others factors) in one aggregated quality index, on the stage of controller optimisation.

8. REFERENCES

[1] Muszyński R., Kaczmarek T.: The elastic servo drive with state controller, *Archives of Electrical Engineering*, Vol. LII No 204-2/2003, Warsaw 2003, pp. 185 - 200.

[2] Beineke S., Wertz H.: Design of extended Kalman filters for high performance position control of electrical drives, the *IEEE/AMSE International Conference on Advanced Intelligent Mechatronics*, September, 1999, Atlanta, USA, pp. 209 – 214.

[3] Szabat K., Orlowska-Kowalska T.: Adaptive control of two-mass system using non-linear extended Kalman filter, IEEE Industrial Electronics, The *32nd Annual Conf. IECON*, Paris, November 2006, pp. 1539–1544.

[4] Babicz M.: Tuning and testing of the servo-drive controller with consideration of the influence of velocity on current change rate and dynamics of drive, *The MSc work* (consultant R. Muszyński), Poznań University of Technology, Institute of Control and Information Engineering, Poznań 2006 (in polish).

[5] Muszyński R., Tests and Criteria for Tuning and Evaluation of Servo-Drive Control System, *International Symposium on Industrial Electronics 2005*, June 2005, Dubrovnik, Croatia, on CD: Volume I "Control Systems and Applications", pp. 101-106.

[6] Deur J., Peric N.: Analysis of speed control system for electrical drives with elastic transmission. Proc. of the *IEEE Int. Symposium on Industrial Electronics* 1999 Bled, Slovenia, v. 2, pp. 624-630.

AUTOMATIC CONTROL SYSTEM OF A SYNCHRONOUS MOTOR EXCITATION

Alexandru Hedeş, Nicolae Muntean, Ion Boldea
Constantin Tudoran*, Ovidiu Muntean*, Radu Babău*, Sever Scridon*
"POLITEHNICA" University of Timişoara, Faculty of Electrical Engineering, Timişoara, Romania
*BEESPEED Automatizări, Timişoara, Romania

Abstract: *The paper presents an industrial equipment designed fo automatic supply control of the DC field circuit of a 5 MW, 10 kV synchronous motor, used in an irrigation pumping system. We introduce the general block diagram of the system, the method used for current detection, the general operation flowchart, the synchronization principle and finally, a brief description of the system implementation in an irrigation station.*

Key Words: *Excitation System/Synchronous Motor/Reactive Power Compensation.*

1. INTRODUCTION

One of the most important goals for many industrial systems represents the plant optimization of electric energy consumption. Electric energy savings are strongly related to the control of the plant power factor (PF). Many high power industrial applications require power drive systems implemented with synchronous motors. One major advantage of a synchronous motor over an induction motor is its ability to operate at a power factor (leading or lagging) that can be controlled by varying the DC field (excitation) current. Excitation systems are of prime importance for the proper operation of synchronous motors. For a synchronous motor operating at a constant terminal voltage and frequency, at a given output power, the dependence between the motor current and the excitation current is shapped as a "V" curve. It can be concluded that there is an optimum value of the excitation current where the correspondent motor current is minimum, at a given output power, e.g. the PF can be equal to 1, [1,2,3].

The DC field exciters of synchronous motors are basically of two types: with constant voltage, and with variable voltage. The variable voltage DC field exciters allow the control of the excitation curent either by means of reactive power (*VAR control*), or by means of power factor (*PF control*), [1, 2, 3, 4].

The basic requirements for power drives systems with synchronous motors are in reference to, [1,2,3,4]:
- the asycronous starting and forcing the motor to lock the stator and field poles into the synchronism;
- the maintain of the synchronous operation regardless the supply voltage and/or load variations;
- the control of the reactive power, or of the power factor in the motor circuit.

The power drive systems with synchronous motors for pumping stations are designed in order to satisfy also additional specific requirements, such as: the load torque particularities, proper operation of hydraulic valves, and automatic system control.

In the paper, a complex high power drive system, with a 5MW/10kV synchronous motor, for an irrigation pumping plant, is presented. There are pointed out the operational features related to the automatic control of the power drive system, based on the motor excitation control.

2. SYSTEM DESCRIPTION

The block diagram of the power drive system is presented in Fig. 1. The DC field of the synchronous motor MS is supplied by the DC generator GEC. The excitation of the DC generator is supplied by the thyristor controlled rectifier DCF. The DC contactor K is used to switch the starting resistor R over the excitation winding of the synchronous motor. The automatic system control is provided by a PLC, that is connected by a serial RS485 MODBUS communication with a centralized remote control unit (REMOTE CONTROL).

The control equipment acquires the proportional signals with both the motor voltage and current (U_l, I_l), provided by voltage and current transformers, and also the signal proportional with the motor excitation current (I_{eM}), provided by a Hall current transducer. The analog U_l, I_l signals are processed by analog signal converters and are converted into unified signals (4-20mA), compatible with the PLC analog inputs. The signal I_l is also applied to a current relay with hysterezis and adjustable levels. This signal is used to detect the decrease of the starting motor current under a set value (i.e. $1,2I_{IN}$), where I_{IN} is the rated motor current, in order to connect the DC field. The current signal level is also used in order to detect the exceeding of the set value.

The following orders are electrically given to the executive elements of the system:
- closing/opening the main circuit breaker in the medium voltage side of the motor;
- connect/disconnect the motor DC field supply;
- opening/closing the control valves.
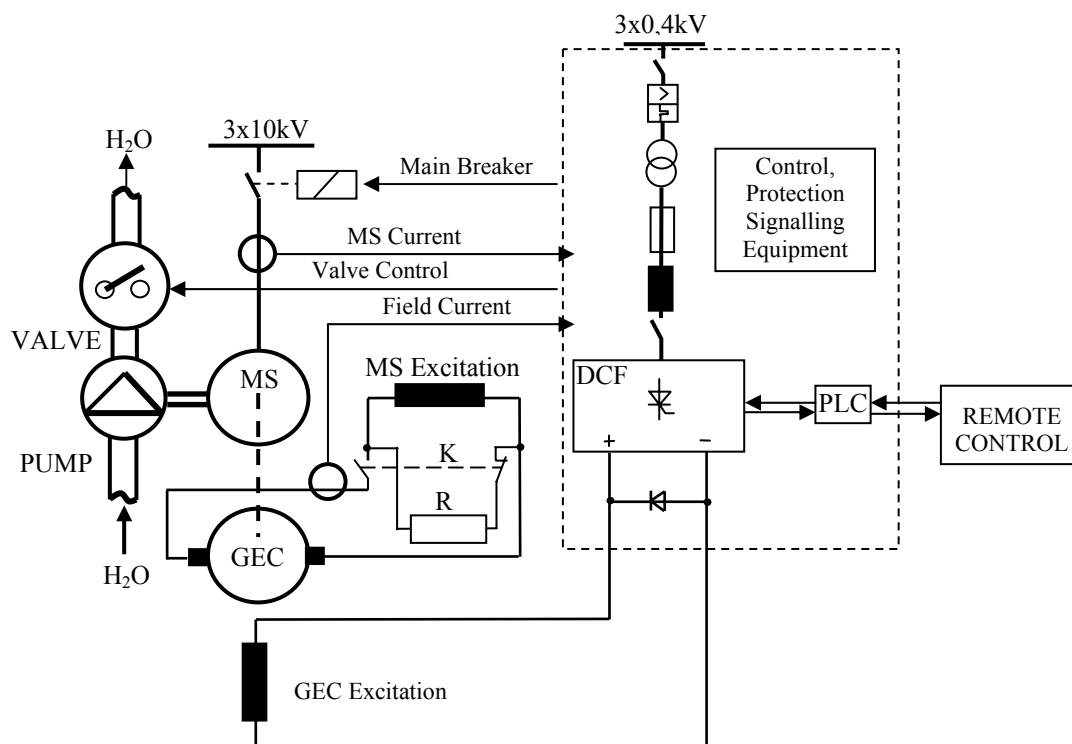
Fig. 1. *The block diagram of a pumping drive system with a synchronous motor.*

3. OPERATIONAL ABILITIES

The operational abilities of the system are as follows:
- the asynchronous starting of the motor MS;
- the synchronization of the motor, by switching out the resistor R of the field circuit and applying excitation to the field;
- the opening or closing of the control valve, with respect to the maintaining in synchronism of the motor at load variations;
- switching out of the motor, and of the GEC excitation, followed by the connection of the resistor R accross the field coil, and the closing of the control valve, in the case of a stop command or an asynchronous operation of the motor for a duration more than 10 sec.

The reference value for the GEC excitation current is given by the PLC.

- The automatic operation procedure of the system is graphically expressed in the logic flowchart of Fig. 2. The starting conditions are assumed as follows: the control valve in closed position, the motor disconnected of the mains, and the MS excitation connected accross the R resistor. In Fig. 2, the "Manual" control mode is denoted by the "Ma" letters, and the "Automat" control mode is denoted by letters "PLC".

The connection of the MS motor field to the DC power supply (GEC) in order to force the synchronism operation of the MS can be achieved in two ways, Fig. 3:

- in "Manual" operation mode, on the basis of input current discrimination I_l, provided by a current relay (Ki) and a time relay (Kt). If in the set starting time, the motor absorbed current decreases under the relay set current level (aprox. $1,2I_{IN}$), the slip between the field and stator decreases, and the motor tends to go into synchronism. If this condition is far to be realized, it means that the syncronism is

not to be achieved, and in consequence the motor must be stopped.

- in "Automat" operation mode, by detecting of two consecutive zero crossing of the motor excitation current I_{eM}, at a time interval of at least approx. 1,5 sec.; at the following zero crossing of the current, a synchronism order is given, with a simultaneously forced of excitation current. After the syncronism order is given, a valve opening command is given, in order to slightly loading the motor. In order to maintain the synchronous operation of the motor, two methods are used:

- in "Manual" operation mode, the main current I_l is the parameter kept under control;
- in "Automat" control mode, the power factor is the parameter under control.

The control parameter is the generator excitation current I_{eG}, provided by DCF; this current appropriately controls the motor excitation curent I_{eM}. Thus, the valve opening process is made with a continously monitoring of the motor main current I_l, and of the motor power factor respectively.

4. SYSTEM IMPLEMENTATION

Two prototypes of such a synchronous motor excitation system were built and industrially implemented. The main data of the system are given in the table 1. The system control equipment was mounted in an electric enclosure, presented in Fig. 4, where can be observed the starting resistor R, mounted on the cabinet roof, the controlled rectifier DCF, the DC contactor K, and the other electrical apparata.

The thermal management of the electric enclosure is achieved by means of a ventilation system.
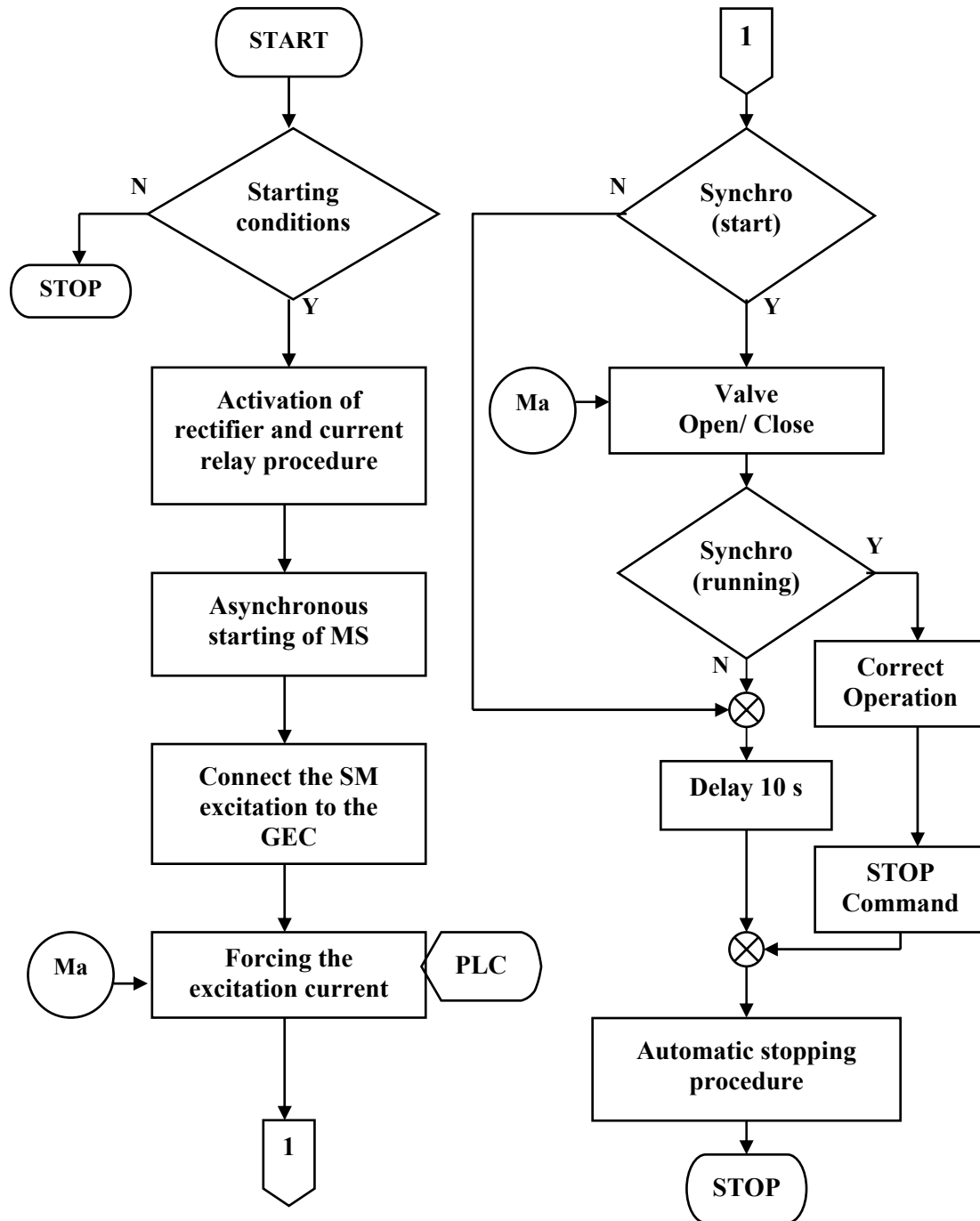
Fig. 2. *The flowchart of system operation.*

Table 1. *The main data of the system.*

| Synchronous motor MS	DC Field Generator GEC
- Rated power, P_o= 5 MW - Synchronous speed, n_s =333 rpm - Rated voltage, U_{IN} =10 kV - Rated current, I_{IN}= 340 A - DC field voltage, U_{eM}=122 VDC - DC field current, I_{eM}=325 A	- Power, P_G= 76/5 kW - Armature voltage, U_G =185/ 40 V - Armature current, I_G =410/ 125 A - DC field current, I_{eG} =8,1 A
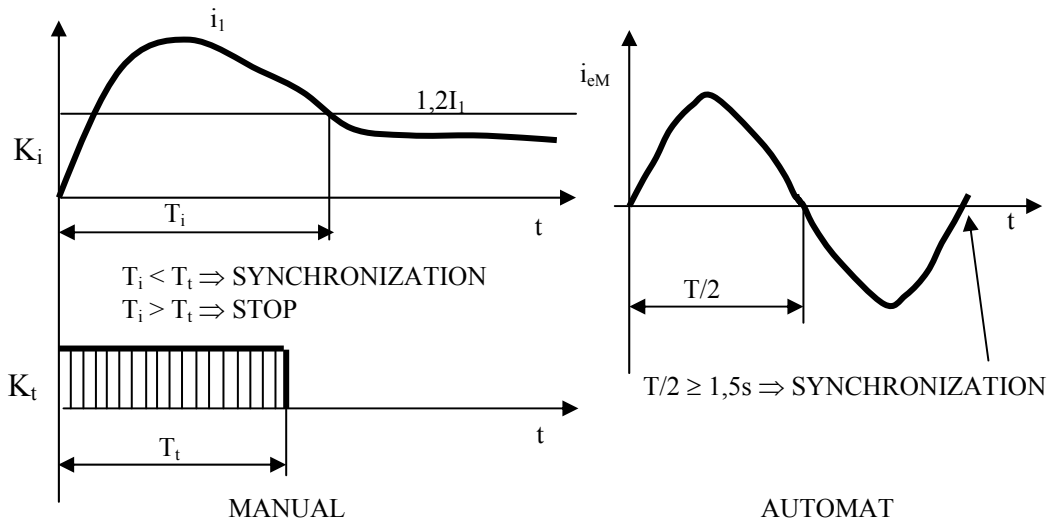
Fig. 3. *The synchronization principle based on current detection.*
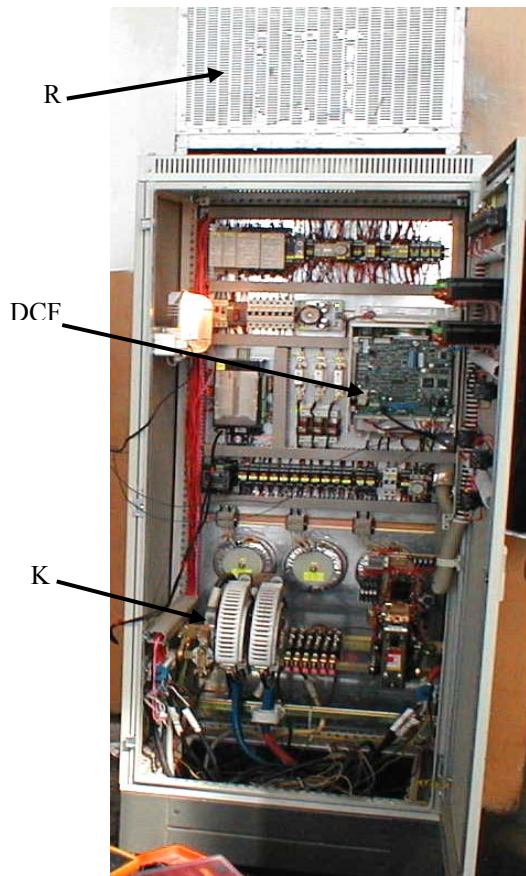
Fig. 4. *Inner view of the control system cabinet.*

Fig. 5. *System implementation in an irrigation pumping station.*

Table 2. *Results before implementation (summer 2000).*

No.	Month	Energy consumption		Pumped volume x10³ m³
		Active MWh	Reactive MVArh	
1	May	1123,2	235,6	4156,3
2	June	2767,8	784,2	9849,6
3	July	4325,7	1150,6	15082,2
4	August	3575,3	948,6	12496,7
5	September	541,7	95,4	1949
TOTAL		**12.333,7**	**3214,4**	**43953,4**

In Fig. 5 is presented a picture of the two systems implementation in an large irrigation pumping station. In the picture, can also be observed a DC generator for DC field of a synchronous motor.

The measurement results for two system implementation are comparatively presented in the table 2, and table 3. The data are refered to the summer of the 2000 year, and of the 2003 year, before and after the implementation of the systems respectively, [5].

From the table 2, it can be observed that the average specific energy consumption is 283,31 kWh/1000m³ pumped water, and 67,49 kVArh/1000m³ pumped water respectively, before the implementation of the system.

Table 3. *Results after implementation (summer 2003).*

No.	Month	Energy consumption		Pumped volume $\times 10^3$ m^3
		Active MWh	Reactive MVArh	
1	May	581,9	39,6	2327,5
2	June	1575,5	106,9	6106,8
3	July	2657,6	185,9	10105,1
4	August	2381	166	9122,6
5	September	243,2	17,3	1013,5
	TOTAL	**7439,3**	**515,7**	**28675,4**

From the table 3, it can be observe that the average specific energy consumptions are reduced, i.e., the active energy is 254,4 kWh/1000m^3 pumped water, and 17,64 kVArh/1000m^3 pumped water respectively. These energy savings are due to the reduction of the reactive power, on the one hand, and to the reduction of the active power losses both in the line conductors and in the motor, on the other hand. It also must be pointed out the decrease of the total motor starting time of approximatively 10 times, including the required loading time of the motor.

5. CONCLUSION

A complex and modern DC field exciter for a high power MV synchronous motor is presented. The motor is integrated into a large power drive for an irrigation pumping station. The automatic control system performs all the process requirements, including the starting and the syncronization procedures, as well as the maintaining of the synchronous operation regardless the line voltage or load variations. The use of control system provides some important improved operational features related to optimum operational conditions for the synchronous motor, and process control. Based on "in situ" measurements, important energy savings can be reported, especially those regarding to the reactive energy. This is the result of a controlled operation of the synchronous motor at a unity power factor.

6. REFERENCES

[1] I. Boldea, *"Transformers and electric machines"*, Editura Didactică și Pedagogică, București, 1994. (in romanian)

[2] L.B.Farr, "*Synchronous Motor Field Controllers and Their Application*", IEEE Trans. on Industry Applications, Vol.30, No.1, Jan/Feb.1994, pp.201-204.

[3] Digital Excitation Applications Task Force of the Excitation Systems Subcommittee, "*Digital Excitation Technology – A Review of Features, Functions, and Benefits*", IEEE Trans. on Energy Conversion, Vol.12, No.3, Sept.1997, pp.255-258.

[4] R.C.Schaefer, "*Excitation Control of the Synchronous Motor*", IEEE Trans. on Industry Applications, Vol.35, No.3, May/June1999, pp.694-702.

[5] A,Hedeș, N.Muntean, I.Boldea, C.Tudoran, O.Muntean, R.Babău, "*Sistem automat de control al excitației motoarelor sincrone*", The VIII-th edition of Timisiensis Academic Days – 2003, Timișoara (RO), May2003, pp.21-31. (in romanian).

INTERCELL TRANSFORMERS AND POWER INTEGRATION

Éric Labouré[(1)], François Forest[(2)], Thierry Meynard[(3)]

[(1)]SATIE, ENS cachan, IUFM Univ Paris XII CNRS, UniverSud, 61 av du President Wilson, F-94230 Cachan, France
[(2)]IES, CNRS UMR 5214, place E. Bataillon, 34095 Montpellier Cedex 5, France
[(3)]LAPLACE, CNRS UMR 5828, 2 rue Camichel 31071, Toulouse Cedex, France

Abstract: *The theoretical advantage of InterCell Transformers over separate inductors is demonstrated in an interleaved power converter in term of power density. The comparison is realized using a geometric optimization of the shape of the magnetic devices. Different practical ways to build InterCell Transformers are also described and discussed.*

Keywords: *InterCell Transformers, interleaved converters, coupled inductors, interphase transformers, design, optimization*

1. INTRODUCTION

It is now well known that interleaved converters can significantly reduce filtering and decoupling by offering apparent frequency increase and current ripple cancellation to the output capacitors. This technique can also improve the transient response and the power density [1], [2]. Today's 12 V input VRM (Voltage Regulator Module) widely used in industry are based on multiphase buck converters with interleaving technique. However, multiphase interleaved buck converters only produces current ripple cancellation effect to the input and the output of the converter. In this structure, the inductor current ripple in each channel is still large and the inductor current ripple frequency is unchanged. Thus, multiphase buck converters with interleaving technique have technical conflicts that can be, for one of them, formulated as follows. When the inductor current slew rate is increased with smaller inductance value to improve the transient response, then the inductor current ripple also increased. Hence, losses increase in silicon due to larger turn-off and turn-on-losses and it also increases the inductor winding losses. This conflict limits the average inductor current in each channel of the multiphase converters. Hence, there is a trade-off between efficiency and transient response [3], [4].

This main drawback can be overcome by using coupled inductors that can be seen for some particular core shape as interphase transformers. Recent studies [5], [6], [7], [8] and [9] show that the current ripple cancellation in a multi-phase buck converter can be extended to the inductors and the switches by multi-phase inductor coupling. In comparison to the uncoupled multi-phase buck, with magnetic coupling, smaller inductors can be used at the same switching frequency without inducing more ripple current. Thus, faster transient response can be achieved without sacrificing converter efficiency. For high number of cells, transformers using the leakage inductance as filtering inductor can replace the inductors.

Hence, these magnetic devices named in this paper InterCell Transformers seem to be a more efficient way to insure current filtering at the output of a power converter.

In this paper, the gain in term of compactness will be evaluated using a design procedure dedicated to these particular devices. Design specifications used as references came from a VRM designed to supply new generation of microprocessor.

2. INTERCELL TRANSFORMERS

2.1. Presentation

The main idea leading to coupled inductors comes from the following analysis:

- An inductor is designed to reduce the high frequency current ripple generated by switching in power converters. Hence, filtering is all the more efficient than inductor has a high inductance value.
- A DC or AC low frequency current also flows through inductors. These components bring the converter power as for example the DC current component at the input or output of a DC-DC converter or the fundamental component in a DC-AC or AC-DC power converter. Note that there is generally no functional need of inductors for these particular current components. Nevertheless, these low frequency current components greatly influence the energy stored by the inductor ($Wem = 1/2Li^2$) as the low frequency current represents a large amount of the total current. However, the inductor sizing directly depends on the maximum amount of stored energy. Hence low volume inductors can be addressed for high current level by reducing the inductance value.

These two items lead to an opposite conclusion. The first one involves using a high permeability materialwhereas the second involves a low permeability material that gives a smaller inductance providing a size reduction but also a worse filtering efficiency. We can notice that a classical inductance is a technological trade-off between these two limits.

Hence, the main idea is to design a magnetic device that offers two possible magnetic paths, one with a low permeability for the low-frequency DC or AC components and the other with a high permeability for the switching harmonics. This can be achieved by coupling or in other words, by merging together the cores of interleaved converter separate inductors. Fig. 1 shows a possible implementation for such device. In this example, the multi-phase coupled inductor is built on a ladder core structure [10]. The low permeability path can be either the different air paths, either one extra gapped leg or a leg realized in a low permeability material.
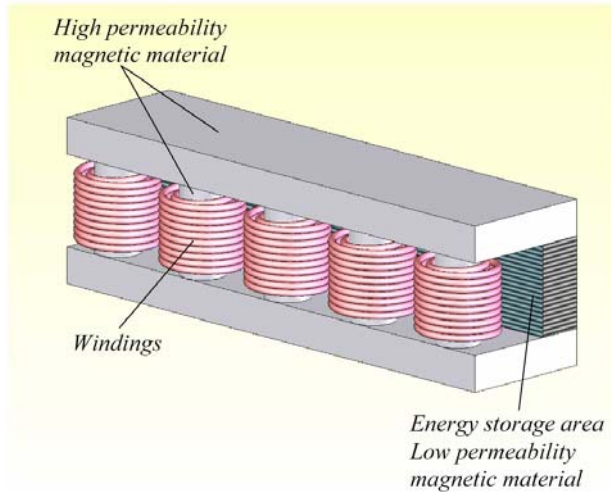
Fig. 1. *Implementation of a coplanar multi-phase coupled inductor.*

If balanced fluxes are desired, a symmetrical structure must be implemented in order to provide balanced reluctance of all magnetic paths (Fig. 2).
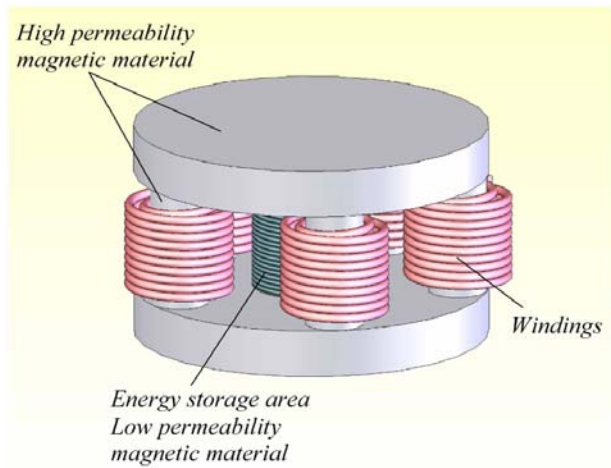

Fig. 2. *Implementation of a balanced multi-phase coupled inductor.*

Such a device can replace the *q* inductors of an interleaved converter (Fig. 3). In this structure, the windings are driven by *q* phase shifted asymmetrical square voltages (Fig. 5).

Components of these *q* voltages have the following properties: DC components are the same and ripple components are phase shifted. Hence harmonic components of the voltages can be split in two families:

- DC components and harmonics at $k \times q \times f$, with k an integer, lead to in-phase fluxes in all the vertical rods of the device and will add up in the common return branch (i.e. the high reluctance area) as depicted in the magnetic circuit model of the coplanar multi-phase coupled inductor of Fig. 1 (see Fig. 4).

- Other harmonics components behave as a balanced voltage network. The sum of vertical rods fluxes is hence null.

2.2. Other examples of implementation

Other geometries give the same effect. For instance,
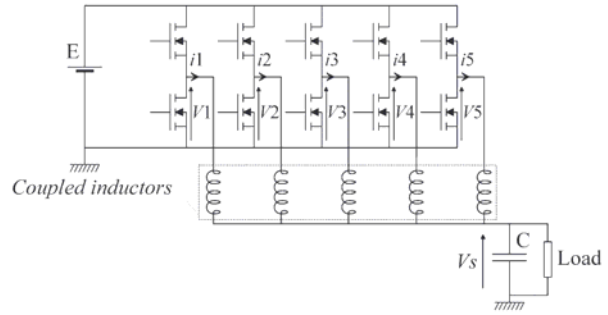
Fig. 3. *Interleaved Buck converter connected to a multi-phase coupled inductor.*
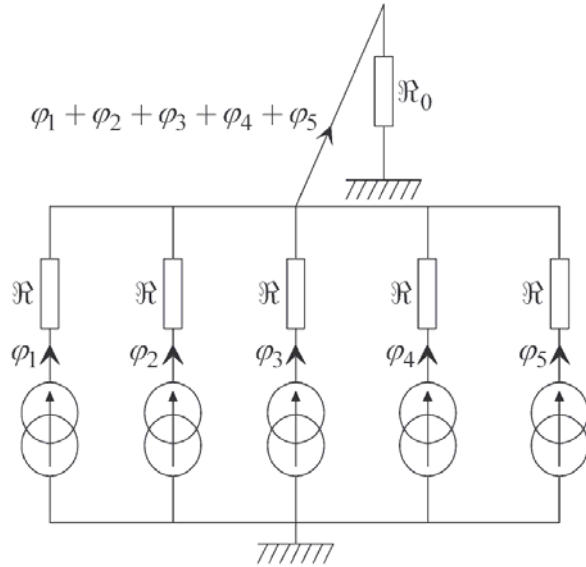
Fig. 4. *Magnetic circuit model for five-phase coupled inductor. R_0 is the reluctance of the energy storage area and R is the reluctance of each vertical rods. In this model, transversal reluctances are neglected.*
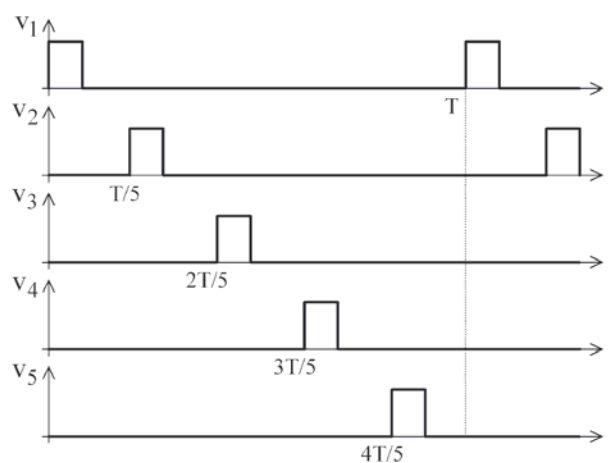

Fig. 5. *Interleaved converter voltagewaveforms.*

These properties meet our requirement as we obtain a low inductance value for the DC component and a large inductance value for almost all alternating components except for harmonics at $k \times q \times f$.

the common return branch can be distributed (Fig. 6).

Another solution consists in doubling the core and the windings, and then the windings can be wound around the

horizontal axis. Hence, each window comprises two groups of conductors with a compensation of the amp-turns, thus improving the flux distribution in the window and reducing the AC resistance (Fig. 7).
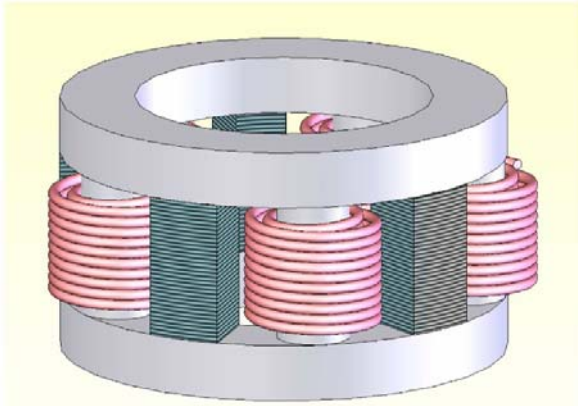

Fig. 6. *Multi-phase coupled inductor with distributed energy storade area.*
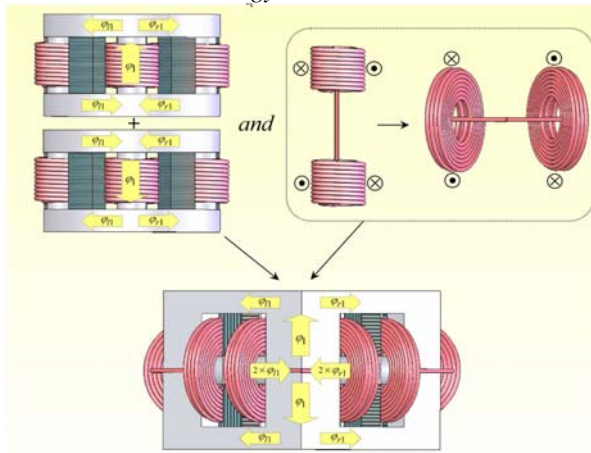
Fig. 7. *Multi-phase coupled inductor using disk coil winding.*

As explained in [11], the last device described above can be split in q cells (Fig. 8) leading to a simpler implementation as standards cores can be used. The devices arranged in circle in Fig. 8 are not magnetically coupled and can be rearranged freely, which makes this configuration applicable.
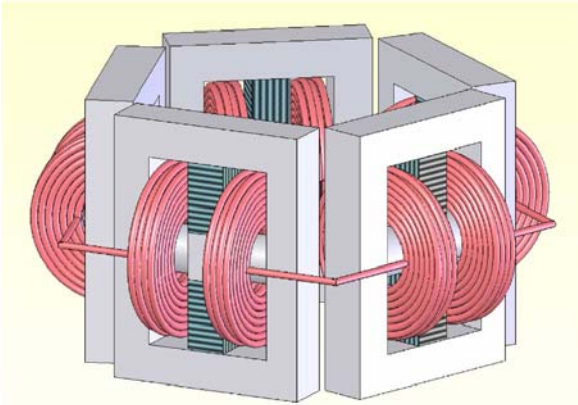

Fig. 8. *Multi-phase coupled inductor using standards cores.*

In all the interphase coupled inductors, the return branches can be removed and replaced by the leakage window path. In this configuration the interphase coupled inductor should be considered as an interphase transformer rather than a set of coupled inductors. There are many possible implementations for multi-phase coupled inductors or interphase transformers and the few examples given here are only some interesting possibilities. Note that, in the next sections, the term of **InterCell Transformer** will be used rather than coupled inductor or interphase transformer as this device clearly provides these two functions.

3. EXPERIMENTAL RESULTS

The electrical scheme of a test bench (Fig. 9) is shown in Fig. 10. It is a five-phase interleaved Buck converter supplied with a 12V DC voltage. The switching frequency is 500 kHz. This interleaved converter is connected to an InterCell Transformer constituted by 5 standard planar E cores (Ferroxcube El4/3.5/5 made of 3F4 magnetic material).
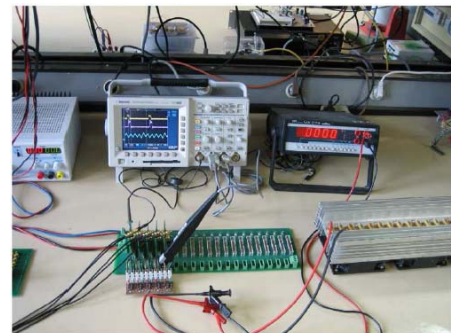

Fig. 9. *Prototype of InterCell Transformer (b) connected to a 5-cell buck converter (a).*
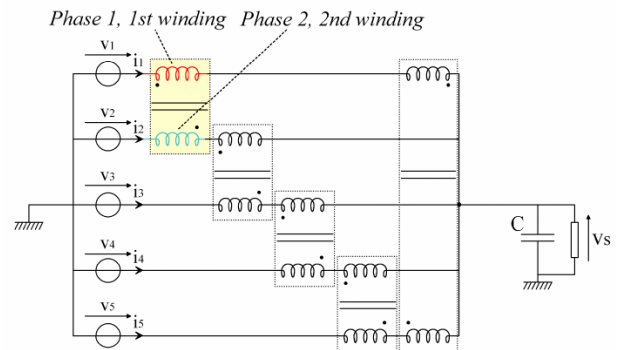
Fig. 10. *Electrical scheme of the test bench.*

Experimental waveforms are shown in Fig. 11 with a duty cycle of 10% like in a VRM that delivers a 1.1V DC output voltage. In Fig. 11 the flux waveform is obtain by numeric integration of the voltage in a 1 turn conductor

wounded around the central leg of the core. Hence, the DC component of the flux is not measured.
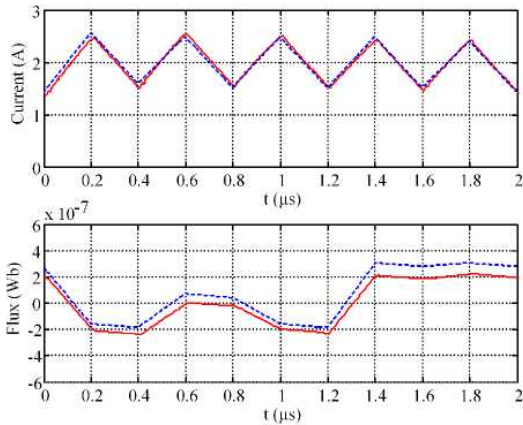

ig. 11: one cell current and flux (solid line: experimental waveform; dotted line: calculated waveform)

Note that a low current ripple is observed whereas the output current of the voltage regulator is only filtered by the leakage inductance of the InterCell Transformers and the apparent frequency of this current is 5 time the switching frequency. Note that for flux waveforms of Fig. 11, phase shifts of the interleaved Buck converter have been modified to reduce maximum flux density that influences core sizing and core losses [11][12].

4. DESIGN AND OPTIMIZATION OF AN INTERCELL TRANSFORMER

In this section, we discuss the design procedure of an InterCell Transformer using standard cores, like in Fig. 8 and in the prototype. This design is realized by looking for the optimal cell shape or cell size obtained for a given power at the output and a given temperature rise. The optimization is carried out starting from a generic shape of the magnetic component. An example of core shape is given in Fig. 12.
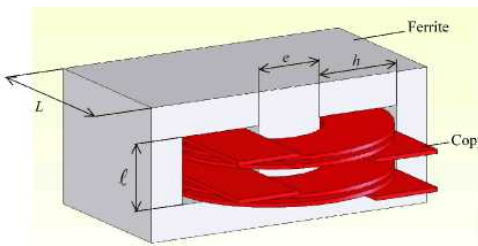

Fig. 12: Example of the generic shape of an InterCell Transformer

As shown in this figure, the generic shapes have four characteristic dimensions called L, l, e and h.

In the design, the current ripple and the cooling strategy must also be defined, this mean for the last point to define if forced-air or free-air cooling with or without heat sink is used and the position of the heat sink. Other information must be input such as material specification giving specific power loss (function of frequency and amplitude of AC-induction in the core) and maximum induction before saturation.

The optimization criterion is the magnetic component volume given by Eq. 1.

$$V_{total} = V_{core} + V_{copper}$$
$$V_{total} = 2 \cdot L \cdot e \cdot (\ell + h + 2 \cdot e) + 2 \cdot \ell \cdot h \cdot (L + 2 \cdot h + e) \quad (1)$$

Electric and magnetic equations are expressed according to the electric scheme and the dimensions of each magnetic device leading to the following area product expression in case of a modified phase-shift [13]:

$$A_p = A_c A_w$$
$$= \frac{P_{tot}}{4 D q K_i (1 - K_v) K_w J B_{max} f} \frac{1 + q^2 K_{\Delta I} 2D(1-D)}{q^2 K_{\Delta I}} \quad (2)$$

With:

- A_c : core section
- A_w : winding area
- P_{tot} : converter output power
- q : number of cells
- D : nominal duty cycle
- J : windings current density
- B_{max} : maximum flux density in the core
- f : switching frequency
- $K_{\Delta I}$: relative current ripple at the output of the converter
- K_i : current factor defined as the ratio of the mean current to the RMS current in the windings
- K_v and K_w are winding factors defined in Fig. 13. The definition of these factors depends on the way the two windings are wounded on the core (see (a) or (b))

In the design, we define 3 geometrical factors depending on the core shape and define as:

$$K_{Fc} = \frac{L}{e}; K_{Fw} = \frac{\ell}{h}; K_F = \sqrt{A_c / A_w} = \sqrt{(L e)/(\ell h)} \quad (3)$$

For homotnetic shape [13], these geometric factors remains constant and all geometric characteristics of the magnetic device can be expressed as a function of the area product and some of these 3 factors. For instance:

$$L = A_p^{\frac{1}{4}} \sqrt{K_F K_{Fc}} \; ; \; e = A_p^{\frac{1}{4}} \sqrt{K_F / K_{Fc}}$$
$$\ell = A_p^{\frac{1}{4}} \sqrt{K_{Fw} / K_F} \; ; \; h = A_p^{\frac{1}{4}} \sqrt{1/(K_F K_{Fw})} \quad (4)$$

Note in Eq. 2 that the leakage window path appears clearly in the design of an InterCell Transformer through the factor K_v but this factor remains unknown and must be defined. In fact, the leakage inductance must be sufficient to guaranty that the maximum current ripple remain lower than an imposed value:

$$K_{\Delta I} = \frac{\Delta i}{\langle i \rangle} = \frac{E}{4 q^2 L_{leakage} f \langle i \rangle} \quad (5)$$
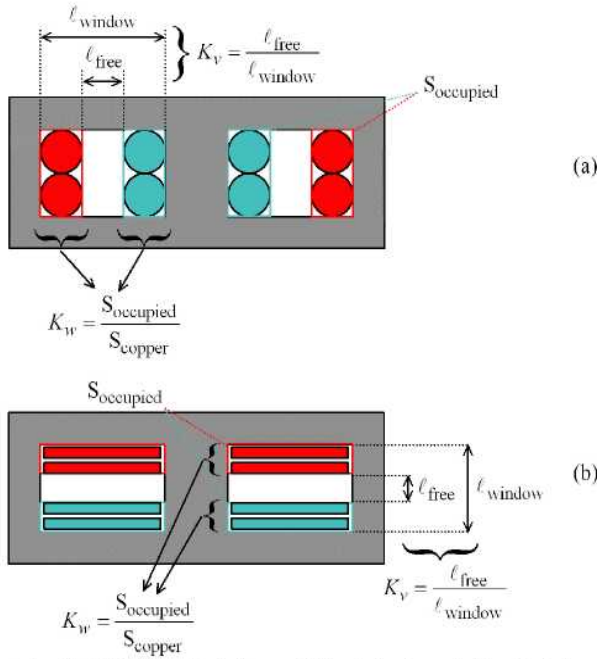
Fig. 13: Definition of winding coefficients for two winding strategies

The core shape, the core size and the thickness of the copper free area also define the leakage inductance:

$$L_{leakage} = n^2 \mu_0 K_v K_{FL} A_p^{\frac{5}{4}} \quad (6)$$

Where:

- n : winding number of turns
- K_{FL} : leakage inductance factor depending on the core shape

From Eq. 2, 5 and 6, an expression giving K_v can be derived:

$$K_v (1 - K_v)^{\frac{3}{4}} =$$

$$\frac{2^{\frac{5}{2}} D^{\frac{1}{4}} B_{max}^{\frac{5}{4}} K_F^2 f^{\frac{1}{4}}}{\mu_0 q^{\frac{7}{4}} P_{tot}^{\frac{1}{4}} \left(\frac{1 + q^2 K_{\Delta I} 2D(1-D)}{q^2 K_{\Delta I}} \right)^{\frac{5}{4}} (K_i K_w J)^{\frac{3}{4}} K_{\Delta I} K_{FL}} \quad (7)$$

If the right part of the previous equality remains lower than 0.3027 there is two solutions for K_v otherwise there is no solution. In the design, we arbitrary choose the lower value of K_v because this value corresponds to the lower value of the area product (Eq. 2) and therefore to the higher power density.

Thermal constraint must also be verified during the optimisation process. The temperature rise must be lower than the required maximum temperature. Eq. 8 gives the expression of this thermal constraint.

$$\sum \left(P_{copper\,loss} + P_{core\,loss} \right) \le H_{th} A_{th} \Delta T$$

giving   (8)

$$\rho J^2 K_w F_1(f, \text{current shape}) V_{copper} + F_2(\Delta B, f) V_{core}$$
$$\le H_{th} A_{th} \Delta T$$

With:

- H_{th} : thermal exchange factor (radiation, convection)
- A_{th} : total exchange surface
- ρ : copper electrical resistivity
- F_1 : corrective function which take into account the increase of the copper losses with frequency
- F_2 : specific power loss function of frequency and amplitude of AC-induction [16]

In Eq. 8, the temperature over the total exchange surface is supposed to be uniform and entirely defined by the thermal exchange factor **[13][14][15].** This simplifying assumption is necessary to take into account the thermal equations in the geometrical optimization of the device. In such a model, a heatsink is taken into account by multiplying the concerned heat-transferring surfaces by a constant coefficient depending only on the shape of the heatsink. In Eq. 8, A_{th} is entirely defined by the device geometry and therefore by the value of the area product and the 3 previously defined geometrical factors.

The global geometric optimisation procedure is described in the graph of Fig. 14. This optimization can be carried out using either a free geometric mode or a homothetic shape strategy [13]. In the first mode the 3 geometrical factors K_{Fc}, K_{Fw}, K_F remains free and are part of the optimization parameters whereas they are constant in the second mode. In other words in the first mode, the optimization procedure calculates the 3 geometrical factors, the switching frequency, the winding current density and the maximum induction that give a minimal volume of the device while the temperature rise over the exchange surface remains lower than the imposed value.

5. EXAMPLE OF DESIGN

An example of design specifications is given in Table 1. These specifications correspond to a Voltage Regulator Module designed to deliver 0.8375 to 1.600 V and 85A. For comparison, we use a commercial VRM module designed with the same specifications. This VRM is an ARTESYN 4-channel interleaved synchronous buck converter (Fig. 15). In this converter, the volume of the four inductors is equal to 1.42 cm³.

TABLE 1
DESIGN SPECIFICATIONS

Parameter	Design value	Commercial VRM
Switching frequency: f_{max}	550 kHz	550 kHz
Maximum output power for a duty cycle of 0.1: P_{tot}	100 W	100 W
Phase current ripple: $K_{\Delta I}$	30 %	40 %
Maximum temperature rise: ΔT	40 °C	40 °C
Inductance:	Unknown before design	176 nH

TABLE 2
DESIGN RESULTS

| Parameter	Design value
Area product:	2.8 mm^4
K_F	1.16
K_{Fc}	0.63
K_{Fw}	9.81
Windings current density: J	19.2 A/mm^2
Maximum flux density in the core: B_{max}	300 mT
Volume of the 10 InterCell transformers:	0.334 cm^3
Total losses in the 10 transformers:	0.79 W
Transformer leakage inductance:	21.8 nH

Fig. 14: Geometric optimization flowchart
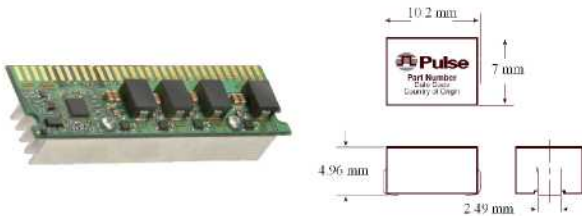
Fig. 15: VRM 10-85-12-u ARTESYN and inductor dimensions

The geometric optimization is carried out in a free geometric mode. For a 10-channel Buck converter (q=10) we obtain the results of Table 2.

The volume occupied by the 10 InterCell transformers is almost 4 times smaller than that of the four inductors. The corresponding InterCell transformer geometry is described in Fig. 16.


Fig. 16: InterCell transformer geometry

6. OUTPUT-FILTER CAPACITANCE

One of the most important issues of the VRM power-stage design is the selection of the output LC-filter parameters. Generally, for VRMs this selection is based not on the output-voltage ripple specification, but on the trade-off between the specified VRM efficiency and transient response.

To keep VRM output voltage Vo within regulation range ΔVo during a load transient of magnitude ΔIo_{max}, the minimum required output-filter capacitance is [3]:

$$C_{min} = \frac{1}{2} \frac{\Delta Io_{max}^2}{\Delta Vo} \left(\frac{Lo}{Vo} - \frac{1}{dIo/dt} \right) \quad (9)$$

With:

dIo/dt : load current slew rate

Lo : output equivalent inductance equal to L_f/q for a q-channel buck converter using uncoupled inductors (L_f) and $L_{leakage}/q$ for InterCell transformers.

From eq. 9, we can notice that, for the same design specifications, a reduction of C_{min} by almost 20 can be reached as $Lo = 44 nH$ in the commercial VRM and $Lo = 2.2 nH$ for the proposed VRM structure.

7. CONCLUSION

The theoretical advantage of InterCell Transformers over separate inductors has been demonstrated.

Different practical ways to build InterCell Transformers have been described. One of them consists in using classical transformers linking each phase to its neighbours.

InterCell Transformer has been realized by using 5 planar "E" cores and experimental results with a 5-channel buck converter are presented.

A design method leading to define the optimum geometry of InterCell transformers is proposed. An example based on a VRM specification shows that InterCell transformer leads to reduce significantly the total volume of the magnetic devices. Moreover, the design shows that an important reduction of the equivalent output inductance can be obtained by employing InterCell transformers. Consequently, the VRM control bandwidth can be increased and the desired transient response can be achieved with a smaller output-filter capacitance than in a classical interleaved structure. This means that it is possible for a VRM structure to remove the OSCON bulk electrolytic capacitors thus leading to a much higher power density compatible with power integration.

8. REFERENCES

[1] X. Zhou, P. Xu, and F. C. Lee, "A high power density, high frequency and fast transient voltage regulator module with a novel current sensing and current sharing technique," in *Proc. IEEE APEC Conf.,* 1999, pp. 289-294.

[2] O. Garcia, P. Zumel, A de Castro, J. A. Cobos, and J. Uceda, "An Automotive 16 phases DC-DC Converter", in *Proc. IEEE PESC Conf.,* 2004, pp 350-355.

[3] Y. Panov and M. M. Jovanovic, "Design consideration for 12-V/1.5-V, 50-A voltage regulator modules," *IEEE Trans. Power Electron.,* pp. 776-783, Nov. 2001.

[4] M. Xu, J. Zhou, K. Yao, F. C. Lee, "Small Signal modeling of a High Bandwidth Voltage Regulator Using Coupling Inductors", *IEEE Trans. Power Electron. ,* vol. 22, no. 2, pp 399-406, March 2007.

[5] P-L. Wong, P. Xu, B. Yang, and F. C. Lee, "Performance Improvements of Interleaving VRMs with Coupling Inductors," *IEEE Trans, on Power Electron.,* pp. 499-507, July 2001.

[6] J. Li, C. R. Sullivan, A. Schultz, "Coupled inductor design optimization for fast-response low-voltage DC-DC converters", in *Proc. IEEE APEC Conf. ,* 2002, pp. 817-823 vol.2.

[7] A. M. Schultz and C. R. Sullivan, "Voltage converter with coupled inductive windings, and associated methods", 2002, *U.S. Patent number 6,362,986,* Volterra Semiconductor Corp.

[8] P. Zumel, O. Garcia, J. A. Cobos, and J. Uceda, "Magnetic Integration for Interleaved Converters", in *Proc. IEEE APEC Conf.,* 2003, pp. 1143-1149.

[9] J. Czogalla, J. Li, C. R. Sullivan, "Automotive Application of Multi-Phase Coupled Inductor DC-DC Converter", in *Proc. IEEE IAS Conf.,* 2003, pp 1524-1529.

[10] J. Li, A. Stratakos, A. Schultz, C. R. Sullivan, "Using Coupled Inductors to Enhance Transient Performance of Multi-Phase Buck Converters" in *Proc. IEEE APEC Conf.,* 2004, pp 1289-1293.

[11] T. Meynard, F. Forest, E. Labouré, V. Costan, A. Cuniére, E.Sarraute, "Monolithic Magnetic Couplers for Interleaved Converters with a High Number of Cells", in *Proc. IEEE CIPS Conf.,* 2006.

[12] F. Forest, T. Meynard, E. Labouré, V. Costan, A. Cuniére, T. Martiré, "Optimization of the Supply Voltage System in Interleaved Converters Using Intercell Transformers", *IEEE Trans. on Power Electron. ,* vol. 22, no. 3, pp. 934-942, May 2007.

[13] F. Forest, E. Labouré, T. Meynard, "Analytic Design Method Based on Homothetic Shape of Magnetic Cores for High Frequency Transformers", *IEEE Trans. on Power Electron. ,* to be published 2007.

[14] W. G. Odendaal, J. Ferreira, "Effects of Scaling High Frequency Transformers Parameters", *IEEE Trans. on Industrial Applications,* vol. 35, n° 4, pp. 932-940, July-August 1999.

[15] W. G. Odendaal, J. Ferreira, "A Thermal Model for High-Frequency Magnetic Components", *IEEE Trans. on Industrial Applications,* vol 35, n° 4, pp. 924-931, July-August 1999.

[16] L. Jieli, T. Abdallah, C. R. Sullivan, "Improved Calculation of Core Loss with nonsinusoidal waveforms", in *Proc. IAS Conf.,* 2001, vol. 4, pp. 2203-2210.

VHDL DESIGNING OF A FOUR MODIFIED PIPELINE STAGES MIPS PROCESSOR ON A FPGA XILINX VIRTEX SYSTEM

Cristian Andy TANASE, Adrian GRAUR
"Stefan cel Mare" University of Suceava, Faculty of Electrical Engineering, Suceava, Romania

Abstract: *This article aims to describe the MIPS processor with four modified pipeline stages. All components of the processor and its external devices (data, program and video memory, VGA controller and character generator) are implemented in VHDL, synthesized on the FPGA XILINX VIRTEX-II XC2V1000-4FG456C development system, called Altium NanoBoard-NB1.*

The architecture developed around the MIPS processor is first described. The architecture contains data, program and video memory and a VGA controller which displays the internal register of a MIPS processor on a VGA monitor, useful to debug running programs.
The register transfer level of the processor and the architecture of the modified pipeline stages are described next. An analogy between the classical MIPS pipeline and this architecture of pipeline is realized. In this architecture branch hazards, data hazard and stalls don't occur due to a modified clock system. The entire system is using two clock signals, shifted with 90º.
Keywords*: MIPS, FPGA, modified pipeline, pipeline hazard*

1. ARCHITECTURE DEVELOPED ON A MIPS PROCESSOR

Figure 1. presents the MIPS processor, connected to a 32-bit *progdata[31..0]* data bus and a 8-bit *progaddr[7..0]* bus to a ROM program memory. The code memory has a capacity of 256 words. Program code (Fibonacci series) is retained in this memory.

The data memory interface is realised through three buses: *datain[7..0]*, bus dedicated to memory data reading, *dataout[7..0]*, dedicated to memory data writing and address bus for data memory, *dataddr[7..0]*. MSB address bus, *dataddr7*, is used for selection of data memory or of I/O memory. When *dataddr7 = '0'*, data memory is selected, whereas for *dataddr7 = '1'*, I/O memory (video memory) is selected. Data memory writing or reading is made through *write* and *read* processor-generated signals. Data memory has a capacity of 128 octets.

I/O interfacing part is also realised by means of three buses and write and read pins. As peripherals, the system has a VGA controller, with its correspondent video memory. Video memory may be accessed both by controller and processor by means of MUX multiplexor. Processor accesses video memory as in the case of data memory, by means of *dataddr7 = '1'* pin and *write* signal. At that point, multiplexor also selects input 1 and allows processor address bus to access video memory. Data is written in memory by *dataout[7..0]* bus. VGA controller scans video memory by 7-pin *pixel_row[9..3]*, connected to *0* multiplexor input. When the processor doesn't write in video memory, *0* input is selected by default. Data read from video memory accesses a character generator that sends character to controller. The controller, in the video part, generates vertical and horizontal synchronizing signals, as well as the value of the displayed pixel. [1]

2. MIPS PROCESSOR INTERNAL ARCHITECTURE (MODIFIED PIPELINE)

2.1 Data path

The MIPS processor data path implemented on a FPGA XILINX VIRTEX-II XC2V1000-4FG456C chip on ALTIUM NANOBOARD-NB1 development platform, follow a classical architecture, as presented in Figure 2.

It is divided in five parts, each part named according to the instruction execution stage:

EI/DI: instruction extraction/decoding and registers file reading;
EX: address execution or calculation;
MEM: access to memory data;
RS: register file rewriting.

The major difference occurring in the functioning of this architecture as compared to the classical one is connected to the way in which system clock time is shared in pipeline distribution.

In classical architecture, each functional unit in the pipeline consumes half of the period of the system clock, except for the execution stage. Considering the fact that the most complex operation is that of „decoding instruction and reading registers file", due to decoding and internal register access logic, the result is that the execution operation can also be compressed as execution during half of clock period. It can also be simplified by compressing ALU entrance multiplexors, by using 2 MUXs with several inputs, instead of four.

As we will see, this leads to the elimination of the majority of hazards. In Figure 3, we have shown the execution of MIPS instructions with modified pipeline as compared to MIPS classical diagram.

Certainly, if execution or „EX" address calculation operation requires two clock periods, this could extend to two clock periods, but there could occur hazard situations.

Also, the pipeline could be even forced into advancement with half of the clock period of the following instruction (that is, an instruction that is executed in half of a clock period and not in a complete period as in Figure 3), but thus, we only used a classical pipeline, with the difference that it executes instructions twice as fast.

In order to realise normal functioning of modified pipeline units, mainly of pipeline registers, two clock signals were used (CLK_MIPS and CLK_TRIG). Thus, the system is controlled by a normal clock with pulse duty factor of 50%, but signals that activate memorization of input values in the pipeline registers are controlled by a clock shifted with 90° from the system clock, as shown in Figure 4. CLK_MIPS, after which pipeline stages are executed. CLK_TRIG is used to activate writing signal in pipeline registers.
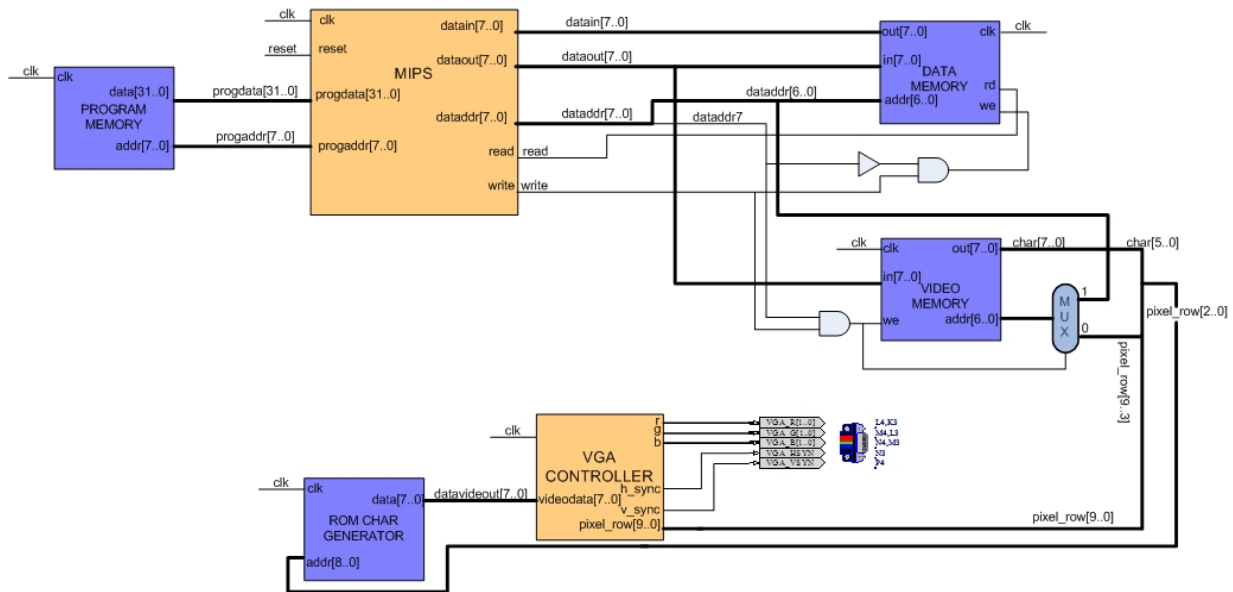
Fig. 1. *MIPS processor system architecture.*

The wave forms in Figure 4 are obtained from logic block in Figure 5. On each level of CLK_MIPS signal, a pipeline stage in executed. Instruction extraction stage is executed on logic level '1'. The signal memorization in pipeline registers is made on each positive or negative front of CLK_TRIG signal. [1] [2]

2.2 Data Hazard and Advancement

This is the only type of hazard occurring in instruction execution. Let us remember that it occurs depending on the following situations:

```
sub $2, $1, $3 #  Register   $2   is
written by subtraction instruction
  and $12, $2, $5 # 1st operator ($2)
depends on subtraction
  or $13, $6, $2 # 2nd operator ($2)
depends on subtraction
```

One may notice that instructions and $12, $2, $5 and or $13, $6, $2 depend on result in $2 obtained by instruction in sub $2, $1, $3. Unit of hazard detection and advancement of result in Figure 6 (U_fwd) has the VHDL code as presented below.

2.3 Data Hazard and Stall

These occur in situations such as:

```
lb $2, 20($0)   #  Register   $2   is
written with value from address 20 in
data memory
  and $4, $2, $5  # 1st operator ($2)
depends on value written in $2
  or $8, $2, $6  # 2nd operator ($2)
depends on value written in $2
```

We may notice that and $4, $2, $5 instruction must wait for two clock cycles till instruction lb $2, 20($0) reaches RS stage to write $2 in the register and instruction and reads it with correct value.

Stall may be obtained through introduction of '0's for control signals for two cycles, which makes pipeline to stop, or compiler to detect such a hazard and to insert two *nop*'s with the same effect. [3][4]

In the architecture presented and implemented, it is no need to use such a detection unit for this type of hazard, due to the fact that RS pipeline stage is superposed with ALU stage (see Figure 3), and by means of the advancement unit, the value that must be written in the memory register is directly passed to ALU as operator. Thus, the circuit and the compiler complexity is reduced. The detection block of data and pipeline stop hazard was not implemented.

2.4 Branch Hazard

As in the case of data hazard and stalls, branch hazard does not occur in this architecture. By means of branch dynamic prediction method, implemented in block (U_jmpctrl), Figure 6, the detection of a branch is accepted as early as DI is made. In this stage, classical architectures introduce a *nop* in order to postpone the extraction of the following instruction, function of the decision already taken. [7]

As one can see in Figure 3, the stage EI/DI of an instruction is executed before stage EI of the following instruction; thus, the following address may be selected earlier, according to the decision taken in *beq* instruction. Also, by means of eliminating this type of hazard, compilers and hardware architecture are much simplified. [4]

Fig. 2. *The MIPS processor system architecture.*
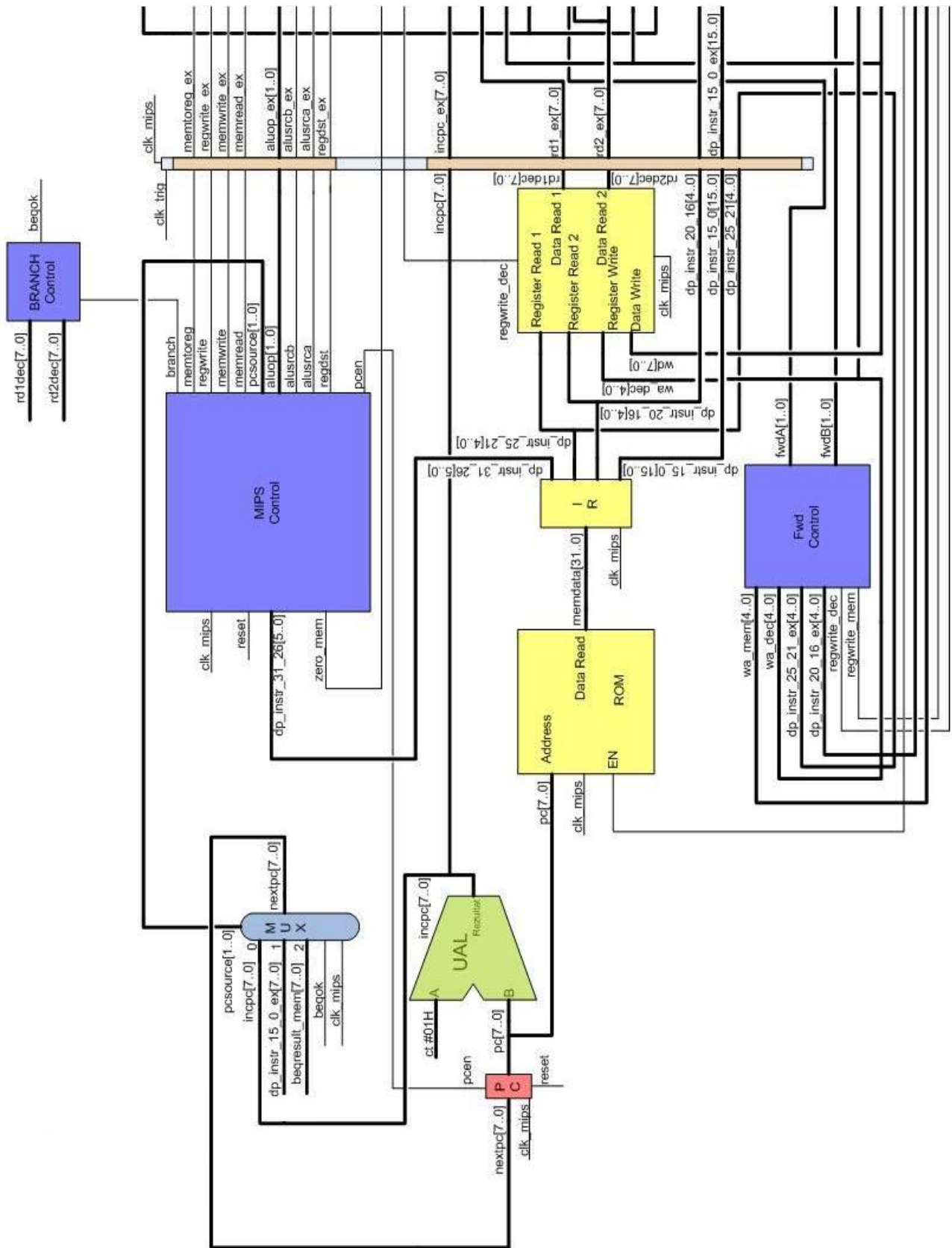
Fig. 2. *The MIPS processor system architecture (continuation).*
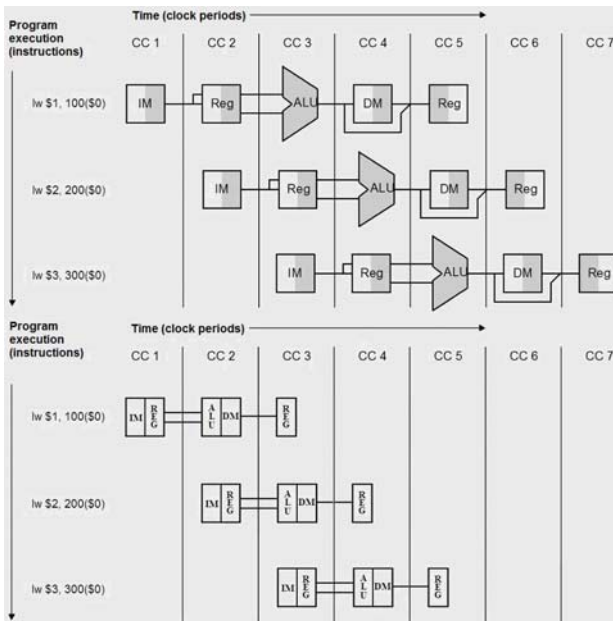
Fig. 3. *Instructions executed in modified pipeline version.*
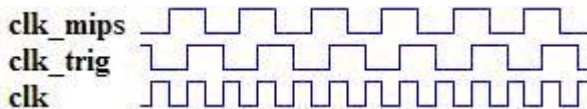
Fig. 4. *The wave forms of clock signals used by MIPS nucleus.*
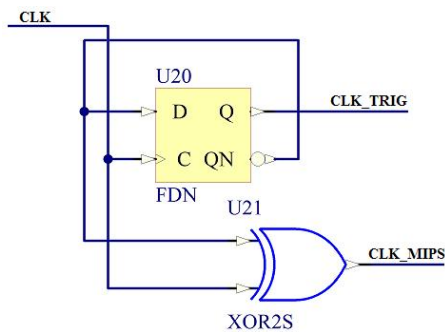
Fig. 5. *The diagram of clock signals generation used by MIPS nucleus.*

2.5 Test Program Execution

A test program was set for execution:

```
#fib.asm
#used registers: $3:n, $4:f1, $5:f2
#returned value is written at
#address 8

fib:
addi $3, $0, 8 #initialisation n=8
addi $4, $0, 1 #initialisation f1=1
addi $5, $0,-1 #initialisation f2=-1
loop:
beq $3, $0, end #loop abort if n=0
add $4, $4, $5 # f1 = f1 + f2
sub $5, $4, $5 # f2 = f1 - f2
addi $3, $3, -1 # n = n - 1
```

```
j loop          # repeats loop
end:
sb $4, 8($0) # retains result at
             #  address 8 DM
lb $8, 8($0) # charges in $8 value
             # from address 8 DM
lb $9, 8($0) # charges in $9 value
             # from address 8 DM
```

The device language code in presented in Figure 7.

Instruction	Address		Hexadecimal Code
addi $3, $0, 8	0	=>	X"20030008"
addi $4, $0, 1	1	=>	X"20040001"
addi $5, $0, -1	2	=>	X"200500ff"
beq $3, $0, end	3	=>	X"10600004"
add $4, $4, $5	4	=>	X"00852020"
sub $5, $4, $5	5	=>	X"00852822"
addi $3, $3, -1	6	=>	X"206300ff"
j loop	7	=>	X"08000003"
end:			
sb $4, 8($0)	8	=>	X"a0040008"
lb $8, 8($0	9	=>	X"80080008"
lb $9, 8($0)	10	=>	X"80090008"

Fig. 7. *The Device Language Code as Generated by Assembler.*

As it is easily noticeable, the assembler did not introduce any nop instruction of pipeline blocking (neither after beq instruction, nor after j instruction). *mipsisa32-elf-gcc* was used as assembler and *mipsisa32-elf-gdb* from GNUPro Toolkit RedHat as simulator. Figure 8 is a simulator Screen Shot. [5]
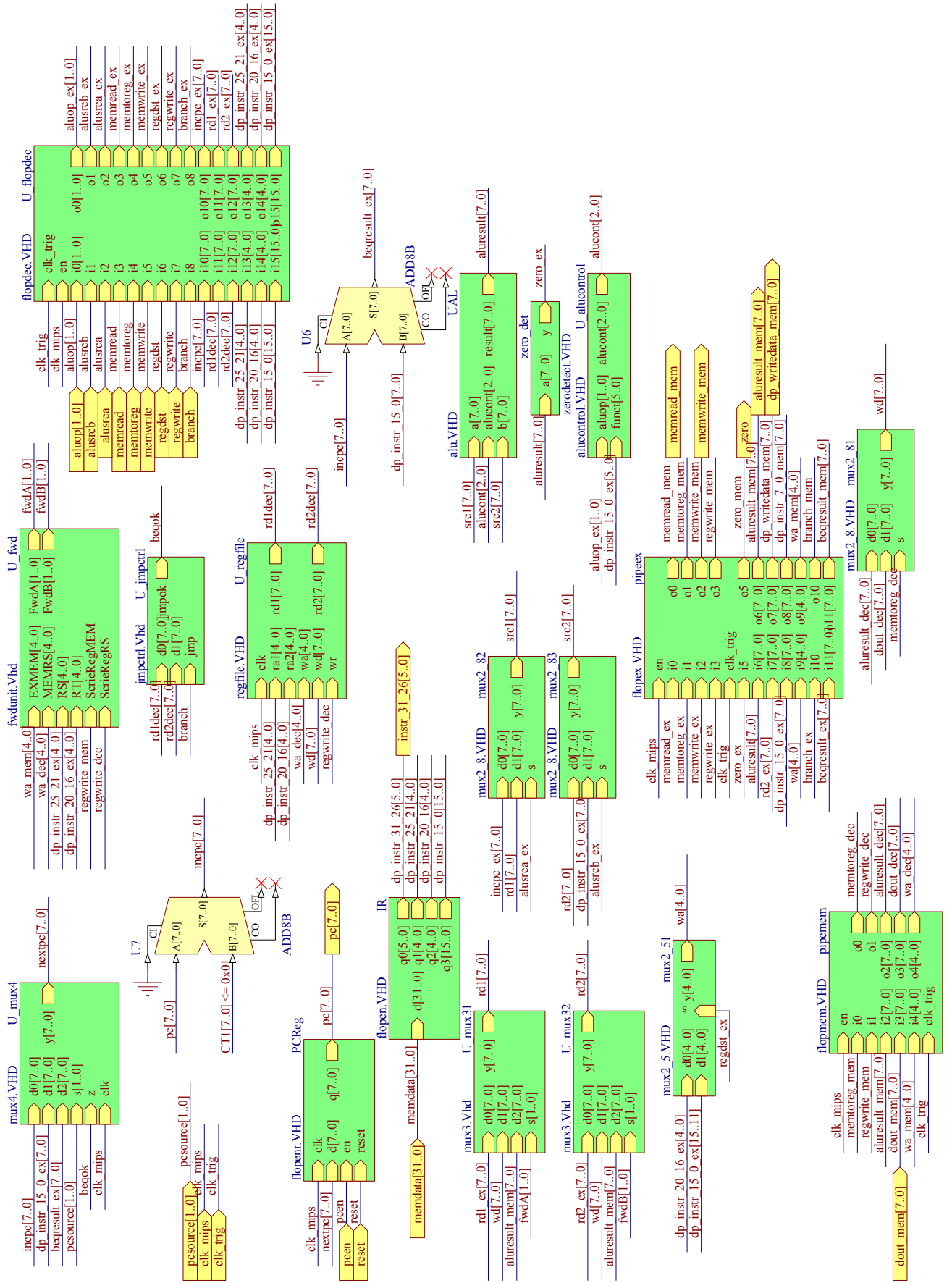
Fig. 6. *The pipeline MIPS internal architecture synthesized VHDL.*

Fig. 8. *GNUPro Debugger Screen Shot.*

In Figure 8 one may notice that the assembler introduces two `nop` instructions after `beq` and `j` instruction, which is not necessary for the described architecture.

The only required restriction is that of avoiding setting the decrementation or incrementation instruction of an indicator before indicator testing instruction, as in the following example:

```
addi $3, $3, -1
beq $3, $0, end
```

but this doesn't affect the economy of the program.

3. CONCLUSIONS

In this model of architecture, hazard situations occur no longer, as the instructions are executed in their logical order (non-out of order) on each clock cycle. Pipeline system does no longer suffer stalls, and the branch instructions are assessed in the first pipeline stage, the following instruction extracted being the logically correct one. Practically, each pipeline level is executed on half a clock period, due to the fact that in the classical pipeline there are also levels that are executed in a half of a clock period. We have constructed a parallel between Fibonacci program generated by MIPS classical assembler in which *nop* instructions introduced by it for pipeline "stopping" are to be noticed and the program written for this architecture in which there is no pipeline stall problem.

4. REFERENCES

[1] David A. Patterson, John L. Hennessy (2002), Organizarea şi Proiecarea calculatoarelor – interfaţa hardware/software, Editura All
[2] Neil H.E. Weste, David Harris (2005), CMOS VLSI Design, 3rd Edition, Pearson Internationla Edition
[3] Coillins R. (1995), Exploiting Instruction Level Parallelism in a Superscalar Architecture, PhD Thesis, University of Hertfordshire, UK,
[4] Murdocca Miles (2000), Principles of Computer Architecture, Editura Prentice Hall
[5] Wakerly John (2002), Circuite Digitale - Principiile şi practicile folosite în proiectare, Editura, Teora
[6] Zwolinski Mark (2004), Digital System Design with VHDL, Editura Prentice Hall

SPECIAL FEATURES IN DESIGNING SINGLE PHASE SERIES ACTIVE POWER FILTER

Mihail Antchev*, Vanjo Gurgulitzov**, Mariya Petkova***

* Technical University - Sofia, Department of Power Electronics, Bulgaria, ** United Technical Collage with Technical University – Sofia, Department of Electroenergy and Automation, Sofia, Bulgaria, *** Technical University - Sofia, Department of Power Electronics, Bulgaria

Abstract: *The proposed paper presents several special features in designing single phase series active power filter. Formulas, which granted the calculation of the required filter power, are enclosed in the paper. Computer simulation results and experimental results proving the effectiveness of the implementation of the series active power filter to improve quality of the supply voltage are enclosed. The study is made under nonlinear and linear load.*
Keywords: *Series Active Power Filter, Design*

1. INTRODUCTION

In general, insufficient quality of electrical power is changes into distribution net parameters, such as its current, its voltage or its frequency, individually or as a combination among them. Changes of those sort lead to disturbance into standard industrial process or to breakings into electrical converters – motors, transformers, etc. [1-3]. The most widespread method to deal with harmonics of consumed current is an implementation of passive filters. Unfortunately, this method has considerable disadvantages [4-5].

At the present days, the most perspective devices [3-4, 6-9] which may be used to deal with the harmonics pollution are active power filters. Their main advantage is their effective operation which is independent on the changes of the load's parameters. Series active power filters (SAPF) are enclosed to improve power quality of the supply voltage of critical consumers. There is a probability to use this filters to improve the power factor of loads with respect to the supply network, actually to fulfill its improvement, shunt active power filters are basically used. The proposed paper is devoted to make a study of several special features in designing series active power filter, which is meant to improve the quality of the supply voltage, and to found in it equations of the three cases of the loading of the power devices in filter's designing.
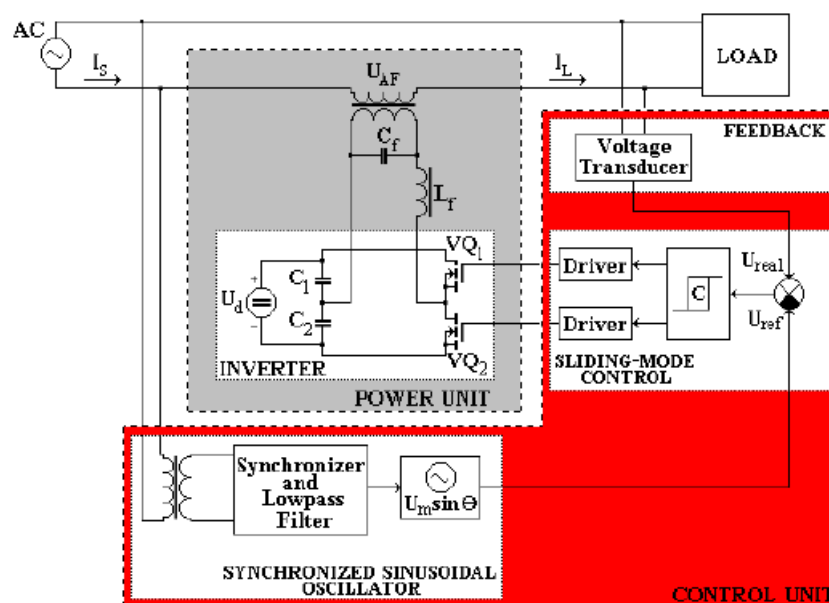

Fig. 1. *Block schema of the series active power filter*

2. FILTER SCHEMATIC

Fig.1. displays a block scheme to implement and to study the filter. The power unit of the filter consists of a transformer, an inverter and a low pass frequency LC filter. The control unit consists of voltage feedback, synchronized sinusoidal oscillator and sliding-mode control block. The voltage feedback is used to monitor the input load voltage. The signal of the feedback is compared with the output of the synchronized sinusoidal oscillator, which output is a sinusoidal signal synchronized with the source voltage. The signal from the comparison is passed to a control system based on sliding mode control, the outputs of which are the driver signals for the inverter's transistors. The transistors are controlled in such a way that the input load voltage to be of sinusoid waveform.

3. MATHEMATICAL DESCRIPTION OF THE THREE POSSIBLE CASES

Three cases for the input load voltage are probable. The first one is when the source voltage is only been filtering and the result is used to supply the load with a sinusoidal voltage U_L equal to the filtered voltage first harmonic U_1. The second case is when a filtering of the source voltage is made

and the load is supplied with a stabilized voltage U_L with a preliminarily set value U_{1R}. The third case uses a monitoring of the effective value of the source voltage U, it is also been filtering and the load is supplied with a sinusoidal voltage U_L equal to the effective value of the source voltage. During the founding of equations for filter loading in the three cases Fig.2 is used. The SAPF is not used for a power factor correction. The effective values of currents consumed before and after the connection of the filter will be approximately equal. The supplying load voltages are different before and after the connection of the filter because of their different harmonic components, but with a sufficient approximation for the study it can be assumed the following equation (see Fig. 2):

$$S \approx S' \tag{1}$$

$$S = U \cdot I$$

$$S' = U \cdot I'$$
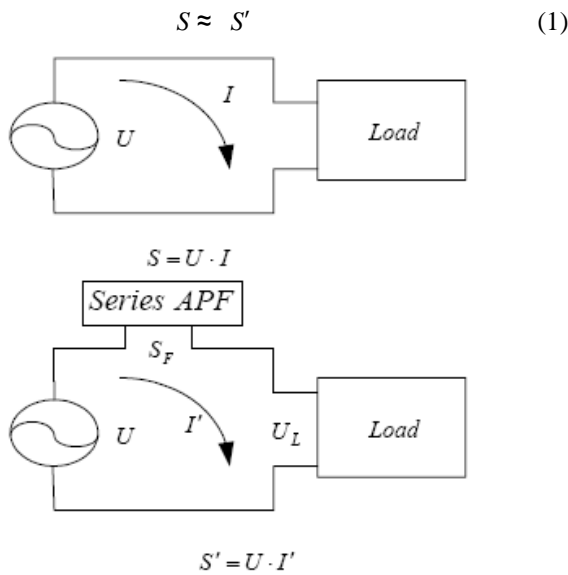
Fig. 2. *Description of the studied system – upper block diagram is when the filter is not connected, lower one – when filter is connected*

3.1. The First Case – $U_L = U_1$

The total power consumed when the filter is not connected is equal to the multiplication of the effective value of the source voltage U by the effective value of the consumed current I, and, when the filter is connected the current I' is the new effective current value. So the total power is:

$$S = U \cdot I' \tag{2}$$

Both sides of the equation (2) are raised to the second power and it is found:

$$S^2 = U^2 \cdot I'^2 = U_1^2 \cdot I'^2 + I'^2 \cdot \sum_{n=2}^{\infty} U_n^2 \tag{3}$$

The ratio of the squares of the filter power S_F and the total consumed power from the source S is as follows:

$$\frac{S_F^2}{S^2} = \frac{I'^2 \cdot \sum_{n=2}^{\infty} U_n^2}{I'^2 \cdot \left(U_1^2 + \sum_{n=2}^{\infty} U_n^2 \right)} = \frac{k_H^2}{1 + k_H^2}$$

(4)

where in k_H is the total harmonic distortion coefficient.

After simple transformations, it is found the relation among the required filter power, load power and the total harmonic distortion coefficient:

$$\frac{S_F}{S} = \sqrt{\frac{k_H^2}{1 + k_H^2}} \approx k_H \tag{5}$$

Also, it is found the relation among the effective value of the source voltage U, its first order harmonic U_1 and the total harmonic distortion coefficient:

$$\frac{U_L}{U} = \frac{U_1}{U} = \upsilon = \sqrt{\frac{1}{1 + K_H^2}} \tag{6}$$
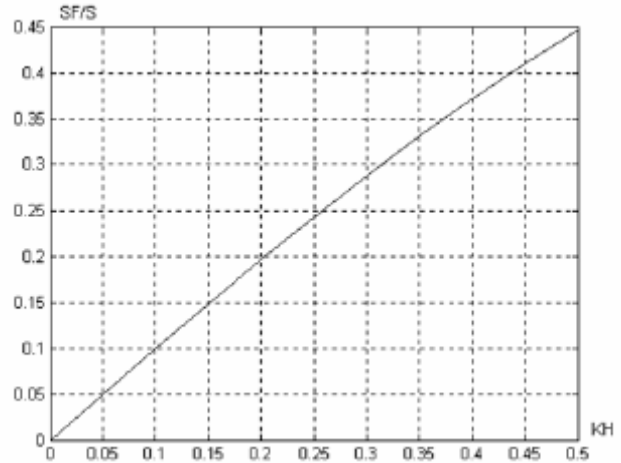

Fig. 3. *Graphical presentation of equation (5)*
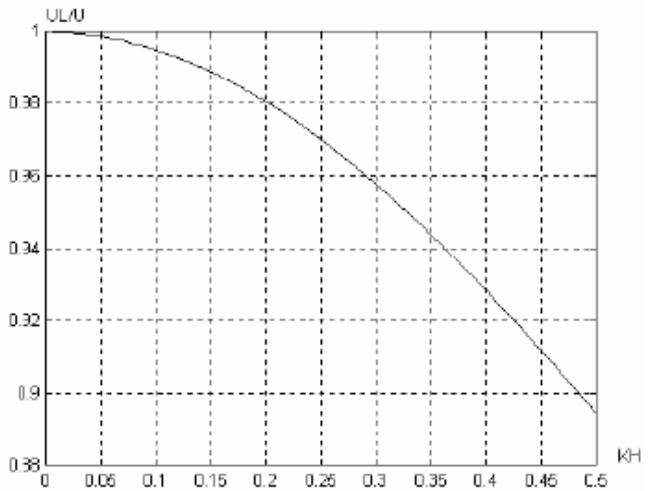
Fig . 4. *Graphical presentation of equation (6)*

The so found equations (5) and (6) are graphically presented at Fig. 3 and Fig. 4 using the software MatLab 7.1.

3.2. The Second Case – $U_L = U_{1R} = const$

From the main case description for the second case follows:

$$U_L = U_{1R} = const \tag{7}$$

If the effective values of the output filter voltage, the reference value of the first order harmonic and the nth order harmonic are U_F, U_{R1} and U_n, then from the filter operation it is obvious that the following equation is valid:

$$U_F^2 = (U_{1R} - U_1)^2 + \sum_{n=2}^{\infty} U_n^2 \tag{8}$$

Let mark the ratio of the reference value of the first order harmonic to the effective value of the first order harmonic of the source voltage with k:

$$k = \frac{U_{1R}}{U_1} \qquad (9)$$

From (8) and (9) it is found the following equation for the filter voltage:

$$U_F = U_1 \cdot \sqrt{(k-1)^2 + k_H^2} \qquad (10)$$

By analogy to the first case, the ratio of the squares of the filter power S_F and the total consumed power from the source S is as follows:
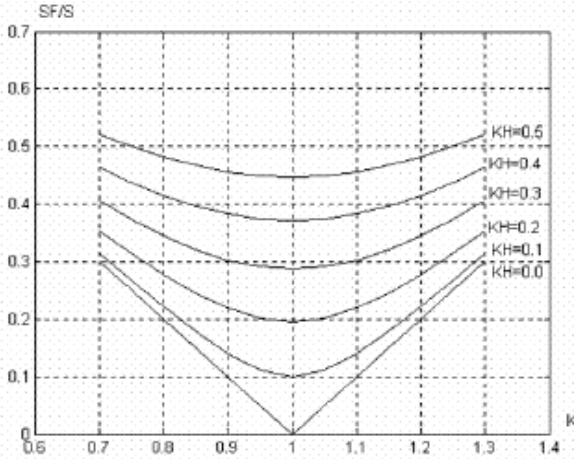

Fig. 5. *Graphical presentation of equation (12)*
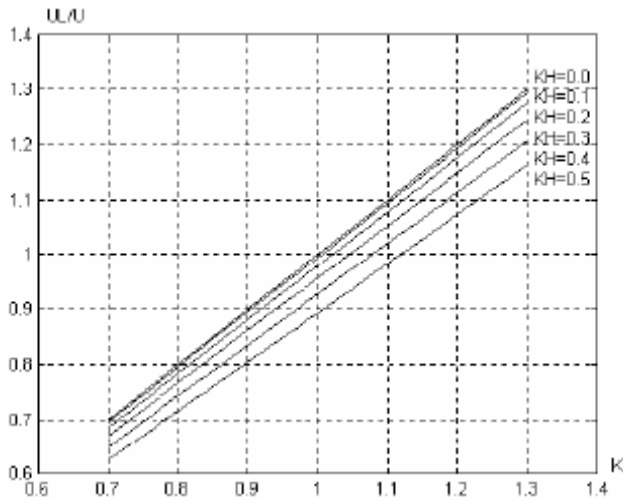
Fig. 6. *Graphical presentation of equation (13)*

$$\frac{S_F^2}{S^2} = \frac{U_1^2 \left[(k-1)^2 + k_H^2 \right] \cdot I}{\left[U_1^2 + \sum_{n=2}^{\infty} U_n^2 \right] \cdot I} = \frac{(k-1)^2 + k_H^2}{1 + k_H^2} \qquad (11)$$

And, the following relations, graphically presented at Fig. 5 and Fig. 6, are found:

$$\frac{S_F}{S} = \sqrt{\frac{(k-1)^2 + k_H^2}{1 + k_H^2}} \qquad (12)$$

$$\frac{U_L}{U} = \frac{U_{1R}}{U} = k \cdot \sqrt{\frac{1}{1 + k_H^2}} \qquad (13)$$

3.3. The Third Case – $U_L = U_{1R} = U$

From the main case description for the second case follows:

$$\frac{U_{1R}}{U} = 1 \qquad (14)$$

Substituting equation (14) in (13) and then using (12) it is obtained the following relations:

$$k = \sqrt{1 + k_H^2} \qquad (15)$$

$$\frac{S_F}{S} = \sqrt{2} \cdot \sqrt{1 - \frac{1}{\sqrt{1 + k_H^2}}} \qquad (16)$$

The relation (16) is graphically presented at Fig. 7.
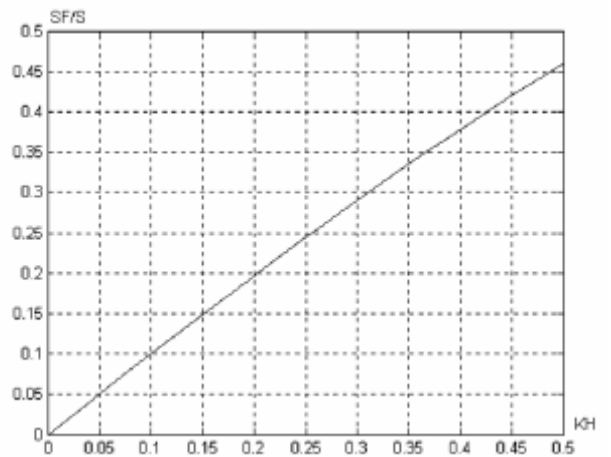
Fig. 7. *Graphical presentation of equation (16)*

4. SIMULATION AND EXPERIMENTAL RESULTS

Based on the shown schema at Fig.1, a simulation (Microsim Release 8.0) and an experimental model are made. Fig. 8 and Fig. 9. display simulation and experimental results in the second case respectively, taken down during operation of the filter with nonlinear load – uncontrolled rectifier with RC-load.
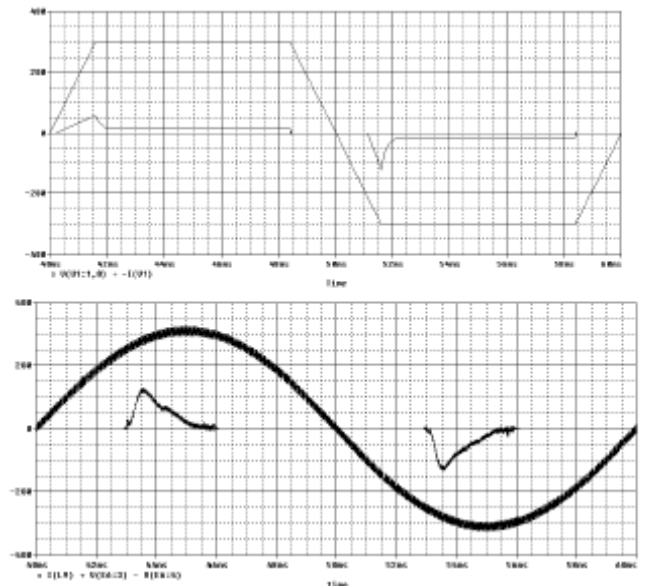
Fig. 8. *Simulation results presented the input load voltage and the load current – at the upper oscillogram are results gained without the filter, at lower one – with the filter*
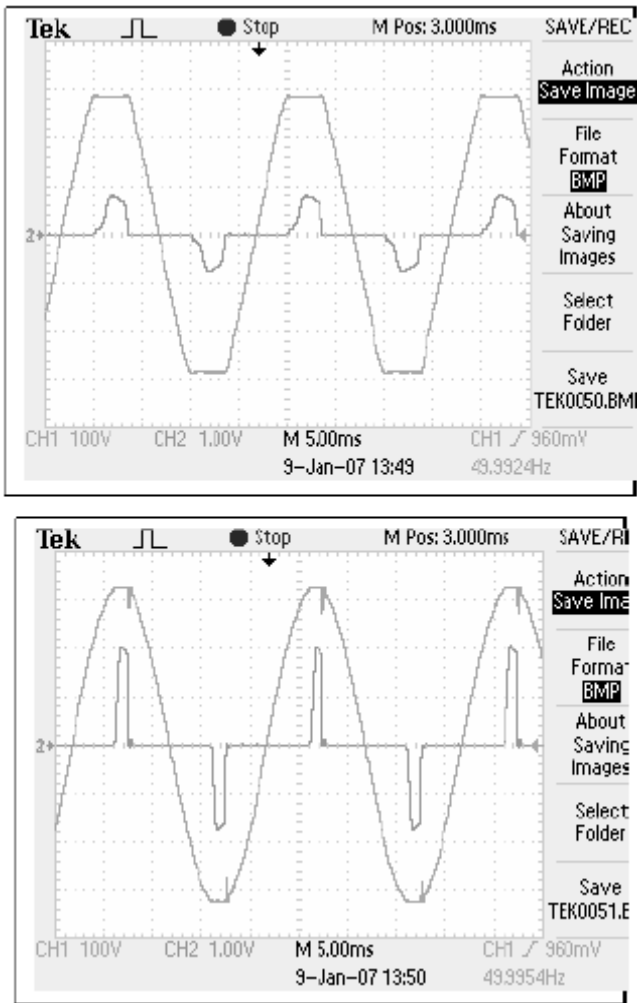
Fig. 9. *Experimental results presented the input load voltage and the load current – at the upper oscillogram are results gained without the filter, at lower one – with the filter*

5. CONCLUSION

Mathematical and graphical relations are found which are useful to define the required total power of the series active power filter in three possible cases.

Both the computer simulation results and the experimental results prove the effectiveness of the implementation of the series active power filter to improve quality of the supply voltage in these three cases.

6. ACKNOLEDGEMENT

7. REFERENCES

[1] Chiasson J. N., L. M. Tolbert, K. J. McKenzie and Z. Du, "*A Complete Solution to the Harmonic Elimination Problem*", IEEE Trans. On Power Electr., Vol.19, No. 2, March, 2004, pp. 491-499.

[2] Marei M.I., E.F. El-Saadany and M.M.A. Salama, "*Flexible Distributed Generation*", Power Engineering Society Meeting, 2002, vol.1, pp.49-53.

[3] Curo Zhak, "*Basic Tehnologies to inrease quality of the electrical power when destributing it*", part1, News in ElectroTechnics, vol.1 (31), 2005.(in russian)

[5] Fang – Zhuo, Jung –Yang, Junfei – Hu and Zhao'an – Wang, "*Study on active power filter used in threephase four-wire system*", Power Electronics and Motion Control Conference, 2000. Proceedings. PIEMC 2000. The Third International, Vol. 3, August 2000, pp.1037-1040.

[6] Karv Shri, "*Active ower Filters*", Electroequipment, vol.4, 2004, pp 74 (in russian).

[7] Pronin M., "*Trends in Active Power Filters*", News in ElectroTechnics, vol.2 (28), 2006.(in russian).

[8] Jacobs J., D. Detjen, C.-U. Karipidis and R. W. De Doncker, "*Rapid Prototyping Tools for Power Electronic Systems: Demonstration with Shunt Active Power Filters*", IEEE Trans. On Power Electr., Vol.19, No. 2, March 2004, pp.500-507.

[9] Peng F.-Z., "*Application Issues of Active Power Filters*", IEEE Industry App. Magazine, September/October 1998, pp.21-30.

ON THE INFLUENCE OF EMC-COIL DESIGN ON ITS BROADBAND IMPEDANCE CHARACTERISTIC

Boguslaw Grzesik, Radoslaw Jez, Szymon Pasko

Silesian University of Technology, Department of Power Electronics,
Electrical Drives and Robotics, Gliwice, Poland
boguslaw.grzesik@polsl.pl, radoslaw.jez@polsl.pl, szymon.pasko@polsl.pl

Abstract: *Influence of coil design on the broadband impedance characteristic of 100 A, 50Ω/50μH+5Ω Line Impedance Stabilization Network (LISN) is presented in this paper. The analyses for different winding coils and its impact on LISN impedance characteristic, are considered. Also magnetic flux density for different winding coils is analysed using Finite Element Method (FEM).*

Keywords: *Electromagnetic Compatybility (EMC), Conducted Emmision, Line Impedance Stabilization Network (LISN)*

1. INTRODUCTION

Nowadays, electromagnetic compatibility has become the most important issue in electrical engineering. Most of electrical devices generate electromagnetic emissions that have bad influence on the operations of the devices in neighbouring environment. Therefore it is necessary to measure electromagnetic emissions and conducted ones in it. Such measurements are needed to apply means reducing the bad influence of the emissions. Moreover, the most products to be sold have to comply with EMC directive [1]. The measurements of conducted emissions are carried out with the Line Impedance Stabilization Network (LISN) - Fig.1. In order to clarify details of measurements it is necessary to carry out thorough analysis of LISN features, where analysis of its coils is included. Information derived from such analysis could be also useful from constructional purpose for new type of LISN.

Line Impedance Stabilization Network (LISN) is inserted in measurement system like is depicted in Fig.1.

The measurement system consists of Line Impedance Stabilization Network (LISN), AC supply mains V_{AC}, equipment under test (EUT) and Spectrum Analyzer (SA). This system allows to measure conducted emissions generated by EUT e.g. power electronic converter. The LISN is inserted in between AC supply mains (V_{AC}) and equipment under test (EUT). It filters fundamental component from RF noises existed in AC supply mains. Therefore EUT is fed by "unpolluted" sinusoidal voltage (e.g. 50 Hz). The RF noises that come from EUT are measured between each phase (live (a1), or neutral (a2)) and ground plane (GP).
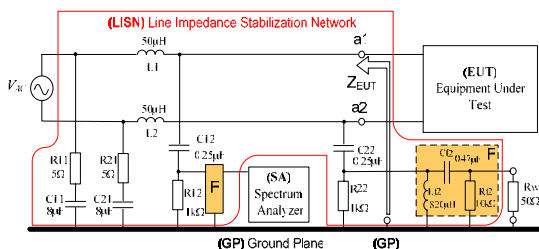

Fig. 1. *System for conducted emissions measurement with LISN 50Ω/50μH+5Ω*

The RF noise from AC supply mains (V_{AC}) are suppressed due to high impedance of L_1 (EMC-coil) for phase

a1 or L_2 for phase a2, and low impedance C_{11} or C_{21}. The noises generated by EUT are flowing to Spectrum Analyzer (SA) via capacitor C_{12} for phase a1 or capacitor C_{22} for phase a2. When measurement is done for one phase, e.g. a1, than the other one has to be terminated with R_w=50 Ω to ensure symmetry of measurement as spectrum analyzer has also input resistance of 50 Ω [2]. The high-pass filter F of LISN prevents the disturbance analyzer from low frequency noise (Fig.1).
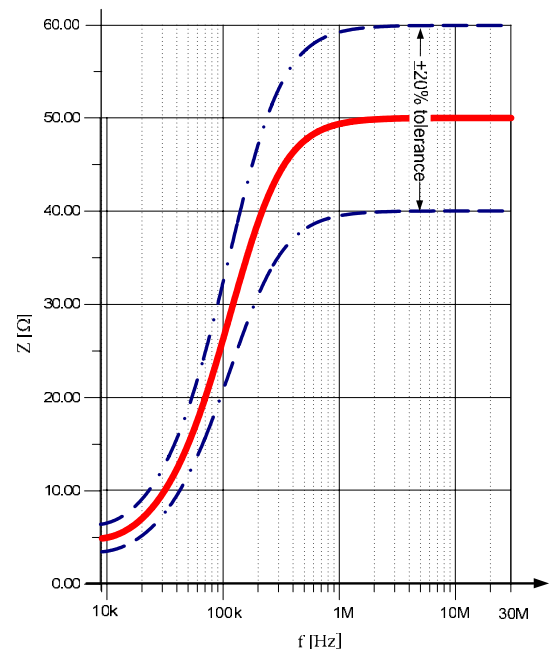
Fig. 2. *Impedance characteristic seen from EUT's port according standard CISPR 16.*

The RF impedance Z_{EUT} of LISN, measured between a1 and GP (or between a2 and GP) is defined in international standards CISPR 16 -1 [3], CISPR 16-2 [4].

The impedance Z_{EUT} characteristic is measured by impedance analyzer with unplugged AC mains supply V_{AC} and phase a2.

The ideal impedance Z_{EUT} is presented in Fig. 2. Its impedance curve is specified in the range 9 kHz to 30 MHz in standard CISPR 16 -1 [3]. The standards assume ±20% tolerance of Z_{EUT} impedance, because in practice the curve differs from a flat 50Ω [5].

2. ANALYSIS AND MEASURMENT OF EMC-COIL

The development of main inductor $L_1 = L_2 = 50$ μH for this network was the main task of this work, because its impedance has strong influence on the impedance Z_{EUT}, (a1-GP, a2-GP). The research has been carried out for the following parameters of the L_1, L_2: i) coreless design of D=140 mm (Fig.4, Fig.10), ii) inductance of coil $L_1=L_2= 50$ μH, iii) maximum value of conducted current I=100 A (50 Hz), iv) two ways of winding: double and single layer, v) both of coils were winded using 10 mm^2 copper conductor, where one is stranded wire insulated with silicon (SILFLEX) - Fig. 3a while the second is enameled massive wire. The research work was carried out due to following plan: i) comparision analysis of enameled wire and SILFLEX stranded wire has been done, ii) the impedance characteristic of coils was measured, iii) the equivalent RLC circuit was measured by impedance analizer Agilent 42941 from 9kHz – 30 MHz, iv) stray capacitance was calculated numerically, v) results verifacation was done with Finite Element Method (FEM).

2.1. Comparison analysis of enameled and SILFLEX stranded wire

The analyzed L_1, L_2 coils were designed for the nominal current value I=100A. This level of current determines the well selected cross-section of wire because of thermal problems. In order to determine the qualitative thermal behavior of the coil FEM analysis of the current density distribution in the single wire was carried out for two assumed wires (SILFLEX stranded wire and enameled wire) and for four cases: i) SILFLEX strand wire, 9 kHz, ii) SILFLEX stranded wire, 30 MHz, iii) enameled wire, 9 kHz, iv) enameled wire, 30 MHz. The results of this analysis are in Fig. 3. Its examinations reveal that distribution of current density near the same of two types of wire resulting near the same power losses. Increasing frequency to 30 MHz one can observe that distributions of current density essentially different. The highest value of current density of SILFLEX strand wire is about 10 times higher than enameled wire. It gives higher power losses in SILFLEX stranded wire (14W/m for 9kHz, 941W/m for 30 MHz). The corresponding losses for enameled wire are (12,76W/m for 9kHz, 284 W/m).The similar behavior is expected for the coils. The filaments of SILFLEX strand wire are coated by Sn layer (0.05 mm). It causes negligible power losses.
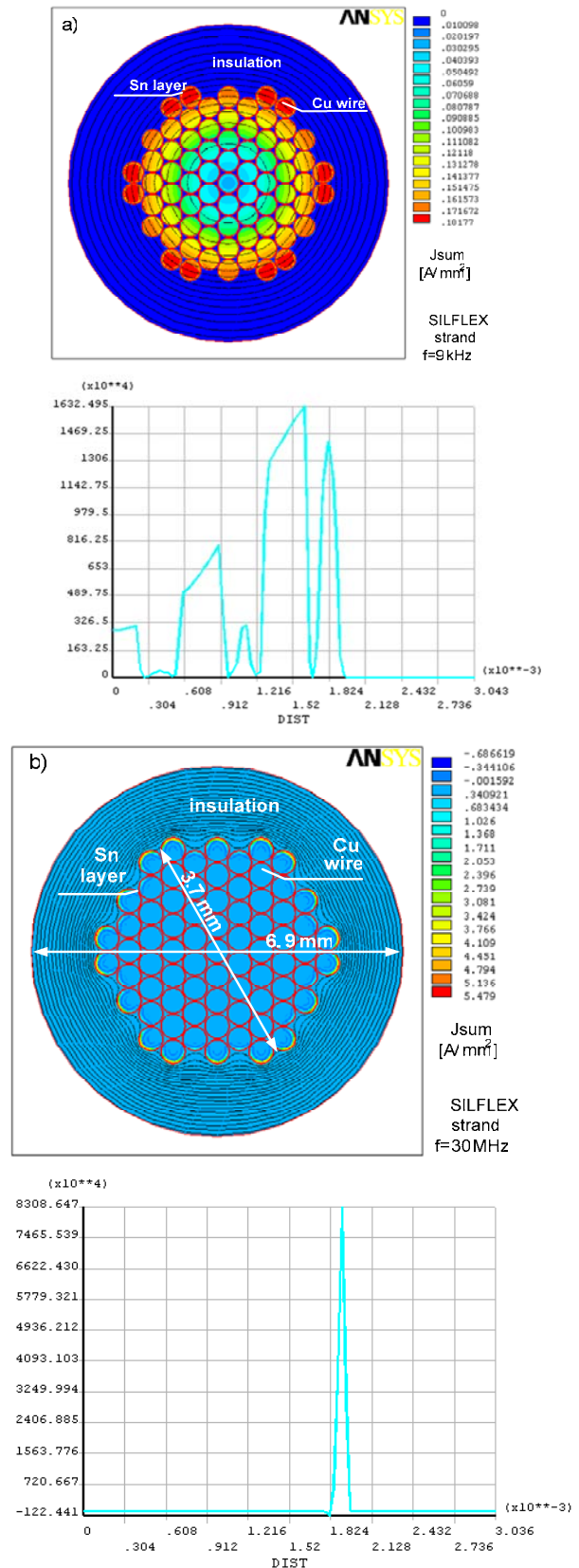

Fig. 3. *AC current density: a) SILFLEX stranded wire (9 kHz), b) SILFLEX strand wire (30 MHz).*
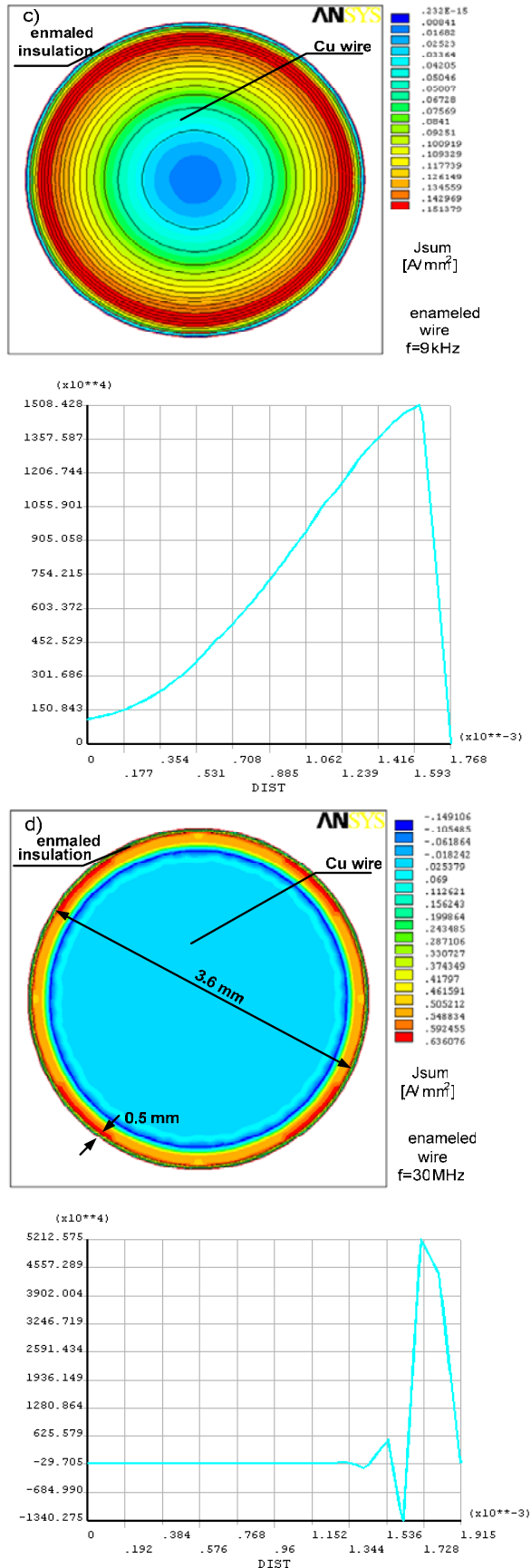
2.2. Double layer coils

The double layer coils are depicted in Fig. 4. Both of them were measured using impedance analyzer Agilent 42941. The results are given in Fig. 5. Each one for two frequencies 9 kHz and 30 MHz.
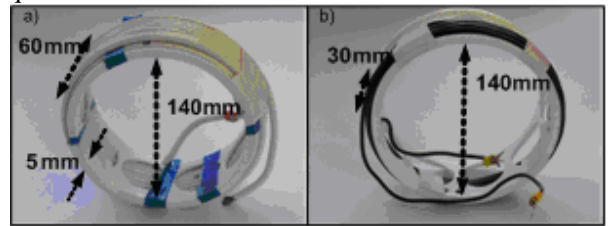

Fig. 4. *Double layer coils of LISN winded by:*
a) SILFLEX stranded wire – 17 turns,
b) enameled wire - 13 turns.

The impedance characteristic in the range of frequency from 9kHz–30MHz for SILFLEX stranded wire double layer coil and enameled wire is presented in Fig. 5. Using the method given in [6] and taking the data from Fig 5b equivalent circuit of the coil made of enameled wire was derived and depicted in Fig. 6. The impedance characteristic of equivalent circuit was check with Pspice and it is with good agreement with measured one (Fig. 5b). Such equivalent circuit is needed for modeling and simulation the whole LISN. In order to obtain more realistic results. Simultaneously harmonic FEM (Finite Element Method) analysis was carrying out (Fig. 7) which gave value of EMC-coil inductance that it is close approximately to $L_1+L_2+L_3$. To have another source of the value of stray capacitances the relevant FEM (electrostatic) analysis was done. The results of it are gathered in Table 1. The value total capacitance of coil made of enameled wire is close to its measure value (Fig. 5b, Fig. 6). The differences between inter-turn capacitances of the SILFLEX stranded wire coil and enameled wire coil are resulting from the thickness of isolation (Table 1).
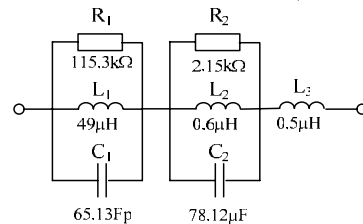
Fig. 6. *Equivalent circuit of double layer coil winded with enameled wire for 9 kHz-30 MHz.*

Table 1: *Capacitances of the double layer coils*

	Wire	
	SILFLEX stranded	enameled
Number of turns	17	13
Inter-turn capacitance of one layer	35.6 pF	64.3 pF
Inter-turn capacitance between turns lying in different layers	27,8 pF	61 pF
Total coil capacitance (C_1-C_2 series connection)	5.1 pF	34.5 pF

Fig. 3. *AC current density: c) enameled wire (9 kHz),*
d) enameled wire (30 MHz).

Apart from measured impedance characteristic of the coil made of enameled wire the characteristic for SILFLEX stranded wire coil was measured and present in Fig.5a. One can indicate four resonances. That makes this coil worse in comparison with the coil made of enameled wire e.g. in case one decides to modify this characteristic to be close to ideal one.

The FEM analysis (Fig. 7) allows for calculations of inductance as a function of frequency (skin effect and proximity phenomenon). To know the influence of given design of the coil on the impedance Z_{EUT} characteristic, seen from port (a1-GP or a2-GP) they were measured and depicted in Fig. 8.

One can notice they are not meet requirements of CISPR 16-1, as they are differing from characteristic given in Fig. 2.

Fig. 5. *Measured impedance characteristic of double layer coils winded with: a) SILFLEX stranded wire, b) enameled wire.*
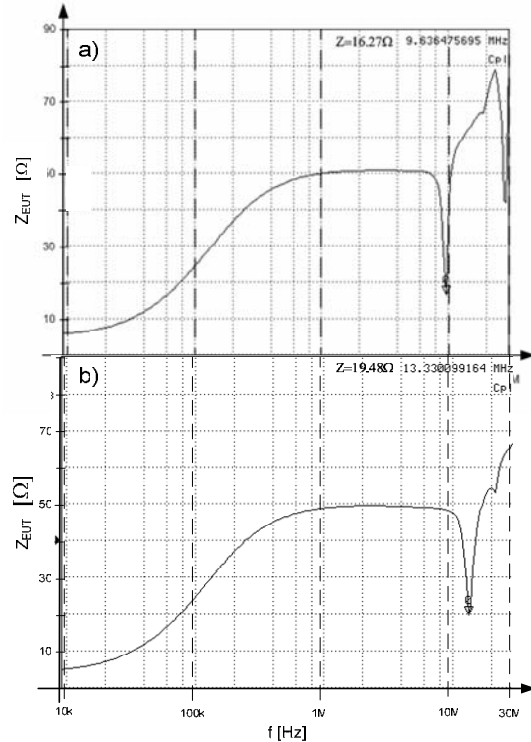
Fig. 8. *Measured impedance characteristic seen from EUT's port for double layer coil winded with: a) SILFLEX stranded wire, b) enameled wire.*

2.3. Single layer coils

The single layer coils are depicted in Fig. 9. The same analysis like for double layer coils was done for single layer coils. The resultant measured impedance characteristics are presented in Fig.10. The resonances in this case are shifted towards higher frequency due to lower capacitances.
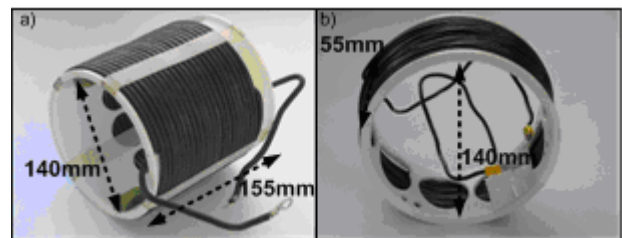
Fig. 9. *Single layer coil of LISN winded by a) SILFLEX stranded wire - 22turns, b) enameled wire - 18 turns.*

The stray capacitance has been calculated using FEM and the results are put in Table 2.

The total capacitance is much lower for single layer, because of lower inter-turn capacitances and there are no capacitances between layers.

Fig. 7. *Magnetic flux density for double layer coils winding enameled wire for: a) 9 kHz, b) 30 MHz.*

The impedance Z_{EUT} characteristic of LISN, seen from EUT's port (a1-GP or a2-GP) are given in Fig.11b. Only the characteristic for coil made if enameled wire is complies with Fig. 2 (CISPR 16-1).

Table 2: *Capacitances in the single layer coils*

	wire	
	SILFLEX	enameled
Number of turns	22	18
Inter-turn capacitance	35.8 pF	64.4 pF
Total coil capacitance	1.71 pF	4.1 pF
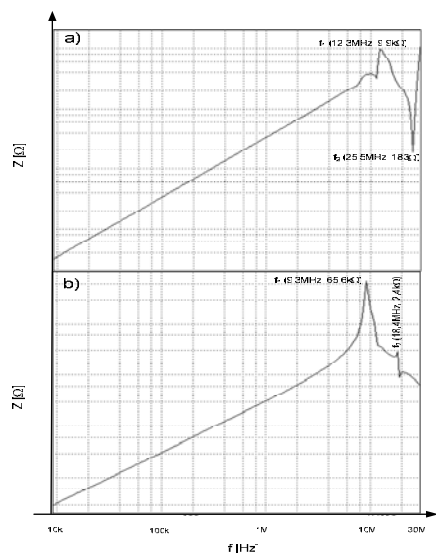
Fig.10. *Measured impedance characteristic of LISN single layer coils winded with: a) SILFLEX strand wire, b) enameled wire.*
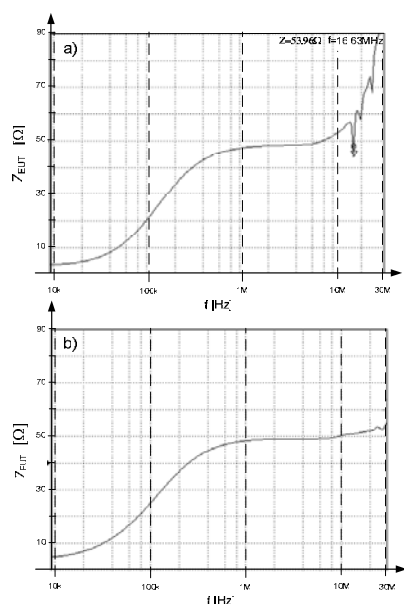
Fig. 11. *Impedance characteristic seen from EUT's port for single layer coils winded with: a) SILFLEX stranded wire, b) enameled wire.*

3. CONCLUSION

1. The research proved that single layer coil is much better candidate than double layer one for LISN (Line Impedance Stabilization Network). This is because of bad influence of interlayer capacitances (Table 2). In the double layer coil the total capacitance is much higher. It is because not only of the capacitance between turns in one layer is higher but also capacitance between turns of different layers has higher value.

2. For proper operation of LISN not only design of coil is important but also such factors as: i) casing construction ii) position of EUT connector (the EUT connector should be mounted near the top of front panel), iii) spacing between the ground plane and the bottom of LISN (it should be minimal).

3. The future works should embrace the following problems: i) broader analysis of construction influence on parameters of the EMC- coil (its length, diameter, number of turns, type of wire and also shape of the whole of the coil), ii) possibility of coil impedance shaping by additional external circuits, iii) influence of parasitic parameters of LISN's elements on Z_{EUT} impedance, iv) the influence of tolerance of Z_{EUT} impedance characteristic on the measurements results of conducted emission (using LISN).

4. REFERENCES

[1] http://www.cemarking.net
[2] M.I Montrose, E. M Nakauchi, „*Testing for EMC Compliance. Approaches and Techniques*", IEEE press, 2004.
[3] CISPR 16-1, „*Specification for radio disturbance and immunity measuring apparatus and methods. Radio disturbance and immunity measuring apparatus*"
[4] CISPR 16-2*, „Specification for radio disturbance and immunity measuring apparatus and methods - Part 2-2: Methods of measurement of disturbances and immunity - Measurement of disturbance power*"
[5] Schaffner-Chase EMC Ltd, „*Calibration and Use of Artificial Mains Networks and Absorbing Clamps*", 1999.
[6] L. Yang et al, „*Modeling and Characterization of a 1KW CCM PFC Converter for Conducted EMI Prediction*",0-7803-8269-2/04 IEEE 2004.

ENERGY CONVERSION IN LUNDELL ALTERNATOR SYSTEMS

Dan Stoia, Mihai Cernat, Adrian Mailat, and Dănuț Ilea

"Transilvania" University of Braşov, Faculty of Electrical Engineering and Computer Science
Brasov, Romania

Abstract: *A Lundell alternator for automobiles is in fact an electromechanical energy conversion device. A relation is derived for the stored magnetic energy as a function of machine reactances, field and terminal voltages.*

The paper focuses mainly on the analysis of Lundell alternator systems along with the load dynamic behaviour and is achieved in terms of energy conversion in accord with the operating mode, with both passive (diode) rectifier and with active rectifiers. The paper offers a useful instrument for Lundell alternator system design and operating stability investigation.

Keywords: *vehicle alternator, Lundell machine, magnetic energy, diode rectifier, switched mode rectifier, load matching.*

1. INTRODUCTION

Automotive electrical power requirements are rising rapidly, and this rise is motivating the development of both higher-power and higher-voltage electrical systems and components. The rising power requirements pose a particular challenge for alternator design because the inherent power limitations of the conventional Lundell alternator are rapidly being approached.

The Lundell or claw-pole alternator is a wound-field synchronous machine whose rotor consists of a pair of stamped pole pieces (claw poles) secured around a cylindrical field winding. The field winding is fed from the stator via a pair of slip rings. The stator is wound in a three-phase configuration and a full-bridge diode rectifier is traditionally connected at the machine output. Regulating the field current controls the alternator system output voltage. A relatively long field time constant and a high armature leakage reactance are characteristic of this type of alternator and tend to determinate its electrical performance.

The continuous increase in power requirements is pushing the limits of conventional automotive power generation and control technology. In this context, a 42 V automotive electrical system was adopted and the diode rectifier has been replaced with a controllable rectifier along with a special load-matching control technique [1]. The new design allows higher levels of output power and efficiency to be achieved as compared to conventional designs.

This paper examines some aspects related to the automotive alternator's (Lundell machine) dynamic behaviour based on constructional and functional similarities existing between this machine and large industrial synchronous machines [2, 3].

The study makes use of the theory and well-known fundamental relations that describe the operation and parameters that are specific to large synchronous generators while seeking analogies to quantities and parameters that are specific to Lundell alternator's operating mode and trying to identify functional aspects that are similar to those of their larger counterparts.

The study focuses on the analysis of the Lundell alternator system along with load system dynamic behaviour and is achieved in terms of magnetic and mechanical (kinetic) energy variation and storage in accord with the Lundell alternator system operating mode. A Lundell machine, being an electromechanical energy conversion device, contains both mechanical and magnetic energy storage elements.

The mechanical energy storage medium is the kinetic energy stored in the rotational inertia of the machine rotor and the coupling with the vehicle engine.

The magnetic energy storage medium is the internal rotating magnetic field, which links the armature and field windings of the machine. The magnitudes of stored kinetic energy and stored magnetic energy are an important factor in the determining the alternator system dynamic performance and its stability.

2. MAGNETIC ENERGY CONVERSION AND DISTRIBUTION

Assuming magnetic linearity, the magnetic energy storage in a synchronous machine is given by the following expression [4, 5]:

$$W_m = \frac{1}{2}\left(\frac{3}{2}\Psi_d i_d + \frac{3}{2}\Psi_q i_q + \Psi_f i_f\right). \tag{1}$$

The relations between the (d, q) flux linkage and currents are:

$$\Psi_d = L_d\, i_d + L_{af}\, i_f, \tag{2}$$

$$\Psi_q = L_q\, i_q, \tag{3}$$

$$\Psi_f = \frac{3}{2}L_{af}\, i_d + L_{ff}\, i_f. \tag{4}$$

Substituting Eq. (2) in Eq. (4) gives:

$$\Psi_f = \frac{3}{2}\frac{L_{af}}{L_d}\Psi_d + L_{ff}\left(1 - \frac{3}{2}\frac{L_{af}}{L_{ff}}\frac{L_{af}}{L_d}\right)i_f. \tag{5}$$

The leakage coefficient between f and d axes σ is defined as:

$$\sigma = 1 - \frac{3}{2}\frac{L_{af}}{L_{ff}}\frac{L_{af}}{L_d}. \tag{6}$$

The leakage coefficient takes into account magnetic circuit saturation of the machine produced by the field current during energy conversion.

Replacing expression (6) in equation (2) yields:

$$W_m = \frac{1}{2}\left(\frac{3}{2}\frac{\Psi_d^2}{L_d} + \frac{3}{2}\frac{\Psi_q^2}{L_q} + \sigma L_{ff}\, i_f^2\right). \tag{7}$$

The field current i_f may be expressed in terms of the "internal" field voltage (the back EMF) E_f:

$$i_f = \frac{\sqrt{2}\, E_f}{\omega L_{af}}. \tag{8}$$

Consequently, relation (7) may be rewritten as:

$$W_m = \frac{3}{4}\left(\frac{\Psi_d^2}{L_d} + \frac{\Psi_q^2}{L_q} + \frac{2\,\sigma}{1-\sigma}\frac{1}{L_d}\frac{E_f^2}{\omega^2}\right). \qquad (9)$$

Using the definition of the machine reactances, relation (7) becomes:

$$W_m = \frac{3}{4\,\omega}\left(\frac{(\omega\,\Psi_d)^2}{X_d} + \frac{(\omega\,\Psi_q)^2}{X_q} + \frac{2\,\sigma}{1-\sigma}\frac{1}{X_d}E_f^2\right) \quad (10)$$

For the case of balanced operation assuming negligible armature resistance, the following expressions may be written for the terms $\omega_0\Psi_d$ and $\omega_0\Psi_q$, respectively

$$\omega\,\Psi_d = \sqrt{2}\,U\cos\theta = E_f + X_d\,I_d$$
$$\omega\,\Psi_q = -\sqrt{2}\,U\sin\theta = X_q\,I_q \qquad (11\ a,\ b)$$

where U is the rms value of the armature voltage (the output voltage) and θ is the load angle.

Substituting relations (11) into equation (10) and rearranging, it results:

$$W_m = \frac{3}{2}\frac{1}{\omega X_d}\left[U^2 + U^2\left(\frac{X_d}{X_q}-1\right)\sin^2\theta + \frac{\sigma}{1-\sigma}E_f^2\right] \quad (12)$$

Relation (12) gives the magnetic energy storage of a Lundell alternator as a function of machine parameters: machine reactances X_d and X_q, the field voltage (the back EMF) E_f, the output voltage U, and the load angle θ.

3. MAGNETIC AND KINETIC ENERGY STORAGE IN VARIABLE OPERATING MODES

An interesting expression for the rate of change of magnetic energy storage can be obtained by working directly with the original definition of W_m given by relation (7).

The resulting value of dW_m/dt will include the rate of change of magnetic energy stored in the Lundell alternator. Because of the assumed magnetic linearity of the machine, it follows that:

$$\frac{d\,W_m}{d\,t} = \frac{3}{2}i_d\frac{d\,\Psi_d}{d\,t} + \frac{3}{2}i_q\frac{d\,\Psi_q}{d\,t} + i_f\frac{d\,\Psi_f}{d\,t}. \qquad (13)$$

For the case of constant armature voltage, negligible armature resistance and balanced operation from relation (13) it follows:

$$\frac{d\,\Psi_d}{d\,t} = \Psi_q\frac{d\,\theta}{d\,t};\qquad \frac{d\,\Psi_q}{d\,t} = -\Psi_d\frac{d\,\theta}{d\,t}. \qquad (14a,\ b)$$

Substituting relations (14) into equation (13) gives:

$$\frac{d\,W_m}{d\,t} = \frac{3p}{2}\left(\Psi_q\,i_d - \Psi_d\,i_q\right)\frac{d\,\theta}{d\,t} + i_f\frac{d\,\Psi_f}{d\,t}, \quad (15)$$

where p is the pole pair number.

The expression of the electromagnetic torque is:

$$\tau_e = \frac{3p}{2}\left(\Psi_q\,i_d - \Psi_d\,i_q\right). \qquad (16)$$

For the assumed armature current conventions, the value of τ_e is positive for generator action. Thus substituting relation (16) into the above gives:

$$\frac{d\,W_m}{d\,t} = \tau_e\frac{d\,\theta}{d\,t} + i_f\frac{d\,\Psi_f}{d\,t}, \qquad (17)$$

The first term of Eq. (17) represents the alternator input power, converted and magnetically stored, in terms of rotor speed, which finally results in the variation of the armature reaction (magnetizing or demagnetizing) field.

The electric power absorbed and magnetically stored by the field winding is expressed by the second term.

Consequently, Eq. (17) describes the alternator's input power (electrical and mechanical) contribution to magnetic energy storage for variable operating modes.

Substituting Eqs. (11) in Eq. (16), with

$$I_q = I\cos\psi,\qquad I_d = I\sin\psi, \qquad (18\ a,\ b)$$

where ψ is the power angle (between the phasor of the back EMF E_f and that of the phase current I), the expression of τ_e can be written as:

$$\tau_e = \frac{3}{\omega}\left[E_f\,I\cos\psi + \left(X_q - X_d\right)I_d\,I_q\right]. \qquad (19)$$

By substituting of expressions (18) in relation (19) it results:

$$\tau_e = \frac{3}{\omega}\left[E_f\,I\cos\psi + \frac{I^2}{2}\left(X_q - X_d\right)\sin 2\psi\right]. \quad (20)$$

Relation (20) gives the electromagnetic torque of a Lundell alternator as a function of machine parameters: machine reactances X_d and X_q, the field voltage E_f, the load current I, and the power angle ψ. The first term represents the field torque (synchronous torque) and the second one represents the reluctance torque.

The kinetic energy in the alternator's rotor can be written as:

$$W_K = \frac{1}{2}J\omega^2,\qquad \frac{d\,W_K}{d\,t} = J\omega\frac{d\,\omega}{d\,t}, \qquad (21\ a,\ b)$$

where

$$\omega = \omega_0 + \frac{d\,\theta}{d\,t};\qquad \frac{d\,\omega}{d\,t} = \frac{d^2\,\theta}{d\,t^2}, \qquad (22\ a,\ b)$$

where ω represents the variable cruising speed and ω_0 the cut-in speed of the Lundell machine; J is the inertia moment of the rotor.

The dynamic torque can be expressed as:

$$\tau_m - \tau_e = J\frac{d^2\,\theta}{d\,t^2} + D\frac{d\,\theta}{d\,t}. \qquad (23)$$

where D is the viscous friction coefficient. The last term take in acount all the loses which are proportional to the speed.

Finally, the kinetic energy variation is:

$$\frac{d\,W_k}{d\,t} = \left(\tau_m - \tau_e\right)\left(\omega_0 + \frac{d\,\theta}{d\,t}\right). \qquad (24)$$

Consequently, a power balance equation for the machine can be written as:

$$P_e = P_m - \frac{d\,W_K}{d\,t} - \frac{d\,W_m}{d\,t}, \qquad (25)$$

where P_e is the electrical power output:

$$P_e = \tau_e\,\omega_0 \qquad (26)$$

and P_m is the mechanical power input:

$$P_m = \tau_m\left(\omega_0 + \frac{d\,\theta}{d\,t}\right). \qquad (27)$$

Relation (27) can be described in terms of an overall power distribution diagram, where the term $\left(\omega_0 + d\,\theta/d\,t\right)$ represents the instantaneous value of the rotor velocity.

4. OUTPUT POWER OF LUNDELL ALTERNATOR-RECTIFIER SYSTEM

Neglecting the stator winding resistance, the output power of the Lundell alternator is given by:

$$P = 3\left[\frac{U\,E_f}{X_d}\sin\theta + \frac{U^2}{2}\left(\frac{1}{X_q} - \frac{1}{X_d}\right)\sin 2\theta\right]. \quad (28)$$

Expressing the output power as a function of the load current I we obtain:

$$P = 3\,E_f\,I\cos\psi + \frac{3}{2}\left(X_d - X_q\right)I^2\sin 2\psi. \quad (29)$$

with

$$\psi = \theta + \varphi \quad (30)$$

where φ is the phase angle, between the voltage and the current.

It can be seen that the output power at a given speed and with a given phase voltage can be controlled only by controlling the back EMF (through the field current control and the power angle ψ). The output power is maximized when the field current is maximized and the load angle is optimum.

Both electric and magnetic loadings, for a given machine volume, are depending on the power angle ψ. When the power angle ψ increases, the electric loading increases as well, whilst magnetic loading decreases, and as a result the machine operation converts from "saturation limited region" to "thermally limited region".

If the alternator is connected to a passive (diode) rectifier the system's the load angle cannot be controlled independently because the diodes will force the phase voltage to be in phase with the current, so

$$\theta = \psi. \quad (31)$$

Therefore, in this system, the output power cannot be increased further without increasing the speed after the field current reaches its limit and the power angle ψ is within the limits of a good energy conversion.

For stable operation, the load angle θ may take values between $\theta=30º$ and $\theta=80º$.

When the alternator is connected to a passive rectifier (the currently used system) only the field current is controlled, so that, at constant voltage a specific output curve will be obtained namely output current I versus speed n. Thei curve is given by equation [2]:

$$I(n) = \sqrt{1 - \left(\frac{n_0}{n}\right)^2}\,I_f'\,\frac{k_\beta}{c_d + \sigma_1} \quad (32)$$

where the following notations have been used

I -   the output DC current of the rectifier;
n -   the alternator's speed;
n_0 -   the alternators cut in (idle) speed;
i_f' -   the field current referred to stator;
k_β -   the pole coverage factor (depending of the rotor claw geometry;
c_d -   the form factor of the machine d-axis;
σ_1 -   the leakage coefficient (depending of the stator slots geometry).

In this system, the output power will be maximum at a specific speed, at full field current and for a load angle φ around $\pi/2$. It becomes obvious that the alternator will deliver maximum power over a wide speed range, when energy conversion is optimized by controlling the power angle ψ. By replacing the passive rectifier with a controlled rectifier (SMR) energy conversion is optimized and the alternator capable of delivering maximum power over a wide speed range.

The new system employs a Lundell machine model which introduces a total phase (reaction) inductance, independent of rotor position but depending on the power angle ψ [8].

The total phase inductance will be [9]:

$$L_a = \sqrt{\left(L_{a1} - \frac{1}{2}L_{a2}\cos(2\psi)\right)^2 + \left(\frac{1}{2}L_{a2}\sin(2\psi)\right)^2} \quad (33)$$

where the following notations have been used

L_{a1} -   stator self-inductance;
L_{a2} -   stator-to-stator mutual inductance;

Notably, the two components of the total inductance vary with rotor position. With regard to this, at $\psi=0$ the total inductance will be:

$$L_a\Big|_{\psi=0} = L_{a1} - \frac{1}{2}L_{a2} = L_d \quad (34)$$

And at $\psi = \pi/2$, respectively:

$$L_a\Big|_{\psi=\pi/2} = L_{a1} + \frac{1}{2}L_{a2} = L_q \quad (35)$$

which signifies that the total inductance will be equal with either the q-axis inductance (Eq. 34), and with the d-axis inductance (Eq. 35), respectively, when the stator reaction flux is in phase with the q-axis current and with the d-axis current, respectively. The L_d şi L_q inductances are independent of rotor position.

This allows to define the output impedance of the machine as:

$$Z(\psi) = \sqrt{\left(R_s\right)^2 + \left(\omega\,L_s\right)^2} \quad (36)$$

with

$$L_s = L_{a1} - \frac{1}{2}L_{a2}\cos(2\psi) \quad (37)$$

$$R_s = r_s + \frac{1}{2}L_{a2}\sin(2\psi) \quad (38)$$

where r_s is the ohmic resistance of the stator winding.

Consequently, the output power of a conventional alternator-rectifier system connected to a DC-side constant voltage U_0 (an ideal voltage source) load can be expressed as:

$$P_{out} = \frac{3\,U_0}{\pi}\frac{\sqrt{E_f^2 - \frac{2}{\pi}U_0^2}}{Z_s} \quad (39)$$

Lundell alternators are characterized by a large value of the armature (stator) winding synchronous inductance. This determines a high output impedance of the system, depending on speed and current, as well as high DC-side resistance which, in turn, requires a high stator back EMF in order to ensure a given output current. Consequently, the alternator's power will be maximum at a given speed for a single output voltage only – the „load matching" voltage.

By maximizing the output power (Eq. 37) with respect to the output voltage U_0, we obtain the "load matching" voltage:

$$U_0 = \frac{\pi E_f}{2\sqrt{2}} \qquad (40)$$

with

$$E_f = \omega L_{af} I_f \qquad (41)$$

where L_{af} is mutual inductance between the armature winding and the field winding.

For this case, the average output current is:

$$I_{med\ x} = \frac{3 \omega L_{af} I_f}{\sqrt{2}\ \pi Z_s} \qquad (42)$$

The maximum power at „load matching" is given by:

$$P_{out\ max\ x} = \frac{3}{4\pi} \frac{(\omega Laf)^2}{w_f} (w_f I_f)^2 \frac{1}{Z_s^2} \qquad (43)$$

From Eqs. (40)-(43), it can be seen that the new system must be capable to ensure both field current and output voltage control. Furthermore, it should be noted that for „load matching" conditions, if the alternator is operated at cruising speed, the load resistance of the system increases due to voltage increase which will result in equalling the inductive component with the resistive component of the output impedance.

$$\omega L_s \approx R_s + R_{SMR} \qquad (44)$$

where the equivalent (variable) resistance R_{SMR} of the switched mode rectifier (SMR) can be written as [9]:

$$R_{SMR} = \frac{U_{01}^2 R_s + U_{01}\sqrt{(\omega L_s)^2 (U_f^2 - U_{01}^2) + R_s U_f^2}}{U_f^2 - U_{01}^2} \qquad (45)$$

with

$$U_{01} = \frac{4}{\pi}\left(\frac{U_0}{2} + U_d\right) \qquad (46)$$

where U_d is the diode forward voltage.
Hence the power angle results as:

$$\psi = \tan^{-1}\frac{\omega L_s}{R_s + R_{SMR}} \qquad (47)$$

Consequently, in the case of load matching, the alternator becomes electromagnetically isotropic and the magnetic energy stored in the machine will be:

$$W_m = \frac{3}{2}\frac{1}{\omega L_s}\left(U_x^2 + \frac{\sigma}{1-\sigma}E_f^2\right) \qquad (48)$$

where U_x is the machine output voltage for matched load condition.

The output power becomes

$$P_{out} = \frac{3}{\pi}\frac{U_0 E_f}{\sqrt{(\omega L_s)^2 + (R_s + R_{SMR})^2}} \qquad (49)$$

With the new system, energy conversion efficiency will increase by around 10% in 14 V alternators, whereas 42 V machines will exhibit around 20% increase in efficiency in currently used power supply systems.
The new system will consequently become more efficient at higher voltages (50 V-52 V).

In SMR-alternator systems, functional efficiency at idle speed is very high when compared with alternator systems using conventional diode rectifiers. The modulation strategy employed in SMR-alternator systems for each phase separately determines the reduction of the power angle ψ, which, in turn, will determine the increase of the output

power even at values below the idle speed of conventional alternator systems. Since this operating mode requires maximum m.m.f., the air gap magnetic flux density will reach its maximum as well. As the output voltage decreases, the equivalent resistance of the SMR will decrease too, which in turn, will determine the decrease of the power angle causing machine demagnetization and reduction of air gap flux density, respectively. Consequently, the stator current will increase, while the back EMF is being controlled through the field current.

The increase of both stator and field currents determine the reduction of the machine demagnetization field. Hence, the average power of a SMR-alternator system that can be obtained below the idle speed point of a conventional alternator will be expressed as

$$P_{out} = 3\left(E_f I\frac{\cos\psi}{2}\right) - 3\left(R_s \frac{I^2}{2}\right) \qquad (50)$$

To increase air gap flux density, SMR Lundell machines can include specific constructional details such as reduced air gap radiuses with the benefit of smaller moments of inertia and lower costs. The machine's equation of motion (23) can also be written as:

$$\frac{d\omega}{dt} = -\frac{D}{pJ}\omega + \frac{\tau_m - \tau_e}{p^2 J} \qquad (51)$$

The model of the SMR Lundell alternator is given by [2]:

$$\underline{U} = \underline{U}_{e0} - \left[r_s + \frac{3}{2}\omega L_{a2}\sin(2\psi)\right]\underline{I} -$$
$$- j\left[\omega L_\sigma + \omega L_{a1} - \frac{3}{2}\omega L_{a2}\cos(2\psi)\right]\underline{I} \qquad (52)$$

5. CONCLUSIONS

The magnetic energy stored in a Lundell alternator may be presented in terms of electromagnetic energy parameters of the machine.

Variations in stored magnetic energy result from electrical power flow into the machine field winding, when the field is varied. The output power can be controlled by controlling the back EMF and the power angle ψ.

By contrast to large industrial synchronous machines, in automotive claw-pole alternators, the amount of stored kinetic energy must be much smaller than the amount of stored magnetic energy ensuring a small mechanical time constant. For that reason, the inertia of automotive alternators is very small.

In Lundell alternator systems with active rectifier (SMR system) at cruising speeds where the maximum power is delivered at the load-matched condition by increasing the voltage and the equivalent SMR ohmic resistance respectively. The efficiency of power conversion improves by 10%-20%.

At idle speed, power conversion can be improved by controlling the power angle and the field current, thus varying the armature reaction by decreasing the equivalent SMR ohmic resistance..

The study provides a useful instrument for Lundell alternator system design and for the investigation of magnetic and thermal operating stability. In this way, the Lundell alternator with SMR system can be designed with high power density of about 12 000 kW/m³. An electromagnetic model more accurate was proposed, the flux linkage, the voltage, the

mutual inductance and the motion equation taken into consideration. Thus the optimal design of Lundell alternator can be made by only taking into account the optimal magnetic-thermal value of the power angle ψ at which the magnetic loading of the field winding leads the electric one.

The developments described here address some of the challenges in automotive power generation and control, for introduction of high-voltage electricaö systems in automobiles.

6. REFERENCES

[1] D.J. Perrault, V. Caliskan, "Automotive Power Generation and Control," *IEEE Trans. on Power Electron.*, Vol. 19, No. 3, May 2004, pp. 618-630.

[2] * * * *"Automotive Electric/Electronic Systems,"* Robert Bosch GmbH, Stuttgart, Germany, 1988.

[3] Th. H. Einstein, "Magnetic Energy Storage in Synchronous Machines," *IEEE Trans. on Power Apparatus and Systems*, Volume PAS-92, Issue 1, Jan. 1973, pp. 346 – 351.

[4] H.E. Jordan, *"Energy-Efficient Electrical Motors and Their Applications,."* New York, Plenum, 1994.

[5] Prabha Kundur, *"Power Stability and Control,"* Mc Graw-Hill Inc., 1994.

[6] J. Rivas, D.J. Perreault, and Th. Keim, "Performance Improvement of Alternators with Switched Mode Rectifiers," *IEEE Trans. on Energy Conversion*, Vol. 19, No. 3, September 2004, pp. 561-568.

[7] A.R. Prased, P.D. Ziogas, and S. Manias, "Active power factor correction technique for three-phase diode rectifiers," *IEEE Trans. on Power Electronics*, Vol. 6, Jan. 1991, pp. 83-92.

[8] G. Dajaku, D. Gerling, "The correct analytical expression for the phase inductance of salient pole machines," *Proceedings EMD*'07, *Antalya*, 2007, pp. 992-996.

[9] V. Caliskan, D.J. Perreault, T.M. Jahns, and J.G. Kassakian, *"Analysis of Three-Phase Rectifiers with Constant-Voltage Loads,"* *IEEE Trans. on Circuits and Systems – I: Fundamental Theory and Applications,* vol. 50, no. 9, Sept. 2003, pp. 1220-1226.

PARAMETRIC PSPICE MODEL OF A PEM FUEL CELL*

Goce L. Arsov

*SS "Cyril and Methodius" University, Faculty of Electrical Engineering and Information Technologies, Skopje,
Republic of Macedonia*

Abstract: *This paper presents a generalized circuit model for a PEM fuel cell that can be used for design and analysis of fuel cell power systems. The PSpice-based model uses bipolar junction transistors and resistors available in the PSpice library. The model includes the phenomena like activation polarization, ohmic polarization and concentration polarization (mass transport effect) present in a PEM fuel cell. Using the parametric modeling the model of a basic fuel cell can be extended to a fuel cell stack. The static and dynamic characteristics obtained through simulation are compared with some experimental results, given in the literature, obtained on a commercial PEM fuel cell module.*
Key Words: *Fuel Cell/Modeling/Simulation/PSpice.*

1. INTRODUCTION

Today, fuel cells of various types have emerged as a promising alternative sources of "clean energy" for applications ranging from automotive industry to residential and commercial installations. This has created a need for a class of specialized power converters geared to interface between the fuel cell device and the end-user appliance, often as a battery charger. Specifications for power conversion equipment depend on the fuel cell's physical properties and manufacturing economics.

The cells' output voltage is dependent on the load. So, there is a need to model the fuel cell for optimizing its performance and also for developing fuel cell power converters for various applications.

The proton exchange membrane fuel cell (PEMFC) has been considered as a promising kind of fuel cell during the last 15 years because of its low working temperature, compactness, and easy and safe operational modes. The proton exchange membrane (PEM) fuel cell is very simple and uses a polymer (membrane) as the solid electrolyte and a platinum catalyst.

A fuel cell stack is composed of several fuel cells connected in series separated by bipolar plates and provides fairly large power at higher voltage and current levels.

Up to now different type of models of PEM fuel cell were proposed.

Almost all models proposed for PEMFC consist of mathematical equations and are not of much use in power converter/system simulation and analysis [1]–[4]. Some other PEMFC models use MATLAB–SIMULINK [5] and PSpice [6], but they are still mathematical in nature. The models include several chemical phenomena present in the fuel cell and hence are complex. Some of the physical variables like pressure and hydrogen input are constrained in a commercial fuel cell module and this makes the fuel cell operation simpler. This also allows the use of a simpler electric circuit model useful to a power electronics designer.

Among the various proposed models the electronic circuit model for a *PEM* fuel cell proposed in [7] is very suitable for this purpose.

Unfortunately, this model suffers from the need to define its parameters for every individual case where fuel cell stacks are used.

The aim of this paper is to extend the model proposed in [7] to a generalized one for a *PEM* fuel cell that can be used for design and analysis of fuel cell power systems with different voltage and current capabilities.

2. I/V CHARACTERISTICS OF A PEM FUEL CELL

Proton exchange membrane fuel cells combine hydrogen and oxygen over a platinum catalyst to produce electrochemical energy with water as the byproduct. Fig. 1 shows the *I–V* characteristic of a typical single cell operating at room temperature and normal air pressure [8]. The variation of the individual cell voltage is found from the maximum cell voltage (or EMF) and the various voltage drops (losses). Multiple factors contribute to the irreversible losses (voltage drop) in an actual fuel cell that cause the cell voltage to be less than its ideal potential [8]. The losses, which are also called polarization, originate primarily from three sources: (a) activation polarization [9], (b) ohmic polarization, and (c) concentration (mass transport) polarization [9], [10]. Each of these is associated with a voltage drop and is dominant in a particular region of current density (low, medium, or high). Fig. 1 shows the different regions and the corresponding polarization effects. The ideal voltage is the maximum voltage that each cell in the stack can produce at a given temperature with the partial pressure of the reactants and products known. For the PEMFC, where pure hydrogen and air are used, the ideal voltage can be calculated based on Gibbs free energy and it is equal to 1.2V at 25°C and atmospheric pressure for a single fuel cell [8]. A higher output voltage is obtained by connecting several cells in series. The area of the cell decides the output current.
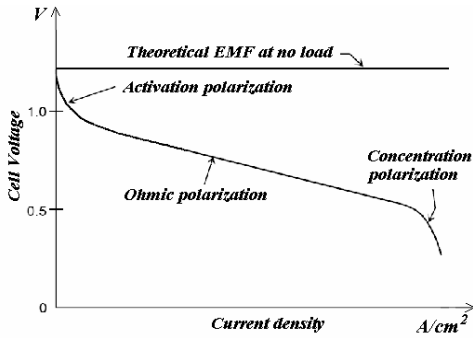
Fig. 1. *I–V characteristic of a single PEM fuel cell.*

The activation polarization loss (dominant at low current density) is present when the rate of the electrochemical reaction at an electrode surface is controlled by sluggish electrode kinetics [9]. Activation losses increase as the current increases. The activation losses can be obtained by Tafel equation [8]:

$$V_A = A \ln\left(\frac{I}{I_o}\right) \qquad (1)$$

where A is the constant, V_A the over-voltage, I the current density, and I_o is the current density at which the voltage begins to drop.

The ohmic region can be described by:

$$V_R = RI \qquad (2)$$

where I is the current density through the cell and R is the total ohmic resistance due to the resistance of the polymer electrolyte membrane to the ions and the resistance of imperfect electrodes [8].

The concentration polarization relates to the change in the concentration of the reactants at the surface of the electrodes as the fuel (hydrogen) is used. This loss becomes significant at higher currents when the fuel and oxidant are used at higher rates and the concentration in the gas channel is at a minimum. In general, the concentration polarization region can be described by [9], [10]:

$$V_C = m I_m e^{n I_m} \qquad (3)$$

where m and n are mass transfer parameters, and I_m is the point where the I–V characteristic starts to deviate from being linear (start of mass transport action).

So, the overall dependence between the voltage and the current density of a fuel cell can be expressed as:

$$V_o = E - V_A - V_R - V_C \qquad (4)$$

where E is the ideal emf of the fuel cell at no load. It should be noted that the parameters used in Eqs. (1) - (4) are dependent on the pressure and temperature in the cell.

The fuel cell can be catastrophically damaged if overloaded. Thus, when designing the fuel cell system the current rating of the cell itself must be taken into account. One way to anticipate the fuel cell current limits is through computer simulation of the fuel cell system using the appropriate simulation model of the cell itself.

3. CIRCUIT MODEL OF PEM FUEL CELL

In [7] a PSpice model for commercial fuel cell has been proposed (Fig. 2). The complete model is developed by modeling the three different operating regions using elements from the PSpice simulation library.
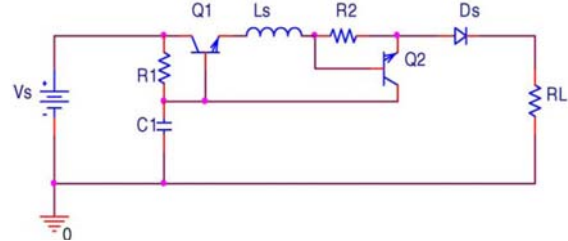

Fig. 2. *PSpice circuit model for a PEM fuel cell module.*

In the model proposed, a diode is used to model the activation polarization of the fuel cell. Actually, the similarity can be seen by comparing Eq. (1) and the diode equation:

$$V_D = n V_T \ln\left(\frac{I_D}{I_s}\right) \qquad (5)$$

where V_D is the voltage across the diode and I_D is the current through the diode, n the empirical constant having values between 1 and 2, I_s the reverse saturation current, and V_T so called "volt-equivalent of temperature".

So, it is reasonable to use a diode to model the activation polarization region in a fuel cell. In the simulation package PSpice, the diode model can be adjusted to match the I–V characteristics of a fuel cell stack by choosing suitable values for the following parameters: Is (saturation current), Rs (parasitic resistance) and N (emission coefficient) [11]. Among the several parameters, N affects the shape of the characteristic most and it has to be chosen to match the I–V characteristics of the diode and the fuel cell stack. In [7] the diode characteristics matches that of the chosen fuel cell for N=80 and Is = 0.02 A. As these values have no real values the proposed model is useful only for simulation purposes but not for realization of fuel cell simulator.

The ohmic polarization can be modeled using a resistor. Instead of using a separate resistor, the "parasitic resistance (R_s)" in the diode is used for this purpose.

To model the concentration, or mass transport overvoltage, a "current limiting circuit" is used. In Fig. 2, the current limiting circuit is composed of two BJTs Q_1 and Q_2 and the current sensing resistor R_2. When, the current through R2 exceeds a set limit, Q_2 starts conducting and reduces the base voltage of Q_1. As a result, the emitter voltage of Q_1 (output voltage) will decrease at an exponential rate similar to Eq. (3). The transistors Q_1 and Q_2 are assumed to be identical with current gain β and base-emitter voltage V_{BE}. Using the basic relations for the voltage to current dependences in a bipolar transistor, assuming that the BJTs have identical parameters and that $\beta \gg 1$, $R_2 \ll R_I$ and $V_{C1,E2} \gg V_{BE}$ [7], the following equation can be written:

$$V_{C_1 E_2} = R_1 I_{CS} e^{R_2 I_O / V_T} \qquad (6)$$

This equation is very similar to (3).

From the above analysis it becomes clear that by appropriate determination of the circuit parameters, the

circuit model shown in Fig. 2 can be used for simulation of the *I–V* characteristics of a specified fuel cell stack. If the characteristic of a specified fuel cell is known or can be measured than the model parameters can be calculated using the method described in [7].

It is shown in [7] that the dynamic response of a fuel cell can be modeled using a capacitor (C_1) and an inductor (L_s) as shown in Fig. 2.

4. PARAMETRIC MODEL OF A PEM FUEL CELL STACK

The described model of PEMFC presented in [7] can give us a good basis for simulation of static and dynamic characteristics of specified fuel cell or fuel cell stack. The investigation of the adaptability of this model has shown two main problems with its application:

1. As the model parameters are determined for every single module, the parameter extraction should be repeated every time when we change the area of the cell or the number of cells in a cell stack;

2. Considering the fact that the transistor parameters are constant (according to the authors of [7] only the transistor area should be changed depending on the current capability of the cell) this model is non applicable for fuel cells where the ideal emf is less than 10 V. (Even more, this model is unacceptable for modeling the single fuel cell where the ideal emf is around 1.2 V.)

These two specified problems can be overcome if some of the model parameters are made dependent on the cell area (fuel cell current capability) and cell ideal emf (number of single cells connected in series in the stack).

To overcome the problem of the voltage drop between the base and the emitter of the BJTs we should introduce the emitter emission coefficient N_f and make that it changes with the cell area and cell ideal emf. The current capability of the cell can be modeled using the parameter proportional with the actual cell area. This parameter should be incorporated in the diode model and in the BJTs models as well.

To match the changes in the concentration polarization region it is, also, necessary to make corresponding adaptations for the resistors R_1 and R_2.

We should note also that, because we change the diode area to match the diode characteristics to the cell current capabilities, we also have to change, in an appropriate way, the diode reverse saturation current.

All these changes in the fuel cell PSpice model characteristics were enabled when the command **.PARAM** was included in the PSpice program package, as well as with the possibility that some model parameters can be defined with mathematical expressions.

We have made modifications of the PSpice fuel cell model presented in [7] by introducing 2 parameters: the *first* – proportional to the number of individual cells connected in series, (or in other words, proportional to the ideal *emf* of the stack to ideal *emf* of a single fuel cell ratio), and the *second* – proportional to the area of the fuel cell (the initial area has been taken to be 1cm^2).

Thus, once the model parameters are extracted for a single fuel cell, as explained in [7], they can be extended to any fuel cell stack module, of the same type, by using parametric modeling incorporated in PSpice simulation package in the following manner:

a) For the diode –

$$n = n_o \cdot m \tag{7}$$

$$A_D = A_{D_o} \cdot k / m \tag{8}$$

$$I_S = I_{S_o} \cdot m \tag{9}$$

where n is the diode emission coefficient, A_D is the diode area and I_S is the diode reverse saturation current;

b) For the transistors –

$$A_Q = A_{Q_o} \cdot k \tag{10}$$

$$n_F = n_{F_o} \cdot m \tag{11}$$

where A_Q is the transistor area and n_F emitter emission coefficient;

c) For the resistors –

$$R_1 = R_{1_o} \cdot m / k \tag{12}$$

$$R_2 = R_{2_o} \cdot m / k \tag{13}$$

d) For the ideal ***emf*** of the fuel cell stack –

$$E = E_o \cdot m \tag{14}$$

e) For the capacitor –

$$C = C_o \cdot k \cdot m; \tag{15}$$

f) For the inductor –

$$L = L_o \cdot m / (k \cdot k^{1/4}) \tag{16}$$

In these equations m is the parameter dependent on the number of fuel cells connected in series (voltage capabilities of the cell), k is proportional to the cell area (current capabilities), and the subscript "o" indicates the initial parameters obtained for the single fuel cell at specified temperature and pressure.

5. SIMULATION RESULTS

To validate the proposed model, extensive simulations were performed.

First we have extracted the parameters for a single PEM fuel cell according to the method described in [7] and the characteristics given in [9]. The simulation results are given in Fig. 3-b, while the corresponding measured characteristics in Fig. 3-a.


(a)

(b)
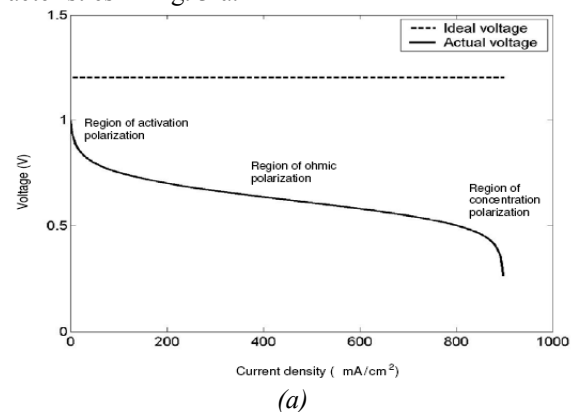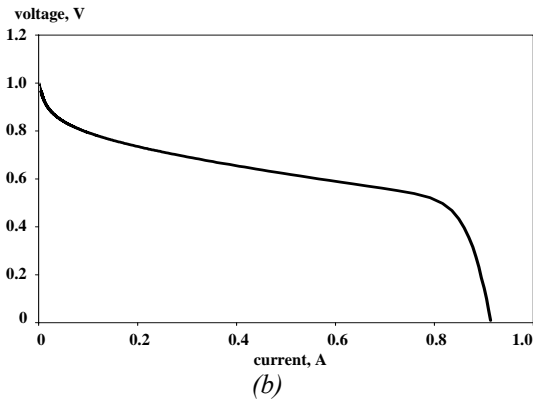
Fig. 3. - *a) characteristics of a real single PEMFC according [9]; b) simulation results using the extended model with k=1, m=1.*


(a)

(b)
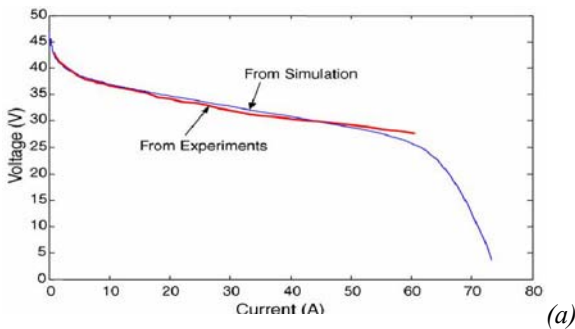
Fig 4. - *a) I-V characteristics of a PEM fuel cell from experiment and simulation [7] [12], b) I-V characteristics of a PEM fuel cell by simulationusing extended model with k=80, m=45.*

The static and dynamic characteristics of different PEM fuel cell stacks obtained through simulation are compared with some experimental results, given in the references, measured on a comercial PEM fuel cell modules, [12]-[14]. Some of them are presented below.

In Fig. 4 we show comparative diagrams obtained experimentaly (given in [7] and [12]) and by simulation with the parametric model for a fuel cell stack 45 V, 60 A. All values of the used parameter can be seen in the PSpice listing given in the appendix.


(a)

(b)
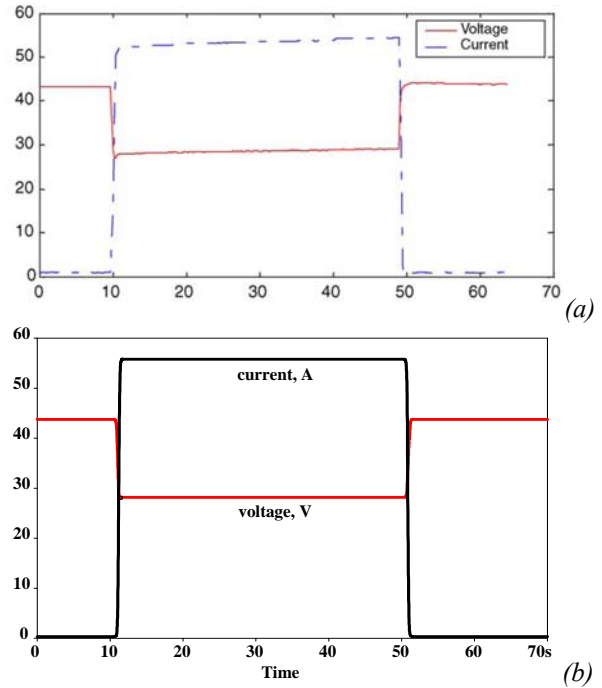
Fig. 5. - *Transient characteristics of a PEM fuel cel: a) experimental waveforms [7], b) simulated waveforms usig extended model with k=80, m=45 (L≅l1.3mH, C≅7.2F).*

For the dynamic response we have used the equations (15) and (16). In the lack of real elementary fuel cell, the initial values C_0 and L_0 were determined using trial and error method. The load was changed suddenly from 124 to 0.5 ohm. The experimental and simulation results are shown in Figs. 5 - *a* and *b*. It is seen that the undershoots in the two waveforms agree.

6. CONCLUSIONS

An extended (parametric) circuit model for the PEM fuel cell stack based on the model presented in [7] is developed. It allows us to develop a generalized model for a *PEM* fuel cell that can be used for design and analysis of fuel cell power systems with different voltage and current capabilities.

The simple model, which can be used in the design of fuel cell power systems uses a diode and a pair of BJTs for describing the static conditions. A capacitor and an inductor are used to represent the dynamic conditions, which occur in switching power systems. All the elements used in the model are from the PSpice library and slight changes are made in the parameter values. The model is validated by comparing the simulation and experimental results obtained on a commercial fuel cell modules.

We should note that because some of the values, for the transistor and diode parameters, have no real values the proposed model is useful only for simulation purposes but not for realization of fuel cell simulator.

Although the model does not include the temperature and pressure dependences of the *I-V* characteristics of a PEM fuel cell these can be easily added in the model by behavioral modeling of the *emf* source and some of the circuit parameters according to the Nernst equation [8].

7. REFERENCES

[1] S. Yerramalla, A. Davari, A. Feliachi, "*Dynamic modeling and analysis of polymer electrolyte fuel cell*", Proceedings of the IEEE Power Engineering Society Summer Meeting, vol. 1, 2002, pp. 82–86.

[2] J.B. van der Merwe, C. Turpin, T. Meynard, B. Lafage, "*The installation, modeling and utilization of a 200W PEM fuel cell source for converter based applications*", Proceedings of the IEEE Power Electronics Specialists Conference, 2002, pp. 333–338

[3] K. Dannenberg, P. Ekdunge, G. Lindbergh, "*Mathematical model of the PEMFC*", J. Appl. Electrochem. 30 (2000) pp. 1377–1387.

[4] A. Kazim, H.T. Liu, P. Forges, "*Modeling of performance of PEM fuel cells with conventional and interdigitated flow fields*", J. Appl. Electrochem. 29 (1999) pp. 1409–1416.

[5] W. Turner, M. Parten, D. Vines, J. Jones, T. Maxwell, "*Modeling a PEM fuel cell for use in a hybrid electric vehicle*", Proceedings of the IEEE Vehicular Technology Conference, 1999, pp. 16–20.

[6] R. Gemmen, P. Famouri, "*PEM fuel cell electric circuit model*", Proceedings of the Power Electronics for Fuel Cells Workshop, 2002.

[7] D. Yu, S. Yuvarajan, "*Electronic circuit model for proton exchange membrane fuel cells*", Journal of Power Sources 142 (2005). pp. 238–242

[8] National Energy Technology Laboratory, "*Fuel Cell Hand Book*", fifth ed., 2000, pp. 2.1–2.9.

[9] J. Larminie, A. Dicks, "*Fuel Cell Systems Explained*", John Wiley & Sons, 2000.

[10] D. Chu, R. Jiang, C. Walker, "*Analysis of PEM fuel cell stacks using an empirical current–voltage equation*", J. Appl. Electrochem. 30 (2000) pp. 365–370.

[11] MicroSim Corporation, "*MicroSim Pspice A/D Reference Manual*", Version 7.1, 1996.

[12] Ballard Power System, "*Nexa Power Module Integration Guide*", 2003.

[13] Robert Balog, "*Low Cost fuel Cell Inverter*", Ilinois's Future Challenge 2001Report, 2001.

[14] "*Data sheet of a 500W fuel cell stack*", BCS Technology, Bryan, 2001.

APPENDIX

```
*Fuel Cell
    .param k=80
    .param m=45
V1 1 0 {1.12*m}
r1 1 2 {30*m/k}
c1 2 0 {0.002*k*m}
q1 1 2 3 npnq1 {4.5*k}
.model npnq1 npn(bf={2500} is={(1e-16)} nf={m/45})
l1 3 4 {60m*m/(k*sqrt(sqrt(k)))}
q2 2 4 5 npnq2 {4.5*k}
.model npnq2 npn(bf={2500} is={(1e-16)} nf={m/45})
r2 4 5 {.02*m/k}
d 5 6 d1 {8*k/m}
.model d1 d(n={2*m} is={.00005*m} rs={1.5*m/k})
*rl1 6 0 {110*2*m/k}
*rl2 6 7 {.45*2*m/k}
*sw 7 0 10 0 s1
*.model s1 vswitch(ron=.1m von=0  roff=1e6 voff=1v)
*vsw 10 0 pwl(0 1 10 1 12 0 50 0 52 1)
*rsw 10 0 10meg
rl 6 0 rmod 1
.model rmod res
*.tran .01 70 0 10m

.DC LIN res rmod(r) .01 500 .05
.OPTIONS ITL4=40
.OP
.lib nom.lib
.probe
.END
```

SINGLE-PHASE SHORT-CIRCUIT CURRENT DISTRIBUTION IN MICROHYDROPLANTS

Constantin Blaj, Dumitru Toader, Marian Greconici

"Politehnica" University of Timişoara, Faculty of Electrical Engineering, Timişoara, Romania

Abstract: *The design of earth installation for microhydroplants must take into account that in neither of the functioning regimes the admissible values of touch voltage and pace voltage not to be exceeded. These voltages reach maximal values when the currents in earth installation are maximal, such as in single-phase short-circuit. In the paper are considered three cases: short-circuit to earth installation of microhydroplants; short-circuit to earth installation of transformer o,4/20kV; short-circuit to earth installation of low voltage consumer (0,4kV). The method of symmetrical components is used, considering that voltages as well as currents have sinusoidal time variation.*

Keywords*: Electrical circuits/ Three-phase networks/Earth installation/ Single-grounding faults*

1. INTRODUCTION

To design a micro hydro power plant (MHC) respectively a small hydroelectric power plant (CHEMP) it was necessary to review and complete the norms for dimensioning the station earthing. The economically dimensioning of the station earthing, taking in consideration all the technical conditions, needs to have the values for the currents, which occur in the most unfavorable regions from the point of view of the protection. For the dimensioning of the station earthing were considered single-phase short-circuit currents, because through these installations the currents have maximum values. The earthing of the substation and the MHC earth electrode or CHEMP earth electrode are made separately, but are connected through a steel flat band. The most common case is the case when to the low voltage bar are connected also consumers that are situated far from the MHC or CHEMP. The calculated results were verified by comparing them with the measured currents. For measurements were produced: a single-phase short-circuit at the MHC earth electrode, a short-circuit at the substation earth electrode, respectively at the consumers that are connected at the low voltage bar.

2. THE MATHEMATICAL MODEL FOR THE SINGLE-PHASE SHORT-CIRCUIT CURRENT CALCULATION

In figure 1 it is presented the single-phase installation scheme on which were calculated the single-phase short-circuit currents and their distribution. Three cases were considered: when the single-phase short-circuit it is at the MHC earth electrode, at the substation earth electrode, respectively at the asynchronous motor carcass. Short-circuit currents and their repartition are determinated by experiment too.
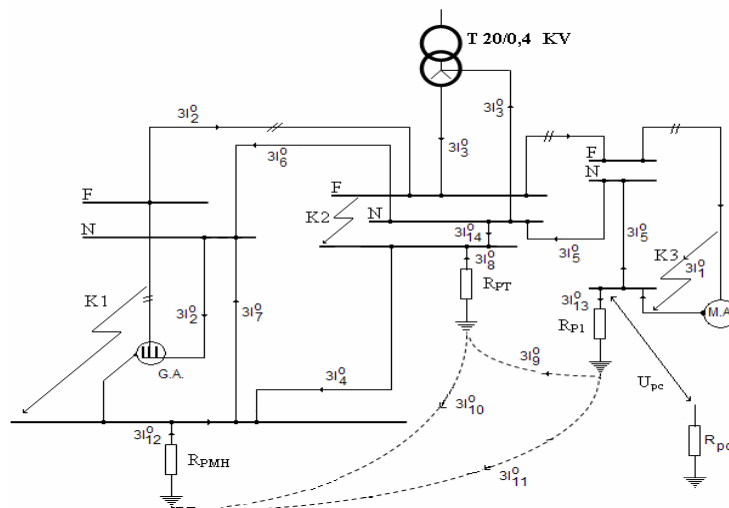

Fig. 1. *Single-phase installation scheme and the short-circuit currents.*

In this figure the notations have the following meaning: T − transformer (20/0.4 kV); H.G.A.- hydro generator made with an asynchronous generator; M.A. − asynchronous motor supplied from MHC or CHEMP; R_{PT} − the substation earth electrode resistance; R_{PMH} − the resistance of the earth electrode of the MHC; R_{P1} − earth electrode resistance of the consumer; R_{P0} − earth electrode resistance from the point considered the null point; $3I_1^0$ − single-phase short-circuit current; $3I_2^0$ − single-phase short-circuit current at the asynchronous generator; $3I_3^0$ − single-phase short-circuit current put out at the system; $3I_4^0$ − current, which flows through the flat band connecting the MHC, earth electrode with the substation earth electrode; $3I_5^0$ − the current through the conductor, which connects the substation null with the consumer null; $3I_6^0$ − the current through the conductor, which connects the substation null with the MHC null; $3I_7^0$ − the current through the cable which connects the MHC null with the MHC station earthing; $3I_8^0$ − the current through the substation plug; $3I_9^0$

– the current through the ground between the consumer plug and the substation; $3I_{10}^0$ – the current through the ground between the substation plug and MHC; $3I_{11}^0$ – the current through the ground between the consumer plug and MHC; $3I_{12}^0$ – the current through the MHC plug; $3I_{13}^0$ – the current through the consumer earthing; $3I_{14}^0$ – the current through

the cable which connects the transformer's null with the earthing of the substation.

For the calculation of the single-phase short-circuit currents was used the symmetrical components method [1, 2]. In figure 2 it is presented the connection mode of the sequence schemes for the three considerate short-circuits [3, 4, 5].
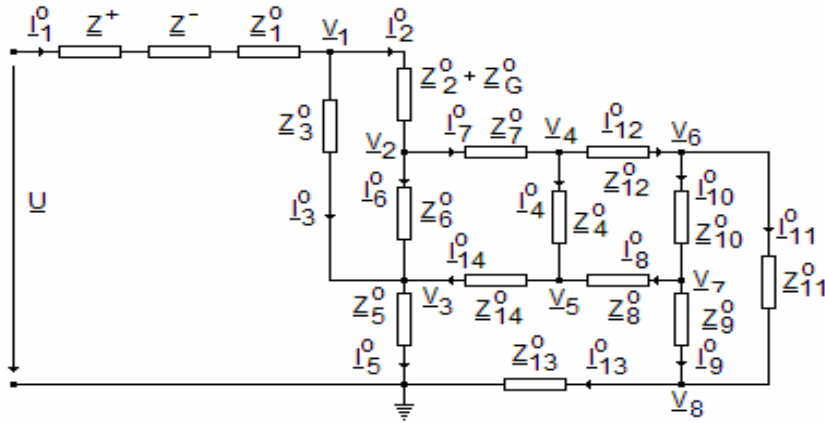

Fig. 2. *The sequences scheme connection mode in single-phase short-circuit case at the MHG plug*

The impedances which appear in the sequences scheme have the following meaning [6, 7]: Z_{1T}, Z_{2T}, Z_{0T} –the sequence impedances of the transformer 20/0.4 kV; Z'_{1L}, Z'_{2L}, Z'_{0L} – the sequence impedances of the electric line from the substation to the MHC bars; Z''_{1T}, Z''_{2T}, Z''_{0T} – the sequence impedances of the electric line from the asynchronous generator terminals to the MHC bars; R_1 – the limitation resistance of the single-phase short-circuit current; $X_{\sigma 1}$ – the dispersion reactance of the asynchronous generator stator; $X'_{\sigma 2}$ – the dispersion reactance of the asynchronous generator rotor reduced at the stator; R'_2/S – the rotor resistance of the asynchronous generator reduced at the stator; C – the phase capacity of the condenser battery on the MHC bars; Z_{1L}, Z_{2L}, Z_{0L} – sequence impedances of the electric line from the substation bars to the consumer; Z_{NA} – the cable impedance, which connects the transformer 20/0.4 kV null to the null substation bars; Z_{NB} – the cable impedance, connecting the MHC null bars with the substation null bars; Z_{NC}– the impedance of the cable connecting the asynchronous generator null with the MHC null bars; Z_{ND} – the cable impedance, connecting the substation null bars with the consumer null control panel; Z_1 – the flat band impedance, connecting the MHC plug with the substation plug; Z'_1 – the steel cable flat band, which connects the consumer control panel null with the earth electrode of the consumer; Z_{N1} – cable impedance, which connects the MHC plug with the MHC null bars; Z_{P1} – the ground impedance between MHC plug and earthing plate of the consumer; Z_{P2} – the ground impedance between the substation plug and consumer plug; Z_P – the ground impedance between MHC plug and the substation plug; R_{P1} – the dispersion consumer earth electrode resistance; R_{PT} – the resistance of the earthing plate of the substation; R_{PMH} - the resistance to earthing of the MHC; ; Z_{Ne} the impedance of the cable that connects the earthing of the transformer to the null, Z_{p3} — the impedance of the earth between the earth plate of the transformer and that of the microhydroplant. In

the scheme from figure 2, the relation that gives the source voltage is the following:

$$\underline{U} = \frac{U_{ff}\frac{1}{j\omega C}}{\underline{Z}^* + \frac{1}{j\omega C}} \quad , \text{ where}$$

$$\underline{U}_{ff} = \frac{\underline{U}_{f1}\left(jX_{\sigma 1} + \underline{Z}''_{1L}\right) + \underline{U}_{f2}\left(\underline{Z}_{1T} + \underline{Z}'_{1L}\right)}{jX_{\sigma 1} + \underline{Z}_{1T} + \underline{Z}''_{1L} + \underline{Z}'_{1L}} \quad (1)$$

The equivalent impedance is:

$$\underline{Z}_E = \frac{\underline{Z}^*\frac{1}{j\omega C}}{\underline{Z}^* + \frac{1}{j\omega C}} \quad = R_E + jX_E, \text{ where}$$

$$\underline{Z}^* = \frac{\left(jX_{\sigma 1} + \underline{Z}''_{1L}\right)\left(\underline{Z}_{1T} + \underline{Z}'_{1L}\right)}{jX_{\sigma 1} + \underline{Z}_{1T} + \underline{Z}''_{1l} + \underline{Z}'_{1L}} \quad (2)$$

$$\underline{Z}^+ = \underline{Z}^- = \frac{\left(Z_{2T} + Z'_{2L}\right)\cdot\dfrac{\left(R'_2 + jX'_\sigma + jX_{\sigma 1} + \underline{Z}''_{2L}\right)\cdot\left(\frac{1}{j\omega C}\right)}{R'_2 + jX'_\sigma + \underline{Z}''_{2L} + \frac{1}{j\omega C}}}{Z_{2T} + Z'_{2L} + \dfrac{(R'_2 + jX'_\sigma + jX_{\sigma 1} + \underline{Z}''_{2L})\cdot\frac{1}{j\omega C}}{R'_2 + jX'_\sigma + jX_{\sigma 1} + \underline{Z}''_{2L} + \frac{1}{j\omega C}}}$$

$$= R_2 + jX_2 \quad (3)$$

In order to calculate the single-phase short-circuit currents on each circuit branch presented in fig. 2 the nodes voltage method it is used. Using this method, for $V_G = 0$, we obtain the following equations (4):

$$V_1\left(\frac{1}{\underline{Z}^+ + \underline{Z}^- + \underline{Z}_1^0} + \frac{1}{\underline{Z}_G^0 + \underline{Z}_2^0} + \frac{1}{\underline{Z}_3^0}\right) - \frac{V_2}{\underline{Z}_2^0 + \underline{Z}_G^0} - \frac{V_3}{\underline{Z}_3^0} = \frac{U}{\underline{Z}^+ + \underline{Z}^- + \underline{Z}_1^0}$$

$$V_2\left(\frac{1}{\underline{Z}_7^0} + \frac{1}{\underline{Z}_G^0 + \underline{Z}_2^0} + \frac{1}{\underline{Z}_6^0}\right) - \frac{V_1}{\underline{Z}_2^0 + \underline{Z}_G^0} - \frac{V_3}{\underline{Z}_6^0} - \frac{V_4}{\underline{Z}_7^0} = 0$$

$$V_4\left(\frac{1}{\underline{Z}_{71}^0} + \frac{1}{\underline{Z}_4^0} + \frac{1}{\underline{Z}_{12}^0}\right) - \frac{V_2}{\underline{Z}_7^0} - \frac{V_5}{\underline{Z}_4^0} - \frac{V_6}{\underline{Z}_{12}^0} = 0$$

$$\underline{V}_3\left(\frac{1}{\underline{Z}_6^0}+\frac{1}{\underline{Z}_5^0}+\frac{1}{\underline{Z}_{14}^0}\right)-\frac{\underline{V}_2}{\underline{Z}_6^0}-\frac{\underline{V}_5}{\underline{Z}_{14}^0}=0$$

$$\underline{V}_5\left(\frac{1}{\underline{Z}_4^0}+\frac{1}{\underline{Z}_{14}^0}+\frac{1}{\underline{Z}_8^0}\right)-\frac{\underline{V}_3}{\underline{Z}_{14}^0}-\frac{\underline{V}_4}{\underline{Z}_4^0}-\frac{\underline{V}_7}{\underline{Z}_8^0}=0$$

$$\underline{V}_6\left(\frac{1}{\underline{Z}_8^0}+\frac{1}{\underline{Z}_{10}^0}+\frac{1}{\underline{Z}_{11}^0}\right)-\frac{\underline{V}_4}{\underline{Z}_{12}^0}-\frac{\underline{V}_7}{\underline{Z}_{10}^0}-\frac{\underline{V}_8}{\underline{Z}_{11}^0}=0$$

$$\underline{V}_7\left(\frac{1}{\underline{Z}_{10}^0}+\frac{1}{\underline{Z}_9^0}+\frac{1}{\underline{Z}_8^0}\right)-\frac{\underline{V}_6}{\underline{Z}_{10}^0}-\frac{\underline{V}_8}{\underline{Z}_9^0}-\frac{\underline{V}_5}{\underline{Z}_8^0}=0$$

$$\underline{V}_8\left(\frac{1}{\underline{Z}_9^0}+\frac{1}{\underline{Z}_{11}^0}+\frac{1}{\underline{Z}_{13}^0}\right)-\frac{\underline{V}_6}{\underline{Z}_{11}^0}-\frac{\underline{V}_7}{\underline{Z}_9^0}=0 \qquad (4)$$

The impedances from the group of relations (4) are:

$$\underline{Z}_1^o=3\cdot R_1 \ ; \quad \underline{Z}_3^o=3\cdot \underline{Z}_{Na} \ ; \quad \underline{Z}_4^o=3\cdot \underline{Z}_1 \ ;$$

$$\underline{Z}_5^o=3\cdot \underline{Z}_1' \ ; \quad \underline{Z}_6^o=3\cdot \underline{Z}_{Nb} \ ; \quad \underline{Z}_7^o=3\cdot \underline{Z}_{N1} \ ;$$

$$\underline{Z}_8^o=3\cdot R_{PT} \ ; \quad \underline{Z}_9^o=3\cdot \underline{Z}_{p2} \ ; \quad \underline{Z}_{10}^o=3\cdot \underline{Z}_{p3} \ ;$$

$$\underline{Z}_{11}^o=3\cdot \underline{Z}_{p1} \ ; \quad \underline{Z}_{12}^o=3\cdot R_{PMH} \ ;$$

$$\underline{Z}_{13}^o=3\cdot R_{p1} \ ; \qquad \underline{Z}_{14}^o=3\cdot \underline{Z}_{Ne} \ ;$$

$$\underline{Z}_2^o+\underline{Z}_G^0=3\cdot \underline{Z}_{Nc}+R_2'+j(X_{\sigma 1}+X_{\sigma 2}') \qquad (5)$$

The currents result as follows:

$$I_1^o=\frac{U-\underline{V}_1}{\underline{Z}^+ + \underline{Z}^- + \underline{Z}_1^o} \ ; \qquad I_2^o=\frac{\underline{V}_1-\underline{V}_2}{\underline{Z}_2^o+\underline{Z}_G^o} \ ; \qquad I_3^o=\frac{\underline{V}_1-\underline{V}_3}{\underline{Z}_3^o} \ ;$$

$$I_4^o=\frac{\underline{V}_4-\underline{V}_5}{\underline{Z}_4^o} \ ; \qquad\qquad\qquad\qquad\qquad I_5^o=\frac{\underline{V}_3}{\underline{Z}_5^o} \ ;$$

$$I_6^o=\frac{\underline{V}_2-\underline{V}_3}{\underline{Z}_6^o} \ ; I_7^o=\frac{\underline{V}_2-\underline{V}_4}{\underline{Z}_7^o} \ ; I_8^o=\frac{\underline{V}_7-\underline{V}_5}{\underline{Z}_8^o} \ ;$$

$$I_9^o=\frac{\underline{V}_7-\underline{V}_8}{\underline{Z}_9^o} \ ; I_{10}^o=\frac{\underline{V}_6-\underline{V}_7}{\underline{Z}_{10}^o} \ ; I_{11}^o=\frac{\underline{V}_6-\underline{V}_8}{\underline{Z}_{11}^o} \ ;$$

$$I_{12}^o=\frac{\underline{V}_4-\underline{V}_{36}}{\underline{Z}_{12}^o} \ ; I_{13}^o=\frac{\underline{V}_8}{\underline{Z}_{13}^o} \ ; I_{14}^o=\frac{\underline{V}_5-\underline{V}_3}{\underline{Z}_{14}^o} \qquad (6)$$

3. NUMERICAL AND EXPERIMENTAL RESULTS

For the considerate situation it were determined the values for the impedances from figure 2. With these values were calculated the nodes voltages (relations 2) respectively the currents from the circuit branches (relations 5).

The values are presented in table 1.

Table 1: *Calculated and measured currents values*

Short-circuit place	MHC plug			Substation plug			Consumer		
Currents	Calcu-lated	Meas-ured	Error %	Calcu-lated	Meas-ured	Error %	Calcu-lated	Meas-ured	Error %
I_{01} (A)	162	150	8	156,3	142,7	8,7	295	282	4,4
I_{02} (A)	74.2	68,2	8	61,7	54,9	11	102	95	6,9
I_{03} (A)	80.3	76	5	102,1	95,4	6,6	193	185,5	3,9
I_{04} (A)	8.2	6,82	2	10,2	9,3	8,8	16	14	12,5
I_{05} (A)	0,.31	0	-	1,58	1,71	-8,9	251,6	242,3	3,7
I_{06} (A)	71	66	7	56,3	52	7,6	45,4	41,3	9
I_{07} (A)	139.4	134,2	3	10,2	9,3	8,8	61	54	11,5
I_{08} (A)	4.3	3,4	26	0,88	0,65	26	2,1	1,9	9,5
I_{09} (A)	0,21	0	-	0,26	0	-	2,3	1,9	17,4
I_{010} (A)	4,2	3,4	23	0,31	0,38	23	0,5	0,49	2,1
I_{011} (A)	0,25	0		1,84	1,71	7,1	43,1	40,3	6,5
I_{012} (A)	3.9	3,4	14	2,15	1,62	25	43,6	40,8	6,5
I_{013} (A)	0,21	0	-	1,58	1,71	-8,9	43,4	40	7,8
I_{014} (A)	12.1	10.15	19	145,2	136,3	6,1	16,2	14,1	13

From the table 1 results that the differences between the calculated currents values and measured currents values are acceptable. Taking in consideration the accepted simplifications in the calculation, the differences are acceptable from a technical point of view. These differences are acceptable also because the possibilities to measure the parameters that appear in the single-phase short circuit current calculation are limited.

4. CONCLUSIONS

When exists connections between the substation null and MHC null, a single phase short-circuite at the MHC earth electrode or at the substation earth electrode will not determinate high values currents through both earth electrodes and trough the consumer earth electrode doesn't exist current. Because of the low cable impedance which connects the substation null with the MHC null, the single-phase short-circuit current values are much bigger than the current which is closed through the earth electrode. For this reason it is not necessary to impose special design conditions from the MHC earth electrode-dimensioning point of view. The two earth electrodes, R_{PT} and R_{MHC}, are connected through a steel band with Z_1 impedance and also the PT null is connected with MHC null, results that the risk of interrupting the connection between the earth electrodes is practically zero.

When the short-circuit is produced at the consumer earth electrode, the current value which is closed through this earth electrode has a value of about 120 A, which determinates a 136 V voltage at the earth electrode. This is a dangerous voltage for the work safety. Although the consumer earth electrode current represents only 14,2 % from the single-phase short-circuit current, this value determinates a dangerous earth electrode voltage. For this reason it is necessary to use a consumer earth electrode with low resistance value and also the connections between the earth electrodes must be made by low impedances cables.

5. REFERENCES

[1] Bercovici, M., Arie, A., Poeată, Al.: *Electric Networks.* Editura Tehnică, Bucureşti, 1974.

[2] Şora, C.: *Fundamentals of Electrotechnics.* Editura didactică şi pedagogică, Bucureşti, 1982.

[3] Toader, D.: *Contributions to the study of broken-and grounded conductor fault in a medium voltage network.* PhD thesis, Universitatea „Politehnica" Timişoara, 1986.

[4] Buta, A., Milea, L., Pană, A.: *The Harmonic Impedance of the Networks of the Electro energetic Systems.* Editura Tehnică, Bucureşti, 2000

[5] Vinţan, M.: *Single Phase Short Circuit in High Voltage Electric Networks.* Editura Matrix Rom, Bucureşti, 2003

[6] Toader, D., Hristea, V.: *The Calculation of the Parameters which Determine the Zero-Sequence Voltage in a Double Broken-and Grounded Conductor Fault in a Medium Voltage Network*, Simpozionul Naţional de Reţele Electrice Timişoara, Oct. 1984, vol. II, pp.138-150

[7] Toader, D., Hărăguş, Şt.: *Variation of the Zero-sequence Voltage in Power Networks with Switchable Neutral Compensation*, Analele Universităţii Oradea, 1999, pp.12-18

INSTRUCTION FOR AUTHORS

Name of the author/s, Affiliation/s

Abstract: *Short instruction for authors is presented in this paper. Works that are to be printed in the review "Electronics" should be typed according to this instruction.*
Keywords: *Review Electronics, Faculty of Electrical Engineering in Banjaluka, Instruction for authors.*

1. INTRODUCTION

In the review "Electronics", we publish the scientific and professional works from different fields of electronics in the broadest sense like: automatics, telecommunications, computer techniques, power engineering, nuclear and medical electronics, analysis and synthesis of electronic circuits and systems, new technologies and materials in electronics etc. In addition to the scientific and professional works, we present new products, new books, B. Sc., M. Sc. and Ph.D. theses.

In order to enable the unification of the technical arrangement of the works, to simplify the printing of the review "ELECTRONICS", we are giving this instruction for the authors of the works to be published in this professional paper.

2. TECHNICAL DETAILS

2.1. Submitting the papers

The works are to be delivered to the editor of the review by the E-mail (elektronika@etfbl.net) or on floppy (or CD) by post mail to the address of the Faculty of Electrical Engineering (Elektrotehnicki fakultet, Patre 5, 78000 Banja Luka, Republic of Srpska, Bosnia and Herzegovina).

2.2. Typing details

The work has to be typed on the paper A4 format, 8.27" width and 11.69" height (21.0x29.7 cm), upper margin of 1" (2.54 cm) and lower margin of 0,59" (1,5 cm), left and right margins of 1,57" (2 cm) and 0,39" (1cm) (mirrored margins). The header and footer are 0,5" (1.27cm) and 57" (2 cm). The work has to be written in English language. Our suggestion to the authors is to make their works on a PC using the word processor MS WORD 97/2000, and for the figures to use the graphic program CorelDraw, if the graphs are not going from the original programs, i.e., from the programs received (like MATLAB).

The title of the work shall be written on the first page, in bold and 12 pt. size. Also, on the first page, moved for one line spacing from title, the author's name together with the name of his institution shall be printed in the letter size (10pt, *Italic)*. The remaining parts of the manuscript shall be done in two columns with 0.5cm distance. The work shall be typed with line spacing 1 (Single) and size not less than 10 pt (like as this instruction). After the title of the work and the name of the author/s, a short content in English language follows, written in italics. The subtitles in the text shall be written in bold, capital letters of the size as in the text (not less than 10 pt.). Each work shall, at the beginning, comprise a subtitle INTRODUCTION, and, at the end, the subtitles CONCLUSION and BIBLIOGRAPHY / REFERENCES.

The operators and size marks that do not use numerical values, shall be written in common letters. The size marks that can use numerical values shall be written in italics. The equations shall be written in one column with right edge numeration. If the breaking of equations or figures is desired, those may be placed over both columns.

Illustrations (tables, figures, graphs etc.) may be wider than one column if necessary. Above a table there shall be a title, for instance: Table 2. *The experimental measuring results.* The same applies to figures and graphs but the accompanying text comes underneath the figure of graphs, for instance: Fig.3: *Equivalent circuit diagram...*

The work should not be finished at the beginning of a page. If the last manuscript page is not full, the columns on that page should be made even. Number of pages should not go over 6.

3. CONCLUSION

This short instruction is presented in order to enable the unification of technical arrangement of the works.

4. REFERENCES

At the end of work, the used literature shall be listed in order as used in the text. The literature in the text, shall be enclosed in square brackets, for instance: ...in [2] is shown ...

ELECTRONICS, Vol. 11, No. 1-2, December 2007.